

A STUDY OF METHODS TO PREDICT AND MEASURE THE TRANSMISSION  
OF SOUND THROUGH THE WALLS OF LIGHT AIRCRAFT

Purdue Research Foundation 520-1288-0353

Numerical Method for Analyzing  
the Optimal Performance of Active  
Noise Controllers

Sponsored by  
NASA

Report No. 0353-8

HL 87-25P

Submitted by:

Christopher G. Mollo, Graduate Research Assistant  
Robert J. Bernhard, Principal Investigator

Approved by:

Raymond Cohen, Director

August 1987

## TABLE OF CONTENTS

	Page
LIST OF TABLES .....	v
LIST OF FIGURES .....	vi
LIST OF SYMBOLS .....	xiii
ABSTRACT .....	xviii
CHAPTER 1 - INTRODUCTION .....	1
CHAPTER 2 - LITERATURE REVIEW .....	6
2.1 Historical Development Of Active Noise Controllers .....	6
2.2 Active Noise Control In Enclosures .....	10
2.2.1 One-Dimensional Enclosures .....	11
2.2.2 Two And Three-Dimensional Enclosures .....	23
2.3 Active Noise Control In Free Space .....	31
2.4 Conclusions .....	35
CHAPTER 3 - THE INDIRECT BOUNDARY ELEMENT METHOD .....	38
3.1 Theory .....	40
3.2 Numerical Implementation .....	47
3.3 Verification .....	57
3.3.1 Spherical Boundary Results .....	58
3.3.2 Rectangular Boundary Results .....	66
3.3.3 Summary .....	72
CHAPTER 4 - AN OPTIMAL ACTIVE NOISE CONTROLLER FOR ENCLOSED SOUND FIELDS WITH COMPLETE SYSTEM DESCRIPTION .....	96
4.1 Problem Formulation .....	97
4.1.1 Introduction .....	97
4.1.2 The Control Objective Function .....	99
4.1.3 IBEM Formulation Of The Control Objective Function .....	101
4.1.4 An Optimal Controller .....	104

	Page
4.2 Case Study Results .....	106
4.2.1 Global Noise Control .....	109
4.2.2 Local Noise Control .....	115
4.2.3 Multiple Secondary Sources .....	118
4.2.4 Nonsymmetric Excitation .....	120
4.2.5 Effects Of Passive Noise Treatments .....	122
4.2.6 Conclusions .....	124
CHAPTER 5 - AN OPTIMAL ACTIVE NOISE CONTROLLER FOR FREE FIELD RADIATION .....	160
5.1 Problem Formulation .....	161
5.1.1 The Control Objective Function .....	161
5.1.2 IBEM Formulation Of The Control Objective Function .....	163
5.1.3 An Optimal Controller .....	166
5.2 Case Study Results .....	167
5.3 Conclusions .....	173
CHAPTER 6 - AN OPTIMAL ACTIVE NOISE CONTROLLER FOR ENCLOSED SOUND FIELDS WITH INCOMPLETE SYSTEM DESCRIPTION .....	183
6.1 Problem Formulation .....	184
6.1.1 IBEM Formulation Of The Control Objective Function .....	185
6.1.2 An Optimal Controller .....	189
6.1.3 Stability .....	190
6.1.4 Observability And Controllability .....	192
6.2 Case Study Results .....	193
6.3 Conclusions .....	199
CHAPTER 7 - CONCLUSIONS AND RECOMMENDATIONS .....	212
7.1 Conclusions .....	212
7.2 Recommendations .....	215
LIST OF REFERENCES .....	218

## LIST OF TABLES

Table	Page
4.1 Eigenfrequencies Of The Rectangular Prism.....	107
5.1 Secondary Source Data For Cases VII-X.....	170
5.2 Secondary Source Data For Cases XI-XIV.....	171
5.3 Secondary Source Data For Cases XV-XVIII.....	172

## LIST OF FIGURES

Figure	Page
2.1 General Schematic Of A One-Dimensional Active Noise Controller.....	11
3.1 Geometrical Description For The Indirect Boundary Element Method Formulation.....	74
3.2 Polar Coordinates For An Element.....	75
3.3 Geometry For Integration Of The Fundamental Pressure Solution In Polar Coordinates.....	76
3.4 Analytical And Numerical Predictions For The Pressure At Half The Radius Of A Pulsating Sphere As A Function Of Frequency ( $\rho_o c = 1.0$ ).....	77
3.5 Adjusted Analytical Solution For The Pressure At Half The Radius Of A Pulsating Sphere ( $\rho_o c = 1.0$ ).....	78
3.6 Effect Of Element Mesh Size On The IBEM Solution For The Pressure At Half The Radius Of A Pulsating Sphere ( $\rho_o c = 1.0$ ).....	79
3.7 Analytical And Numerical Pressure Predictions At Half The Radius Of A Pulsating Sphere For The Low Frequency Regime ( $\rho_o c = 1.0$ ).....	80
3.8 Analytical And Numerical Predictions Of The Pressure Distribution For The Exterior Of A Pulsating Sphere At $k=0.01$ ( $\rho_o c = 1.0$ ).....	81
3.9 Analytical And Numerical Predictions Of The Pressure As A Function Of Frequency For The Exterior Of A Pulsating Sphere ( $\rho_o c = 1.0$ ).....	82
3.10 Analytical And Numerical Predictions For The Pressure At Half The Radius Of A Rigid Wall Sphere With A Point Source At The Center ( $\rho_o c = 1.0$ ).....	83

Figure	Page
3.11 Analytical And Numerical Predictions For The Pressure At Half The Radius Of A Sphere With Free Field Impedance Boundary Conditions And A Point Source At The Center ( $\rho_o c = 1.0$ ).....	84
3.12 80 Element Rectangular Cavity Model.....	85
3.13 Analytical And Numerical Predictions Of The Pressure Distribution Near The Center Of The Driven-Rigid Cavity At $k=2.0$ ( $\rho_o c = 415.0$ ).....	86
3.14 Analytical And Numerical Predictions Of The Pressure Distribution Along An Edge Of The Driven-Rigid Cavity At $k=2.0$ ( $\rho_o c = 415.0$ ).....	87
3.15 Effect Of Element Mesh Size On The IBEM Solution For The Pressure Distribution Along The Center Of A Driven-Rigid Cavity At $k=2.0$ ( $\rho_o c = 415.0$ ).....	88
3.16 Effect Of Element Mesh Size On The IBEM Solution For The Pressure Distribution Along An Edge Of A Driven-Rigid Cavity At $k=2.0$ ( $\rho_o c = 415.0$ ).....	89
3.17 Effect Of Element Mesh Size On The Behavior Of The Quantity $\tau$ In The Fundamental Solutions For Domain Locations Close To The Boundary.....	90
3.18 Analytical And Numerical Pressure Predictions As A Function Of Frequency For A Location In The Center Of A Driven-Rigid Cavity ( $\rho_o c = 415.0$ ).....	91
3.19 Analytical And Numerical Pressure Predictions As A Function Of Frequency For A Location In The Center Of A Driven-Rigid Cavity ( $\rho_o c = 415.0$ ).....	92
3.20 Analytical And Numerical Pressure Predictions As A Function Of Frequency For A Location Near The Corner Of A Driven-Rigid Cavity ( $\rho_o c = 415.0$ ).....	93

Figure	Page
3.21 Analytical And Numerical Pressure Predictions As A Function Of Frequency For A Location Near The Corner Of A Driven-Rigid Cavity ( $\rho_c = 415.0$ ).....	94
3.22 Analytical And Numerical Pressure Predictions For The Driven-Infinite Cavity At $k=2.0$ ( $\rho_c = 415.0$ ).....	95
4.1 System Schematic For The Active Control Of Sound Fields With Complete System Description.....	127
4.2 Optimal Active Noise Controller Performance For A Secondary Source At Pulsating Polyhedron Center, Global Control (Case 1).....	128
4.3 The Normalized Optimal Secondary Source Strengths For A Secondary Source At Pulsating Polyhedron Center, Global Control (Case 1).....	129
4.4 The Uncontrolled And Controlled Pressure Distributions For Case 1 At (a) $k=4.0$ And (b) $k=5.0$ .....	130
4.5 Optimal Active Noise Controller Performance For A Secondary Source At Half The Radius Of A Pulsating Polyhedron, Global Control (Case 2)....	131
4.6 The Normalized Optimal Secondary Source Strengths For A Secondary Source At Half The Radius Of A Pulsating Polyhedron, Global Control (Case 2)....	132
4.7 Optimal Active Noise Controller Performance For Closely Coupled Primary And Secondary Sources A Distance $d$ Apart In A Rigid Wall Polyhedron, Global Control.....	133
4.8 The Normalized Optimal Secondary Source Strengths For Closely Coupled Primary And Secondary Sources A Distance $d$ Apart In A Rigid Wall Polyhedron, Global Control.....	134
4.9 Optimal Active Noise Controller Performance For Closely Coupled Primary And Secondary Sources A Distance $0.01m$ Apart In A Rigid Wall Polyhedron, Global Control (Case 6).....	135

Figure	Page
4.10 The Normalized Optimal Secondary Source Strengths For Closely Coupled Primary And Secondary Sources A Distance 0.01m Apart In A Rigid Wall Polyhedron, Global Control (Case 6).....	136
4.11 Optimal Active Noise Controller Performance For A Secondary Source Located A Distance d From A Distributed Noise Source, Global Control.....	137
4.12 The Normalized Optimal Secondary Source Strengths For A Secondary Source Located A Distance d From A Distributed Noise Source, Global Control.....	138
4.13 Optimal Active Noise Controller Performance For A Secondary Source At (0.5m,0.5m,0.7808m) In A Driven-Rigid Cavity, Global Control (Case 10).....	139
4.14 The Normalized Optimal Secondary Source Strengths For A Secondary Source At (0.5m,0.5m,0.7808m) In A Driven-Rigid Cavity, Global Control (Case 10).....	140
4.15 Optimal Active Noise Controller Performance For A Secondary Source At (0.5m,0.5m,1.5288m) In A Driven-Rigid Cavity, Global Control (Case 11).....	141
4.16 The Normalized Optimal Secondary Source Strengths For A Secondary Source At (0.5m,0.5m,1.5288m) In A Driven-Rigid Cavity, Global Control (Case 11).....	142
4.17 The Normalized Optimal Secondary Source Strengths For One-Point Local Control Using One Secondary Source At Center Of Pulsating Polyhedron (Case 12).....	143
4.18 The Uncontrolled And Controlled Pressure Distributions For Case 12 At $k=2.0$ .....	144
4.19 The Normalized Optimal Secondary Source Strengths For One-Point Local Control Using One Secondary Source In A Driven-Rigid Cavity (Case 13).....	145
4.20 The Normalized Optimal Secondary Source Strengths For A Secondary Source Located A Distance d From An Observation Point In A Pulsating Polyhedron....	146



Figure	Page
4.21 Optimal Active Noise Controller Performance For Two Secondary Sources In A Pulsating Polyhedron, Global Control (Case 17).....	147
4.22 The Normalized Optimal Secondary Source Strengths For Two Secondary Sources In A Pulsating Polyhedron, Global Control (Case 17).....	148
4.23 Optimal Active Noise Controller Performance For Four Secondary Sources In A Pulsating Polyhedron, Global Control (Case 18).....	149
4.24 Profile Schematic Of An Oscillating Polyhedron....	150
4.25 Optimal Active Noise Controller Performance For Two Closely Coupled Secondary Sources At Center Of Oscillating Polyhedron, Global Control (Case 19).....	151
4.26 The Normalized Optimal Secondary Source Strengths For Two Closely Coupled Secondary Sources At Center Of Oscillating Polyhedron, Global Control (Case 19).....	152
4.27 The Normalized Optimal Secondary Source Strengths For Two Tightly-Coupled Secondary Sources At The Center Of A Pulsating 48 Sided Polyhedron.....	153
4.28 Optimal Active Noise Controller Performance For Different Values Of Resistive Passive Noise Treatment Component, Global Control.....	154
4.29 The Normalized Optimal Secondary Source Strengths For Different Values Of Resistive Passive Noise Treatment Component, Global Control.....	155
4.30 Optimal Active Noise Controller Performance For Different Values Of Reactive Passive Noise Treatment Component, Global Control.....	156
4.31 The Normalized Optimal Secondary Source Strengths For Different Values Of Reactive Passive Noise Treatment Component, Global Control.....	157
4.32 Optimal Active Noise Controller Performance For Different Values Of Passive Noise Treatment Surface Area.....	158

Figure	Page
4.33 The Normalized Optimal Secondary Source Strengths For Different Values Of Passive Noise Treatment Surface Area.....	159
5.1 Geometrical Description Of Cylindrical Shell Model.....	175
5.2 Comparison Of Optimal Controller Performance For Changes In Secondary Source Location (Along Z-axis) About Shell Model ( $a=0.1m$ ).....	176
5.3 Comparison Of Optimal Controller For Changes In Secondary Source Location (Along Z-axis) About Shell Model ( $a=0.1m$ ).....	177
5.4 Comparison Of Optimal Controller Performance For Changes In Secondary Source Location (Along X-axis) About Shell Model ( $a=0.1m$ ).....	178
5.5 Comparison Of Optimal Controller For Changes In Secondary Source Location (Along X-axis) About Shell Model ( $a=0.1m$ ).....	179
5.6 Comparison Of Optimal Controller Performance For Multiple Secondary Sources Symmetrically Located About Pulsating Sphere ( $a=1.0m$ ).....	180
5.7 Comparison Of Optimal Controller Performance For Multiple Secondary Sources Symmetrically Located About Shell Model ( $a=0.1m$ ).....	181
5.8 Comparison Of Optimal Controller Performance For Multiple Secondary Sources Asymmetrically Located About Shell Model ( $a=0.1m$ ).....	182
6.1 System Schematic For The Active Control Of Sound Fields With An Incomplete System Description.....	200
6.2 Block Diagram Representation Of The Active Noise Control System.....	201
6.3 Schematic Of The System For Case 1.....	202
6.4 Real And Imaginary Components Of (a) $H^0(\omega)$ And (b) The Impulse Response Function For Case 1.....	203
6.5 Bode Diagram For Case 1.....	204

Figure	Page
6.6 Real And Imaginary Components Of (a) $H^0(\omega)$ And (b) The Impulse Response Function For Case ii.....	205
6.7 Bode Diagram For Case ii.....	206
6.8 Real And Imaginary Components Of (a) $H^0(\omega)W(\omega)$ For $\omega = 171.5$ rad/sec And (b) The Corresponding IFFT For Case ii.....	207
6.9 Real And Imaginary Components Of (a) $H^0(\omega)W(\omega)$ For $\omega = 514.5$ rad/sec And (b) The Corresponding IFFT For Case ii.....	208
6.10 Real And Imaginary Components Of (a) $H^0(\omega)$ And (b) The Impulse Response Function For Case iii.....	209
6.11 Bode Diagram For Case iii.....	210
6.12 Real And Imaginary Components Of (a) $H^0(\omega)W(\omega)$ For $\omega = 171.5$ rad/sec And (b) The Corresponding IFFT For Case iii.....	211

## LIST OF SYMBOLS

<u>Symbol</u>	<u>Description</u>
$A$	Area of a boundary element
$ATN$	Attenuation
$a$	A characteristic dimension
$B$	Boundary
$B^-$	Boundary excluding small region around a singularity
$B_i$	Boundary element containing the known boundary condition
$B_j$	Boundary section contained by the $j^{th}$ element
$\bar{B}_i$	Vector locating the centroid of the $i^{th}$ element
$B_s^-$	Boundary element containing a singularity but excluding a small region about the singularity
$\bar{b}$	Vector locating a point on the boundary
$\bar{b}_I$	Vector locating the $I^{th}$ point on the boundary
$\bar{b}_i$	Vector locating a point on the $i^{th}$ boundary element
$\bar{b}_j$	Vector locating a point on the $j^{th}$ boundary element
$\bar{b}_s$	Vector locating a point on $B_s^-$
$c$	Wave speed
$c_b$	Singularity free term
$c_s$	Volume velocity units conversion factor

D	Domain
d	A distance
e	Natural logarithm base
f	Frequency in Hertz (Hz)
I	Identity matrix
j	$\sqrt{-1}$
k	Wavenumber
L	A length
l	A length
$\hat{n}$	Unit vector normal to the boundary
$n_{cp}$	Number of observation points
$n_{ps}$	Number of primary sources
$n_{ss}$	Number of secondary sources
ne	Number of elements
np	Number of domain locations
ns	Number of point sources
p	Acoustic pressure
$p^*$	Fundamental pressure solution
$\underline{p}$	Column vector of observation point pressures
$\underline{p}_d$	Column vector of detector location pressures
Q	Volume velocity source strength
$\underline{Q}_s^o$	Column vector of optimal volume velocity secondary source strengths
$Q_{sn}$	Volume velocity source strength of noise producing mechanism
q	Volume velocity source strength

$q_b$	Volume velocity source strength of an element
$\underline{q}_s$	Column vector of volume velocity secondary source strengths
$\underline{q}_s^o$	Column vector of optimal volume velocity secondary source strengths
$R(\theta)$	Limit of polar integration
$r$	A distance
$S$	Diagonal matrix of elemental surface areas
$s$	Surface area
$T_{nd}$	Transfer function matrix between noise source strengths and detector pressures
$T_{no}$	Transfer function matrix between noise source strengths and observation pressures
$T_{sd}$	Transfer function matrix between secondary source strengths and detector pressures
$T_{so}$	Transfer function matrix between secondary source strengths and observation pressures
$t$	Time
$U_o$	Surface velocity amplitude
$u$	Particle velocity
$u^*$	Fundamental velocity solution
$\hat{v}$	Unit vector at a domain location
$\bar{v}_d$	Vector locating a domain location
$\bar{v}_s$	Vector locating a source
$W$	Weighting matrix
$W(n)$	Window function
$w$	Weighting factor
	Sound power

$X, Y, Z$	Cartesian coordinates
$\bar{x}_d$	Vector locating a domain location
$\bar{x}_s$	Vector locating a point source
$z$	Specific acoustic impedance
$\underline{\alpha}$	Column vector of elemental boundary conditions
$\Omega$	Solid angle in steradians
$\omega$	Frequency in rad/sec
$\omega_h$	Window cut-off frequency
$\Delta\omega$	Discrete frequency step size
$\Pi$	Control objective function
$\Pi^o$	Optimal value of the control objective function
$\Pi_{pp}$	Uncontrolled value of the control objective function
$\pi$	3.14159...
$\psi$	Point source strength
$\underline{\psi}$	Column vector of source strengths
$\underline{\psi}_p$	Column vector of primary source strengths
$\underline{\psi}_s$	Column vector of secondary source strengths
$\underline{\psi}_s^o$	Column vector of optimal secondary source strengths
$\rho_o$	Equilibrium density of air
$\sigma(\bar{b})$	Fictitious source distribution
$\underline{\sigma}$	Column vector of fictitious source strengths
$\sigma_i$	Fictitious source strength of the $i^{\text{th}}$ element
$\sigma_j$	Fictitious source strength of the $j^{\text{th}}$ element
$\theta$	Limit of polar integration

$\theta$	Angular polar coordinate
$\zeta$	Complex scalar



## ABSTRACT

Mollo, Christopher Gerard. M.S.M.E., Purdue University. August 1987. A Numerical Method For Analyzing The Optimal Performance Of Active Noise Controllers. Major Professor: Dr. R.J. Bernhard, School of Mechanical Engineering.

An optimal active noise controller is formulated and analyzed for three different active noise control problems. The first problem formulated is the active control of enclosed or partially enclosed harmonic sound fields where the noise source strengths and enclosure boundary description are known. The enclosure boundary is described by either pressure, velocity, or impedance boundary conditions. The second problem formulated is the active control of the free field power radiated from a distributed noise source with a known time harmonic surface velocity. The third problem formulated is the active control of enclosed or partially enclosed harmonic sound fields where the noise source strengths or enclosure boundary description may not be known. All three formulations are derived using an indirect boundary element technique. Formulation and verification of an indirect boundary element method is presented. The active noise controller formulations for enclosures are capable of analyzing

systems with generalized enclosure shapes, point noise sources, and/or locally reacting impedance boundary conditions. For each formulation, representative results of optimal active noise controller case studies are presented, and some general conclusions are drawn.

## CHAPTER 1

### INTRODUCTION

Individuals are subjected to sound practically every moment of the day. The various sounds one encounters throughout the day can be classified into two general categories: (1) desired or welcomed sound or (2) unwanted sound or noise. It has long been recognized that noise can dramatically affect many aspects of human life. There has been much attention paid to the study of noise and its effects on people. Research has been conducted on the effects of noise on such aspects as blood pressure, hearing loss, sleep disturbances, cardiovascular systems, maternity, occupational stress, and auditory fatigue. Most of the literature addresses the problem of noise in the work place or noise in transportation vehicle passenger compartments. Excessive noise in the work place generally reduces employee productivity and is sometimes considered a health hazard. Likewise, a passenger's comfort level is adversely affected by excessive passenger compartment noise. Consequently, methods of reducing noise continue to

be studied with significant interest.

For the most part, noise is attenuated by means of passive methods. Passive methods either absorb energy from the acoustic system through the use of materials such as foams or block the transmission of acoustic energy with barriers. When the wavelength of the sound is small (i.e., the frequency is high), passive methods perform quite well. However, passive methods are inefficient when attenuation of relatively low frequency noise is desired. Very thick sound absorbing surfaces or heavy barriers are needed to effectively attenuate low frequency noise.

On the other hand, active noise attenuation methods perform best in the relatively low frequency regime (below 500 Hz) [1]. The concept of active noise attenuation was first documented by Paul Lueg in his 1934 U.S. Patent [2]. Lueg's concept of active noise attenuation is based on the principle of destructive interference of sound waves. The noise in the environment is attenuated by introducing additional sound energy of an appropriate form into the system. In general, the functional mechanisms of active noise attenuation are not as simple as Lueg described and to this day are not completely understood.

The objective of the research presented in this thesis is to develop a generalized numerical technique for evaluating the optimal performance of active noise

controllers. Most of the analysis of active noise controllers to date has been analytically performed for one-dimensional acoustic systems with plane wave propagation. Some analytical/numerical analysis of active noise controllers for two and three-dimensional acoustic systems has been reported. Analysis of two and three-dimensional acoustic systems has been restricted to regularly shaped geometries such as cylinders and rectangular prisms. However, some of the desired applications for active noise control involve acoustic systems with irregularly shaped boundaries and complex noise fields such as aircraft cabins and automobile passenger compartments. As the geometry and thus, the noise field becomes increasingly complex, analytical derivation of an optimal active noise controller becomes unrealistic. Hence, a need exists for a numerical analysis method for the evaluation of an optimal active noise controller for the generalized acoustic system.

Three numerical active noise controller optimization formulations were developed during the course of the research. The formulations were developed for different system configurations and assumptions. All formulations were implemented using an indirect boundary element method. The first formulation solves for the optimal transfer function between the noise source(s) and the controller actuator(s) which minimizes a performance criterion. The

analysis is performed for cavity active noise control problems where complete descriptions of the noise sources and cavity boundary are known. The second formulation solves for the optimal transfer function between the noise source and the controller actuator(s) such that the free field power radiated from the system is minimized. A surface velocity description of the noise source is assumed to be known. The third formulation is similar to the first except that no prior knowledge of the noise source magnitudes and phasing is assumed. The magnitude and phasing of the noise source(s) is deduced at measurement locations. The third formulation calculates an optimal transfer function between the measurement location(s) and the controller actuator(s) such that a performance criterion is minimized.

The thesis is organized as follows. Chapter 2 presents a literature review on active noise controllers for one-dimensional and three-dimensional systems. The development and verification of an indirect boundary element method is contained in chapter 3. Chapter 4 presents the development and results for the cavity problem where the noise source(s) and boundary description are known. The development and results for the free field radiation problem are discussed in chapter 5. The development and results for the cavity problem where the noise source(s) are of unknown value are discussed in

chapter 6. Conclusions and recommendations for further work are presented in chapter 7.

## CHAPTER 2

### LITERATURE REVIEW

Due to the capability of digital control systems, research investigations of active noise control (ANC) has been conducted with renewed emphasis over the last few years. Because this renewed interest in ANC is relatively young, there are only a limited number of researchers heavily involved in the field. However, a substantial body of literature is accumulating on the subject. This chapter provides a general summary of articles relating to the research presented in this thesis. First, a brief historical development of active noise controllers is presented. Second, articles pertaining to ANC problems in enclosures and articles addressing ANC in free space are discussed. Finally, some overall conclusions are drawn from the literature review.

#### 2.1 Historical Development Of Active Noise Controllers

In 1934 Paul Lueg filed for a patent which was subsequently granted to him in 1936 as Patent No.



2,043,416, "Process of Silencing Sound Oscillations" [2]. Lueg's patent is generally recognized as the first document on the process now labeled as active noise control. In Lueg's patent, he made practical use of the well known phenomenon of superposition of linear systems. For linear acoustic systems, the principle of superposition states that the acoustic response at a point in space is the sum of the acoustic responses at that point due to a number of individual sources. The principle of superposition is the basis for the phenomenon of constructive and destructive interference of acoustic waves. Lueg suggested that noise could be attenuated through destructive interference by artificially introducing additional sound into the system.

Lueg outlined the process of using destructive interference to eliminate noise for several situations. The first situation Lueg considered was a one-dimensional waveguide containing noise at a single frequency. The active noise controller consisted of a microphone, an amplifier, and a loudspeaker located downstream of the microphone. The noise in the waveguide was detected by the microphone, amplified, delayed, and reintroduced back into the waveguide by the loudspeaker. The electronic system (amplifier) delays the microphone signal such that the sound introduced by the loudspeaker is  $180^{\circ}$  out-of-phase with the noise at the loudspeaker location. Thus,

destructive interference results, and the noise does not propagate beyond the loudspeaker. Many of the modern active noise control solutions for plane waves in a one-dimensional waveguide (duct) are essentially based on Lueg's original concept. The second situation was that of a sinusoidal point noise source in free space. The detector microphone and cancellation loudspeaker were positioned equidistant from the noise source (but not necessarily at the same location). The output of the microphone is phase inverted and immediately input to the loudspeaker. A cancellation region in the near field of the loudspeaker results. The third situation considered non-sinusoidal noise. For non-sinusoidal noise, the noise would be detected at the loudspeaker location, phase inverted, and reintroduced at the loudspeaker.

Because the electronics were not adequate at the time of Lueg's patent, he was unable to implement his ideas and there was no demonstrated progress in the field of active noise control until Harry Olson published his "electronic sound absorber" in 1953 [3]. Olson furthered his ideas in a publication in 1957 [4]. The electronics field had advanced enough that Olson was successful in developing hardware and performing some initial laboratory experiments. Olson's "sound absorber" was a loudspeaker enclosed in a cabinet with a microphone positioned directly

in front of the loudspeaker. The output of the microphone drove the loudspeaker via an amplifier. Olson's system created a "zone of silence" in front of the absorber. Olson was able to attain a maximum of almost 25 dB of reduction at the microphone location with greater than 10 dB of reduction from 30-210 Hz. However, performance degraded rapidly for locations away from the microphone. Olson's device did show promising results for the limitations of the electronics available in the 1950's.

Also during the mid 1950's, W.B. Conover investigated the possibility of reducing electronic transformer hum by active means [5,6,7]. Conover used loudspeakers in cabinets positioned near the transformer's encasing to cancel the near-field acoustic pressure radiated from the transformer. Using a 15,000 kVA transformer, Conover obtained almost 30 dB reduction at 50 feet and 10 dB at 125 feet along the transformers axis [8]. However, Conover's active noise controller caused the near-field pressure to increase at other angular positions about the transformer.

Due to the mixed successes of Olson and Conover, the investigations of ANC were limited during the late 1950's and early 1960's. A new accelerated interest in ANC developed in 1968 with the publications of M.J.M. Jessel and his coworkers in France. Warnaka defines the modern era of ANC as beginning with Jessel's work [1]. Warnaka

suggests three reasons for the renewed interest in active noise control:

- advanced control systems technology including the development of adaptive systems,
- improved comprehension of the physics of acoustical systems, and most importantly
- the availability of sophisticated, inexpensive control made possible by solid state electronics.

The works of Jessel and others, delineating "the modern era," will be discussed in detail in the next sections.

## 2.2 Active Noise Control In Enclosures

The field of active noise control can be divided into two categories: control of noise in enclosures, and control of noise in free space. A special case of active noise control in enclosures occurs when the noise propagates in only one dimension of the enclosure at the highest frequency considered. This special case is often referred to as active noise control for one-dimensional ducts and is conceptually the simplest active noise control problem. Consequently, the active attenuation of noise in one-dimensional ducts has received the greatest attention.

### 2.2.1 One-Dimensional Enclosures

The acoustic one-dimensional system is a long, rigid wall duct where the transverse dimensions of the duct are smaller than half the wavelength of the highest frequency considered. Consequently, acoustic waves (plane waves) travel only in the longitudinal direction. A typical schematic of a one-dimensional active noise control system is shown in Figure 2.1. The noise in the duct is generated by a source "upstream" and travels toward the right. The one-dimensional enclosure is applicable to such systems as air conditioning, heating, and ventilation ducts where the noise source is usually an axial fan or muffler and engine induction systems.

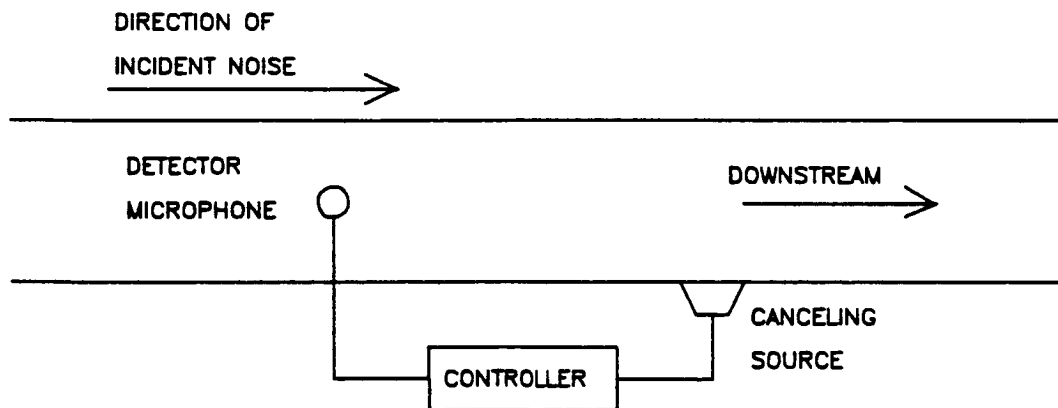


Figure 2.1 - General Schematic Of A One-Dimensional Active Noise Controller

Researchers A.R.D. Curtis, P.A. Nelson, S.J. Elliott, and A.J. Bullmore have analytically investigated the active control of one-dimensional enclosed sound fields [9,10]. The model used was a long, thin tube with rigid ends. A noise (primary) source of known strength was located at the left end of the tube and a canceling (secondary) source was located at the right end. A transfer function between the primary source strength and the secondary source strength was analytically derived in the frequency domain for three control strategies. The first control strategy considered was the acoustic virtual earth. The acoustic virtual earth requires that the secondary source is driven such that a pressure null is created directly in front of the secondary source. The second strategy investigated was the absorbing termination. The absorbing termination requires that the secondary source is driven such that no reflections occur at the secondary source. The last control strategy is referred to as an optimal termination. The method of an optimal termination requires that the secondary source is driven such that the total acoustic energy in the enclosure is minimized. Of the strategies considered, the optimal termination provided the greatest reduction in the acoustic energy. However, the optimal termination required noncausal action of the secondary source while the other

two strategies were causal. A noncausal solution was deemed acceptable only if an a priori measurement of the primary source strength is available or when the excitation is periodic.

Curtis et al. arrived at some important conclusions in their study of one-dimensional systems. It was concluded that minimization of the acoustic potential energy is a more suitable method than minimization of the total acoustic energy if sound pressure is the quantity to be reduced. The secondary source was shown to be most effective when it was positioned at a pressure antinode. If a single secondary source is well located, it is able to cancel most of the resonant sound field and additional secondary sources are unnecessary. The greatest reductions in the acoustic potential energy attained with the optimal termination occurred at the resonant frequencies of the duct. At the duct antiresonant frequencies, no reduction in the acoustic potential energy was possible.

S.J. Elliott and P.A. Nelson analytically investigated the implications of causality for the one-dimensional system [11]. The system considered was composed of a detector microphone upstream of a secondary source. The detector microphone measured the incident traveling plane waves originating from a noise source. The output of the detector microphone was input to a controller with transfer

function  $T_1(\omega)$ . The controller drives the secondary source. Causality was determined by examining the inverse Fourier transform of  $T_1(\omega)$ . Damping in the duct was accounted for by using a complex wavenumber. The first case considered  $T_j(\omega)$  such that no sound propagated past the secondary source. For the first case, the impulse response function of  $T_1(\omega)$  was causal and infinite in duration. For the second case,  $T_1(\omega)$  was solved such that the total sound power in the duct was minimized (i.e., to control the traveling waves in both directions). For the second case, the controller impulse response function had a causal and a noncausal part. If the controller was constrained to be causal, the optimal causal controller turned out to be the causal portion of the unconstrained controller. Thus, even for a noncausal situation, an optimal causal controller does exist which will provide some amount of attenuation.

An application of the acoustic virtual earth for attenuating broadband noise in an open ended duct with no flow was described by M.C.J. Trinder and P.A. Nelson [12]. The active noise control system was composed of a detector microphone, controller, and a secondary source. The controller was designed by experimentally measuring open loop transfer functions. A well recognized problem of active noise controllers is that the acoustic interaction



between the canceling source and the detector microphone can cause instability of the control system. To alleviate the acoustic feedback problem between the secondary source and the detector microphone, Nelson and Trinder placed the detector microphone in the near field of the secondary source at a position of minimum near-field response. The position of minimum near-field response was determined by an iterative experimental procedure. The first three modes of the duct were attenuated up to a maximum of 20 dB. The control system was band limited to 400 Hz and below.

Researcher C.F. Ross experimentally investigated the cancellation of plane waves in a duct [13]. The active noise control system used by Ross was similar to that of Trinder and Nelson. A duct 10m long and having a 50cm square cross section was driven by a loudspeaker with random noise input at one end of the duct. The duct was open at the other end. The incident plane waves were detected by a three microphone array. The three microphone array provided the ability to detect only forward traveling waves thus eliminating the acoustic feedback problem. The secondary source was a loudspeaker built into a wall of the duct at a location downstream of the detector array. An observer microphone, positioned downstream of the secondary source, was used to evaluate performance. The controller transfer function was designed in the frequency domain with

the objective of canceling all sound past the secondary source. The controller was a digital filter whose coefficients were determined by the least squares method of system identification. Ross' system provided approximately 15-20 dB of attenuation over the frequency range 60-300 Hz with peaks as high as 35 dB.

In a landmark paper, M.A. Swinbanks analyzed the very complex and general problem of active noise control in a long duct with uniform flow [14]. Swinbanks was interested in finding a localized distribution of point sources located about the duct wall such that plane wave disturbances propagating downstream in the flow would be attenuated. Swinbanks' approach to the problem was an in-depth fluid dynamics analysis from which he arrived at several conclusions. An array of two separated source "rings" would generate plane waves in one direction only. The unidirectional property of such an array was deemed beneficial in avoiding the instability problem. Swinbanks states that for a circular duct, three sources should be used in each source ring, while for a rectangular duct four sources are needed per ring. Likewise, a unidirectional detector array can be formed by two rings of microphones. Swinbanks also notes that the effect of cross modes at the detector can be eliminated if such a directional sensor is used. The useful frequency range for the two-ring source

array was calculated to be  $2\frac{1}{3}$  octaves. It was also found that by adding a third ring of sources to the canceling array, the useful frequency range increased by two octaves.

In a later paper, Swinbanks discusses many general aspects of active noise and vibration control and reviews some current applications [15]. One particular aspect discussed by Swinbanks is the stability of a general active noise controller. The configuration Swinbanks discussed was originally proposed by Wanke [16]. Wanke proposed that the canceling source/detector interaction could be electronically subtracted out of the detector output. The transfer function between the canceling source and the detector would be measured a priori and electronically implemented as a filter. The input to the canceling source would be the input to the filter. The output of the filter is subtracted from the detector output. Thus, the input to the controller would contain only the noise source component of the response at the detector. The obvious disadvantage to Wanke's approach is that the system will go unstable if the canceling source/detector transfer function ever changed.

Researchers T. Enokida et al. [17] and M. Takahashi et al. [18] have proposed an active noise control system for one-dimensional ducts called the dual sensing microphone (DSM) system. The DSM system is a method for eliminating

the acoustic feedback between the canceling source and the detector microphone. Two microphones are positioned equidistant from the secondary source. One microphone is located upstream from the canceling source while the other is located downstream. The acoustic feedback component of the total signal is eliminated by subtracting the output signal of one microphone from the other. Hence, the controller input is the difference of the two microphone signals. The DSM system was demonstrated using a duct 0.35m x 0.35m x 13m. The duct was driven at one end by a loudspeaker with 20-1000 Hz white noise input. Attenuation levels of 15 dB or more were achieved over a frequency range of 70-700 Hz.

A system similar to the DSM system is the "Chelsea dipole" developed by H.G. Leventhall and Kh. Eghtesadi [19,20]. The Chelsea dipole system uses two canceling sources a distance  $d$  apart. The detector microphone is positioned centrally between the two canceling sources. The two canceling sources are driven  $180^\circ$  out-of-phase. Thus, the components of the acoustic response at the microphone location due to each source cancel, and theoretically no acoustic feedback will occur. The Chelsea dipole is "tuned" to a central operating frequency,  $f_o = \frac{c}{\lambda_o}$ , by choosing  $d = \frac{\lambda_o}{2}$ . Experimental analysis of the Chelsea dipole showed a significant level of attenuation

(approximately 25 dB) was possible around the central operating frequency, but only about 10 dB of attenuation on average was achieved at frequencies away from  $f_0$ . Nonideal factors such as cross modes and irregular frequency response of the speakers were found to degrade the performance of the Chelsea dipole.

In addition to the Chelsea dipole system, researchers W.K.W. Hong, Kh. Eghtesadi, and H.G. Leventhall have theoretically and experimentally investigated the performance of tightly-coupled active noise control systems [21]. Most duct noise attenuator systems have the feedback (detector) microphone and the canceling source separated by a relatively large distance. Hong et al. have proposed two systems, a tight-coupled monopole (TCM) and a tight-coupled tandem (TCT), where the feedback microphone(s) is located in the near field of the canceling source(s). The TCT is two TCMs in series. The idea of tightly-coupled systems can be traced back to Olson [3]. As was the case for the Chelsea dipole, cross modes and nonideal system components caused a decrease in performance of the tightly-coupled systems. In order to reduce the effects of higher order (cross) modes, Hong et al. placed an absorptive lining opposite the canceling source(s).

The TCM was originally known as the Chelsea monopole [22,23]. Hong et al. modeled the transfer functions of the

canceling source/detector interaction and controller for the classic monopole attenuator (Figure 2.1) as simple time delays. The Chelsea monopole had two distinctive features. First, the canceling source/detector interaction was electronically subtracted out of the detector output (as proposed by Wanke). Second, the detector microphone was located in very close proximity to the canceling source. Because the detector was very close to the canceling source, the time delays were assumed to be zero, and thus, the transfer functions were simply unity gains. Consequently, the overall controller transfer function (including the subtraction of the source/detector interaction) approached infinity, which Hong et al. noted was equivalent in practice to a high gain amplifier. Hence, the TCM is simply a microphone, a power amplifier, and a canceling source.

Expressions for the attenuation at a field point downstream of the canceling source were analytically derived for the TCM and the TCT systems. The incident noise in a duct (of rectangular cross section) was assumed to be low enough in frequency that plane wave behavior could be assumed. However, since the feedback microphone was in the canceling source near field, plane wave behavior could not be assumed in calculations involving the pressure at the feedback microphone. To calculate the contribution

of the pressure at the feedback microphone due to the canceling source(s), Green's function for radiation in a finite space with reflection coefficients was used. For the absorptive lining, the reflection coefficient was included for a locally reacting material.

Experimental verification of the analytical results was performed at discrete frequencies of 98 Hz, 155 Hz, and 216 Hz by Hong et al. The duct had dimensions 0.45m x 0.6m x 10m. The quantity examined for verification purposes was the level of attenuation over a plane (perpendicular to the axis of the duct). The experimental results supported the analytical results in general. The performance of the TCT and TCM for broadband random noise band limited from 0-500 Hz was determined. The TCT provided slightly better performance with a 20 dB minimum attenuation level over three and one-half octave bands from 30-330 Hz.

The applicability of superposition for active noise control systems has been debated among certain researchers. J.E. Ffowcs Williams et al. [24] argue that the impedance that the control source encounters changes when the noise sources are present. Thus, if an optimal active noise controller transfer function is in part found by experimentally measuring various system transfer functions with the noise source inactive, the controller transfer function will suboptimal when the noise source is

operating. However, M.A. Swinbanks considers Fflowcs Williams' argument to be false [15]. Swinbanks argues that the experimentally measured transfer functions are invariant functions regardless if a noise source is present or not. Swinbanks states that the change in impedance that the canceling source encounters when the noise source is operating is accounted for by the ratio of the cancellation point/noise source and detector/noise source transfer functions. R.J. Silcox and S.J. Elliott support Swinbanks' argument by analytically illustrating that for finite impedance sources, the principle of superposition is applicable for the active noise control problem [25].

Researcher R.D. Ford has analytically investigated the power requirements for one-dimensional active noise control systems [26,27]. Ford considered two active noise control system arrangements. The first system employed a single ring of canceling sources which were driven such that the acoustic pressure was zero downstream of the ring. Upstream of the canceling sources a standing wave was formed. Because the acoustic pressure near the ring of canceling sources was zero, no power could flow into or out of the canceling sources. However, the canceling sources did internally absorb power electrically and mechanically. Ford hypothesises two explanations on the mechanisms at work: (1) the canceling sources inhibit the noise source



from radiating power because the radiation impedance of the primary source had become totally reactive, or (2) the noise source power is dissipated in the section of the duct between the noise source and the canceling sources.

Ford also considered a system with a unidirectional dipole absorber. A unidirectional dipole is created by situating two rings of canceling sources a distance  $d$  apart (Swinbanks' proposed system). The upstream ring (ring 2) is driven with the same amplitude as the downstream ring (ring 1) but with the signal inverted and delayed by  $d/c$  where  $c$  is the speed of sound. For the unidirectional dipole, the noise field upstream of ring 2 is unaffected, a standing wave is formed between the two canceling rings, and the pressure is zero downstream of ring 1. Ring 2 was found to absorb power while ring 1 had zero power flow. Hence, it is possible to remove power from the system if a unidirectional dipole is used as the canceling source. Ford performed several experiments where the acoustic power input of the canceling source(s) was monitored. The experimental results reinforced the theory.

### 2.2.2 Two And Three-Dimensional Enclosures

A significant body of research of relevance to the research presented in this thesis has been conducted by A.J. Bullmore, S.J. Elliott, P.A. Nelson, and A.R.D. Curtis

[28,29,30]. Bullmore et al. have investigated the active control of harmonic enclosed sound fields. Because pressure is the acoustic parameter sensed by humans, the selected control objective was to minimize the total time averaged acoustic potential energy,  $E_p$ . For an enclosure of volume  $V$ ,  $E_p$  is given by

$$E_p = \frac{V}{4\rho_0 c^2} \int_V |p(\bar{x}, \omega)|^2 dV \quad (2.1)$$

where  $p(\bar{x}, \omega)$  is the time harmonic acoustic pressure at a location described by  $\bar{x}$ . The quantity  $p(\bar{x}, \omega)$  is written as a truncated sum of the normalized characteristic modal functions of the enclosure and the complex mode amplitudes.

The complex mode amplitudes were written as a sum of two components. The first component was the contribution of some unspecified noise (primary) source distribution. The second component was the contribution of a set of point canceling (secondary) sources which were employed to control the noise field. Due to the orthogonal properties of the mode shapes, when the solution for  $p(\bar{x}, \omega)$  is substituted into equation 2.1, an expression for  $E_p$  results which is a positive definite, quadratic function of the complex secondary source strengths. A positive definite quadratic function has a single unique global minimum. Thus, there exists a unique combination of secondary source

magnitudes and phasing such that  $E_p$  is minimized.

Because minimization of  $E_p$  requires exact knowledge of the pressure distributions due to the primary and secondary sources, Bullmore et al. have proposed a more practical control objective. The practical control objective they have proposed is to minimize the sum of the pressure magnitudes squared at a discrete number ( $N$ ) of sensor locations:

$$J_p = \frac{V}{4\rho_0 c^2 N} \sum_{n=1}^N |p_n|^2 \quad (2.2)$$

Minimization of  $J_p$  does not guarantee minimization of  $E_p$ . In fact, Bullmore et al. point out that that  $E_p$  may even increase at minimum  $J_p$ . As  $N$  approaches infinity, minimization of  $J_p$  converges to minimization of  $E_p$ .

Bullmore et al. performed computer simulations for a two-dimensional harmonically enclosed sound field [28]. A lightly damped rectangular cavity was excited by a single harmonic primary point source operating at low frequency (50-300 Hz). The primary source was modeled as a small rectangular piston mounted in the enclosure surface. The secondary sources (at various locations in the cavity) were likewise modeled as small rectangular pistons mounted in the enclosure surface.

Several important conclusions can be drawn from the computer simulations of Bullmore et al. First, the largest reductions in  $E_p$  were attained when the secondary source was in close proximity to the primary source. Second, appreciable reductions in  $E_p$  are possible even if the secondary sources are remote from the primary source provided that the secondary sources were located at maxima of the uncontrolled sound field. Third, for remotely located secondary sources, the significant reductions in  $E_p$  occur around the acoustic resonances of the cavity. Fourth, minimization of  $J_p$  was approximately equivalent to minimization of  $E_p$  as long as the sensor locations were chosen such that all of the dominant modes were detected.

The computer simulation findings of Bullmore et al. were verified experimentally [29]. The experiments were conducted using a shallow rectangular enclosure identical to that modeled in the computer simulations. The experimental results were in close agreement with the simulation predictions.

A.J. Bullmore, P.A. Nelson, and S.J. Elliott have also applied their formulation to the study of harmonically excited cylindrical enclosed sound fields [31]. A cylindrical enclosure is of interest because it approximates an aircraft passenger cabin. A computer simulation was performed for a thin, closed cylindrical

shell excited by two harmonic external point forces of equal magnitude and phase. The secondary sources were modeled as small piston sources on the cylindrical surface. The acoustic response (noise field) of the cavity was assumed to be due only to the structural response of the cylindrical shell. The quantities  $E_p$  and  $J_p$  as defined in equations 2.1 and 2.2 respectively, were used as the cost functions. At a driving frequency of 132 Hz, 10 secondary sources provided 5.7 dB of reduction in  $E_p$ . For a similar discretized study using the same 10 secondary sources and 24 sensor locations,  $J_p$  was reduced by 4.3 dB. Performance was found to degrade with decreasing numbers of secondary sources. Bullmore et al. suggested that maximum minimization of  $E_p$  is achieved by placing the secondary sources where they can most effectively couple into the dominant modes excited by the primary sources while least exciting previously unexcited modes.

The active control of harmonic noise fields inside an aircraft fuselage has also been studied by H.C. Lester and C.R. Fuller [32]. The aircraft fuselage was modeled as an infinitely long, uniform, thin, flexible cylinder. A pair of dipoles of known amplitude, phase, and placement external to the cylinder were used to simulate the sound field created by twin propellers. The dipoles drove the interior acoustic pressure field through

structural/acoustic coupling. Monopole canceling sources were introduced into the interior for noise field control. A "payoff function", defined as the area weighted mean square pressure over the propeller plane, was computed from

$$\Lambda(P_{\alpha}) = \frac{1}{A_0} \int_0^a \int_0^{2\pi} |p(r, \theta)|^2 r dr d\theta \quad (2.3)$$

where  $A_0$  is the cross sectional area at the propeller plane and  $a$  is the radius. The amplitudes of the control sources ( $P_{\alpha}$ 's) were solved such that the payoff function is minimized. Coupled shell/acoustic equations were used to solve for the acoustic pressures at the propeller plane in terms of the control source amplitudes. The resulting payoff function was a positive definite quadratic function of the control source amplitudes, and thus, a single global minimum was found.

Through computer simulations, Lester and Fuller were able to arrive at some interesting conclusions. Using only a few (2 to 8) "judiciously placed" controllable compact sources, reductions of 20-25 dB were attained over a substantial portion of the cylinder's cross section. When modal density was low, the canceling sources were able to create an acoustic modal pattern similar to the uncontrolled acoustic field but opposite in phase. Lester and Fuller thus concluded that the control sources should be located such that they are effective in creating the

anti-phase modal pattern which is responsible for attenuating the noise.

Some basic experiments on the active control of noise in enclosures were carried out by Warnaka et al. [33]. First, noise attenuation in an anechoic environment at 500 Hz was investigated. A noise source (waveguide) and a canceling source (waveguide) were positioned next to each other in one wall with openings into the anechoic room. The magnitude and phase of the canceling source was manually adjusted such that maximum attenuation was achieved. A maximum of 70 dB of reduction in sound pressure level was achieved locally with 20 dB or more reduction over approximately 80% of the 25cm x 76cm area in front of the waveguides. Second, for a fuselage model 178cm long and 36cm in diameter with near rigid terminations at the ends, 20 to 35 dB of reduction was achieved everywhere within the model. The model was sinusoidally excited at 400 Hz. Similar results were obtained for an excitation frequency of 190 Hz.

Research by L.J. Oswald on the attenuation of diesel engine noise inside passenger compartments using an active noise control scheme has shown several interesting results [34]. Actual engine noise was experimentally attenuated in a medium-duty truck cab up to a maximum of 30 dB at the driver's head location. One speaker located at the front

lower corner of the cab was used as the canceling source. The maximum level of noise reduction occurred at the natural frequencies of the cab. It was also found that minimum energy for cancellation of an acoustic mode is required if the canceling source was located at an antinode of the mode. Work by Oswald also showed that the size of attenuated region will be at least one-quarter wavelength for frequencies up to 200 Hz.

Researcher T.S. Berge also experimentally investigated the possibility of reducing low frequency (below 200 Hz) noise in a vehicle cab [35]. Berge's goal was to actively attenuate the high noise level of the fundamental engine firing frequency at idle speed (30 Hz). An open loop filter between a feedback microphone and a cancellation speaker was adjusted such that the sound pressure level was minimized at the driver's head location. The canceling source was mounted directly behind the driver's head location. The sound pressure level at the fundamental firing frequency was reduced by 15.7 dB. However, broadband cancellation was not achieved, and the sound pressure level actually increased at other frequencies when the active noise controller was functioning.

In work similar to that of Oswald and Berge, M. Nadim and R.A. Smith addressed the problem of providing a spatial zone of attenuation about the driver's head location in a



tractor cab [36]. Two high efficiency ported loudspeakers were remotely placed in the foot-rest of a tractor cabin. A feedback microphone was located just above the operator's head height. Loudspeakers external to the cab were used to simulate exhaust noise. Significant reduction in the sound pressure level occurred at the cab resonances and at very low frequencies. A typical value was 26 dB at 50 Hz.

### 2.3 Active Noise Control In Free Space

Researchers P.A. Nelson, A.R.D. Curtis, and S.J. Elliott have investigated the active attenuation of sound in an unbounded medium [30]. The objective of their work was to minimize the total sound power,  $w$ , radiated from a system composed of harmonically time varying point monopole sources. The total sound power output of the system was formulated in terms of the primary (noise) and secondary (canceling) source strengths. The expression for  $w$  was found to be a positive definite, quadratic function of the complex secondary source strengths. Hence, for multiple secondary sources, the total sound power function is a quadratic hypersurface having a single unique global minimum. It follows that there exists a unique combination of secondary source magnitudes and phasing which minimizes  $w$ .

After formulating the problem, Nelson et al. performed an analytical study of the performance of active noise control of a single point primary source. Twelve secondary sources were placed in an icosahedral array about the primary source. The solution for the complex secondary source strengths which minimized  $w$  required that all secondary sources be either  $180^\circ$  out-of-phase or in-phase with the primary source. Appreciable reductions in  $w$  were found to be possible only if the secondary sources were no greater than one-half a wavelength away from the primary source. Significant improvements in the reduction of  $w$  occurred with an increasing number of secondary sources within the one-half wavelength criterion.

Nelson et al. also considered the more general case of sound power absorption of incident plane waves using compact secondary sources [37]. Expressions for the secondary source strengths which minimized  $w$  were derived for monopole, dipole and longitudinal quadrupole canceling sources. The technique used in the development of the source power equations was developed by Levine [38]. For a simple monopole secondary source, it was found that the secondary source absorbs power and that its volume velocity must be in anti-phase to the incident plane pressure wave. The maximum power absorbed for a dipole and a longitudinal

quadrupole were three times and five times that for the monopole, respectively.

G.A. Mangiante and M.J.M. Jessel have developed a theoretical technique for examining the cancellation of sound in free space [39,40,41]. The technique is an application of Huygen's principle. The technique is formulated for a noise source group which radiates into free space. A surface,  $Z_0$ , is constructed which completely encloses the noise source group and consequently divides free space into subspace  $V_1$ , inside  $Z_0$ , and subspace  $V_2$ , outside  $Z_0$ . Huygen's principle states that it is possible to distribute a set of (Huygen) sources over  $Z_0$  such that there will be no radiation into  $V_1$  and no change in the sound field in  $V_2$ . If the Huygen sources are phase inverted and operate in conjunction with the original noise source group, then the sound field in  $V_1$  will be unchanged and the sound field will be zero in  $V_2$ . Thus, Mangiante and Jessel proposed that in theory it is possible to completely cancel a radiated noise field (outside of  $Z_0$ ) by enclosing the noise sources with a surface of phase inverted Huygen sources (absorbing sources).

Several practical conclusions were drawn by Jessel and Mangiante from computers studies they conducted. In practice, only a discrete number of absorbing sources can be used. The discrete absorbing sources must have cardioid

radiation patterns with the direction of radiation pointing into the cancellation region. Attenuation was found to increase with the number of absorbing sources employed. The absorbing sources should be located close to the noise source for improved performance. Active absorption performs well for frequencies below 1000 Hz.

Researcher O.L. Angevine evaluated an experimental implementation of Mangiante and Jessel's theory [42]. Angevine was interested in actively attenuating the hum of an electric transformer. A transformer casing was excited by a loudspeaker within the casing. The loudspeaker was operated at frequencies of 125 Hz, 250 Hz, and 500 Hz. The required cardioid radiation pattern was obtained by using "tripoles." A tripole was defined as a monopole and dipole operating in close proximity. The amplitude and phase of each tripole was adjusted by an automatic control system such that the pressure at a microphone location 0.5m in front of the tripole was minimized. Using 26 tripoles surrounding the transformer casing, attenuation at the microphone locations averaged 16 dB at 125 Hz and 8 dB at 250 Hz. Attenuation was found to increase approximately linearly with increasing number of tripoles.

Another application of the free space radiation problem is the active attenuation of vehicle exhaust noise which has been experimentally investigated by M.C.J.

Trinder, G.B.B. Chaplin, and P.M. Nelson [43]. Two canceling speakers with single ports were mounted near an exhaust outlet. An adaptive control system was used which adapted to achieve a minimum sound pressure level at a microphone location near the exhaust outlet. A frequency range of 0-500 Hz was considered. On a dynamometer test bed, the relative sound pressure level at the dominant harmonic of 50 Hz was attenuated by more than 25 dB. Although the broadband performance of the system was satisfactory overall, the sound pressure level did increase slightly at some frequencies. The results were less encouraging for an on-road test which was conducted. The relative sound pressure level at the dominant peak (63 Hz) was reduced by approximately 8 dB. The overall reduction (0-500 Hz) was 6 dB.

#### 2.4 Conclusions

Several important conclusions can be drawn from the literature summarized in this chapter. Numerous articles were cited where active noise control systems were experimentally shown to provide significant (15 dB or more) attenuation for a variety of practical applications such as air conditioning/heating ducts, exhaust noise, electronic transformer hum, and passenger cabin noise. The control of noise fields in either an enclosure or free space is possible using a small number of compact controllable

sources. For enclosed noise fields, active noise control is most beneficial at the natural frequencies of the enclosure. For free space active noise control, the canceling sources should be located within one-half wavelength of the primary source. In general, because passive noise control methods are efficient at the higher frequencies, active noise control is limited to the low frequency range (below 500 Hz). Moreover, as the frequency of the noise increases, computationally quicker controllers are needed to operate at the required sampling rate.

From the research of Bullmore et al. and Lester et al., a reasonable control objective for enclosed noise fields is the minimization of the mean squared pressures at a number of discrete sensor locations. If a control objective of a form similar to Bullmore et al. or Lester et al. is used, the control objective equation is a positive definite, quadratic function of the canceling source strengths. Therefore, there is a unique combination of secondary source strengths which provide a global minimization of the control objective function.

Stability of active noise control systems is a well recognized problem. Instability is caused by the positive (acoustic) feedback between the canceling source(s) and the detector microphone(s). For one-dimensional systems, stability is usually attained by using either directional

sensors or directional canceling sources. For higher dimensional systems, directional sources or sensors are less straightforward and other methods must be used to ensure stability.

The analytical/numerical procedures for higher dimensional systems presented in this chapter were not generalized methods. The methods of Bullmore et al. and Lester et al. are limited to regularly shaped enclosures where the characteristic modal functions are known. All of the analysis for the one-dimensional system were specific to a particular system or configuration. Because some desired active noise control applications involve complex cavities (such as an automobile and aircraft cabins), a generalized method for evaluating an optimal active noise control scheme is needed.

In addition, critical issues such as the influence of damping, asymmetric source distributions, and attenuation of noise near irregularly shaped distributed sources require more capable analysis procedures in order to evaluate active noise controller performance. However, it is characteristic of numerical techniques that the physics of the modeled behavior are less obvious. The analytical studies cited in this chapter will be used to help understand and explain the results found in the numerical studies.

## CHAPTER 3

## THE INDIRECT BOUNDARY ELEMENT METHOD

As will be seen in chapters 4, 5, and 6, derivation of optimal active noise controllers require a predictive scheme to calculate acoustic quantities, namely pressure, in a domain of interest. The domain of interest could be, for example, the interior of a cavity or the space surrounding a radiating machine. For simple geometries possessing one-dimensional plane wave acoustic behavior, it is possible to derive an optimal controller solution [9,13,14,21]. However, to calculate the optimal controller for systems with generalized geometries possessing three-dimensional acoustic behavior, a numerical predictive scheme is necessary. Multiple parameter optimization and multi-input, multi-output controller optimization can be performed with little difficulty if a numerical analysis method is employed. Hence, for reasons of generality and versatility, a numerical predictive scheme was used.

For calculation of the acoustical quantities, the indirect boundary element method (IBEM) was chosen for its



versatility, relative computational simplicity, and efficiency. Two other numerical methods could possibly have been employed: a direct boundary element method (DBEM) or a finite element method (FEM). The DBEM formulation results in a matrix equation involving two matrices. The IBEM formulation results in a matrix equation involving only one matrix. Thus, the IBEM requires about half the number of calculations to form the needed matrix equation. The FEM requires that the complete problem domain be discretized. The IBEM (and DBEM) require that only the domain boundary be discretized. Thus, the geometric models of the problem are much larger for the FEM. Moreover, the FEM provides the solution at every node in the geometric model of the system whereas the IBEM provides the solution only at a chosen set of locations in the domain. For the problem presented in this thesis, the solution is usually desired at only a few locations. Therefore, use of the FEM would provide unneeded information.

Furthermore, the basis functions used in FEMs are usually polynomials whereas the boundary element methods use the fundamental solution for a source in free space. The fundamental solutions for the boundary element methods are obtained from the governing partial differential equation of the particular problem at hand. Because the fundamental solutions are specific to the problem, the IBEM

and the DBEM provide a more accurate solution with greater efficiency than the FEM.

The formulation of the IBEM presented in the next two sections is brief and customized. A more thorough and general development of the IBEM can be found in Banerjee and Butterfield [44], Brebbia and Walker [45], and Kipp [46].

### 3.1 Theory

The acoustic system to be modeled by the IBEM is illustrated in Figure 3.1. The system consists of a domain,  $D$ , enclosed by a boundary,  $B$ . The location of a point on the boundary is given by vector  $\bar{b}$ . The method can also model systems with acoustic point sources present. An acoustic point source of strength  $\phi$  is located by vector  $\bar{x}_s$ . A domain location,  $x_d$ , is described by vector  $\bar{x}_d$ . A unit vector normal to the boundary is represented by  $\hat{n}$ . Figure 3.1 represents analysis of a problem where the domain is enclosed by the boundary. The IBEM can also provide solutions for problems where the domain is external to the boundary. For external domain analysis the direction of  $\hat{n}$  is reversed from that shown in Figure 3.1, i.e., the normal vector always points into the domain.

The IBEM is a numerical approximation of Huygen's principle. Huygen's principle states that if the boundary

of the domain is replaced by a distribution of fictitious sources such that the conditions at the boundary are reproduced, then the conditions in the domain are likewise reproduced. It follows that the Huygen's principle formulation requires that the boundary conditions corresponding to a well posed boundary value problem be known. The boundary conditions formulated in this investigation are acoustic pressure, particle velocity, and specific acoustic impedance. Calculation of quantities in the problem domain using the IBEM is essentially a two step process. First, the fictitious source distribution is solved such that it reproduces the conditions at the boundary as specified by the boundary value problem. Second, the quantities of interest at locations in the domain or on the boundary are found from the fictitious source distribution. In this work, the quantity of interest in the domain is the acoustic pressure.

Because the first step in the IBEM is to solve for the fictitious source distribution given the boundary conditions, expressions relating the known boundary conditions to the fictitious source distribution are needed. The acoustic pressure at a point on the boundary,  $\bar{b}_I$ , due to the fictitious source distribution is given by

$$p(\bar{b}_I) = \int_B \sigma(\bar{b}) p^*(\bar{b}, \bar{b}_I) dB \quad (3.1)$$

where  $\sigma(\bar{b})$  is the fictitious source distribution along the boundary and  $p^*(\bar{b}, \bar{b}_I)$  is the fundamental pressure solution. The fundamental pressure solution is an influence function which relates the effect of a unit point source at  $\bar{b}$  to the pressure at  $\bar{b}_I$ . The fundamental pressure solution for this formulation is the free space Green's function:

$$p^*(\bar{b}, \bar{b}_I) = \frac{1}{r} e^{-jkr} \quad (3.2)$$

where

$$r = |\bar{b}_I - \bar{b}| \quad (3.3)$$

The quantity  $k$  in equation 3.2 is the wavenumber and  $j = \sqrt{-1}$ . Other fundamental solutions could be used depending on the physical problem. For example, if an infinite reflecting plane is present in the problem, image sources would be included in the fundamental solution [47].

Similarly, the velocity normal to the boundary at  $\bar{b}_I$  due to the fictitious source distribution is given by

$$u(\bar{b}_I) = \int_B \sigma(\bar{b}) u^*(\bar{b}, \bar{b}_I) dB \quad (3.4)$$

The quantity  $u^*(\bar{b}, \bar{b}_I)$  is the fundamental velocity solution which is an influence function of a unit point source at  $\bar{b}$  on the velocity at  $\bar{b}_I$ . The fundamental velocity solution is obtained from the fundamental pressure solution by Euler's equation:

$$u^*(\bar{b}, \bar{b}_I) = \frac{-1}{jk\rho_0 c} \frac{\partial p^*(\bar{b}, \bar{b}_I)}{\partial \hat{n}} \quad (3.5)$$

where  $\rho_0$  is the equilibrium density of the air and  $c$  is the speed of sound. Equation 3.5 can be rewritten as

$$u^*(\bar{b}, \bar{b}_I) = \frac{-1}{jk\rho_0 c} \hat{n} \cdot \nabla p^*(\bar{b}, \bar{b}_I) \quad (3.6)$$

or

$$u^*(\bar{b}, \bar{b}_I) = \frac{(\hat{n} \cdot \nabla r)}{jk\rho_0 c} \left( -\frac{1}{2} + \frac{jk}{r} \right) e^{-jkr} \quad (3.7)$$

The pressure and velocity of a point on the boundary are also influenced by the acoustical point sources present in the domain of the problem. The effect of a point source(s) of strength  $\phi$  located at  $\bar{x}_s$  on the pressure at  $\bar{b}_I$  is

$$p(\bar{b}_I) = \int_B \sigma(\bar{b}) p^*(\bar{b}, \bar{b}_I) dB + \sum_{k=1}^{ns} \phi_k p^*(\bar{x}_{s,k}, \bar{b}_I) \quad (3.8)$$

where  $ns$  is the number of point sources present. Likewise, the contribution of the point source(s) on the velocity at  $\bar{b}_I$  is

$$u(\bar{b}_I) = \int_B \sigma(\bar{b}) u^*(\bar{b}, \bar{b}_I) dB + \sum_{k=1}^{ns} \phi_k u^*(\bar{x}_{s,k}, \bar{b}_I) \quad (3.9)$$

The integrands in equations 3.8 and 3.9 contain a singularity. The singularity occurs in the fundamental

solutions when  $r=0$  or  $\bar{b}=\bar{b}_I$ . The fundamental pressure solution has a  $\frac{1}{r}$  singularity which can be eliminated by evaluating the boundary integral using a polar coordinate system. The polar coordinate system transformation will be discussed in more detail in section 3.2. The fundamental velocity solution has a  $\frac{1}{r^2}$  singularity which is strong and must be treated as a Cauchy principal value [48]. The procedure is to exclude a small region about the point of singularity in the boundary integral. The boundary integral over the small region is accounted for by the addition of a "free term." Thus, equation 3.9 becomes

$$u(\bar{b}_I) = j \frac{4\pi}{k\rho_0 c} c_b \sigma(\bar{b}_I) + \int_{B^-} \sigma(\bar{b}) u^*(\bar{b}, \bar{b}_I) dB^- + \sum_{k=1}^{ns} \phi_k u^*(\bar{x}_{s,k}, \bar{b}_I) \quad (3.10)$$

where  $B^-$  is the boundary excluding the small region about the singularity point. For a singularity located on a smooth part of the boundary  $c_b = -\frac{1}{2}$ . If the singularity is located at a corner of the boundary, then  $c_b = -\frac{\Omega}{4\pi}$  where  $\Omega$  is the solid angle (in steradians) of the domain encompassed by the boundary corner [49].

Impedance boundary conditions may also be modeled with the IBEM. Assuming a locally reacting boundary, the specific acoustic impedance at  $\bar{b}_I$  is given by

$$z(\bar{b}_I) = \frac{p(\bar{b}_I)}{u(\bar{b}_I)} \quad (3.11)$$

Rearranging equation 3.11 results in an alternate form:

$$p(\bar{b}_I) - z(\bar{b}_I)u(\bar{b}_I) = 0 \quad (3.12)$$

Substitution of the boundary integrals into equation 3.12 yields

$$\begin{aligned} \int_B \sigma(\bar{b}) p^*(\bar{b}, \bar{b}_I) dB - z(\bar{b}_I) \int_{B^-} \sigma(\bar{b}) u^*(\bar{b}, \bar{b}_I) dB^- \\ + \sum_{k=1}^{ns} \psi_k [p^*(\bar{x}_{s,k}, \bar{b}_I) - z(\bar{b}_I) u^*(\bar{x}_{s,k}, \bar{b}_I)] \\ - j \frac{4\pi}{k\rho_0 c} z(\bar{b}_I) c_b \sigma(\bar{b}_I) = 0 \end{aligned} \quad (3.13)$$

Equations 3.8, 3.10, and 3.13 are the necessary equations to solve for the fictitious source distribution along the boundary of the domain of interest. Equation 3.8 is used if pressure boundary conditions are known at  $\bar{b}_I$ . If velocity boundary conditions are given at  $\bar{b}_I$ , then equation 3.10 is evaluated. Likewise, equation 3.13 is evaluated if locally reacting impedance boundary conditions are specified at  $\bar{b}_I$ .

Once the fictitious source distribution is calculated, the acoustic pressure or particle velocity at locations in the domain or at the boundary can be found. The pressure at  $\bar{x}_d$  is given by

$$p(\bar{x}_d) = \int_B \sigma(\bar{b}) p^*(\bar{b}, \bar{x}_d) dB + \sum_{k=1}^{ns} \phi_k p^*(\bar{x}_{s,k}, \bar{x}_d) \quad (3.14)$$

The component of the velocity in the direction of the unit vector  $\hat{v}$  at  $\bar{x}_d$  is

$$u(\bar{x}_d) = \int_B \sigma(\bar{b}) u^*(\bar{b}, \bar{x}_d) dB + \sum_{k=1}^{ns} \phi_k u^*(\bar{x}_{s,k}, \bar{x}_d) \quad (3.15)$$

where

$$u^*(\bar{v}_s, \bar{v}_d) = \frac{-1}{jk\rho_0 c} \hat{v} \cdot \nabla p^*(\bar{v}_s, \bar{v}_d) \quad (3.16)$$

and  $\bar{v}_s$  and  $\bar{v}_d$  are vectors locating a source and a domain location respectively. Provided that  $\bar{x}_d$  is not located on the boundary, the boundary integrals of equations 3.14 and 3.15 do not contain a singularity. If  $\bar{x}_d$  is located on the boundary, the resulting singularity is evaluated with fundamentally the same procedure that was used for the fictitious source solution. When  $\bar{x}_d$  is on the boundary, equation 3.15 becomes

$$u(\bar{x}_d) = j \frac{4\pi}{k\rho_0 c} c_b \sigma(\bar{x}_d) + \int_{B^-} \sigma(\bar{b}) u^*(\bar{b}, \bar{x}_d) dB^- + \sum_{k=1}^{ns} \phi_k u^*(\bar{x}_{s,k}, \bar{x}_d) \quad (3.17)$$

where  $c_b = 0$  if the domain is exterior to the boundary, or  $c_b = -1$  if the domain is enclosed by the boundary. The singularity present in equation 3.14 when  $\bar{x}_d$  is located on the boundary can be removed by a conversion to polar



coordinates as will be shown in the next section.

### 3.2 Numerical Implementation

The IBEM evaluates the boundary integrals developed in the proceeding section on a piecewise basis. The boundary is discretized into a number of sections referred to as boundary elements. The boundary integral equations are evaluated over each element and summed together for the complete boundary solution.

A noncompatible, triangular, linear, superparametric element is used in this investigation to discretize the boundary. A superparametric element uses a higher order interpolation for the geometric mapping than the functional mapping. Noncompatible elements do not require that the parametric elemental properties be continuous across the elements. Anticipating the need for models with a large number of elements, a computationally simple element was chosen so that results could be obtained with reasonable computer capacity and time. Consequently, an element with linear geometric characteristics and constant functional characteristics was chosen. Although such elements are quite efficient, modeling errors occur when the boundary is curved [50]. The modeling errors will be discussed in section 3.3.

An IBEM using compatible, quadratic isoparametric elements was studied by Kipp [46] and found to provide accurate results for curved surfaces. However, enforcing compatibility of the elements caused poor results for models which contained corners or edges. Kipp suggested that a noncompatible element be used to model geometries with corners or edges.

Using the discretized boundary, equation 3.8 can be rewritten as

$$p(\bar{b}_I) = \sum_{j=1}^{ne} \int_{B_j} \sigma(\bar{b}_j) p^*(\bar{b}_j, \bar{b}_I) dB_j + \sum_{k=1}^{ns} \psi_k p^*(\bar{x}_{s,k}, \bar{b}_I) \quad (3.18)$$

where  $ne$  is the number of elements in the boundary element model, and  $B_j$  is the boundary section contained by the  $j^{th}$  element. Likewise, equation 3.10 can be written as

$$u(\bar{b}_I) = j \frac{4\pi}{k\rho_0 c} c_b \sigma(\bar{b}_I) + \int_{B_s^-} \sigma(\bar{b}_s) u^*(\bar{b}_s, \bar{b}_I) dB_s^- + \sum_{\substack{j=1 \\ j \neq s}}^{ne} \int_{B_j} \sigma(\bar{b}_j) u^*(\bar{b}_j, \bar{b}_I) dB_j + \sum_{k=1}^{ns} \psi_k u^*(\bar{x}_{s,k}, \bar{b}_I) \quad (3.19)$$

where  $B_s^-$  represents the boundary element enclosing the singularity but excluding the small region around the singularity. Because the elements used in this formulation

are geometrically flat, the elemental boundary integral over  $B_s^-$  in equation 3.19 is evaluated over a flat surface. For a flat surface, the vectors  $\hat{n}$  and  $\nabla r$  in the fundamental velocity solution will always be perpendicular. Thus, the fundamental velocity solution is zero over  $B_s^-$  and

$$\int_{B_s^-} \sigma(\bar{b}_s) u^*(\bar{b}_s, \bar{b}_I) dB_s^- = 0 \quad (3.20)$$

By applying equation 3.20 and the boundary discretization principle, equation 3.13 can be rewritten as

$$\begin{aligned} & \sum_{j=1}^{ne} \int_{B_j} \sigma(\bar{b}_j) p^*(\bar{b}_j, \bar{b}_I) dB_j \\ & - z(\bar{b}_I) \sum_{\substack{j=1 \\ j \neq s}}^{ne} \int_{B_j} \sigma(\bar{b}_j) u^*(\bar{b}_j, \bar{b}_I) dB_j \\ & + \sum_{k=1}^{ns} \phi_k [p^*(\bar{x}_{s,k}, \bar{b}_I) - z(\bar{b}_I) u^*(\bar{x}_{s,k}, \bar{b}_I)] \\ & - j \frac{4\pi}{k\rho_0 c} z(\bar{b}_I) c_b \sigma(\bar{b}_I) = 0 \end{aligned} \quad (3.21)$$

The constant functional characteristic of the element implies that the fictitious source distribution, the pressure, and the velocity are constant over the element. Thus, a given boundary condition is assumed representative of the entire element. However, the IBEM requires for a constant functional element that the boundary condition be applied at a single point on the element. The location where the boundary condition will be applied is the

centroid of the element. Because the fictitious source distribution is constant over the element,  $\sigma(\bar{b}_j)$  can be removed from the elemental boundary integral. Applying the boundary conditions at the centroid of the element, equation 3.18 becomes

$$p(\bar{B}_i) = \sum_{j=1}^{ne} \sigma_j \int_{B_j} p^*(\bar{b}_j, \bar{B}_i) dB_j + \sum_{k=1}^{ns} \phi_k p^*(\bar{x}_{s,k}, \bar{B}_i) \quad (3.22)$$

where  $\bar{B}_i$  is the vector locating the centroid of the  $i^{th}$  element, and  $\sigma_j$  is the fictitious source strength of the  $j^{th}$  element. The point located by  $\bar{b}_i$  is contained by the  $i^{th}$  element. Similarly, equation 3.19 becomes

$$u(\bar{B}_i) = j \frac{4\pi}{k\rho_0 c} c_b \sigma_i + \sum_{\substack{j=1 \\ j \neq i}}^{ne} \sigma_j \int_{B_j} u^*(\bar{b}_j, \bar{B}_i) dB_j + \sum_{k=1}^{ns} \phi_k u^*(\bar{x}_{s,k}, \bar{B}_i) \quad (3.23)$$

and equation 3.21 becomes

$$\begin{aligned} & \sum_{j=1}^{ne} \sigma_j \int_{B_j} p^*(\bar{b}_j, \bar{B}_i) dB_j \\ & - z(\bar{B}_i) \sum_{\substack{j=1 \\ j \neq i}}^{ne} \sigma_j \int_{B_j} u^*(\bar{b}_j, \bar{B}_i) dB_j \\ & + \sum_{k=1}^{ns} \phi_k [p^*(\bar{x}_{s,k}, \bar{B}_i) - z(\bar{B}_i) u^*(\bar{x}_{s,k}, \bar{B}_i)] \\ & - j \frac{4\pi}{k\rho_0 c} z(\bar{B}_i) c_b \sigma_i = 0 \end{aligned} \quad (3.24)$$

A system of  $n$  equations for the  $n$  unknown  $\sigma$ 's is obtained by writing the appropriate equation for each element. The system of equations can be compactly written in matrix form as

$$[A]\{\sigma\} + [C]\{\phi\} = \{\alpha\} \quad (3.25)$$

where  $\{\sigma\}$  contains the values of the fictitious source strengths and  $\{\phi\}$  contains the point source strengths. If element  $i$  has a pressure boundary condition, then

$$A_{ij} = \int_{B_j} p^*(\bar{b}_j, \bar{B}_i) dB_j \quad ; j \neq i \quad (3.26a)$$

$$A_{ii} = \int_{B_i} p^*(\bar{b}_i, \bar{B}_i) dB_i \quad (3.26b)$$

$$C_{ik} = p^*(\bar{x}_{s,k}, \bar{B}_i) \quad (3.26c)$$

$$\alpha_i = p(\bar{B}_i) \quad (3.26d)$$

If element  $i$  has a velocity boundary condition, then

$$A_{ij} = \int_{B_j} u^*(\bar{b}_j, \bar{B}_i) dB_j \quad ; j \neq i \quad (3.27a)$$

$$A_{ii} = j \frac{4\pi}{k\rho_0 c} c_b \quad (3.27b)$$

$$C_{ik} = u^*(\bar{x}_{s,k}, \bar{B}_i) \quad (3.27c)$$

$$\alpha_i = u(\bar{B}_i) \quad (3.27d)$$

The matrix terms for impedance boundary conditions on element  $i$  are

$$A_{ij} = \int_{B_j} p^*(\bar{b}_j, \bar{B}_i) - z(\bar{B}_i) u^*(\bar{b}_j, \bar{B}_i) dB_j \quad ; j \neq i \quad (3.28a)$$

$$A_{ii} = \int_{B_i} p^*(\bar{b}_i, \bar{B}_i) dB_i - j \frac{4\pi}{k\rho_0 c} z(\bar{B}_i) c_b \quad (3.28b)$$

$$C_{ik} = p^*(\bar{x}_{s,k}, \bar{B}_i) - z(\bar{B}_i) u^*(\bar{x}_{s,k}, \bar{B}_i) \quad (3.28c)$$

$$\alpha_i = 0 \quad (3.28d)$$

Examining equations 3.25 through 3.28, one finds  $[A]$  has dimensions  $ne \times ne$ ,  $[C]$  is  $ne \times ns$ ,  $\{\sigma\}$  is of length  $ne$ ,  $\{\phi\}$  is of length  $ns$ , and  $\{\alpha\}$  has a length of  $ne$ .

From equations 3.26, 3.27, and 3.28, it is apparent that the diagonal of  $[A]$  contains the integrals of singular functions. The integral of the singularity due to the fundamental velocity solution has already been accounted for by the free term. The remaining boundary integral containing a singularity is that of the fundamental pressure solution over the  $i^{th}$  element:

$$\int_{B_i} p^*(\bar{b}_i, \bar{B}_i) dB_i = \int_{B_i} \frac{1}{r} e^{-jk r} dB_i \quad (3.29)$$

The quantity  $r$  is the distance between the point of integration,  $\bar{b}_i$ , and the centroid of the element,  $\bar{B}_i$ . The  $\frac{1}{r}$  term causing the singularity can be removed from the elemental boundary integral by a conversion to polar coordinates [51]. When the elemental boundary integral in equation 3.29 is evaluated in a polar coordinate system,  $dB_i$  is replaced with  $rdrd\theta$  (the differential area in polar coordinates). Furthermore, if the centroid of the element coincides with the origin of the polar coordinate system,

the  $r$  in equation 3.29 is identical to the  $r$  in the differential area for polar coordinates, and equation 3.29 becomes

$$\int_{B_i} p^*(\bar{b}_i, \bar{B}_i) dB_i = \int_{\theta} \int_r e^{-jkr} dr d\theta \quad (3.30)$$

Figure 3.2 illustrates the concept presented above.

The double integral in equation 3.30 is evaluated by dividing the element into three triangular sections as shown in Figure 3.3. The point  $c$  in Figure 3.3 is the centroid of the element, i.e., the origin of the polar coordinate system. The double integral is evaluated for each section and the results are summed for the total solution. For one section the double integral becomes

$$\int_{\theta} \int_r e^{-jkr} dr d\theta = \int_0^{\theta} \int_0^{R(\theta)} e^{-jkr} dr d\theta \quad (3.31)$$

Evaluating the inner integral yields

$$\int_{\theta} \int_r e^{-jkr} dr d\theta = \frac{1}{k} \int_0^{\theta} (e^{-jkR(\theta)} - 1) d\theta \quad (3.32)$$

From trigonometric relationships it can be shown that

$$R(\theta) = \frac{\frac{d_1 d_2}{d_3} \sin \theta}{\sin[\pi - \sin^{-1}(\frac{d_2}{d_3} \sin \theta) - \theta]} \quad (3.33)$$

The integral in equation 3.32 can be evaluated using a

numerical integration procedure. The numerical integration procedure used to evaluate the integral over  $\theta$  in equation 3.32 is a 10-point Gauss-Legendre quadrature [52].

The off-diagonal terms of  $[A]$  are computed using essentially a one point Gauss-Legendre quadrature to approximate the elemental boundary integrals. The location of the integration point is the centroid of the element and the weighting factor is the element area. The integral of the fundamental pressure solution over the  $j^{\text{th}}$  element is approximately

$$\int_{B_j} p^*(\bar{b}_j, \bar{B}_i) dB_j \approx p^*(\bar{B}_j, \bar{B}_i) A_j \quad (3.34)$$

where  $A_j$  is the area of the  $j^{\text{th}}$  element. Similarly,

$$\int_{B_j} u^*(\bar{b}_j, \bar{B}_i) dB_j \approx u^*(\bar{B}_j, \bar{B}_i) A_j \quad (3.35)$$

Such an elementary approximation to the elemental boundary integrals was chosen for computational simplicity. If the fundamental solutions vary greatly over the elements, equations 3.34 and 3.35 will be poor approximations of the actual integral. As will be demonstrated in the next section, the one point quadrature was found to be an adequate approximation for most circumstances.

After the terms of  $[A]$ ,  $[C]$ , and  $\{\alpha\}$  have been evaluated and assembled into matrix form, equation 3.25 is



solved for the unknown  $\sigma$ 's using a complex linear equation solver. The routine used in this investigation is LEQTLIC available from the International Mathematics and Statistics Library (IMSL). LEQTLIC solves a system of complex linear equations of the form  $[A]\{x\} = \{b\}$  where  $\{x\}$  contains the unknowns. Equation 3.25 can be put in appropriate form as

$$[A]\{\sigma\} = \{\alpha\} - [C]\{\psi\} \quad (3.36)$$

After the fictitious source strength of each element is known, equation 3.14 is used to find the pressure at a domain location. Using the boundary discretization process, equation 3.14 becomes

$$\begin{aligned} p(\bar{x}_d) = & \sum_{j=1}^{ne} \sigma_j \int_{B_j} p^*(\bar{b}_j, \bar{x}_d) dB_j \\ & + \sum_{k=1}^{ns} \phi_k p^*(\bar{x}_{s,k}, \bar{x}_d) \end{aligned} \quad (3.37)$$

If the values of pressure at a number of domain locations is desired, a matrix equation can be derived of the form

$$\{p\} = [D]\{\sigma\} + [E]\{\psi\} \quad (3.38)$$

where  $\{p\}$  is a vector of length  $np$  and  $np$  is the number of domain locations. For the  $i^{th}$  domain location

$$D_{ij} = \int_{B_j} p^*(\bar{b}_j, \bar{x}_{d,i}) dB_j \quad (3.39a)$$

$$E_{ik} = p^*(\bar{x}_{s,k}, \bar{x}_{d,i}) \quad (3.39b)$$

As in equation 3.34, the elemental boundary integral of equation 3.39a is evaluated using the one point quadrature approximation:

$$\int_{B_j} p^*(\bar{b}_j, \bar{x}_{d,i}) dB_j \approx p^*(\bar{B}_j, \bar{x}_{d,i}) A_j \quad (3.40)$$

where  $A_j$  is the area of the  $j^{\text{th}}$  element.

Implicit in equation 3.40 is the premise that  $\bar{x}_{d,i}$  is not located on the boundary. If  $\bar{x}_{d,i}$  is located on the boundary, the technique used to evaluate equation 3.26b can be used to evaluate  $D_{ij'}$  where the  $j'$  subscript denotes the element number which contains the domain location. The acoustic pressure is one of the physical variables which was assumed to be constant over the element. Therefore, evaluating the pressure at  $\bar{x}_{d,i}$  is equivalent to calculating the pressure at the centroid of the element which contains  $\bar{x}_{d,i}$ . The  $D_{ij'}$  term then becomes

$$D_{ij'} = \int_{B_{j'}} p^*(\bar{b}_{j'}, \bar{B}_{j'}) dB_{j'} \quad (3.41)$$

Equation 3.41 is identical to equation 3.26b, and thus, the technique used to evaluate equation 3.26b can be directly applied to equation 3.41.

### 3.3 Verification

As previously mentioned, the physical quantity of interest for the study of active noise controllers is the acoustic pressure. Thus, acoustic pressure solutions were examined for verification purposes. The IBEM was used to solve several acoustical problems which have known analytical solutions. A spherical and a rectangular prism boundary geometry were used in the verification process. Both the interior and exterior domains of the spherical geometry were examined. Verification using the rectangular prism involved only interior domain studies. The results presented in the next two sections are a representative subset of the complete verification process. Results from verification studies not presented are summarized where appropriate.

All acoustical problems analyzed with the IBEM for verification purposes are characterized by harmonically time varying solutions:

$$p(x,y,z,t) = p(x,y,z) e^{j\omega t} \quad (3.42)$$

where  $\omega$  is the excitation frequency. The IBEM solves for the steady state magnitude and relative phase of the time harmonic solution,  $p(x,y,z)$ . Thus, the time dependent component of the solutions is not included in the analysis.

### 3.3.1 Spherical Boundary Results

Analytical expressions for the acoustic response due to spherically shaped geometries are easily derived and well understood. For uniform boundary conditions over a spherical surface (a spherically symmetric problem), both the interior and exterior responses vary in only the radial direction.

Two models of a spherical boundary were used in verifying the IBEM code. Both models approximated the shape of a sphere, one meter in radius, centered about the origin. One model approximates the sphere using 48 elements while the other uses 96 elements. In both models the nodes of the elements were located on the sphere surface. Each model was constructed so that the centroids of the elements were equidistant from the center of the sphere and all the elements had equal area.

The first problem analyzed was the interior sound field created by a pulsating sphere. A pulsating sphere has a uniform radial time harmonic surface velocity. The analytical solution for the acoustic pressure inside a pulsating sphere of radius  $a$  is [53]

$$p(r) = \frac{j k \rho_0 c a^2 U_0}{\sin(ka) - ka \cos(ka)} \frac{\sin(kr)}{r} \quad (3.43)$$

where  $U_0$  is the amplitude of the surface velocity. Note,

the pressure at a particular radial location becomes infinite whenever

$$\sin(ka) - ka \cos(ka) = 0 \quad (3.44)$$

or

$$\tan(ka) = ka \quad (3.45)$$

The transcendental equation 3.45 is nonlinear, and thus, the roots of the equation, which are the natural frequencies of the cavity, must be solved iteratively. The first three natural frequencies occur at  $ka=0$ ,  $ka=4.49$ , and  $ka=7.72$ .

A comparison of the acoustic pressure as given by the analytical solution and by the IBEM for a radial location of  $\frac{a}{2}$  is presented in Figure 3.4. The surface velocity amplitude was 1m/s. Examination of Figure 3.4 reveals that there is an apparent frequency shift of the IBEM solution. This shift in frequency is caused by the geometric modeling of the curved spherical surface with flat elements. The sphere was modeled by placing the nodes of the flat elements on the sphere surface. Thus, the centroids of the elements are within the spherical boundary being modeled, and the boundary element model is circumscribed by the sphere. The boundary conditions of the problem are applied at the centroids of the elements, and the elemental

boundary integrals are calculated using the centroids as the numerical integration point for the quadrature. Consequently, the 96 element model resembles a sphere of slightly smaller radius than the analytical model, and thus, higher natural frequencies are predicted by the indirect boundary element method.

When the analytical solution is recalculated using an adjusted sphere radius corresponding to the radial location of the elemental centroids, the analytical solution and the IBEM solution are nearly identical. Figure 3.5 demonstrates the result. The radial location of the elemental centroids is  $r=0.9437m$ . Figure 3.5 suggests that when modeling curved surfaces with flat, linear elements, the model should be constructed such that the centroids of the elements are located on the curved surfaces.

Accurate IBEM results at the pressure node at  $k=6.28$  in Figure 3.5 further demonstrates that the frequency shift of the IBEM results is caused by geometric modeling errors. The pressure node results from the  $\sin(kr)$  term in equation 3.43. Because  $\sin(kr)$  is independent of sphere radius, geometric modeling errors should not affect the accuracy of the IBEM in predicting the pressure node. Figure 3.5 shows that the IBEM solution is not shifted in frequency at the pressure node.

To further demonstrate the modeling effects of using geometrically linear elements to model curved surfaces, the IBEM results for two models with different element mesh sizes are presented in Figure 3.6. The acoustic pressure at  $r = \frac{a}{2}$  for the interior of a pulsating sphere was computed using a 48 element model and a 96 element model. The 96 element model is geometrically a closer approximation to the actual sphere than the 48 element model. Thus, the IBEM results obtained with the 96 element model are characterized by a less pronounced shift in frequency. For curved surfaces, the IBEM results will converge to the analytical solution as the number of elements increases until a point where the element size becomes so small that the elemental boundary integral approximation becomes inaccurate.

The IBEM results for the prediction of the sound field inside a pulsating sphere diverge from the analytical solution in the very low frequency regime. This behavior is demonstrated in Figure 3.7 using the 48 element model to compute the pressure at half the sphere radius. Similar behavior has been reported by Kipp [46] using an IBEM and by Gardner [47] using a DBEM. As in this work, Gardner uses a one point quadrature to approximate the elemental boundary integrals. Gardner shows that the divergence is a result of the one point quadrature approximation. Results

for the low frequency region improved with the use of higher order Gauss-Legendre quadratures. However, as shown in Figure 3.7, the IBEM results obtained with the one point quadrature remain reasonably accurate for wavenumbers as low as approximately  $k=0.7$  which corresponds to a frequency of 38 Hz. For frequencies much below 38 Hz, active noise controllers perform poorly due to hardware limitations. Consequently, IBEM analysis in the very low frequency region is unnecessary for the study of active noise controllers.

Prediction of the acoustic pressure in the field exterior to a pulsating sphere was the next problem analyzed with the IBEM. The analytical solution for the exterior sound field created by a pulsating sphere is [54]

$$p(r) = \frac{j k \rho_o c U_o a^2}{1 + j k a} \frac{e^{-j k (r-a)}}{r} \quad (3.46)$$

Equation 3.46 can be rewritten as

$$p(r) = \frac{j k \rho_o c Q}{1 + j k a} \frac{e^{-j k (r-a)}}{4 \pi r} \quad (3.47)$$

where  $Q$  is known as the volume velocity source strength. The volume velocity source strength is the surface integral of the velocity normal to the surface:

$$Q = \int_s \vec{u} \cdot \hat{n} \, dS = 4 \pi a^2 U_o \quad (3.48)$$



where  $\hat{n}$  is a unit vector normal to the surface.

Figure 3.8 shows the comparison of the IBEM results with the analytical solution for the exterior of a pulsating sphere of 1m radius. The surface velocity of the sphere was 1m/s and the wavenumber was 0.01. The IBEM results are in excellent agreement with the analytical solution.

For further verification, the acoustic pressure at a single field point exterior to a pulsating sphere was computed for a range of frequencies. The field point was at a radial distance of 10m and the surface velocity was 1m/s. Figure 3.9 illustrates the results. Note that the boundary element method solution diverges from the analytical solution at the interior eigenfrequencies. This phenomenon, labeled a uniqueness problem, is well documented in the literature. The interior eigenfrequencies are the frequencies where the pressure at the boundary is zero for the interior problem. From equation 3.43, the interior eigenfrequencies for a spherical cavity are found to occur at  $\sin(ka)=0$ . For a sphere of unit radius the eigenfrequencies are  $k=\pi, 2\pi, 3\pi$ , etc.. However, the eigenfrequencies apparent in Figure 3.9 are slightly larger than those calculated for the sphere of unit radius. The IBEM predicts slightly larger values for the eigenfrequencies because the eigenfrequencies result

from the interior problem and are a function of sphere radius. Thus, the geometric modeling errors as discussed for the interior problem affect the eigenfrequency solution. For an adjusted sphere radius of  $a=0.9437m$  (the radial location of the elemental centroids for the 96 element model), the first two interior eigenfrequencies are  $k=3.329$  and  $k=6.658$  which closely correspond to the frequencies at which the IBEM solution diverges. Although there is no known procedure for improving the boundary element method solutions at the eigenfrequencies, it is important to realize the existence of this phenomenon when the IBEM is utilized for radiation problems.

The point source modeling capability of the IBEM was verified by investigating the sound field created by a point source at the center of a rigid wall sphere. The point source had a volume velocity source strength of  $1 \text{ m}^3/\text{sec}$ . For this analysis, the 48 element sphere model with velocity boundary conditions of magnitude zero were used. The analytical solution for a point source at the center of a rigid wall sphere of radius  $a$  is [50]

$$p(r) = \frac{jk\rho_o cQ}{4\pi r} \frac{\sin k(r-a) + ka \cos k(r-a)}{ka \cos(ka) - \sin(ka)} \quad (3.49)$$

where  $Q$  is the volume velocity strength of the point source. Figure 3.10 shows a comparison of the IBEM results with the analytical solution for the acoustic pressure at

$r = \frac{a}{2}$ . In Figure 3.10, the frequency shift in the IBEM solution is apparent as expected because the 48 element model is a rough approximation of a sphere. However, the point source modeling capability of the IBEM otherwise appears to be valid.

The 48 element sphere model was used to verify the impedance boundary condition capability of the IBEM. A point source with volume velocity source strength of  $0.5 \text{ m}^3/\text{sec}$  was positioned at the center of the model. The sphere model was given impedance boundary conditions which corresponded to the impedance for free field radiation. The pressure field created by a point source (monopole) with volume velocity source strength  $Q$  radiating into a free field is [55]

$$p(r) = \frac{jk\rho_o cQ}{4\pi} \frac{e^{-jkr}}{r} \quad (3.50)$$

where  $r$  is the distance from the point source. The specific acoustic impedance is given by

$$z = \frac{p}{u} = -jk\rho_o c \frac{\partial p}{\partial r} \quad (3.51)$$

Substituting equation 3.50 into equation 3.51 gives the specific acoustic impedance as

$$z(r) = \frac{jk\rho_o cr}{1 + jkr} \quad (3.52)$$

The analytical and IBEM predictions for the acoustic pressure at  $r=\frac{a}{2}$  as a function of frequency are shown in Figure 3.11. The IBEM results are in excellent agreement with the analytical solution. The specific acoustic impedance boundary conditions were calculated at the radial locations of the element centroids which removed the geometric modeling error from the problem.

### 3.3.2 Rectangular Boundary Results

For verification purposes, the rectangular cavity was analyzed as a one-dimensional system. Analytical expressions for the pressure distribution in one-dimensional systems are readily available and easily evaluated. The frequency and method of excitation were chosen such that one-dimensional behavior was ensured. Two models of a rectangular cavity were used in the verification process. Both models have dimensions of 1.04775m x 1.02235m x 1.8288m. One model uses 80 elements while the other uses 156 elements. The 80 element model is shown in Figure 3.12.

The first acoustic problem considered was that of a driven-rigid cavity. The end of the cavity at  $Z=1.8288\text{m}$  was given a uniform velocity boundary condition of 1m/s. The other five sides of the cavity were rigid. The

analytical solution of the driven-rigid cavity of length  $L$  is [56]

$$p(x) = \frac{-j\rho_o cU_o}{\sin(kL)} \cos k(L-x) \quad (3.53)$$

where  $U_o$  is the velocity of the driven wall and  $x$  is the distance of a field point from the driven wall.

The accuracy of the IBEM results for the rectangular cavity were found to depend on the geometrical location at which the solution was obtained. For analysis of the results, solution locations were categorized into four qualitative groups:

- locations in the central portion of the cavity
- locations along a midsection of a cavity wall
- locations along an edge
- locations near a corner

Results obtained with the 80 element model are compared to the analytical solution in Figures 3.13 and 3.14. The IBEM results in Figure 3.13 were calculated along the line described by  $X=0.5m$ ,  $Y=0.5m$  (along the central portion of the cavity). The IBEM results shown in Figure 3.14 were computed for locations along the line described by  $X=0.1m$ ,  $Y=0.1m$  (along an edge). Overall, the IBEM results compare well with the analytical solution. The results calculated

along the line through the middle of the of the cavity degrade slightly in accuracy near the ends of the cavity. The data in Figure 3.14 shows this same behavior but to a greater degree. Thus, the performance of the IBEM is least accurate for domain locations in close proximity to a corner of the cavity.

A smaller element size improves the accuracy of the IBEM results for locations near a corner. The data in Figure 3.13 is replotted in Figure 3.15 along with the results obtained with the 156 element model. Note that the accuracy of the results for both models is approximately the same. However, when the data for the 80 element model is compared with the results obtained using the 156 element model, an overall improvement in the accuracy is found for the domain locations near cavity corners as shown in Figure 3.16.

The loss in accuracy of the IBEM solution for domain locations near a corner is a result of the one point quadrature approximation to the elemental boundary integrals. As a domain location approaches a point on a boundary element, the value of  $r$  in the fundamental solutions for that domain location approach zero at the boundary point. Depending on the size of the element and where the domain location is situated relative to the element, the value of  $r$  over the element may vary from

relatively small quantities to much larger quantities as shown in Figure 3.17a. Because of the  $\frac{1}{r}$  factor in the fundamental pressure solution and the  $\frac{1}{r^2}$  factor in the fundamental velocity solution, large variations as  $r$  approaches zero cause the fundamental solutions to behave as high order functions. Since the one point quadrature poorly integrates high order functions, the elemental boundary integrals for the elements close to the domain location are not accurately approximated (equation 3.40). Smaller element size improves the results because the relative change in the value of  $r$  is less over a smaller element as shown in Figure 3.17b. As shown by Gardner [47], using higher order quadratures for approximating the elemental boundary integrals also improves the boundary element method results for domain locations near the boundary.

The acoustic pressure as a function of frequency was analyzed at particular locations in the driven-rigid cavity. A comparison of the analytical solution with the IBEM predictions for the pressure at a location in the central portion of the cavity (0.5m,0.5m,1.0m) is presented in Figures 3.18 and 3.19. The 80 element model was used to obtain the results in Figure 3.18. The IBEM predictions presented in Figure 3.19 were acquired with the 156 element model. Comparison of Figures 3.18 and 3.19 shows both

models perform equally well for centrally located domain positions. The beginning of the IBEM solution divergence from the analytical solution for the low frequency regime is evident in both Figure 3.18 and 3.19. This divergence is of the same nature as that discussed for the interior of a pulsating sphere. For the driven-rigid cavity problem, the IBEM solution reverses slope at approximately  $k=0.1$  (5.5 Hz). Using the 80 element model, the pressure as a function of frequency was calculated for a domain location near the middle of a side-wall. The results were identical to those shown in Figure 3.18. Figure 3.20 shows the 80 element model results for a domain location near a corner of the cavity (0.1m,0.1m,0.1m). Figure 3.21 shows the results for the 156 element for the same location. For reasons previously discussed, the 156 element model provides a more accurate solution at the domain location near a corner but still shows some error.

The driven-infinite cavity was the next acoustical construct analyzed with the IBEM. The analytical solution for the pressure as a function of position in the cavity is given by

$$p(x) = \rho_0 c U_0 e^{-jkx} \quad (3.54)$$

where  $x$  is the distance from the driven end and  $U_0$  is the amplitude of the time harmonic velocity function at the



driven end. The particle velocity along the cavity is

$$u(x) = U_0 e^{-jkx} \quad (3.55)$$

The specific acoustic impedance at a point in the cavity is given by

$$z(x) = \frac{p(x)}{u(x)} = \rho_0 c \quad (3.56)$$

Thus, the driven-infinite cavity problem can be modeled by the rectangular cavity by specifying the specific acoustic impedance boundary condition with a value of  $\rho_0 c$  for the wall opposite the driven end.

The IBEM solutions for the driven-infinite cavity using the 80 element model and the 156 element model are presented in Figure 3.22. Note that the scale has been expanded significantly. The velocity at the driven end was 1m/s and the wavenumber was 2. The 156 element model had slightly better accuracy overall. The maximum error for the 80 element model is approximately 5.5% while the maximum error for the 156 element model is approximately 3%. For higher values of wavenumber the accuracy of the IBEM deteriorated particularly at locations near the cavity ends. Consistent with the results for the driven-rigid cavity, the performance of the IBEM degraded for the driven-infinite cavity problem at domain locations near a corner.

An interesting aspect of the convergence of the boundary element methods is apparent in Figure 3.22. Unlike finite element methods, boundary element methods cannot be mathematically proven to converge to the true solution as the element size is decreased. Consequently, boundary element method results may not systematically approach the true solution with decreasing element size. This feature is noticeable in Figure 3.22. The 80 element model overpredicts the analytical solution while the 156 element model basically underpredicts the analytical solution.

### 3.3.3 Summary

In the preceding sections, it has been shown that the IBEM (as developed in this thesis) is a viable method for the prediction of the acoustic pressure in sound fields. However, there are several phenomena which must be acknowledged. First, when modeling curved surfaces with geometrically flat elements, the model should be constructed such that the centroids of the elements lie on the curved surfaces. Second, the pressure solution for exterior problems diverges from the true solution at the eigenfrequencies of the corresponding interior problem. Third, the IBEM results are inaccurate for the very low frequency regime of interior problems. However, this problem is irrelevant for this work because active noise

controllers are unable to operate at such low frequencies. This low frequency inaccuracy potentially can be overcome with better integration. Fourth, although the IBEM results for the rectangular cavity were excellent overall, the accuracy of the IBEM solution does degrade at domain locations in close proximity to a corner. The results for domain locations near a corner do improve, however, with a finer discretization.

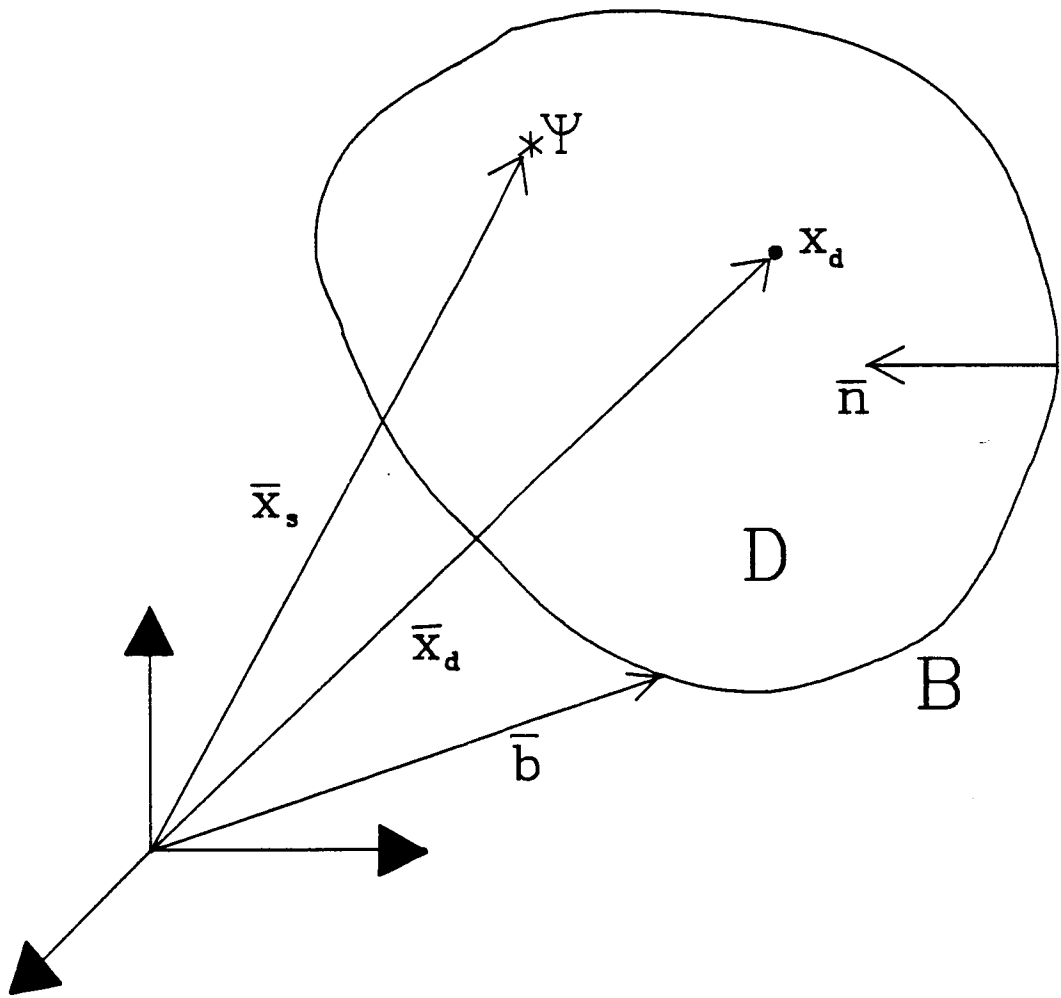


Figure 3.1 - Geometrical Description For The Indirect Boundary Element Method Formulation

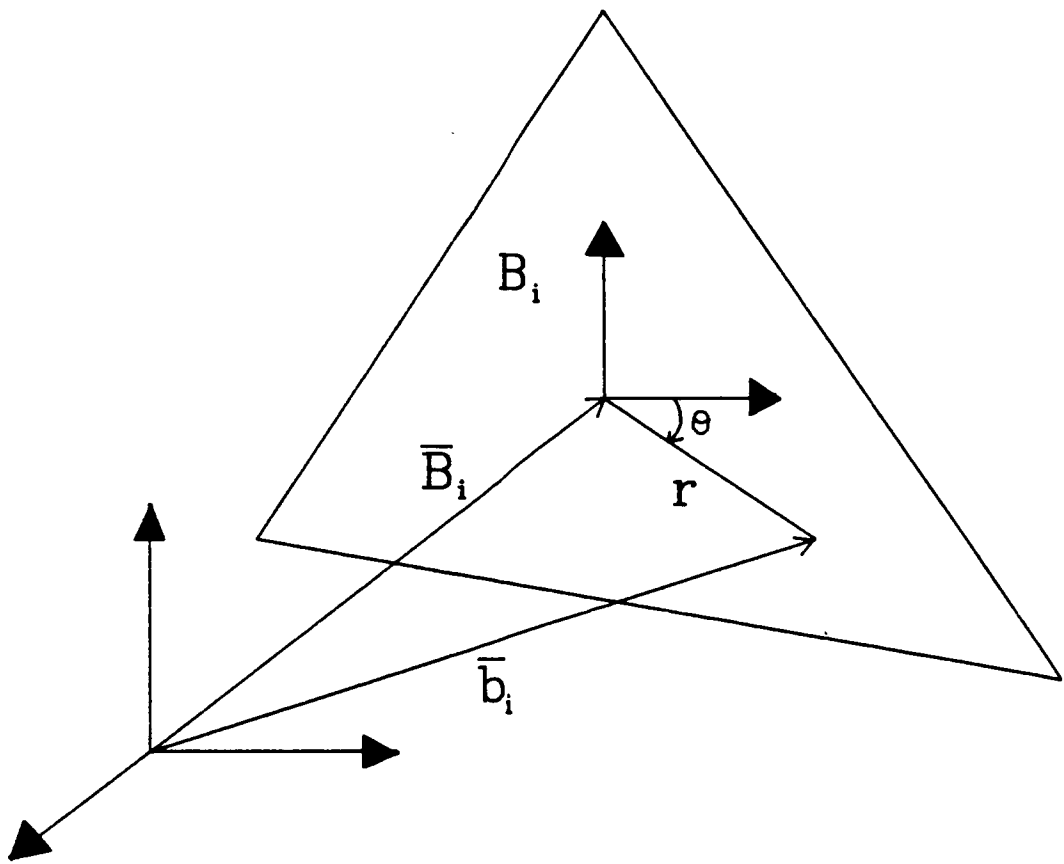


Figure 3.2 - Polar Coordinates For An Element

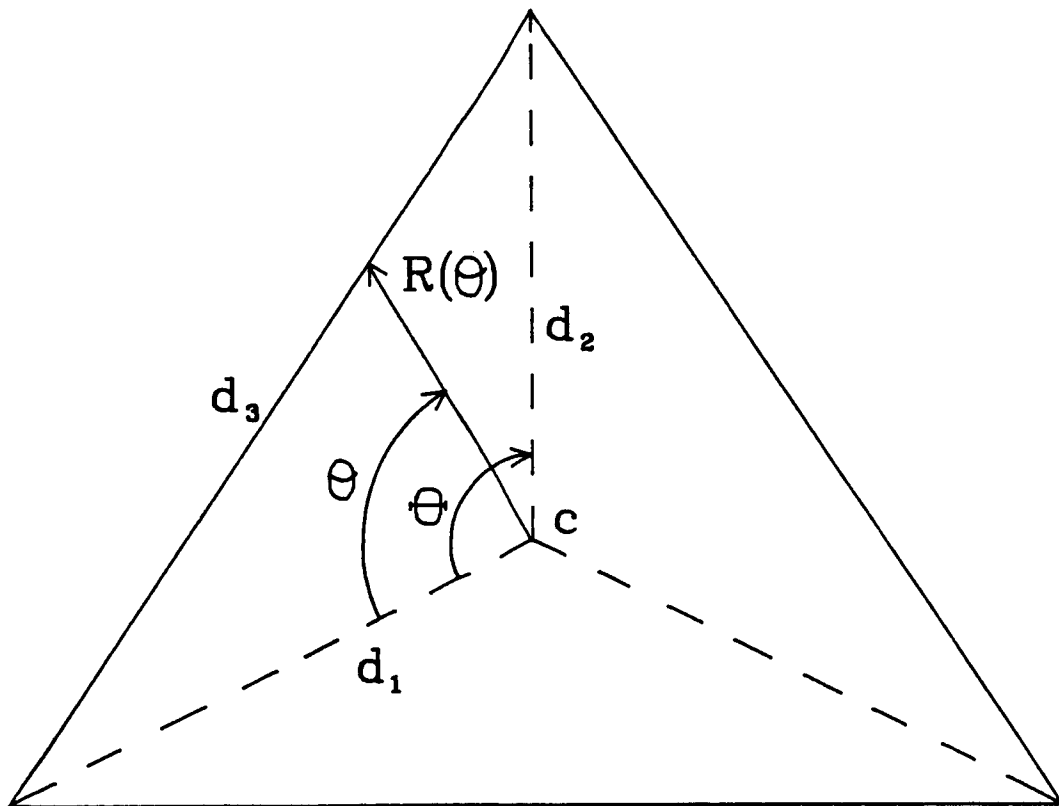


Figure 3.3 - Geometry For Integration Of The Fundamental Pressure Solution In Polar Coordinates

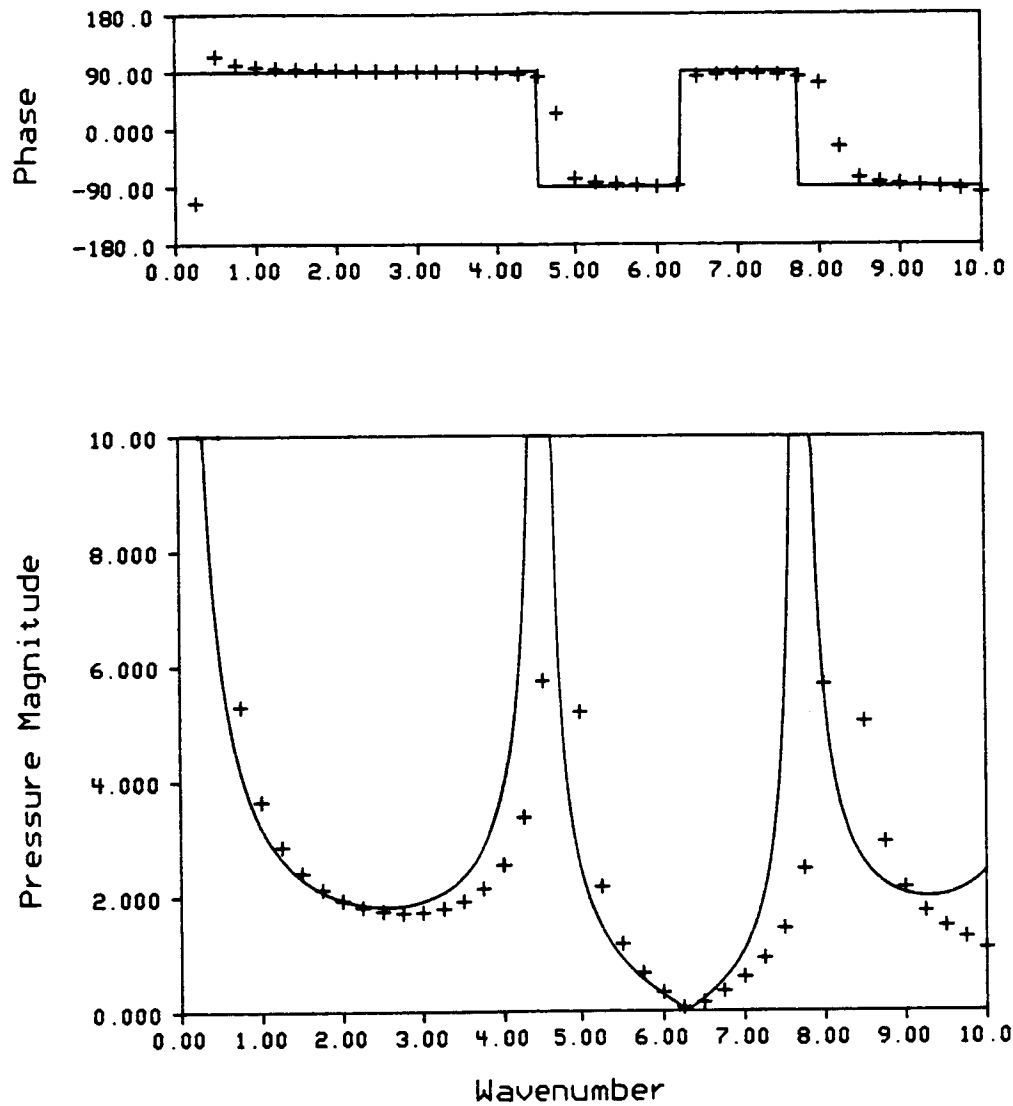


Figure 3.4 - Analytical And Numerical Predictions For The Pressure At Half The Radius Of A Pulsating Sphere As A Function Of Frequency ( $\rho_0 c = 1.0$ ).

— Analytical Solution  
 + 96 Element Model IBEM Solution

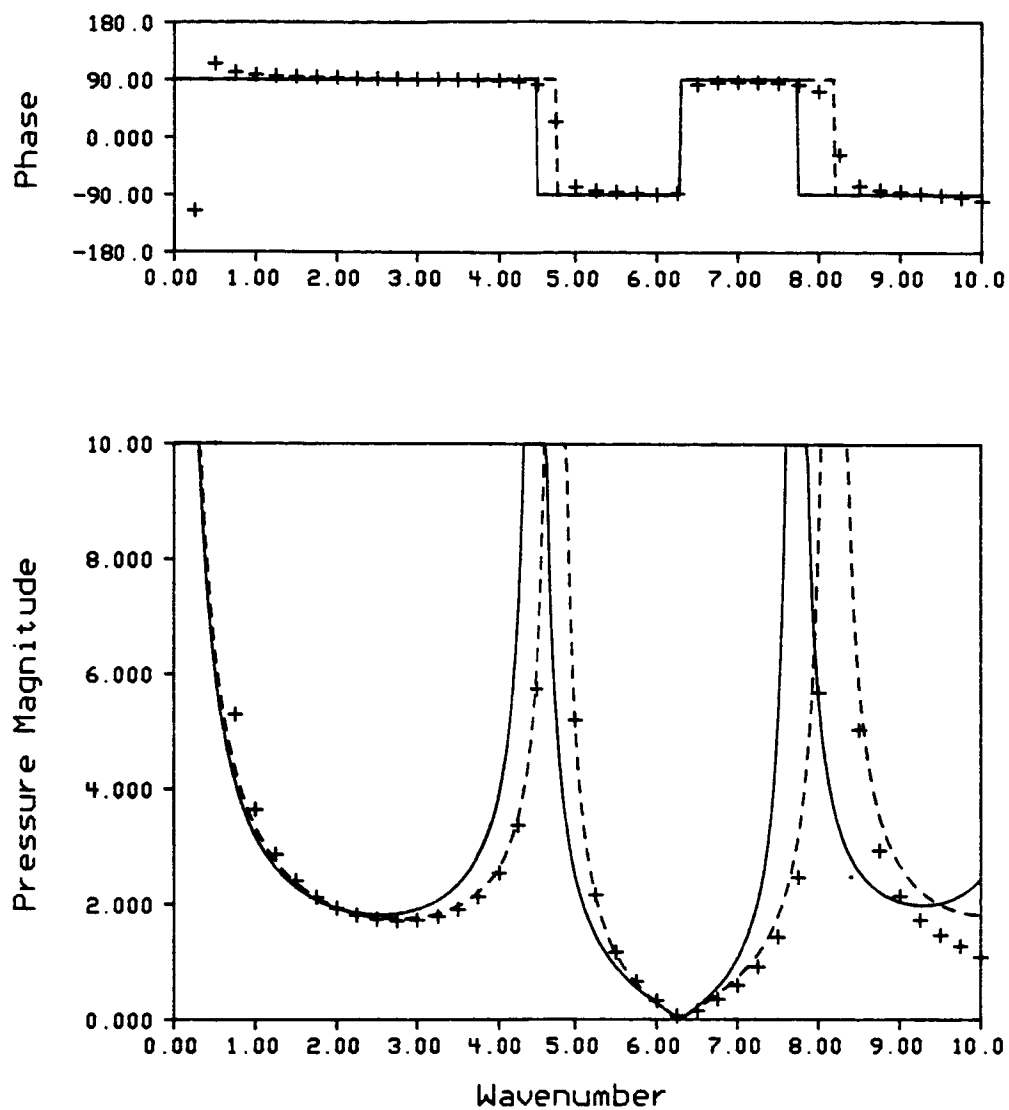


Figure 3.5 - Adjusted Analytical Solution For The Pressure At Half The Radius Of A Pulsating Sphere ( $\rho_c = 1.0$ ).

— Analytical Solution With  $a=1.0$   
 - - - Analytical Solution With  $a=0.9437$   
 + 96 Element Model IBEM Solution



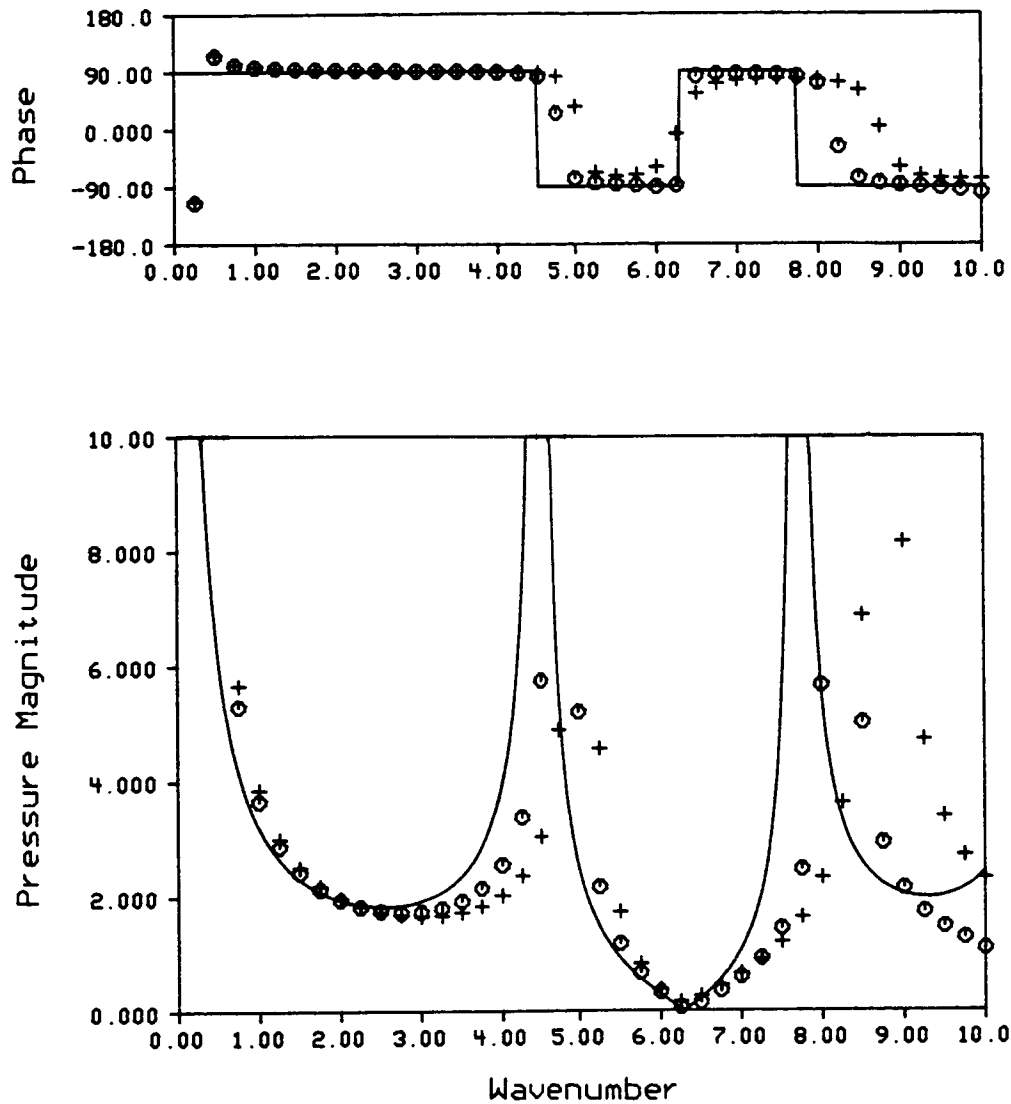


Figure 3.6 - Effect Of Element Mesh Size On The IBEM Solution For The Pressure At Half The Radius Of A Pulsating Sphere ( $\rho c = 1.0$ ).

— Analytical Solution  
 o 96 Element Model IBEM Solution  
 + 48 Element Model IBEM Solution

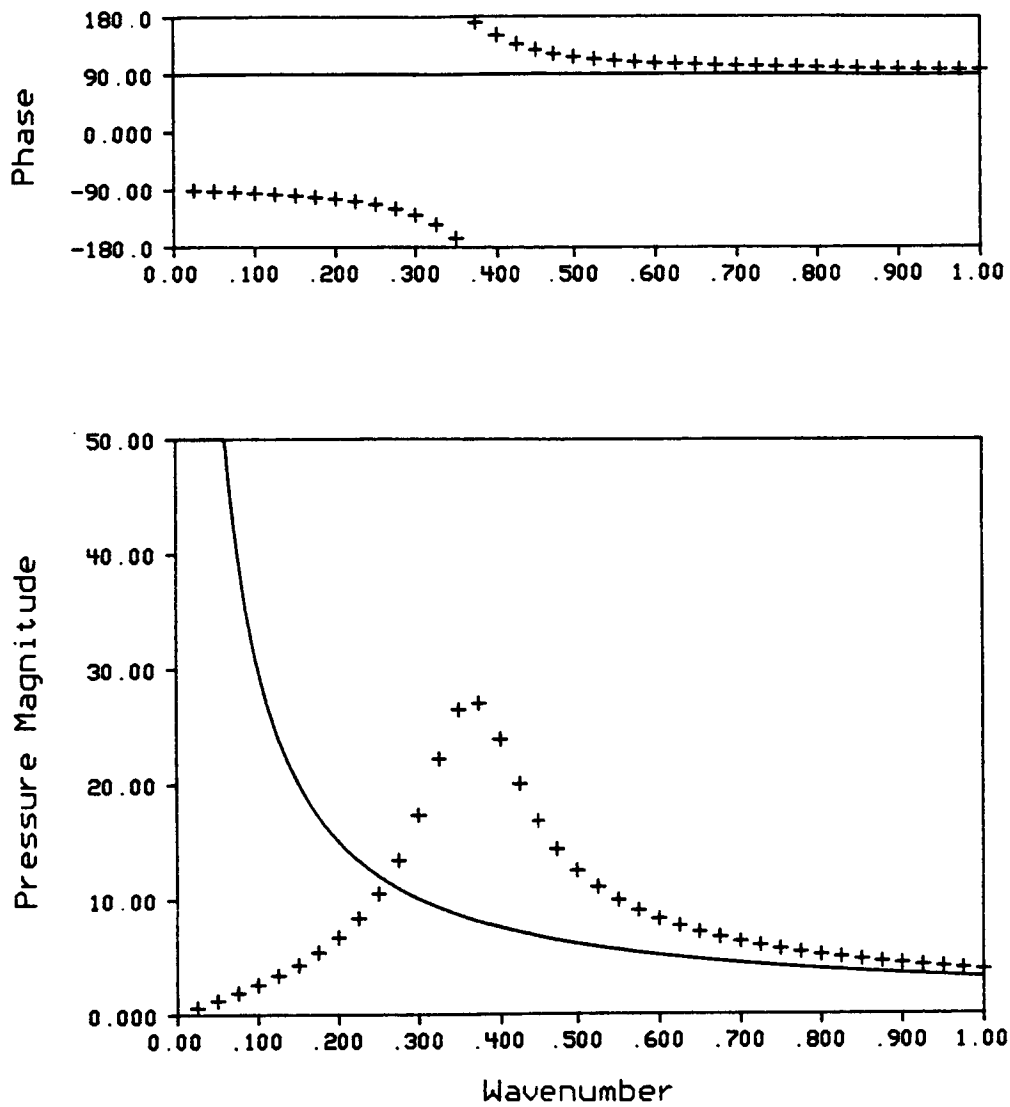


Figure 3.7 - Analytical And Numerical Pressure Predictions  
At Half The Radius Of A Pulsating Sphere For  
The Low Frequency Regime ( $\rho c = 1.0$ ).

— Analytical Solution<sup>0</sup>  
+ 48 Element Model IBEM Solution

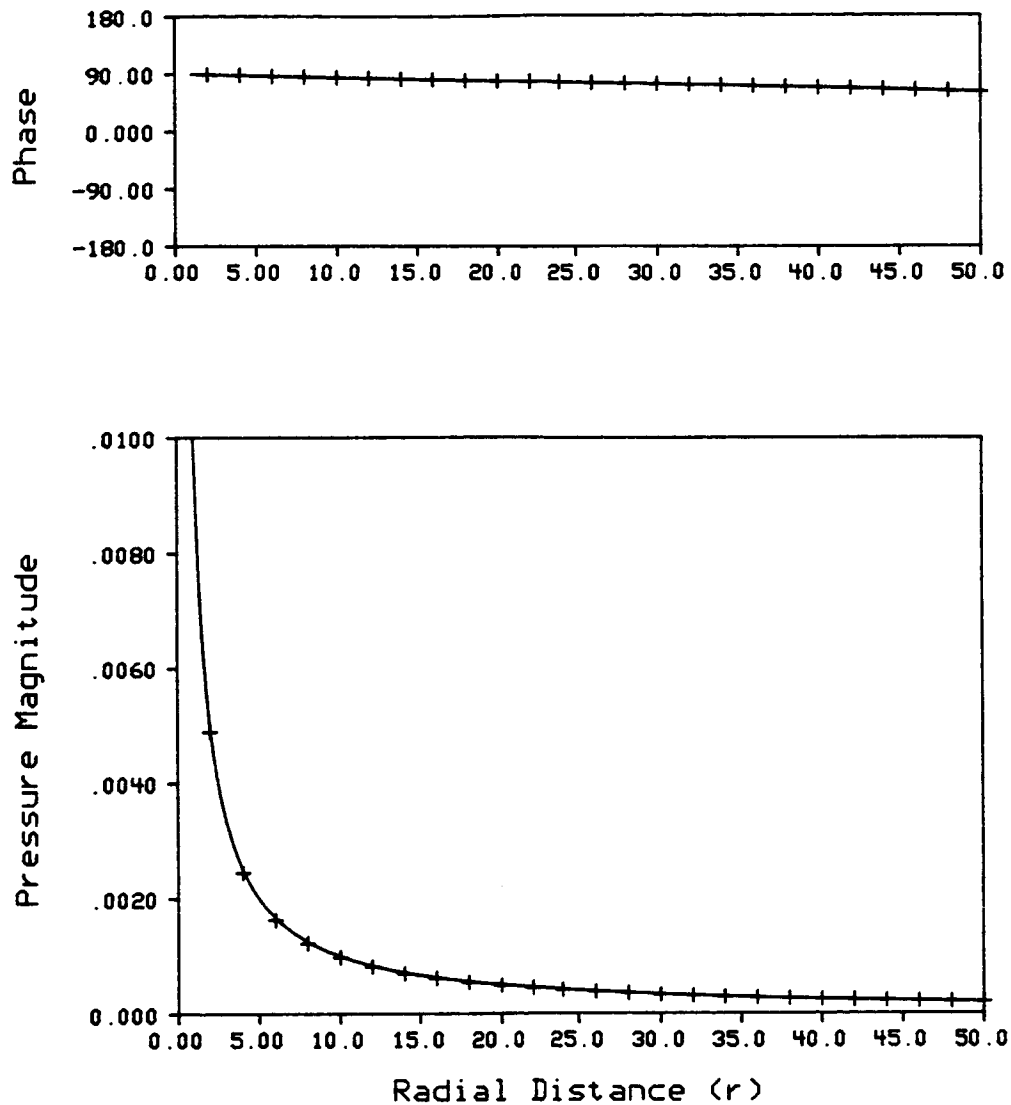


Figure 3.8 - Analytical And Numerical Predictions Of The Pressure Distribution For The Exterior Of A Pulsating Sphere At  $k=0.01$  ( $\rho_c = 1.0$ ).

— Analytical Solution  
 + 96 Element Model IBEM Solution

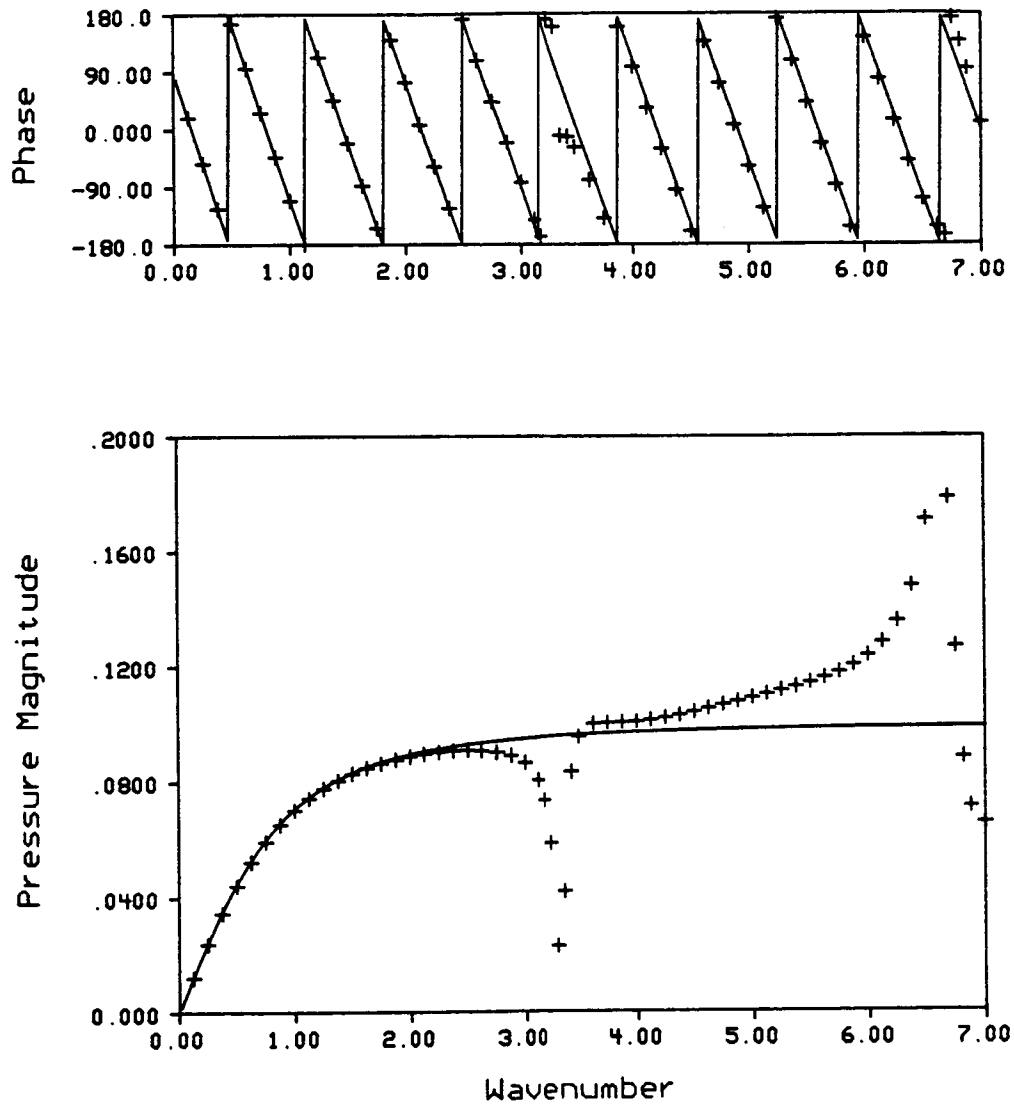


Figure 3.9 - Analytical And Numerical Predictions Of The Pressure As A Function Of Frequency For The Exterior Of A Pulsating Sphere ( $\rho_c = 1.0$ ).

— Analytical Solution  
 + 96 Element Model IBEM Solution

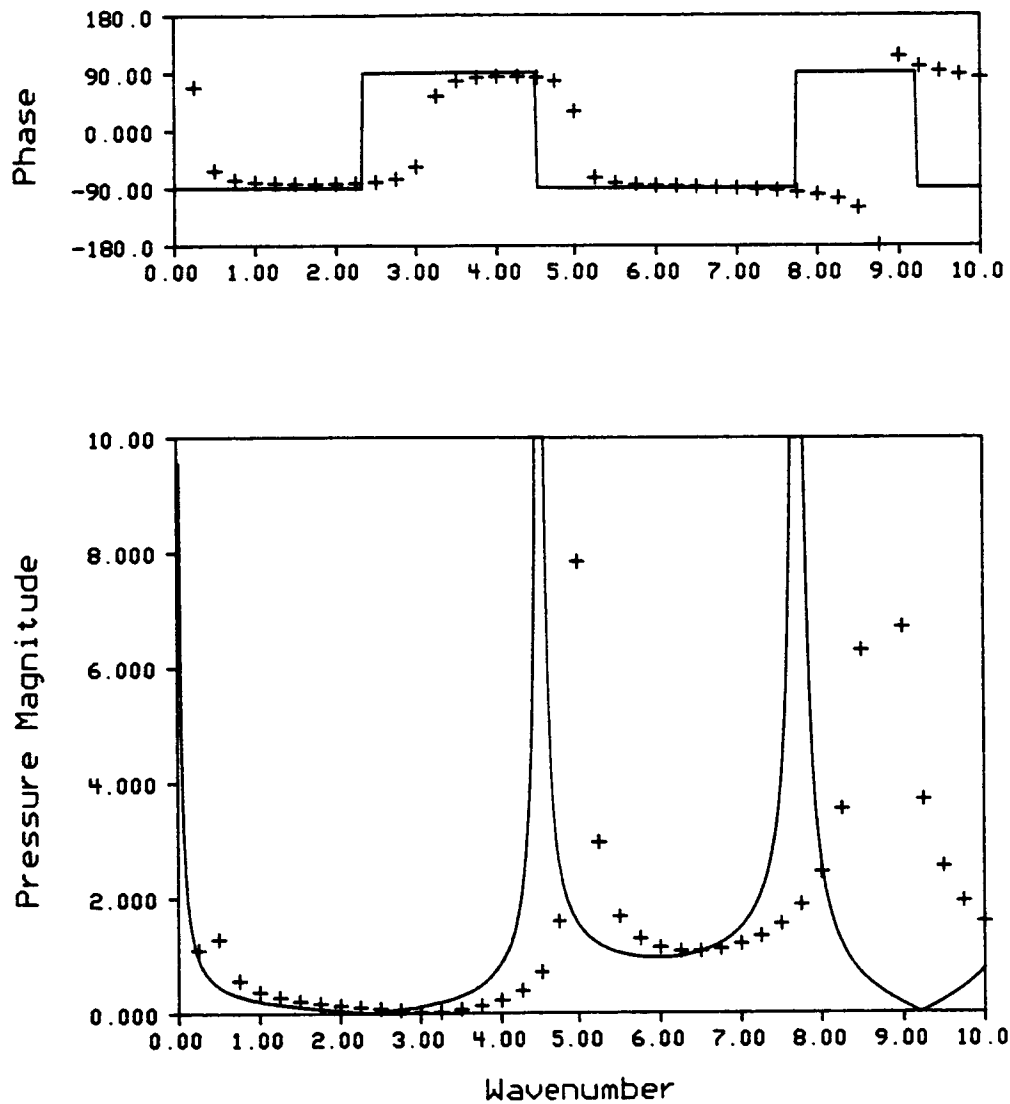


Figure 3.10 - Analytical And Numerical Predictions For The Pressure At Half The Radius Of A Rigid Wall Sphere With A Point Source At The Center ( $\rho_c = 1.0$ ).

— Analytical Solution  
 + 48 Element Model IBEM Solution

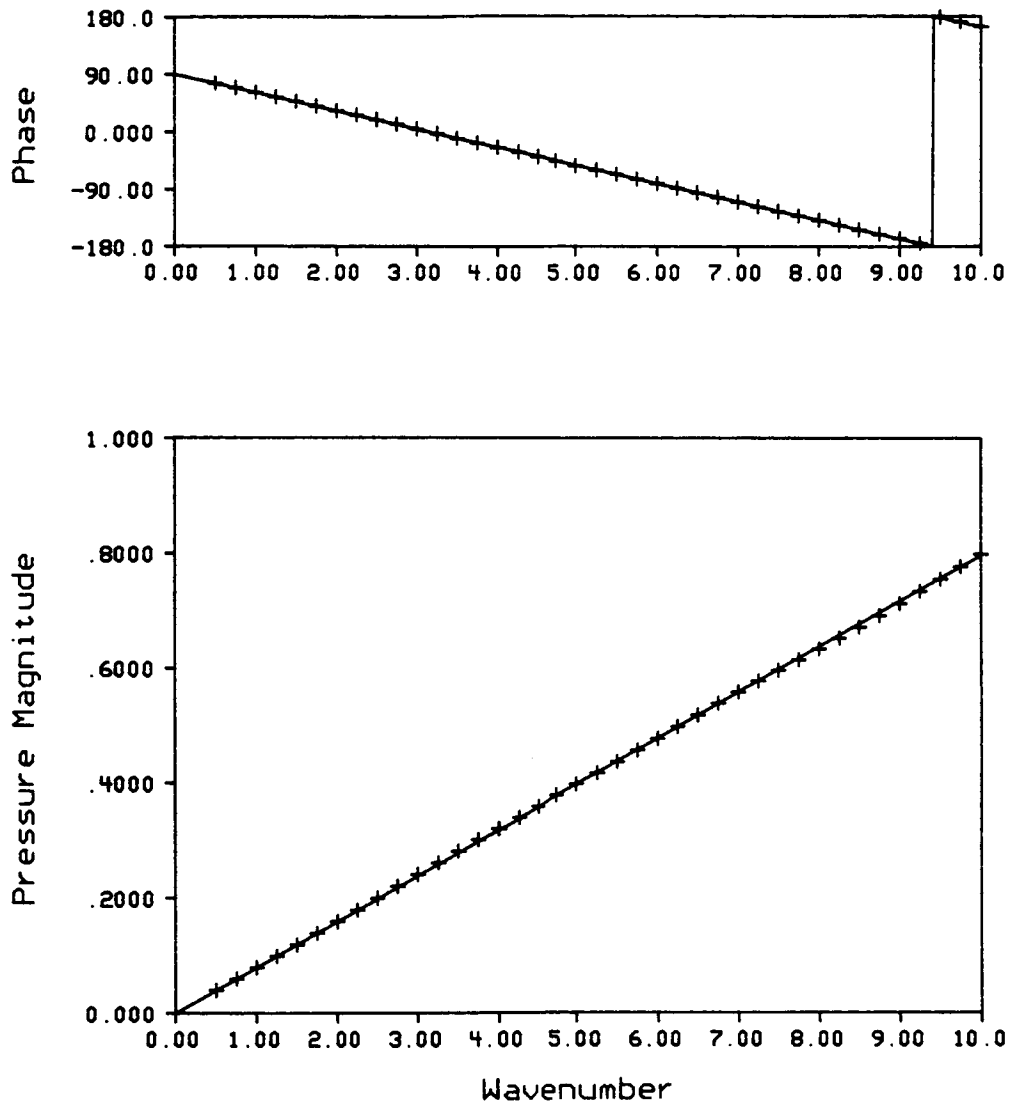


Figure 3.11 - Analytical And Numerical Predictions For The Pressure At Half The Radius Of A Sphere With Free Field Impedance Boundary Conditions And A Point Source At The Center ( $\rho_o c = 1.0$ ).

— Analytical Solution  
 + 48 Element Model IBEM Solution

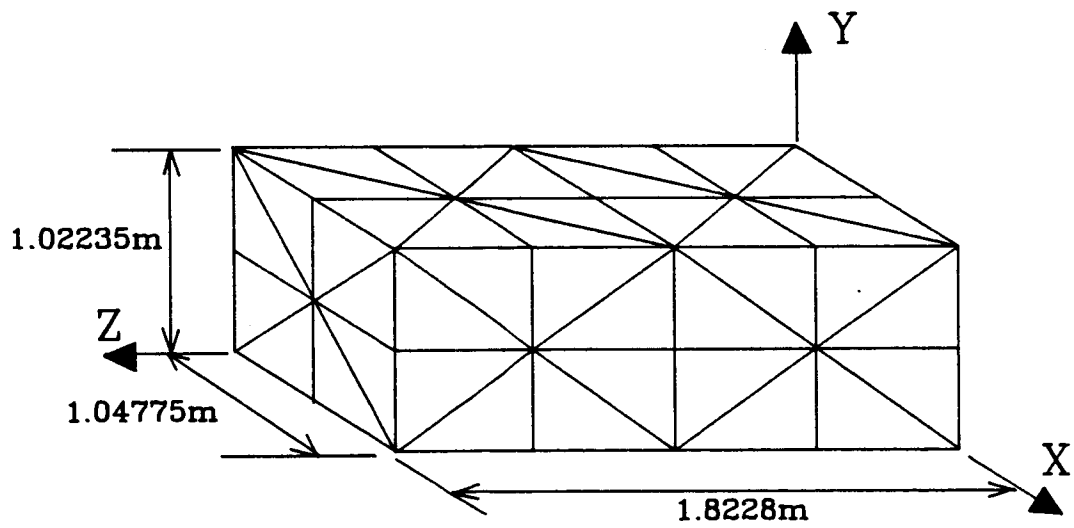


Figure 3.12 - 80 Element Rectangular Cavity Model

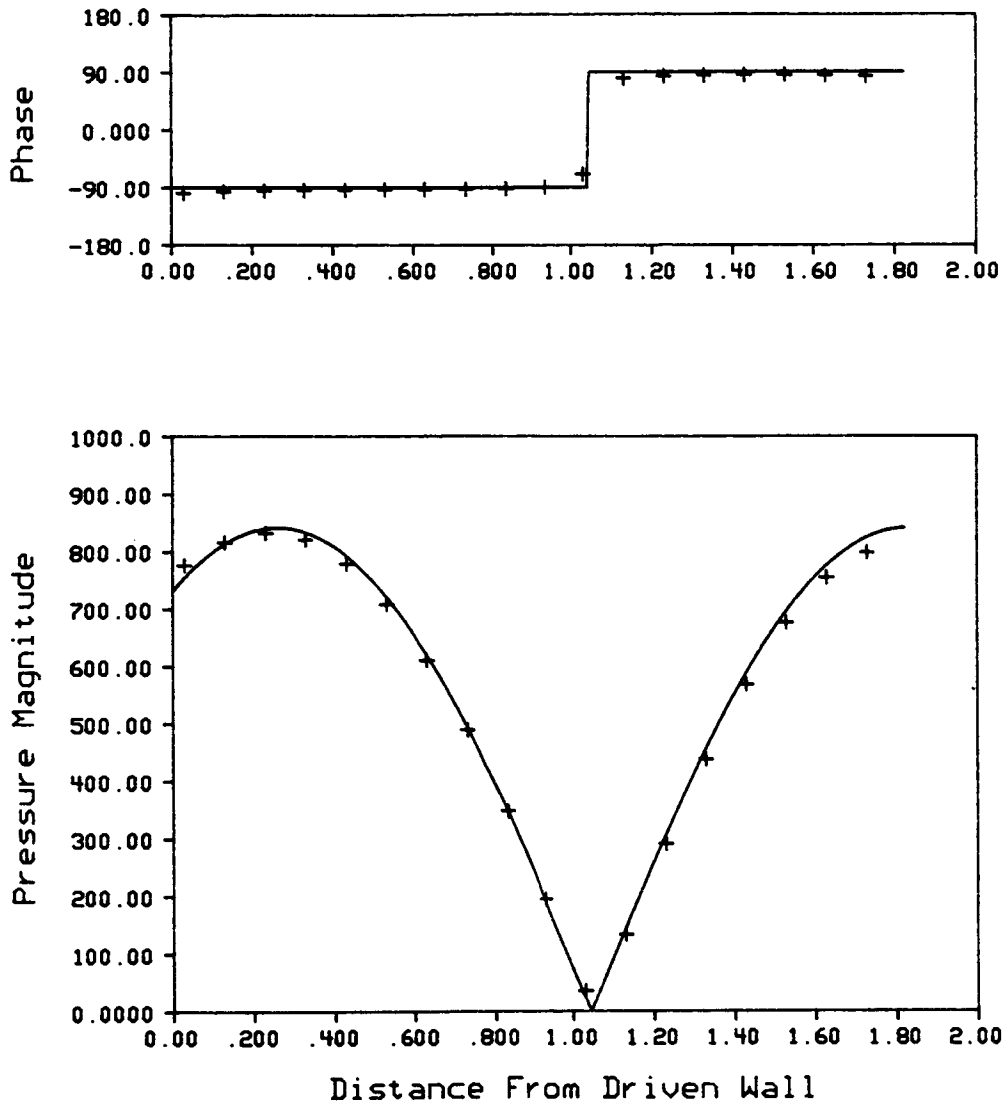


Figure 3.13 - Analytical And Numerical Predictions Of The Pressure Distribution Near The Center Of The Driven-Rigid Cavity At  $k=2.0$  ( $p_c = 415.0$ ).

— Analytical Solution  
 + 80 Element Model IBEM Solution



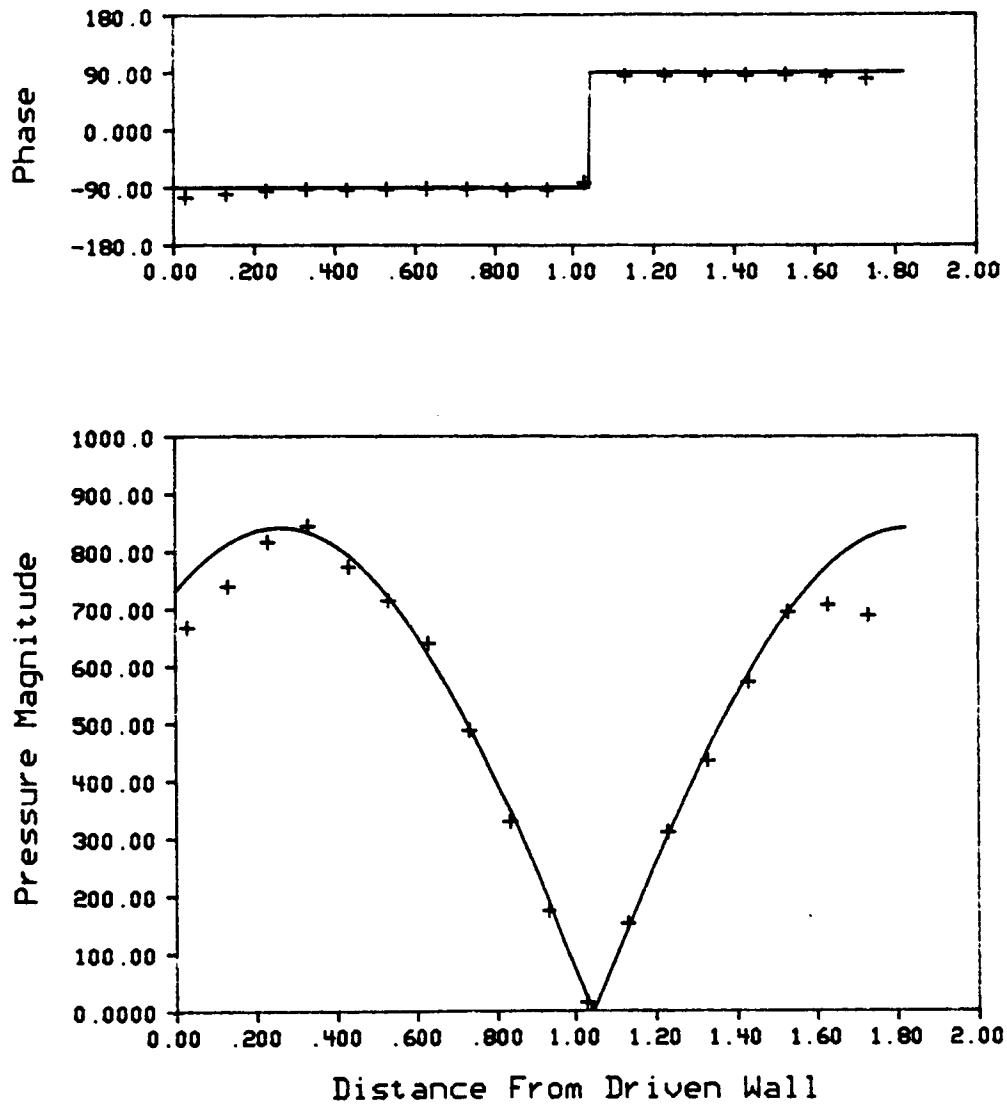


Figure 3.14 - Analytical And Numerical Predictions Of The Pressure Distribution Along An Edge Of The Driven-Rigid Cavity At  $k=2.0$  ( $\rho_o = 415.0$ ).

— Analytical Solution  
 + 80 Element Model IBEM Solution

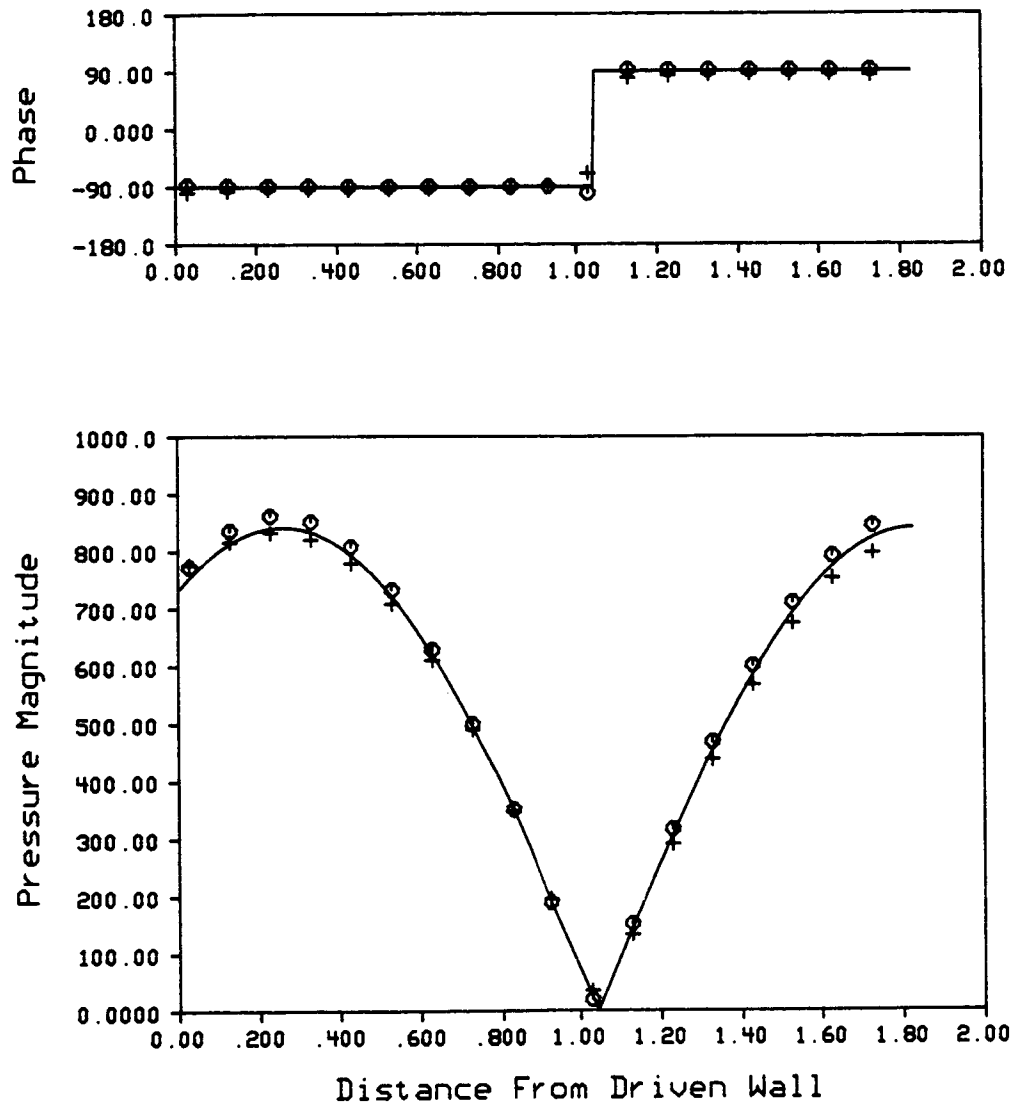


Figure 3.15 - Effect Of Element Mesh Size On The IBEM Solution For The Pressure Distribution Along The Center Of A Driven-Rigid Cavity At  $k=2.0$  ( $\rho_c = 415.0$ ).

o — Analytical Solution  
 + 80 Element Model IBEM Solution  
 o 156 Element Model IBEM Solution

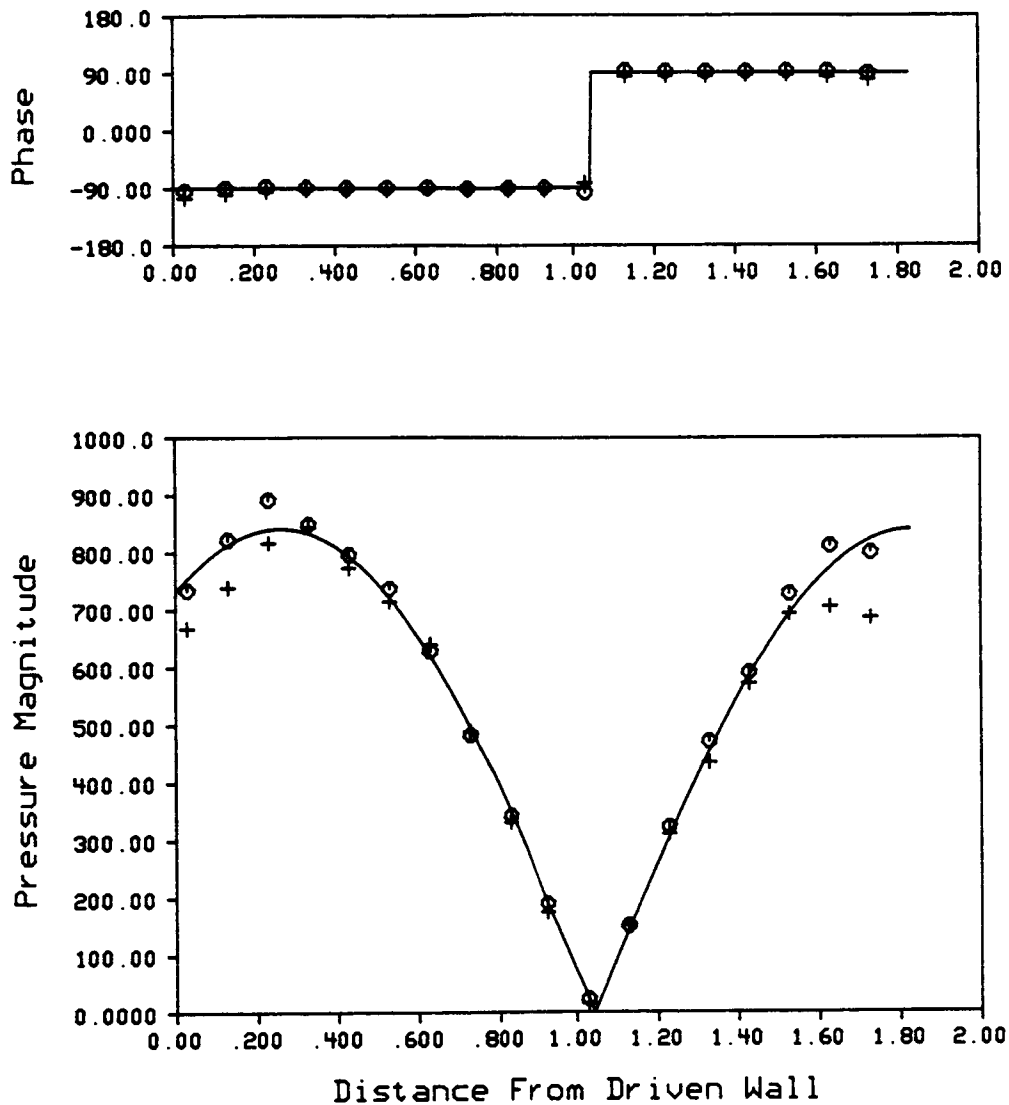
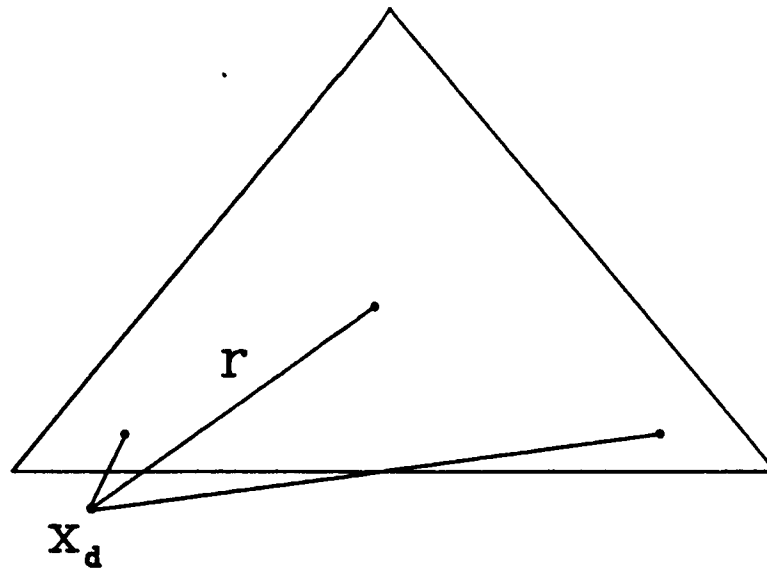
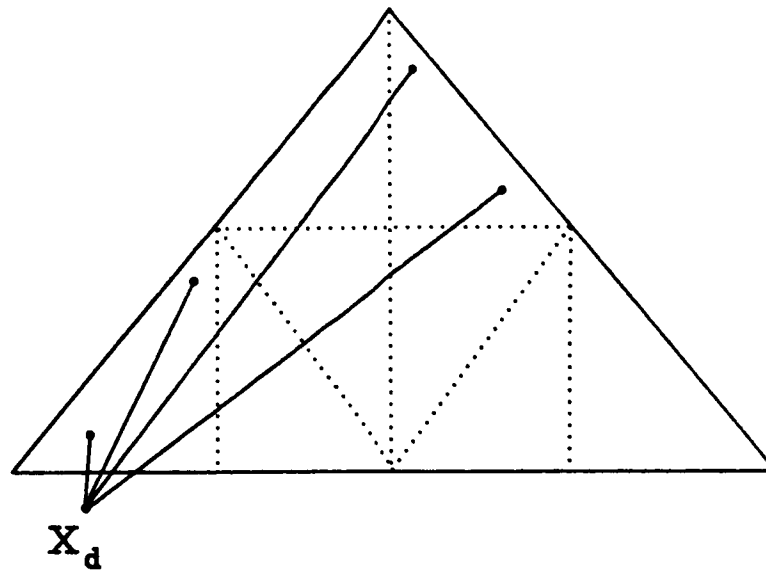


Figure 3.16 - Effect Of Element Mesh Size On The IBEM Solution For The Pressure Distribution Along An Edge Of A Driven-Rigid Cavity At  $k=2.0$  ( $p_c = 415.0$ ).

o — Analytical Solution  
 + 80 Element Model IBEM Solution  
 o 156 Element Model IBEM Solution



(a)



(b)

Figure 3.17 - Effect Of Element Mesh Size On The Behavior Of The Quantity  $r$  In The Fundamental Solutions For Domain Locations Close To The Boundary

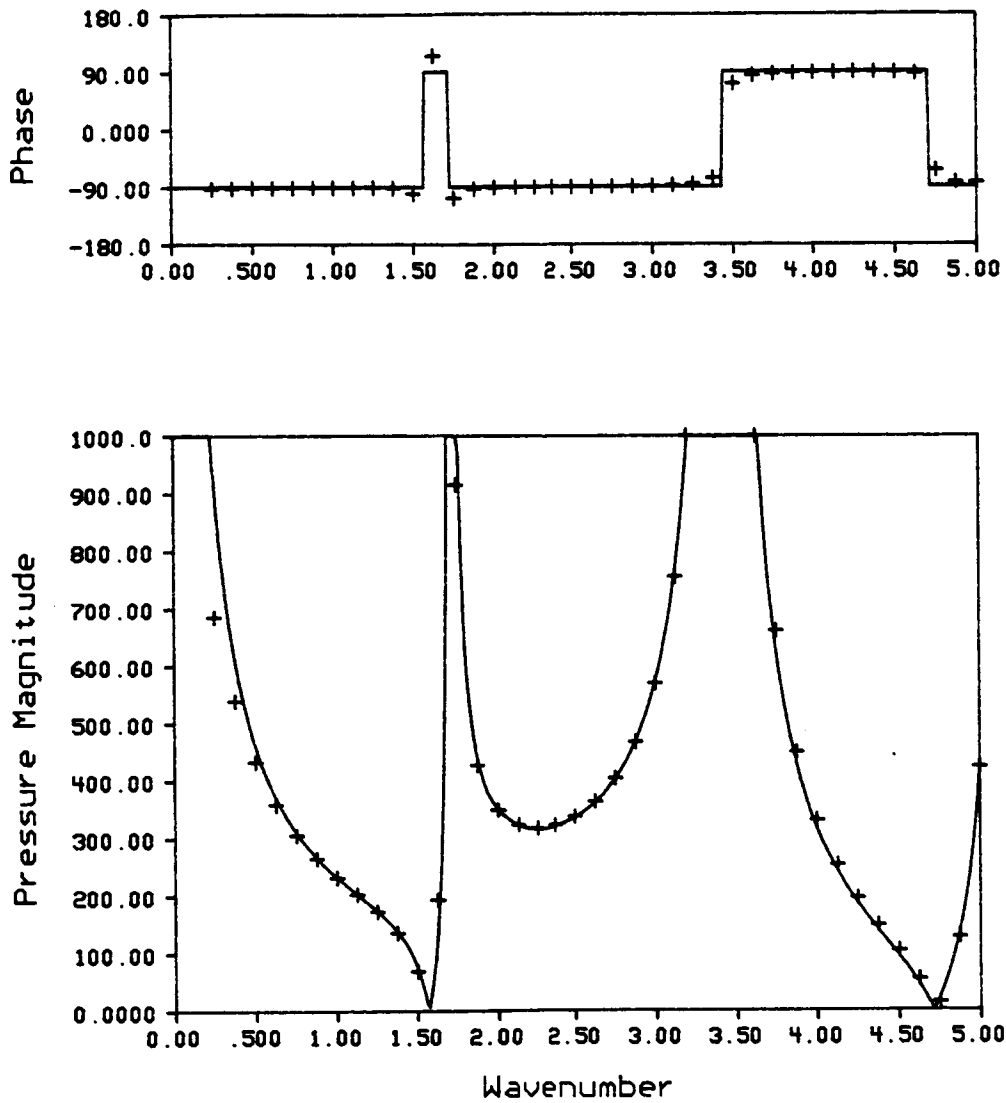


Figure 3.18 - Analytical And Numerical Pressure Predictions  
As A Function Of Frequency For A Location In  
The Center Of A Driven-Rigid Cavity  
( $\rho_c = 415.0$ ).

— Analytical Solution  
+ 80 Element Model IBEM Solution

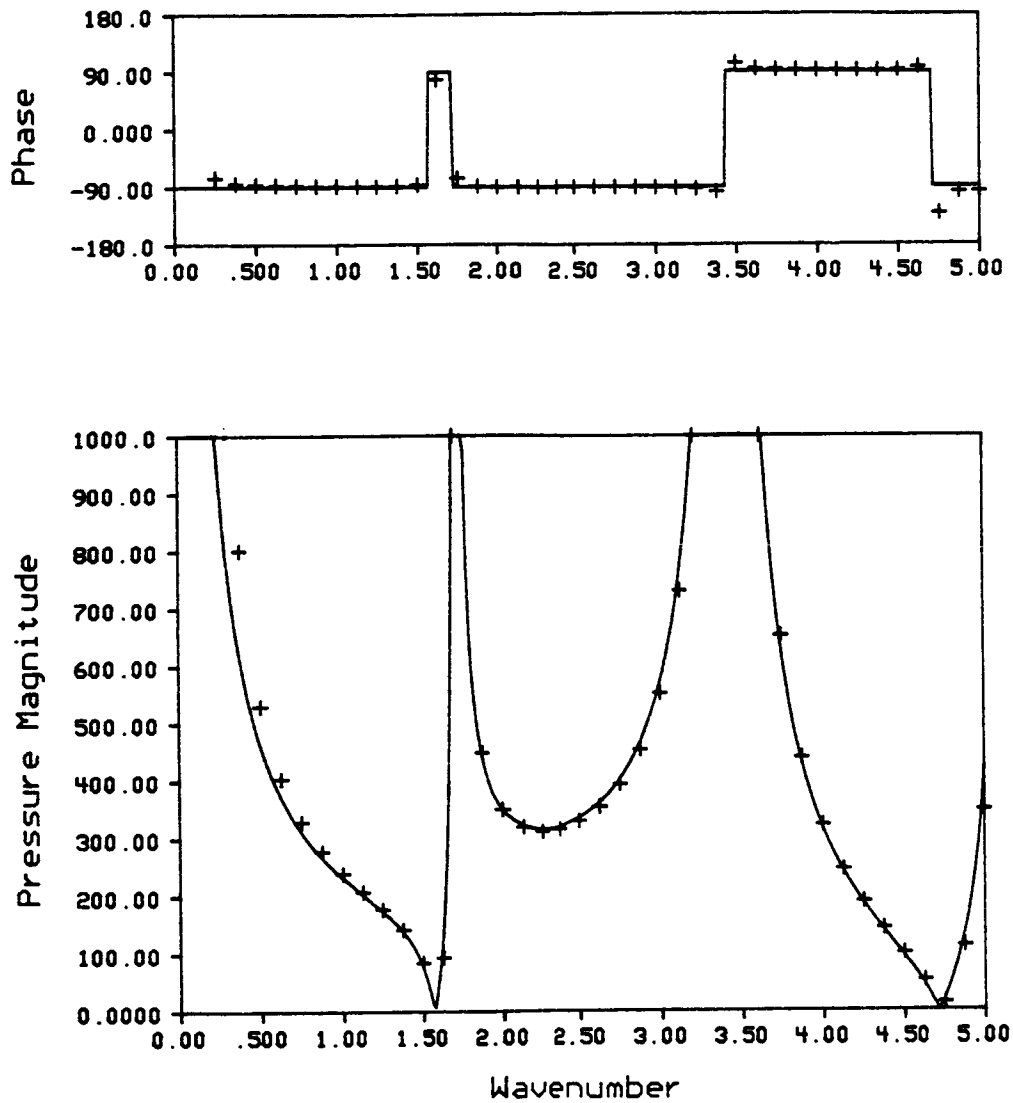


Figure 3.19 - Analytical And Numerical Pressure Predictions As A Function Of Frequency For A Location In The Center Of A Driven-Rigid Cavity ( $p_o = 415.0$ ).

— Analytical Solution  
 + 156 Element Model IBEM Solution

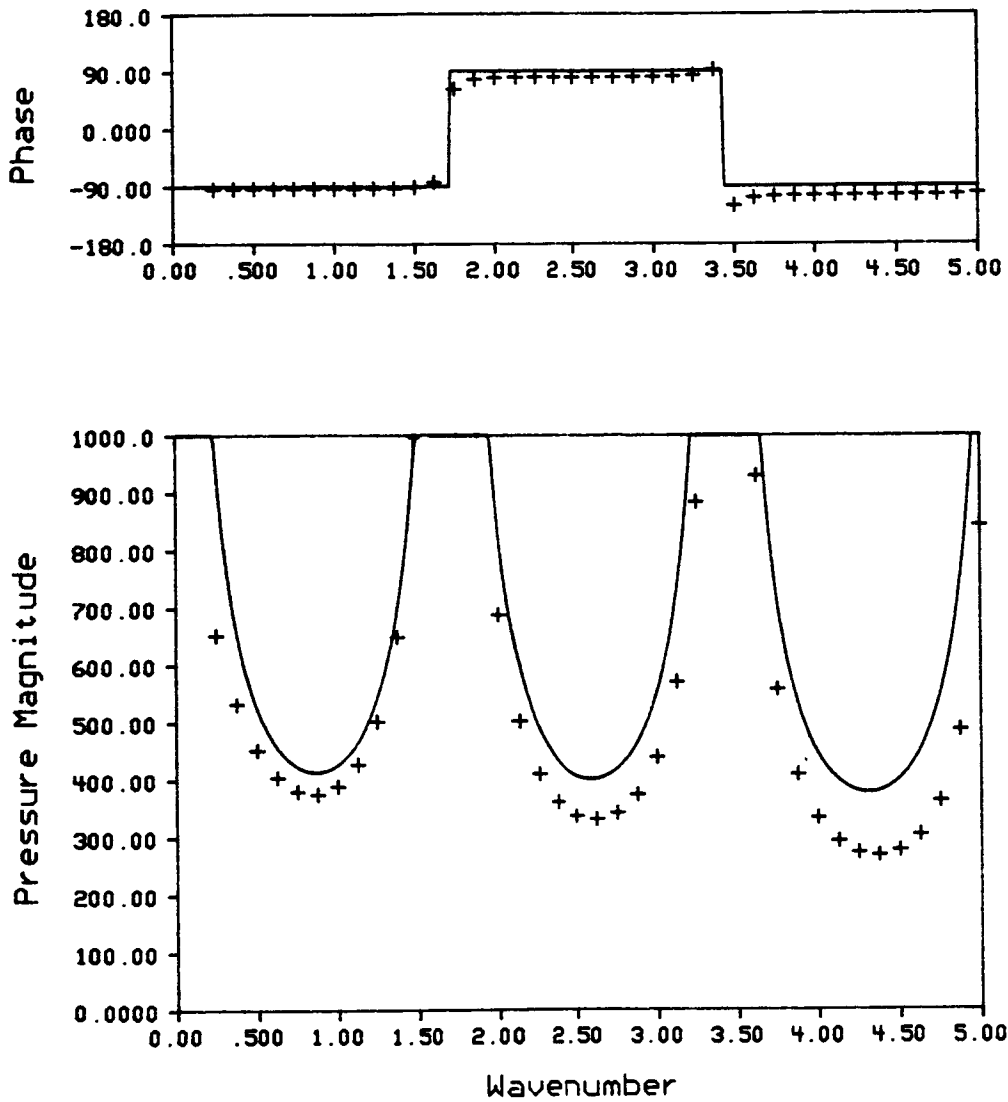


Figure 3.20 - Analytical And Numerical Pressure Predictions  
As A Function Of Frequency For A Location  
Near The Corner Of A Driven-Rigid Cavity  
( $\rho_c = 415.0$ ).  
 — Analytical Solution  
 + 80 Element Model IBEM Solution

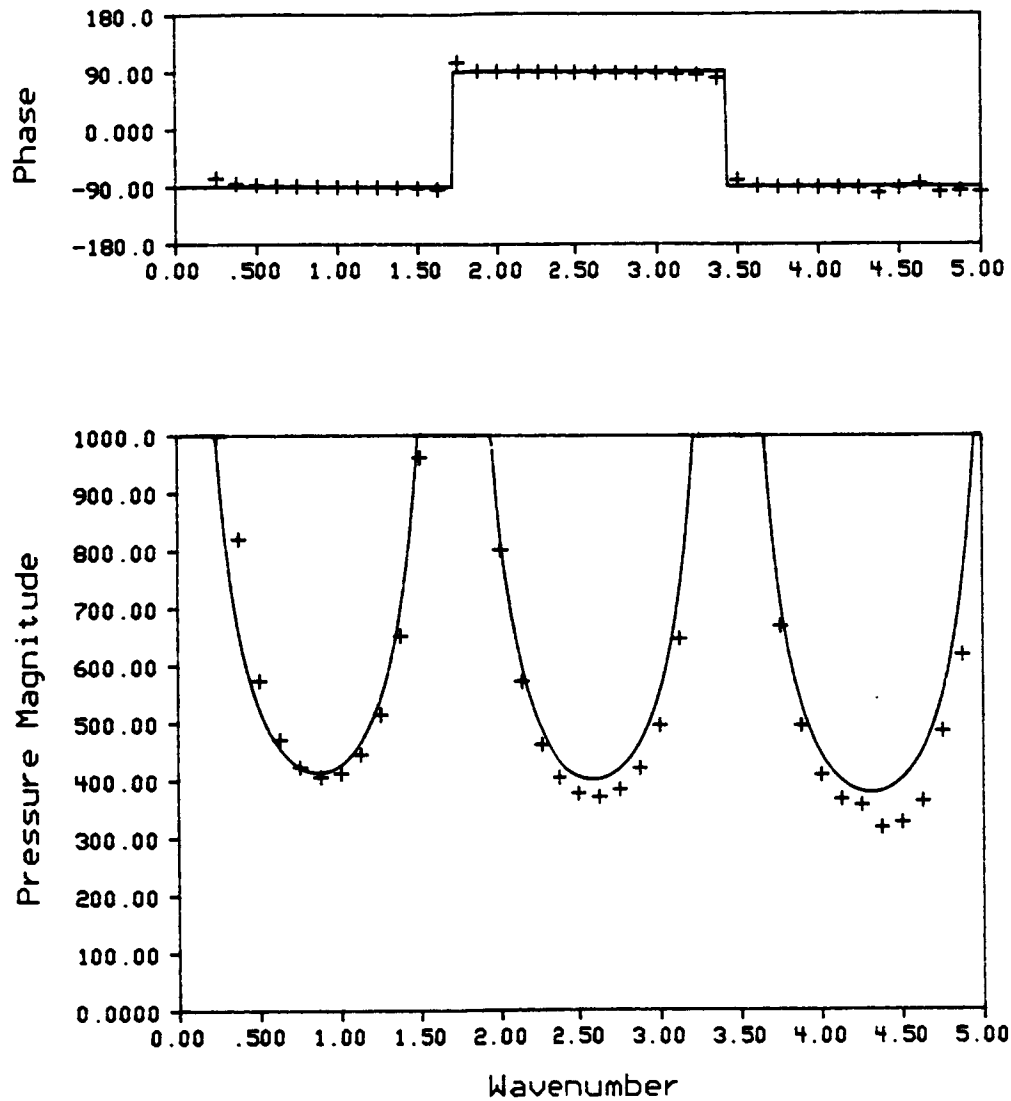


Figure 3.21 - Analytical And Numerical Pressure Predictions  
As A Function Of Frequency For A Location  
Near The Corner Of A Driven-Rigid Cavity  
( $\rho_c = 415.0$ ).

— Analytical Solution  
+ 156 Element Model IBEM Solution



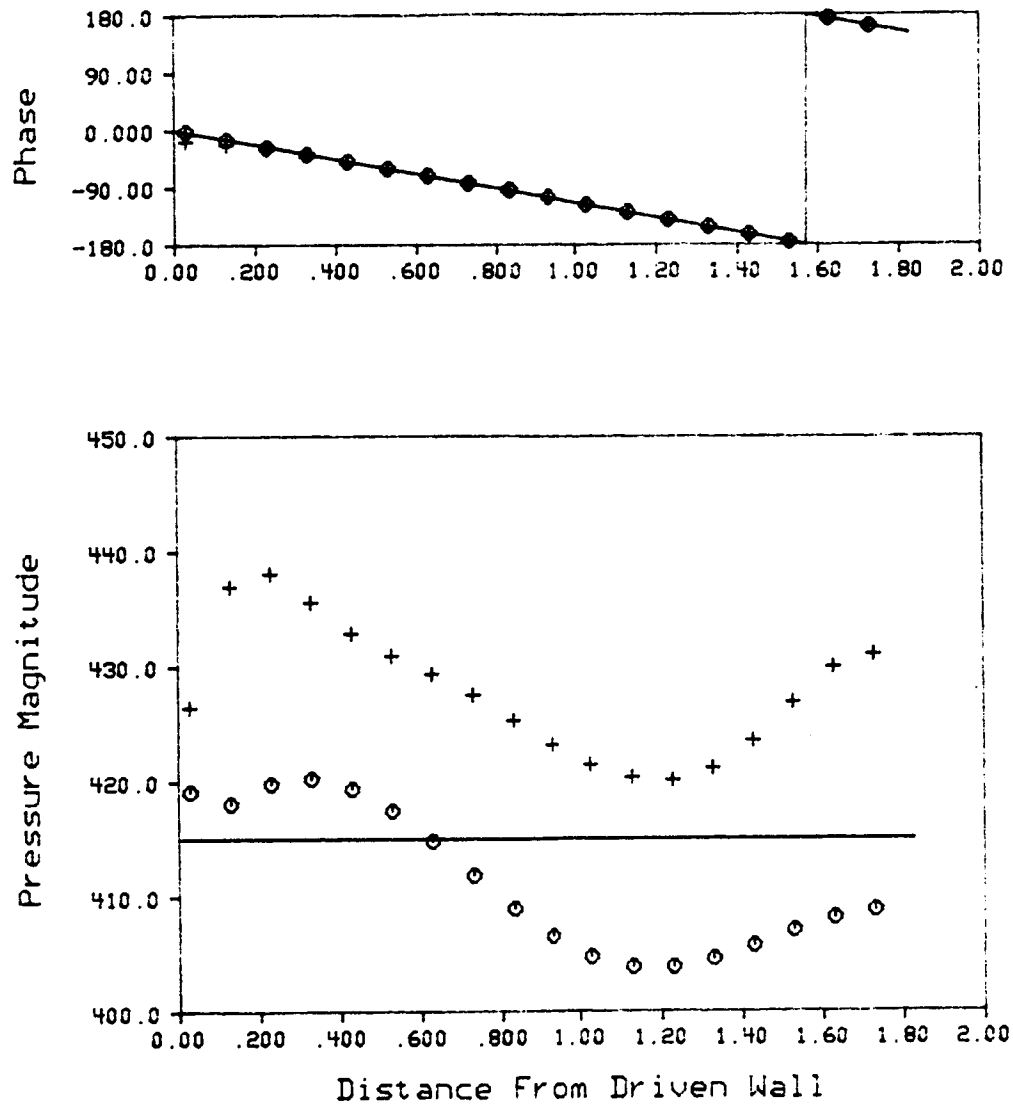


Figure 3.22 - Analytical And Numerical Pressure Predictions For The Driven-Infinite Cavity At  $k=2.0$  ( $p_o c = 415.0$ ).

— Analytical Solution  
 + 80 Element Model IBEM Solution  
 o 156 Element Model IBEM Solution

## CHAPTER 4

AN OPTIMAL ACTIVE NOISE CONTROLLER FOR ENCLOSED  
SOUND FIELDS WITH COMPLETE SYSTEM DESCRIPTION

This chapter presents the definition and formulation of a generalized technique to find an optimal active noise controller in completely or partially enclosed sound (noise) fields and evaluation of optimal active noise controllers for various system characteristics. Four assumptions are made about the system configuration for the algorithm formulated in this chapter. First, the sound field has a harmonic dependence of the form  $e^{j\omega t}$ . Second, the boundary has a known geometrical description and the conditions at the boundary are known. Third, any point noise sources in the system have a known source strength. Fourth, the canceling sources locations are known, and the secondary sources are modeled as monopoles. Thus, the performance of active noise controllers operating under ideal circumstances will be investigated. Such topics as stability, observability, and causality will be addressed in chapter 6.

#### 4.1 Problem Formulation

In the following sections, a formulation of an optimal active noise controller is discussed and an expression for the optimal active noise controller using the IBEM formulation is derived. In the subsequent formulation, capital letters will denote matrix quantities.

##### 4.1.1 Introduction

The active noise control problem addressed in this chapter is that of controlling harmonic, enclosed sound fields. No restrictions are placed on the shape of the enclosure or the sound propagation within the enclosure. A general schematic of the system is shown in Figure 4.1. The system is comprised of four components: the enclosure boundary, point noise source(s), controllable point source(s), and observation point(s).

For this particular investigation, the enclosure boundary must have a known set of boundary conditions corresponding to a well-posed boundary value problem. Either acoustic pressure, particle velocity, or locally reacting specific acoustic impedance is assumed to be known at every point on the boundary. In addition, the geometry of the boundary must be completely described by a fixed set of Cartesian coordinates. The specific acoustic impedance boundary condition can be used to model an open portion of

the enclosure. Thus, the enclosure need not be complete.

Two types of point acoustical sources are possible in the system. The first type is the uncontrollable point noise source which hereafter will be referred to as a primary source. Primary sources have a time harmonic volume velocity source strength of known amplitude and relative phase. The positions of the primary sources must be given by the coordinate system describing the boundary.

The second type of point source is the controllable point source which will be referred to as a secondary source. The secondary sources are introduced into the enclosure to control the noise field. The objective is to solve for the unknown amplitude and phasing of the secondary sources such that a control objective function is minimized. The positions of the secondary sources must be specified.

Observation points are locations within the enclosure where attenuation is desired. The secondary source strengths are determined such that the sound field is minimized at the observation points. The locations of the observation points must be known.

An uncontrolled harmonic sound (noise) field is created in the enclosure by either the enclosure boundary effects or the primary noise sources or a combination of

both. Given all of the specifications of the system, the objective is to determine an optimal controller. The optimal controller, as defined for the current research, is the modulus and phasing of the secondary sources which minimize the acoustic response at the observation points. The control objective function is computed from the acoustic response at the observation points. Because the control objective function is derived as a function of the unknown secondary source strengths, an expression for the optimal controller can be obtained by minimizing the control objective function with respect to the secondary source strengths.

#### 4.1.2 The Control Objective Function

As stated by Bullmore et al. [28], a practical control objective is to minimize the acoustic response (pressure) at a number of discrete locations in the enclosure. Consequently, the control objective function chosen for the current research is a weighted sum of the magnitudes of the pressure squared at the observation points:

$$\Pi = \sum_{i=1}^{n_{cp}} |p_i|^2 w_i \quad (4.1)$$

where,  $p_i$  is the acoustic pressure at the  $i^{\text{th}}$  observation point,  $w_i$  is the weighting factor at the  $i^{\text{th}}$  observation point, and  $n_{cp}$  is the number of observation points.

Observation point weighting permits many possible control strategies. Two strategies of active noise control are considered here. The first strategy is referred to as local control. Local control is characterized by utilization of one or few equally weighted observation points. By using a local control scheme, it is likely that the overall noise level will increase at other locations in the enclosure while the noise is attenuated at the observation points. The increase in the overall noise level at the other locations is deemed acceptable for a local control scheme. A typical example of local control is attenuation of noise at a passenger's head location in a transportation vehicle.

The second strategy of active noise control problems is termed global control. Global control is characterized by an attenuation of the noise level throughout the enclosure. Global control is accomplished in this investigation by utilizing a "fine" grid of observation points throughout the enclosure and weighting each appropriately. A typical example of global control might be the overall attenuation of noise throughout an aircraft fuselage.

A practical method of weighting the observation points in a global control problem is volume weighting. The entire enclosure volume is divided into local volumes such

that each observation point is apportioned a local volume. Volume weighting is achieved by using the local volume as the weighting factor for the corresponding observation point. The local volume is chosen so that the observation point is at the centroid of the volume. When volume weighting is used, the control objective function resembles the total time averaged acoustic potential energy of the enclosure.

#### 4.1.3 IBEM Formulation Of The Control Objective Function

If the acoustic pressures at the observation points are written in complex form, the control objective function of equation 4.1 can be rewritten as

$$\Pi = \underline{p}^H \underline{W} \underline{p} \quad (4.2)$$

where  $[\underline{W}]$  is a  $n_{cp} \times n_{cp}$  diagonal matrix with the values of the weighting function ( $w_i$ 's) on the diagonal, and  $\underline{p}$  is a column vector representing the pressures at the observation points. The H superscript denotes the hermitian transpose.

From the IBEM formulation of section 3.2, the pressures at a set of domain locations are given by equation 3.38 as

$$\underline{p} = \underline{D} \underline{\sigma} + \underline{E} \underline{\psi} \quad (3.38)$$

Because there are two types of point sources (primary and

secondary) in the problem domain,  $[E]$  and  $\underline{\psi}$  are partitioned as

$$E\underline{\psi} = \begin{bmatrix} E_p & | & E_s \end{bmatrix} \begin{bmatrix} \underline{\psi}_p \\ \text{---} \\ \underline{\psi}_s \end{bmatrix} = E_p \underline{\psi}_p + E_s \underline{\psi}_s \quad (4.3)$$

where  $\underline{\psi}_p$  contains the primary source strengths, and  $\underline{\psi}_s$  contains the secondary source strengths. The  $i,j$  element of  $[E]_p$  represents the influence of the  $j^{\text{th}}$  primary source on the  $i^{\text{th}}$  observation point. Likewise, the  $i,j$  element of  $[E]_s$  represents the influence of the  $j^{\text{th}}$  secondary source on the  $i^{\text{th}}$  observation point. Utilizing equation 4.3, equation 3.38 can be rewritten as

$$\underline{p} = D\underline{\sigma} + E_p \underline{\psi}_p + E_s \underline{\psi}_s \quad (4.4)$$

However,  $\underline{\sigma}$  is unknown and is not necessary for the solution of the problem. From equation 3.36,  $\underline{\sigma}$  may be found as

$$\underline{\sigma} = A^{-1}(\underline{\alpha} - C\underline{\psi}) \quad (4.5)$$

Partitioning  $[C]$  and  $\underline{\psi}$  as

$$C\underline{\psi} = \begin{bmatrix} C_p & | & C_s \end{bmatrix} \begin{bmatrix} \underline{\psi}_p \\ \text{---} \\ \underline{\psi}_s \end{bmatrix} = C_p \underline{\psi}_p + C_s \underline{\psi}_s \quad (4.6)$$

enables equation 4.5 to be rewritten as



$$\underline{\sigma} = A^{-1}(\underline{\alpha} - C_p \underline{\phi}_p - C_s \underline{\phi}_s) \quad (4.7)$$

Substituting equation 4.7 into equation 4.4 gives

$$\underline{p} = DA^{-1} \underline{\alpha} + (E_p - DA^{-1} C_p) \underline{\phi}_p + (E_s - DA^{-1} C_s) \underline{\phi}_s \quad (4.8)$$

The pressures at the observation points are only a function of the (potential) noise sources from the boundary,  $\underline{\alpha}$ , the primary sources,  $\underline{\phi}_p$ , and the secondary sources,  $\underline{\phi}_s$ .

Substituting equation 4.8 into equation 4.2 gives an expression for the control objective function in terms of the noise sources and the secondary sources as

$$\Pi = \underline{\phi}_s^H R^H W R \underline{\phi}_s + \underline{v}^H W R \underline{\phi}_s + \underline{\phi}_s^H R^H W \underline{v} + \underline{v}^H W \underline{v} \quad (4.9)$$

where

$$R = E_s - DA^{-1} C_s \quad (4.10)$$

$$\underline{v} = DA^{-1} \underline{\alpha} + (E_p - DA^{-1} C_p) \underline{\phi}_p \quad (4.11)$$

Thus, the control objective function is written in terms of the IBEM formulation. Note that  $\underline{v}$  is exclusively a function of the noise sources and that  $\underline{v}^H W \underline{v}$  is the value of the control objective function without the active noise controller. If  $n_{ss}$  denotes the number of secondary sources, then  $[R]$  is  $n_{cp} \times n_{ss}$  and  $\underline{v}$  is of order  $n_{cp}$ .

#### 4.1.4 An Optimal Controller

The control objective function written in terms of the IBEM formulation, equation 4.9, is a real, positive definite, quadratic function of the secondary source strengths. Such a function has a single unique global minimum [30]. Hence, there is a unique solution for the complex secondary source strengths which globally minimize the sound field at the observation points. The complex secondary source strengths which minimize the control objective function are given when the derivative of  $\Pi$  with respect to both the real part of  $\underline{\psi}_s$ ,  $\underline{\psi}_s^{(R)}$ , and the imaginary part of  $\underline{\psi}_s$ ,  $\underline{\psi}_s^{(I)}$ , is equal to zero [30]:

$$\frac{\partial \Pi}{\partial \underline{\psi}_s^{(R)}} + j \frac{\partial \Pi}{\partial \underline{\psi}_s^{(I)}} = 0 \quad (4.12)$$

Utilizing equation 4.12, the minimum value of the control objective function is found to occur when

$$\mathbf{R}^H \mathbf{W} \mathbf{R} \underline{\psi}_s + \mathbf{R}^H \mathbf{W} \mathbf{v} = 0 \quad (4.13)$$

The unknown secondary source strengths which minimize  $\Pi$  are

$$\underline{\psi}_s^0 = -(\mathbf{R}^H \mathbf{W} \mathbf{R})^{-1} \mathbf{R}^H \mathbf{W} \mathbf{v} \quad (4.14)$$

where  $\underline{\psi}_s^0$  denotes the values of the optimal secondary source strengths (the optimal controller). The corresponding minimum value of the control objective function is

$$\Pi^0 = \Pi(\underline{\phi}_s = \underline{\phi}_s^0) = \underline{v}^H \underline{W} \underline{v} + \underline{v}^H \underline{W} \underline{R} \underline{\phi}_s^0 \quad (4.15)$$

The attenuation due to the optimal active noise controller is evaluated as

$$ATN = 10 \log \frac{\Pi_{pp}}{\Pi^0} \quad (4.16)$$

where  $\Pi_{pp} = \Pi(\underline{\phi}_s = 0)$  and ATN denotes attenuation.

A special case of active noise control in enclosures occurs when the number of secondary sources equals the number of observation points. If this condition occurs, then  $[R]$  is square, and equation 4.14 reduces to  $\underline{\phi}_s^0 = -R^{-1} \underline{v}$  (assuming  $[R]$  is nonsingular). Substituting the solution for  $\underline{\phi}_s^0$  into equation 4.15 gives

$$\Pi^0 = \underline{v}^H \underline{W} \underline{v} - \underline{v}^H \underline{W} \underline{R} \underline{R}^{-1} \underline{v} \quad (4.17)$$

Since  $\underline{R} \underline{R}^{-1} = [I]$  where  $[I]$  is the identity matrix, it can be seen that  $\Pi^0 = 0$ . Therefore,  $n$  secondary sources are capable of completely canceling the noise at  $n$  locations in the cavity. If  $[R]$  is singular, the matrix does not consist of independent equations. A singular  $[R]$  matrix is probably an indication that the secondary sources are located such that they do not excite independent modal responses, or the observation points do not independently observe the sources. Such a situation is unlikely in most cavities unless the observation points are coincident.

#### 4.2 Case Study Results

In this section, the optimal solutions for a number of active noise control system configurations are presented. For each configuration, the optimal active noise controller (secondary source strengths) and corresponding performance were computed over a frequency band. As is characteristic of boundary element methods, analysis of the problem is performed at a discrete frequency. By analyzing the problem at a series of frequencies, the optimal controller as a function of frequency can be obtained.

The optimal controller was analyzed for two different enclosure shapes. The first enclosure considered is a 48 sided polyhedron centered about the origin. The polyhedron approximates the shape and acoustical behavior of a sphere with a 1.0m radius. Because of the symmetry of the polyhedron, the mechanisms at work can be understood, and thus, conclusions about the behavior of active noise controllers are straightforward. The polyhedron was modeled using 48 triangular superparametric boundary elements.

The second enclosure is a rectangular prism with dimensions of 1.04775m x 1.02235m x 1.8288m (shown in Figure 3.12). The eigenfrequency values for the rectangular prism with rigid walls are given in Table 4.1.

Table 4.1 - Eigenfrequencies Of The Rectangular Prism

Mode (m,n,q)	k <sub>mng</sub>	f <sub>mng</sub> (Hz)
(0,0,1)	1.72	93.9
(1,0,0)	2.998	163.7
(0,1,0)	3.073	167.8
(0,0,2)	3.43	187.2
(1,0,1)	3.46	188.9
(1,1,0)	4.29	234.2
(1,1,1)	4.62	252.2

The rectangular prism was modeled with 80 triangular superparametric boundary elements.

For purposes of analysis, the optimal secondary source strengths are normalized with respect to the volume velocity source strength of the noise producing mechanism,  $Q_{sn}$ . The volume velocity source strengths of the optimal secondary sources are given by

$$Q_s^o = \frac{4\pi}{jk\rho_0 c} \psi_s^o \quad (4.18)$$

For each enclosure a lattice of volume weighted observation points was developed for analysis of global noise control problems. A nonsymmetric lattice of 48 evenly distributed observation points was constructed for the 48 sided polyhedron. The spherical domain inscribed by the polyhedron was divided into six concentric spherical shells. Each shell was then divided into eight equal

volume sections. The observation points were positioned at the centroids of the spherical shell subsections. The weighting factors were the corresponding volumes of the subsections. To obtain a nonsymmetric distribution of observation points, each spherical shell was rotated about the X-axis, Y-axis, and Z-axis (in that order) by  $15^\circ$  with respect to the neighboring shell on its inside surface. For the rectangular prism, a symmetric grid of 72 evenly distributed, volume weighted observation points was developed.

Active noise control problems involving the 48 sided polyhedron enclosure were analyzed from  $k=0.5$  to  $k=10.0$  (27 Hz to 546 Hz). For active noise control problems in the rectangular prism enclosure, analysis was performed from  $k=0.125$  to  $k=5.0$  (7 Hz to 273 Hz). The value of  $\rho_0 c$  was 415.0 Pa's/m (air at  $20^\circ\text{C}$ ) for all case studies presented in this chapter.

If the enclosure boundary was the noise producing mechanism, then  $Q_{sn}$  was computed from the surface integral of the normal velocity:

$$Q_{sn} = \int_s \bar{u} \cdot \hat{n} \, dS \quad (4.19)$$

where  $\hat{n}$  is a unit vector normal to the enclosure surface. If the noise field was generated by a set of primary sources,  $Q_{sn}$  was computed from

$$Q_{sn} = \frac{4\pi}{jk\rho_0 c} \sum_{i=1}^{n_{ps}} \phi_p(i) \quad (4.20)$$

where  $n_{ps}$  is the number of primary sources.

#### 4.2.1 Global Noise Control

The system configuration for case 1 was a single secondary source at the center of the 48 sided polyhedron which was uniformly pulsating with a time harmonic normal surface velocity  $u_n = 1.0\text{m/s}$ . There were no primary sources in the problem. Global noise control was sought; i.e., the set of 48 volume weighted observation points were used.

Figure 4.2 shows the performance of the optimal controller, and Figure 4.3 presents the optimal controller versus frequency. There are several noteworthy features of Figures 4.2 and 4.3. First, the control objective function for optimal control approaches zero in the low frequency limit. In the low frequency limit, the optimal active noise controller adds and subtracts volume from the system such that all the energy in the system is kinetic (the fluid moves as a lumped mass), and hence  $\Pi^0$ , which resembles minimum potential energy, approaches zero [9]. Second, the only frequencies at which significant global attenuation occurs is at very low frequencies and at the natural resonances of the cavity ( $k=5.0$  and  $k=8.75$ ). Third, the optimal active noise controller is completely

ineffective at the antiresonances (frequencies of minimum noise field response). Note that with the active noise controller, the potential energy is almost uniformly the same as found at the antiresonances. Fourth, the optimal secondary source strength is less than the volume velocity of the enclosure boundary for all frequencies considered. Thus, efficient global noise control is possible at low frequencies and at the enclosure natural frequencies. Away from the natural frequencies, the global attenuation is much less, but the secondary source strengths are correspondingly reduced.

Figure 4.4 presents the pressure profiles of the uncontrolled and controlled sound fields for case 1 at frequencies of low attenuation and high attenuation. In Figure 4.4a, note that sound field was not uniformly reduced. The effect of the secondary source is dramatic despite the small level of attenuation achieved. However, at the first enclosure resonance ( $k=5.0$ ), global attenuation was attained as shown in Figure 4.4b. To ensure global attenuation at every frequency, a finer observation point mesh could be used.

The system configuration studied for case 2 is identical to that of case 1 except that the secondary source was positioned at half the distance from the center of the polyhedron to its boundary. The results for case 2



are presented in Figures 4.5 and 4.6. Comparing Figures 4.5 and 4.2, it can be seen that the attenuation is still greatest at the natural frequencies but is much lower for case 2. Also note that the required optimal secondary source strengths at the frequencies of maximum attenuation are larger for case 2. Moreover, the control objective function with the secondary source operating is not uniform over frequency in case 2.

The optimal active noise controller for case 1 achieved better performance because the secondary source was positioned at an antinodal location of all enclosure modes. All eigenfunctions of the pulsating polyhedron have a maximum at the center. Consequently, the secondary source was able to excite eigenfunctions of the same form as those produced by the noise source (good modal coupling). However, if the secondary source is positioned away from the antinodal locations, as was the situation in case 2, its effectiveness is reduced as seen in Figure 4.5 [28,31,32].

Cases 3, 4, and 5 further demonstrate the importance of modal coupling for global noise control. For cases 3, 4, and 5, a single secondary source was positioned a distance of 0.1m, 0.2m, and 0.3m, respectively, away from a primary source at the center of a rigid 48 sided polyhedron. The results for cases 3, 4, and 5 are shown in

Figures 4.7 and 4.8. The benefit of modal coupling is apparent in Figure 4.7. The attenuation increased at all frequencies as the secondary source approached the primary source. The increase in the attenuation is a result of the fact that when the secondary source is close to the primary source, it can effectively couple into the same modes excited by the primary source. In Figure 4.8, note that as the secondary source approaches the primary source, the optimal controller and primary source combination is approaching the form of a dipole (equal in magnitude and  $180^\circ$  out of phase).

Case 6 extended the analysis of cases 3, 4, and 5. Case 6 was identical to cases 3, 4, and 5 except that the secondary source was located 0.01m away from the primary source. The results of case 6 are presented in Figures 4.9 and 4.10. Note that the secondary source formed a dipole with the primary source. Cases 3 through 6 suggest that if the noise source is compact, the canceling source(s) should be placed as close as possible to the noise source for maximum attenuation of the noise field [28].

Cases 7, 8, and 9 demonstrate the effect of the placement of secondary sources for the global noise control of a distributed source. Four adjacent sides of the 48 sided polyhedron were given velocity boundary conditions of 1.0m/s. The remaining 44 sides were given rigid wall

boundary conditions. A secondary source was situated along a radial line (from the center of the polyhedron) to the centroid of the vibrating surface of the combined four sides. The secondary source was located at distances of 0.1m, 0.2m, and 0.3m away from the centroid of the four sides for cases 7, 8, and 9, respectively. The results are shown in Figures 4.11 and 4.12. Figures 4.11 and 4.12 suggest that placing a secondary source in close proximity to a distributed noise source is not necessarily advantageous.

The placement of remotely located secondary sources for the global control of noise fields created by distributed sources was analyzed using the rectangular cavity. The end of the rectangular cavity at  $Z=1.8288\text{m}$  was given velocity boundary conditions of  $1.0\text{m/s}$  while the rest of the enclosure was rigid. The set of 72 volume weighted observation points was used. For case 10, a single secondary source was located at  $(0.5\text{m}, 0.5\text{m}, 0.7808\text{m})$ . For case 11, the secondary source was located at  $(0.5\text{m}, 0.5\text{m}, 1.5288\text{m})$ . Figures 4.13 and 4.14 display the results of case 10 while Figures 4.15 and 4.16 show the results of case 11.

Note that the secondary source placement of case 11 results in increased performance of the optimal active noise controller at frequencies around  $k=2.0$ . At the

frequency corresponding to a wavenumber of 2.0, the secondary source for case 10 is positioned at a nodal location of the uncontrolled sound field while for case 11 the secondary source is at an antinodal location. Because the secondary source was located at an antinodal location for case 11, it was able to excite a response similar spatially to the uncontrolled sound field but opposite in phase. However, if the secondary source is located at a nodal location (case 10), the secondary source is unable to excite a modal pattern which will effectively control the noise field. At high frequencies, neither secondary source position is such that a similar field can be generated, and thus, the performance is poor.

Hence, if global narrow-band attenuation is desired using remotely located secondary sources, the secondary sources should be placed at an antinodal location of the noise field. For broadband global noise reduction, optimal placements for the secondary sources are locations where all eigenfunctions of the enclosure have a maximum, such as the center of a 48 sided pulsating polyhedron or the corners of a rigid wall rectangular prism.

The sudden local minima at  $k=3.0$  in the attenuation curves of Figures 4.13 and 4.15 are due to presence of cross modes in the enclosure. The noise source in cases 10 and 11 is such that it only excites longitudinal modes of

the cavity. However, the secondary source is capable of exciting both longitudinal and cross modes. The  $(1,0,0)$  and the  $(0,1,0)$  cross modes have natural frequencies at approximately  $k=3.0$ . Consequently, at  $k=3.0$  a nonzero secondary source strength would excite previously unexcited modes while attempting to cancel the noise field and thus cause the overall sound pressure level to increase. Hence, the optimal solution is a near-zero secondary source strength; i.e., any attempt to attenuate the noise field would result in an overall increase in sound pressure level due to high cross mode response at  $k=3.0$ . The local minimum at  $k=1.25$  in Figure 4.13 is a result of the fact that the combined acoustic responses at the observation points due to the secondary source has a minimum at  $k=1.25$ .

#### 4.2.2 Local Noise Control

The local control at one observation point using a single secondary source was studied in case 12. The single secondary source was at the center of a uniformly pulsating 48 sided polyhedron with a surface velocity of  $1.0\text{m/s}$ . The observation point was at one-half the distance from the center to the polyhedron boundary. Figure 4.17 presents the optimal controller as a function of frequency. Because the number of secondary sources equaled the number of observation points, the secondary source completely attenuated the noise field at the observation point.

The unbounded maximum at  $k=3.15$  represents uncontrollability. At approximately  $k=3.15$ , the acoustic modal response of the secondary source has a pressure zero at the observation point. Thus, the secondary source is unable to influence the acoustic response at the observation point. Consequently, the required optimal secondary source strength tends towards infinity.

The pressure distributions of the uncontrolled and controlled noise fields at  $k=2.0$  for case 12 are shown in Figure 4.18. Notice that the only locations at which the noise field was reduced were those neighboring the observation point (radial position=0.5m). At locations near the secondary source, the magnitude of the sound pressure level increased dramatically.

In a study similar to case 12, case 13 examined local control at one observation point in a driven-rigid rectangular cavity. The wall at  $Z=1.8288\text{m}$  was given velocity boundary conditions of  $1.0\text{m/s}$  while the rest of the cavity was rigid. A single secondary source was located at  $(0.5\text{m}, 0.5\text{m}, 0.7808\text{m})$  and the observation point was at  $(0.5\text{m}, 0.5\text{m}, 1.5288\text{m})$ . Figure 4.19 shows the results for case 13. The relatively high secondary source strength required at  $k=2.0$  results from the fact that at  $k=2.0$  the observation point is near an antinodal location of the uncontrolled sound field while the secondary source is near

a nodal location of the uncontrolled sound field.

By studying the results of cases 12, 13, and others not presented here, a general strategy for placement of secondary sources was developed. For local control it is important to locate the secondary source(s) such that the response at the observation point(s) due to the secondary source(s) is maximum or near maximum for all frequencies considered. This strategy includes the situation where the secondary source is brought very close to the observation point such as with ear defenders. If the observation point is at a nodal location of the secondary source modal pattern for a particular frequency, then infinite secondary source strength will be required for local control (uncontrollability). In general, if the observation point is at a location of high noise field response and the secondary source is at a location of low noise field response, then large (not infinite) secondary source strengths will be required. However, if the secondary source can effectively excite a mode unexcited by the noise field which has an antinode near the observation point, then it is irrelevant whether the secondary source is located near a node of the noise field or not.

The effect of closely coupling the observation point and the secondary source for a one-point local control scheme was investigated in cases 14, 15, and 16. A single

observation point was positioned at half the distance (from the center) to the boundary of a uniformly pulsating 48 sided polyhedron with a surface velocity of 1.0m/s. The secondary source was located at distances of 0.1m, 0.2m, and 0.3m away from the observation point for cases 14, 15, and 16 respectively. The optimal secondary source strengths are shown in Figure 4.20. Note that no one particular secondary source position is advantageous for all frequencies. However, the average normalized optimal secondary source strengths for cases 14, 15, and 16 are 0.221, 0.350, and 0.471 respectively. Thus, for broadband purposes, it is advantageous to locate the secondary source as close as possible to the observation point.

#### 4.2.3 Multiple Secondary Sources

The merits of using multiple secondary sources for global noise control were investigated. The results of a case study (case 17) analogous to that of case 1, except that two secondary sources were employed, are presented in Figures 4.21 and 4.22. The two secondary sources were positioned at half the distance to the 48 sided polyhedron boundary and  $180^\circ$  apart. Comparing Figures 4.2 and 4.21, it can be observed that in the lower frequency regime the two secondary sources provided slightly better attenuation than the single secondary source. However, for the higher frequencies the single secondary source gave better



performance for less required source strength.

Extending the analysis of case 17, a system with four secondary sources was examined (case 18). The system configuration was identical to case 1 with the exception that multiple secondary sources were used. The secondary sources for case 18 were located at  $(0.25\text{m}, 0, 0)$ ,  $(0, 0.75\text{m}, 0)$ ,  $(0, -0.5\text{m}, 0)$ , and  $(-0.75\text{m}, 0, 0)$ . The results of case 18 are presented in Figure 4.23. Comparing Figures 4.2 and 4.23, it can be seen that overall the four secondary sources did not provide significantly better performance than the single secondary source. In general, the combined optimal secondary source strengths of the four secondary sources were slightly greater than the optimal source strength of the single secondary source in case 1 (at any particular frequency).

The results of cases 1, 17, and 18 suggest that a single, optimally located secondary source provides the best overall performance for global noise control. An optimally located secondary source is positioned such that the secondary source effectively couples into the dominant modes of the uncontrolled sound field for all frequencies at which reduction is desired. These conclusions are only expected to be valid for cases of simple sound fields where optimal secondary source locations can be identified.

#### 4.2.4 Nonsymmetric Excitation

An example of a (spherically) nonsymmetric excited sound field is the oscillating 48 sided polyhedron which is shown in profile in Figure 4.24. The distribution of the velocity normal to the surface is given by  $u_n = u_x \cos\theta$  where  $x$  is the direction of oscillation. The oscillatory motion of the polyhedron creates a pressure distribution which is a function of radial position and angular position, i.e., spherically nonsymmetric.

A single secondary source positioned at the center of the oscillating polyhedron ( $u_x = 1.0\text{m/s}$ ) was found to be completely ineffective for global noise reduction. However, two secondary sources positioned at  $(0.01\text{m}, 0, 0)$  and  $(-0.01\text{m}, 0, 0)$  were found to provide significant global attenuation at the cost of relatively large secondary source strengths (case 19). The results of case 19 are shown in Figures 4.25 and 4.26. As shown in Figure 4.25, significant global attenuation was only attained in the narrow-band regions about the natural frequencies of the enclosure.

In Figure 4.26, note that the optimal solution for the secondary source strengths is a dipole. The dipole form of the solution can be explained by examining the radiation pattern produced by the secondary sources. The radiation

pattern of a dipole has two lobes along the axis of the dipole (the X-axis for case 19). The pressure distribution function of the uncontrolled sound field in case 19 also has maxima along the X-axis. Hence, the radiation pattern of the secondary sources took on a form similar to the uncontrolled sound field pressure distribution. The radiation pattern of the single secondary source had a spherically symmetric form and hence was unable to achieve any attenuation. Likewise, if the two secondary sources would have been positioned along the Y-axis or Z-axis, negligible attenuation would have resulted.

To further demonstrate the same concept, two secondary sources were positioned at  $(0.01\text{m}, 0, 0)$  and  $(-0.01\text{m}, 0, 0)$  inside the uniformly pulsating polyhedron of case 1. The form of the optimal solution for the two secondary secondary sources was found to be that of a monopole, as shown in Figure 4.27. Note, the combined source strengths of the two secondary sources equals the source strength of the single secondary source of case 1 (Figure 4.3). Thus, for a spherically symmetric noise field, a canceling source with a spherically symmetric radiation pattern provided optimal performance.

#### 4.2.5 Effects Of Passive Noise Treatments

The effects of passive noise treatments at the enclosure boundaries on active noise controller requirements and performance were investigated for the rectangular prism. Passive noise treatments were modeled using locally reacting, specific acoustic impedance boundary conditions. Changes in active noise controller requirements were studied for variations of three passive noise treatment parameters: the resistive component, the reactive component, and passive noise treatment surface area. For cases 20 through 27, the noise producing mechanism was a primary source at (0.5m,0.5m,0.25m) with a volume velocity source strength of  $1.0 \text{ m}^3/\text{sec}$ , and a single secondary source was located at (0.5m,0.5m,1.579m).

Cases 20, 21, 22, and 23 examined the effect of changes in the resistive component. Case 20 is used as a reference; all of the enclosure walls were rigid. The wall at  $Z=0$  was given specific acoustic impedance boundary conditions of  $50+j0$ ,  $200+j0$ , and  $350+j0 \text{ Pa's/m}$  for cases 21, 22, and 23 respectively. The results of case 20-23 are shown in Figure 4.28 and 4.29. The frequencies of maximum attenuation for case 20 are the eigenfrequencies associated with the (0,0,1), (1,0,0), (0,1,0), (0,0,2), and (1,0,1) modes (see Table 4.1).

The introduction of the resistive boundary condition at the wall at  $Z=0$  caused a shift in the eigenfrequencies of the cavity and hence the frequencies at which maximum attenuation occurred. As the value of the resistance increases, the modal response of the cavity becomes increasingly damped. Because active noise controllers function most effectively at the enclosure resonances, the overall performance of the active noise controller decreases with increasing values of resistance as shown in Figure 4.28. The average values of attenuation for cases 20, 21, 22, and 23 were 4.85, 3.69, 3.01, and 2.90 dB, respectively. As shown in Figure 4.29, the increasing values of the resistive component did not cause significant increases in optimal secondary source strength.

To examine the effects that changes in the reactive component have on active noise controller requirements, the wall at  $Z=0$  was given impedance boundary conditions of  $200-j1500$ ,  $200+j0$ , and  $200+j1500$  Pa's/m (cases 24, 22, and 25 respectively). The results of cases 22, 24, and 25 are shown in Figure 4.30 and 4.31. The presence of a reactive component increased the magnitude of the cavity resonances. Consequently, the overall performance of the active noise controller increased with the addition of a reactive component. Changes in the sign of the reactive component altered the eigenfrequencies but had no significant effect

on the overall active noise controller requirements.

The surface area of the passive noise treatment was increased by increasing the number of walls with impedance boundary conditions. An impedance boundary condition of  $200 + j0 \text{ Pa}\cdot\text{s/m}$  was applied to the walls at  $Z=0$  for case 22;  $Z=0$  and  $X=0$  for case 26;  $Z=0$ ,  $X=0$ , and  $X=1.04775\text{m}$  for case 27. The results of cases 22, 26, and 27 are shown in Figures 4.32 and 4.33. As was the case for the increasing value of the resistive component, the enclosure response became increasingly damped as the number of absorbing walls increased. For more than one absorbing wall, significant attenuation was not possible except at the very low frequencies.

#### 4.2.6 Conclusions

From the results presented in the previous sections, several conclusions can be drawn. First, efficient global noise control is possible at low frequencies and at the enclosure resonances. Second, for broadband global noise control, the secondary source(s) should be positioned at antinodal locations of all enclosure modes. Third, if global control of a compact noise source is sought, the secondary source(s) should be located as close as possible to the compact noise source. However, if the noise source is distributed, maximum global noise control is attained

when the secondary source is at an antinodal location, and it is irrelevant if the antinodal location is remote or not. Fourth, for local control, the secondary source(s) should be located such that the response at the observation point(s) due to the secondary sources is large. Thus, for local control it is not always advantageous to locate the secondary source at an antinodal location of the uncontrolled sound field. Fifth, for broadband local control, it is beneficial to position the secondary source(s) close to the observation point(s) to achieve lower required secondary source strength(s). Sixth, for low modal density acoustic fields, effective global control can be achieved using only one or few judiciously placed secondary sources. Additional secondary sources do not provide any significant improvement in the performance. Lastly, resistive passive noise treatments cause a decrease in the effectiveness of active noise controllers, but the total, combined performance due to the passive noise treatments and the active noise controller remains about the same.

Although some of the results presented here could have been obtained with an analytical procedure, the numerical method provides great versatility. Changes in system parameters such as enclosure shape, secondary source positioning, and boundary conditions are easily

accommodated with the numerical procedure. A numerical method becomes necessary when the enclosure has a complex nongeneralized shape, distributed sources, or distributed damping. Although some of the results presented here are documented in the literature, they were presented to demonstrate the validity of the method.



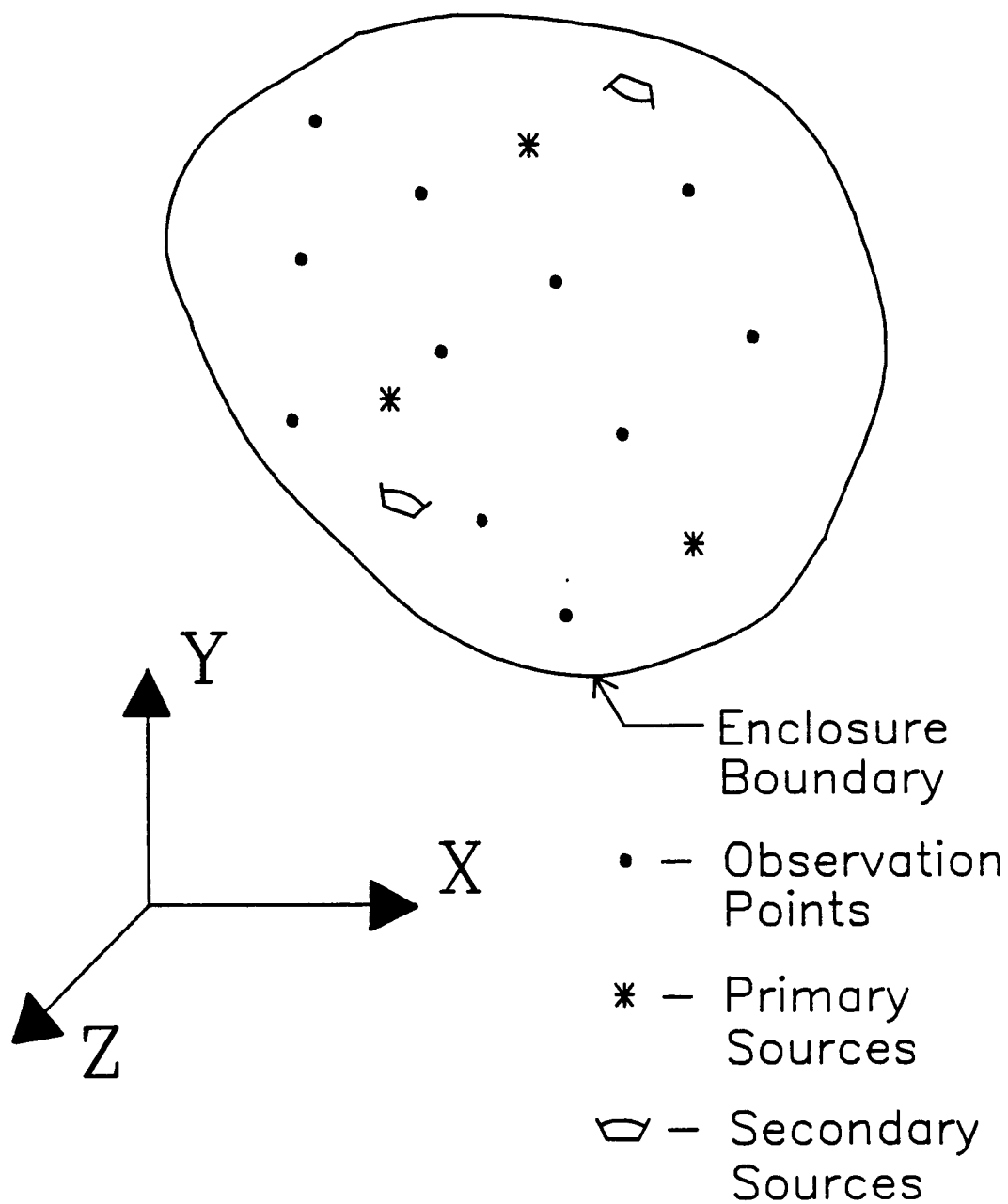


Figure 4.1 - System Schematic For The Active Control Of Sound Fields With Complete System Description

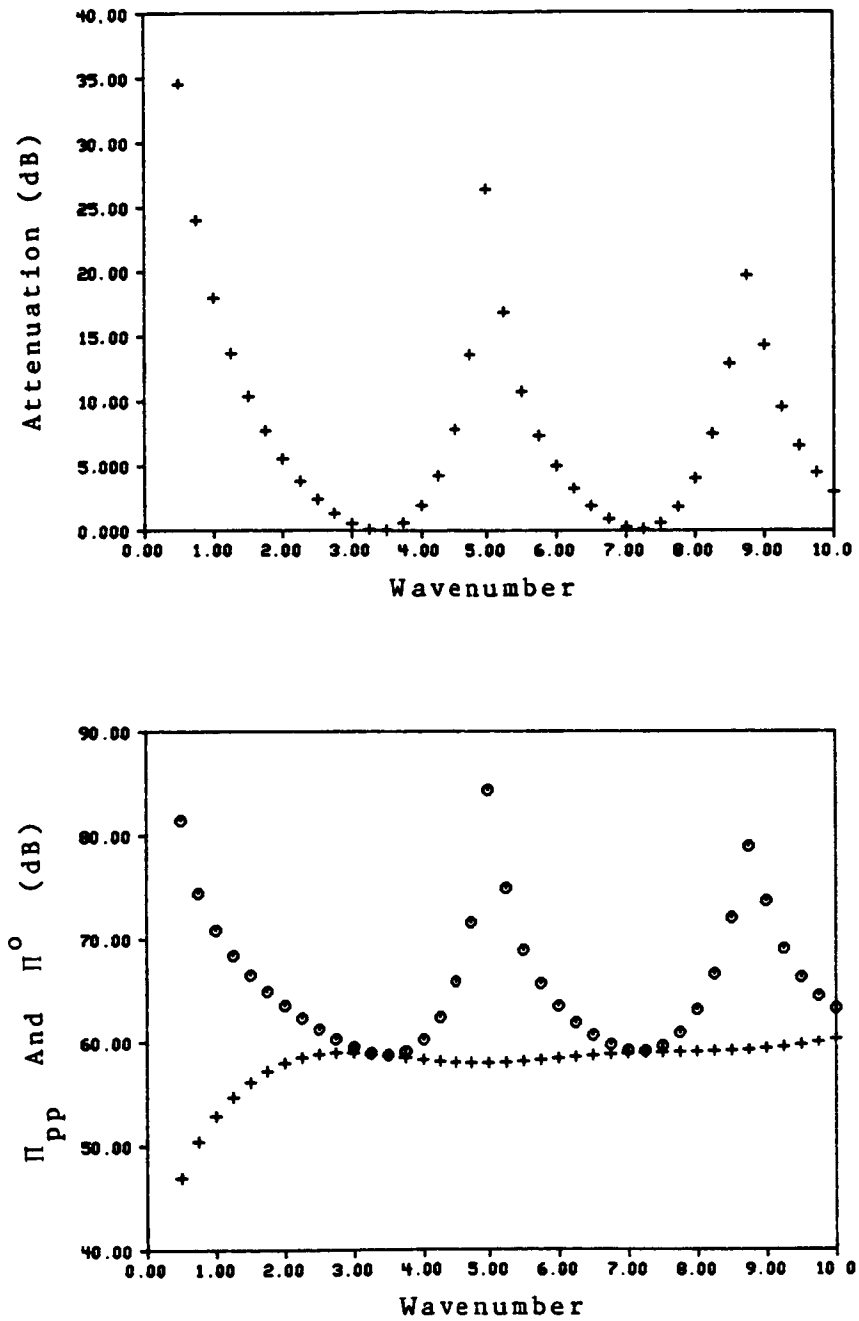


Figure 4.2 - Optimal Active Noise Controller Performance For A Secondary Source At Pulsating Polyhedron Center, Global Control (Case 1).

+ -  $\Pi^o$   
 o -  $\Pi_{pp}$

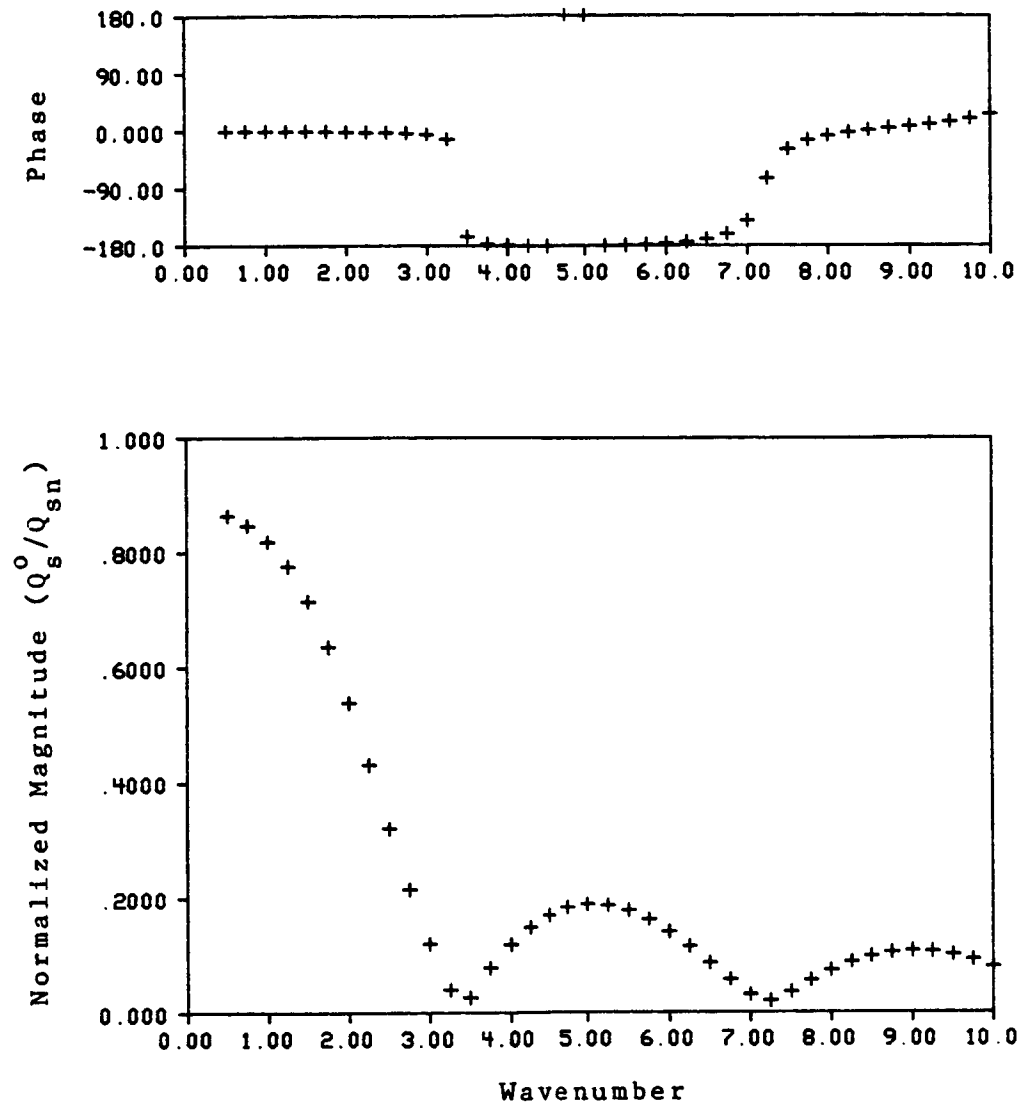
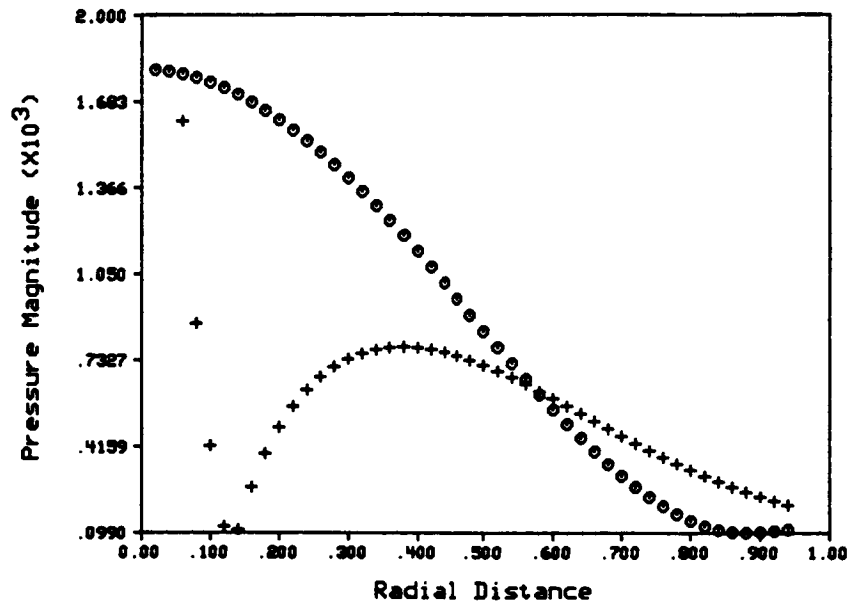
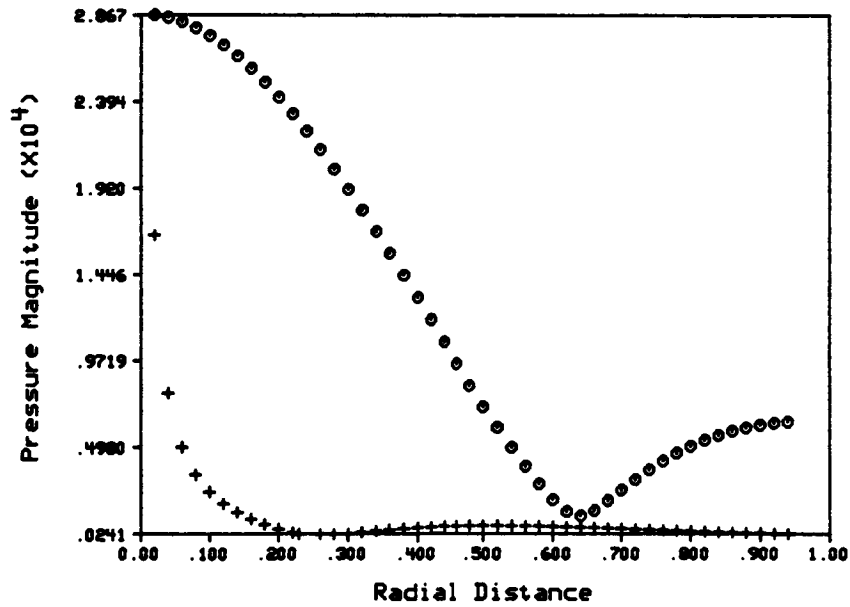


Figure 4.3 - The Normalized Optimal Secondary Source Strengths For A Secondary Source At Pulsating Polyhedron Center, Global Control (Case 1)



(a)



(b)

Figure 4.4 - The Uncontrolled And Controlled Pressure Distributions For Case 1 At (a)  $k=4.0$  and (b)  $k=5.0$ .

o - Uncontrolled Pressure Distribution  
+ - Controlled Pressure Distribution

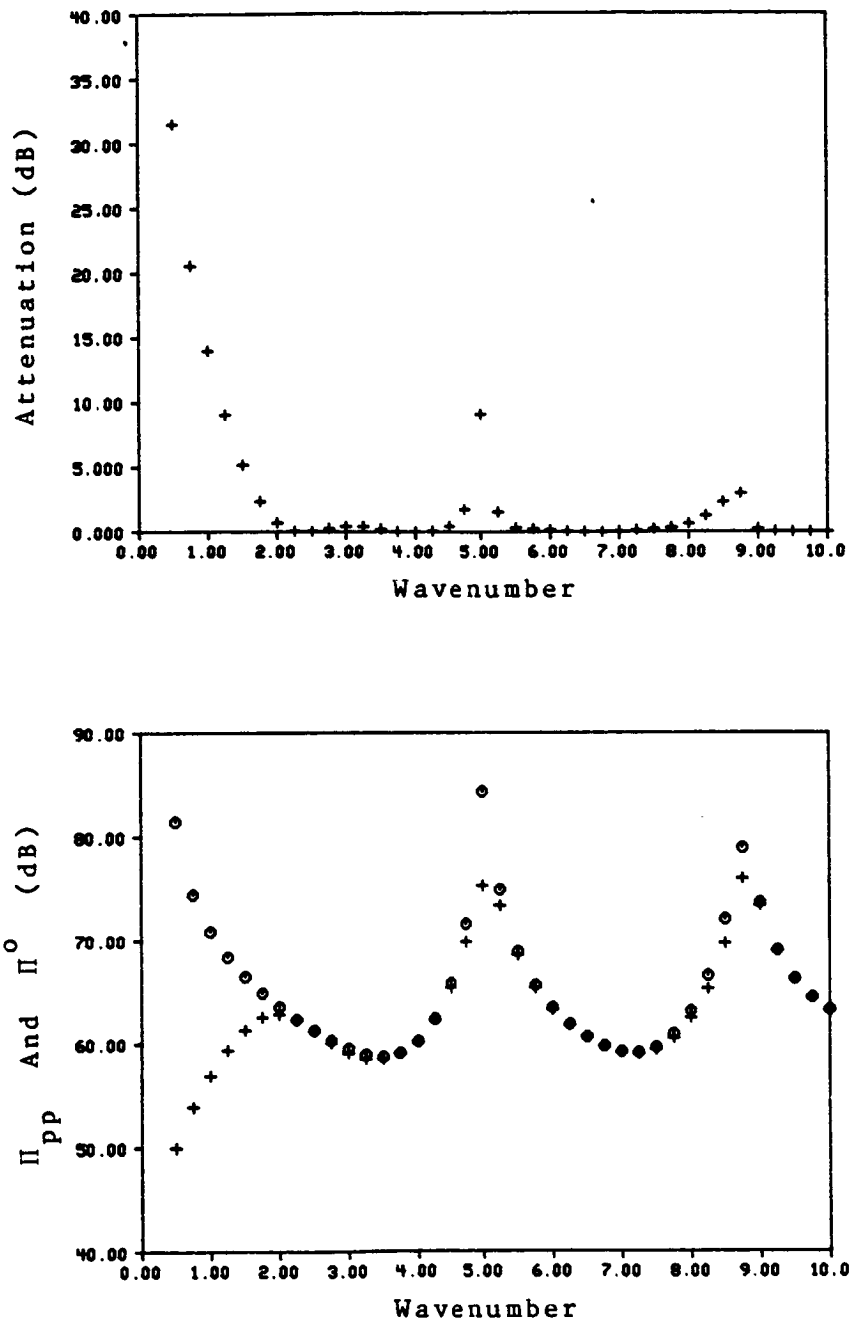


Figure 4.5 - Optimal Active Noise Controller Performance For A Secondary Source At Half The Radius Of A Pulsating Polyhedron, Global Control (Case 2).

+ -  $\Pi^o$   
o -  $\Pi_{pp}$

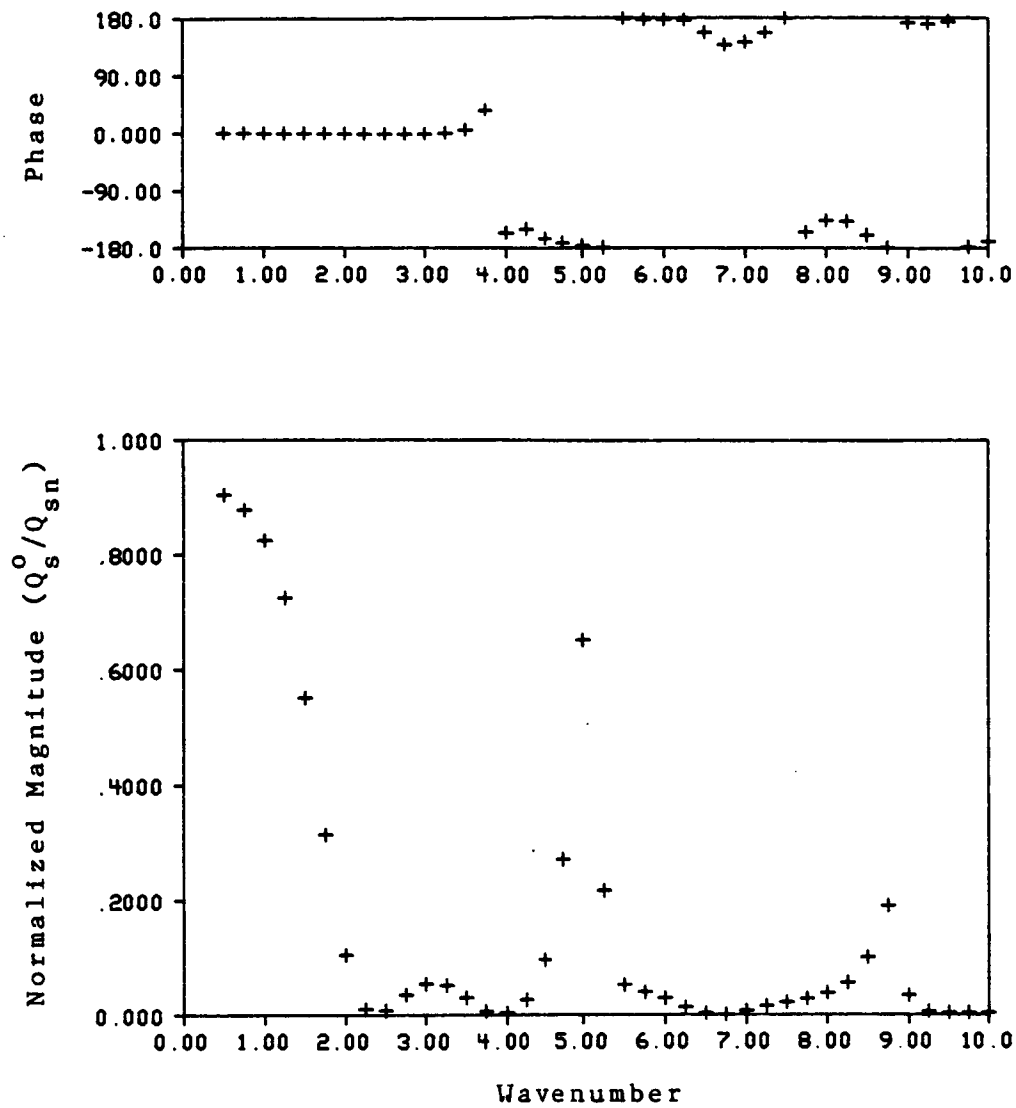


Figure 4.6 - The Normalized Optimal Secondary Source Strengths For A Secondary Source At Half The Radius Of A Pulsating Polyhedron, Global Control (Case 2)

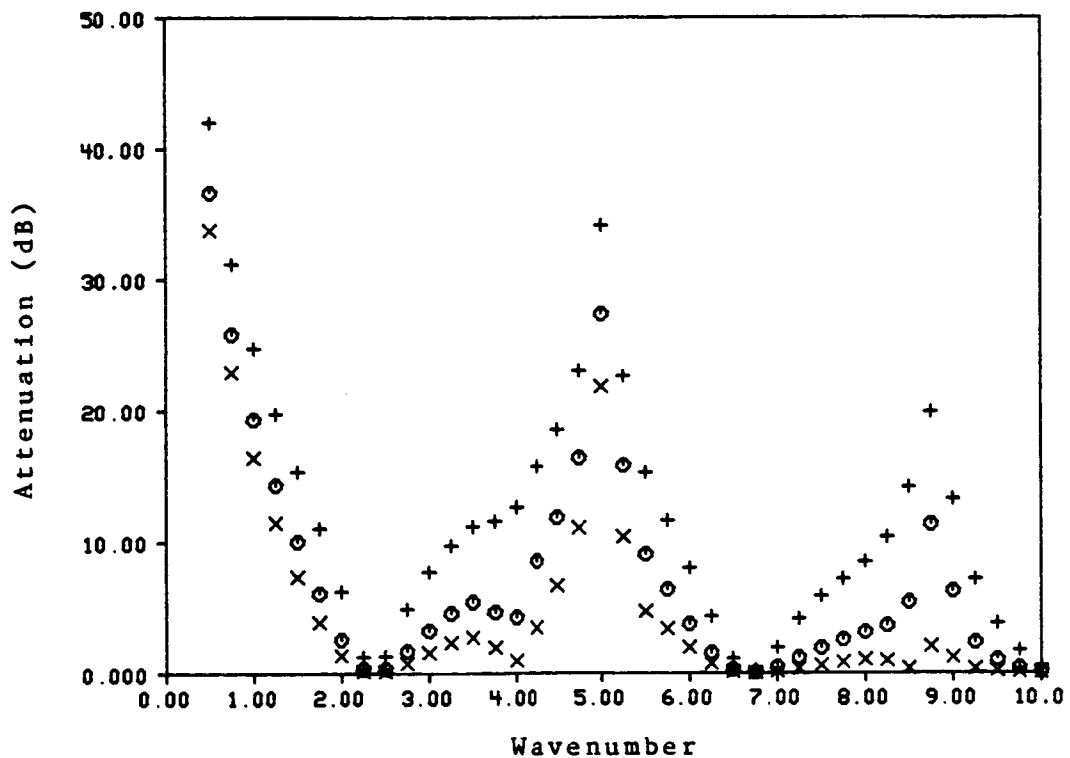


Figure 4.7 - Optimal Active Noise Controller Performance For Closely Coupled Primary And Secondary Sources A Distance  $d$  Apart In A Rigid Wall Polyhedron, Global Control.

+ -  $d=0.1\text{m}$  (Case 3)

o -  $d=0.2\text{m}$  (Case 4)

x -  $d=0.3\text{m}$  (Case 5)

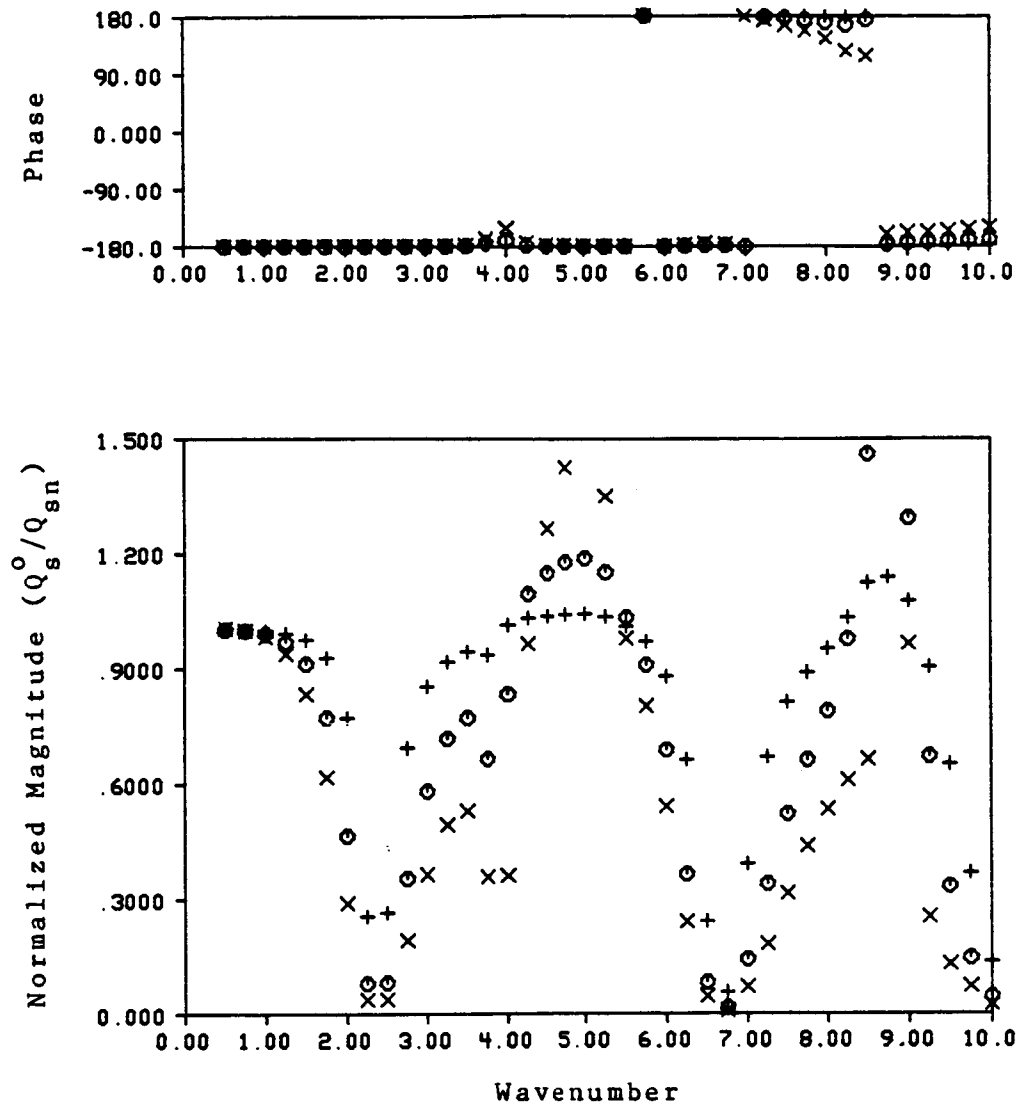


Figure 4.8 - The Normalized Optimal Secondary Source Strengths For Closely Coupled Primary And Secondary Sources A Distance  $d$  Apart In A Rigid Wall Polyhedron, Global Control.

+ -  $d=0.1\text{m}$  (Case 3)  
 o -  $d=0.2\text{m}$  (Case 4)  
 x -  $d=0.3\text{m}$  (Case 5)



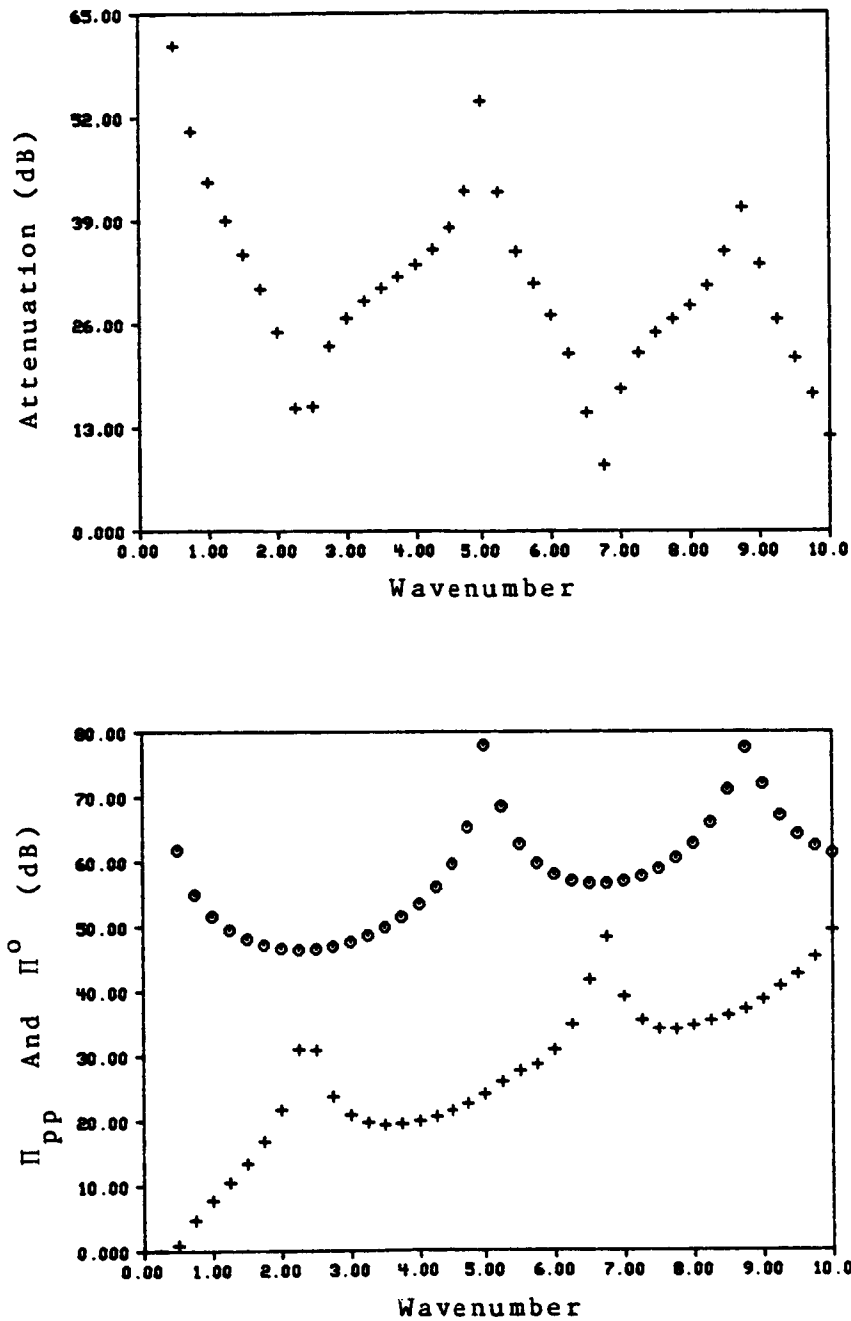


Figure 4.9 - Optimal Active Noise Controller Performance For Closely Coupled Primary And Secondary Sources A Distance 0.01m Apart In A Rigid Wall Polyhedron, Global Control (Case 6).

+ -  $\Pi_o$   
o -  $\Pi_{pp}$

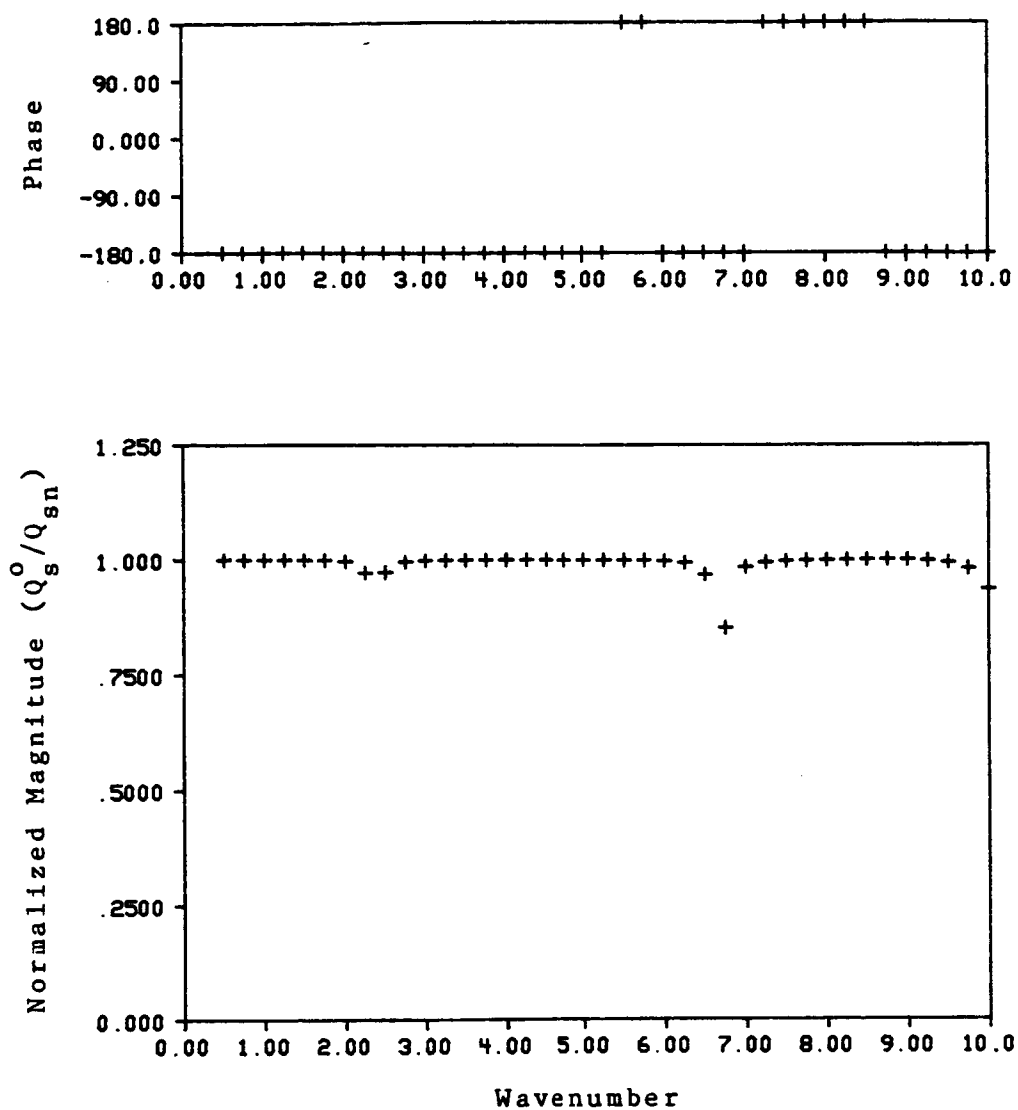


Figure 4.10 - The Normalized Optimal Secondary Source Strengths For Closely Coupled Primary And Secondary Sources A Distance 0.01m Apart In A Rigid Wall Polyhedron, Global Control (Case 6)

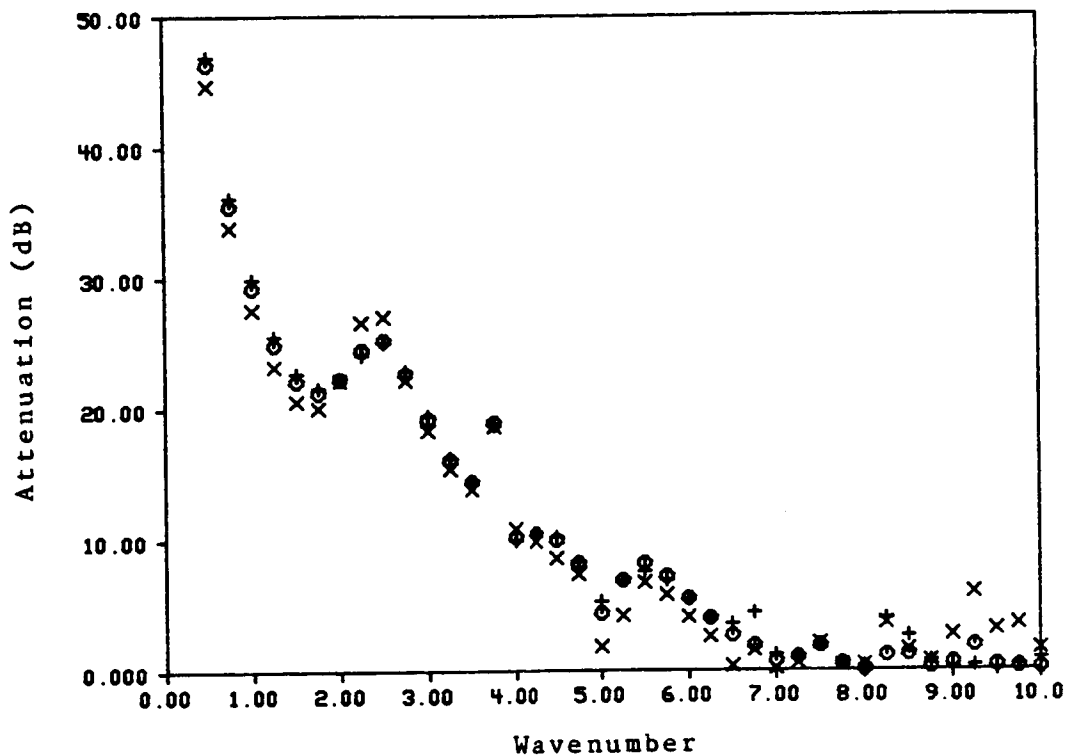


Figure 4.11 - Optimal Active Noise Controller Performance For A Secondary Source Located A Distance  $d$  From A Distributed Noise Source, Global Control.

+ -  $d=0.1\text{m}$  (Case 7)

o -  $d=0.2\text{m}$  (Case 8)

x -  $d=0.3\text{m}$  (Case 9)

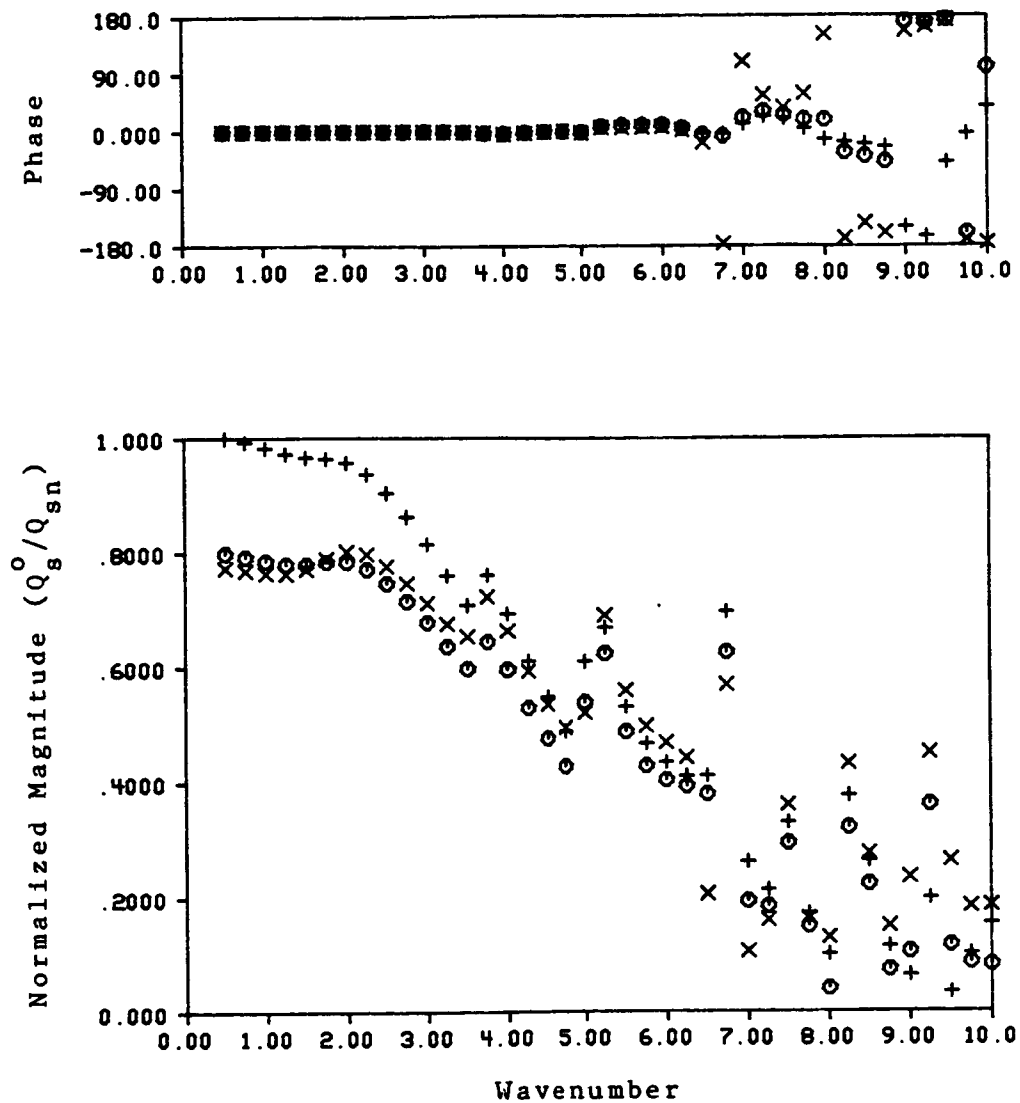


Figure 4.12 - The Normalized Optimal Secondary Source Strengths For A Secondary Source Located A Distance  $d$  From A Distributed Noise Source, Global Control.

- + -  $d=0.1\text{m}$  (Case 7)
- o -  $d=0.2\text{m}$  (Case 8)
- x -  $d=0.3\text{m}$  (Case 9)

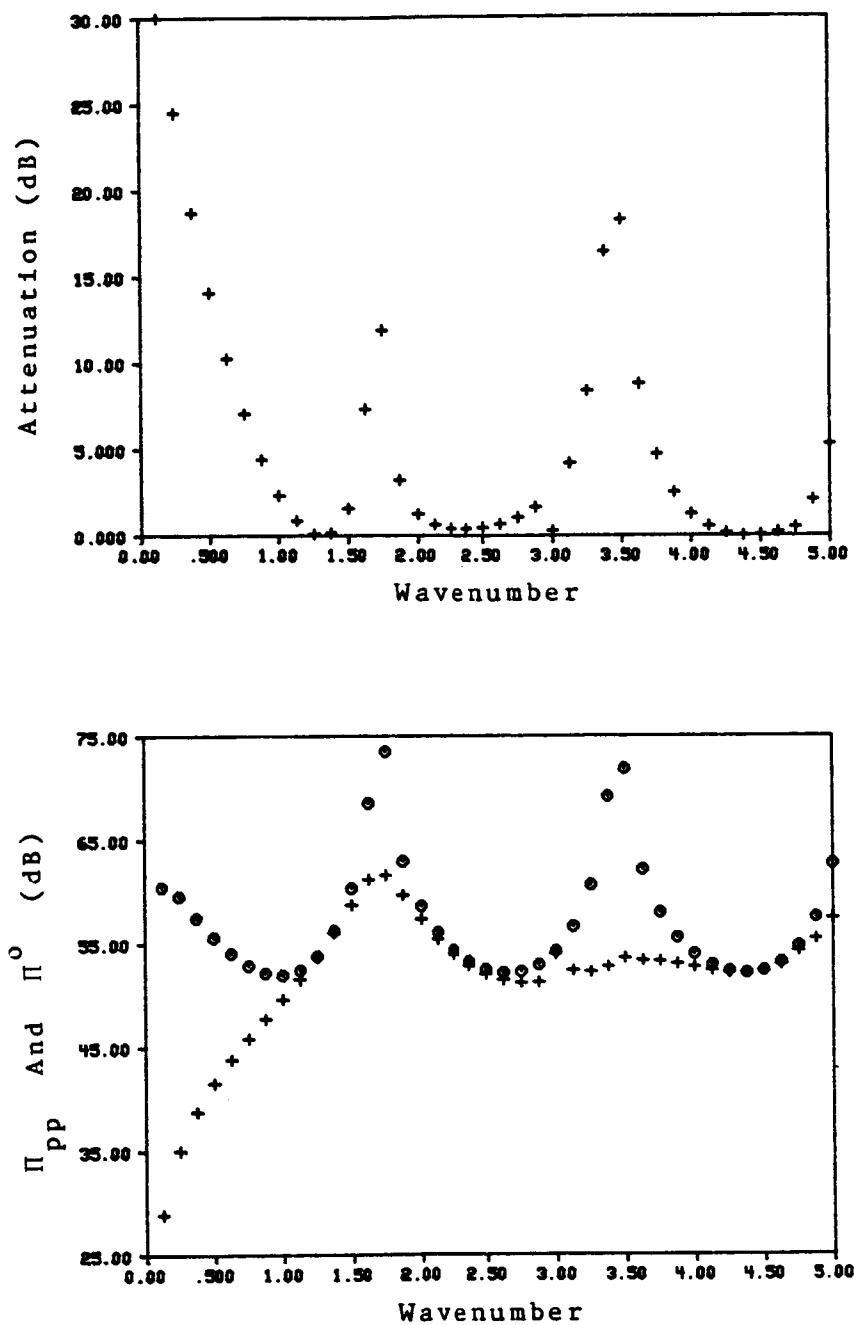


Figure 4.13 - Optimal Active Noise Controller Performance For A Secondary Source At (0.5m,0.5m,0.7808m) In A Driven-Rigid Cavity, Global Control (Case 10).

+ -  $\Pi^o$   
o -  $\Pi_{pp}$

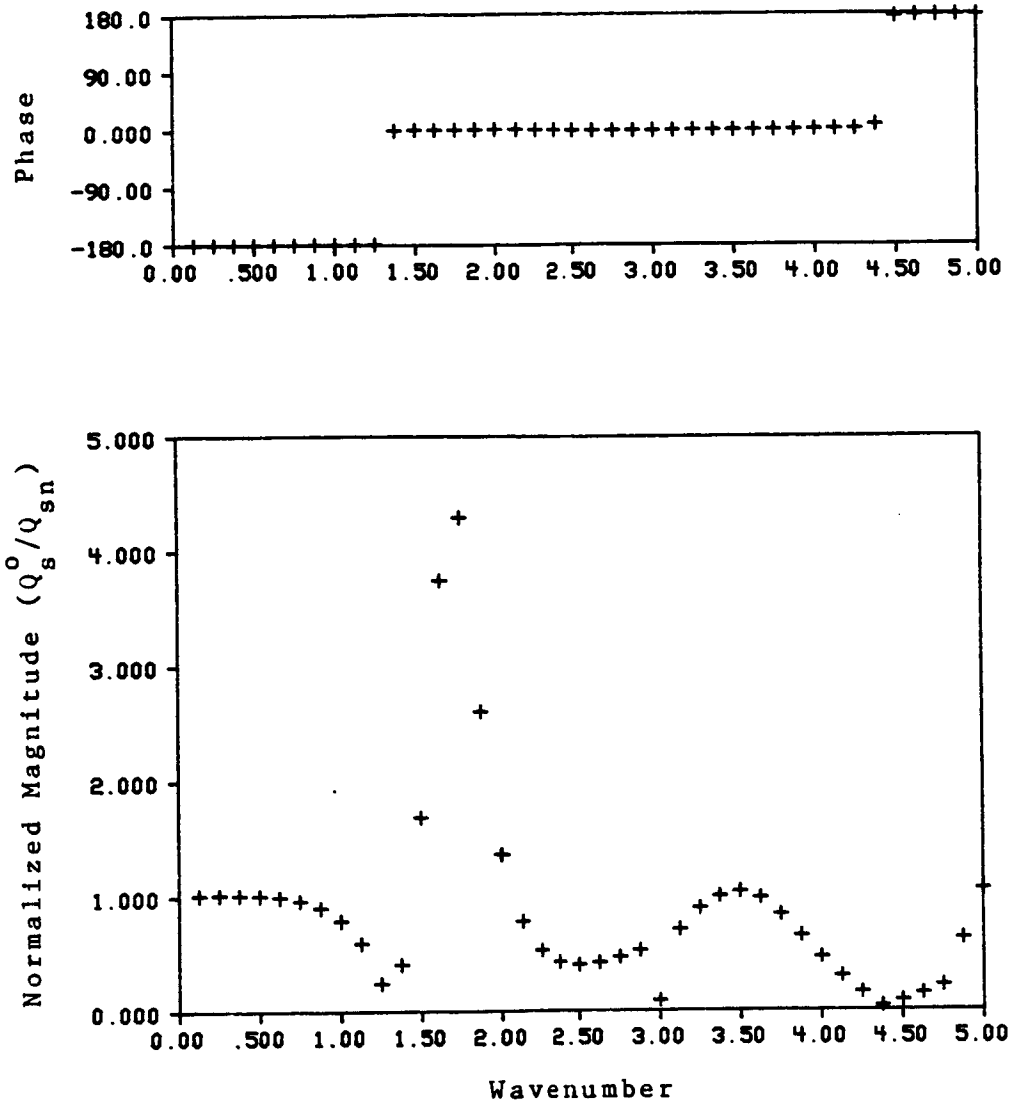


Figure 4.14 - The Normalized Optimal Secondary Source Strengths For A Secondary Source At (0.5m,0.5m,0.7808m) In A Driven-Rigid Cavity, Global Control (Case 10)

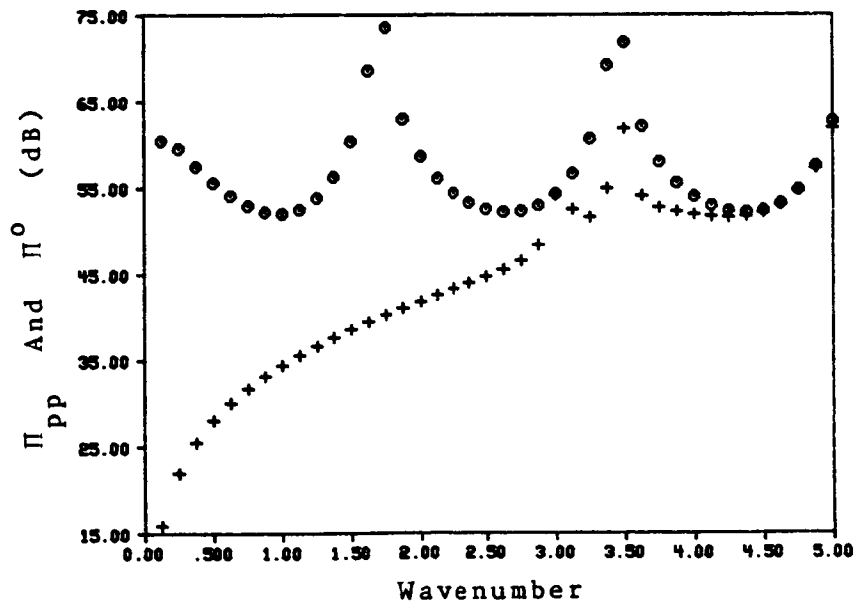
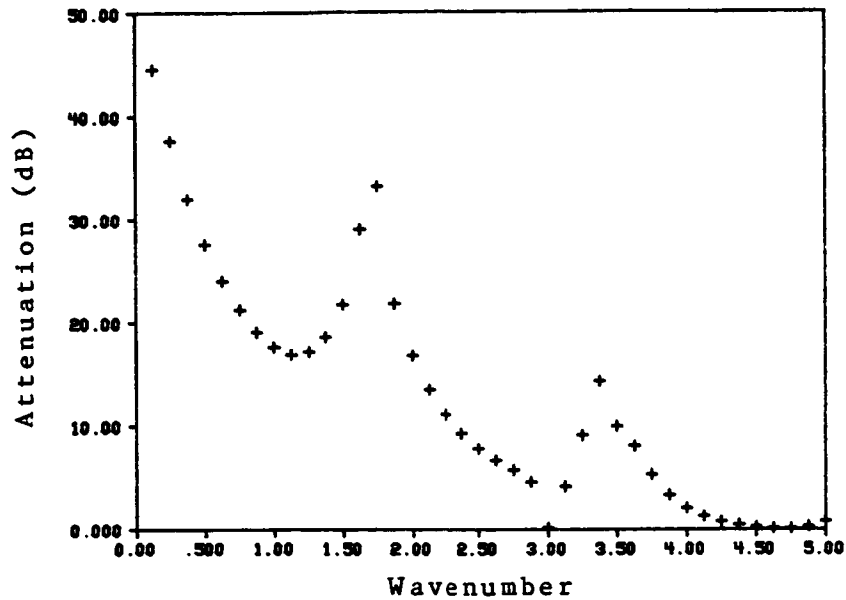


Figure 4.15 - Optimal Active Noise Controller Performance For A Secondary Source At (0.5m,0.5m,1.5288m) In A Driven-Rigid Cavity, Global Control (Case 11).

+ -  $\Pi_o$   
o -  $\Pi_{pp}$

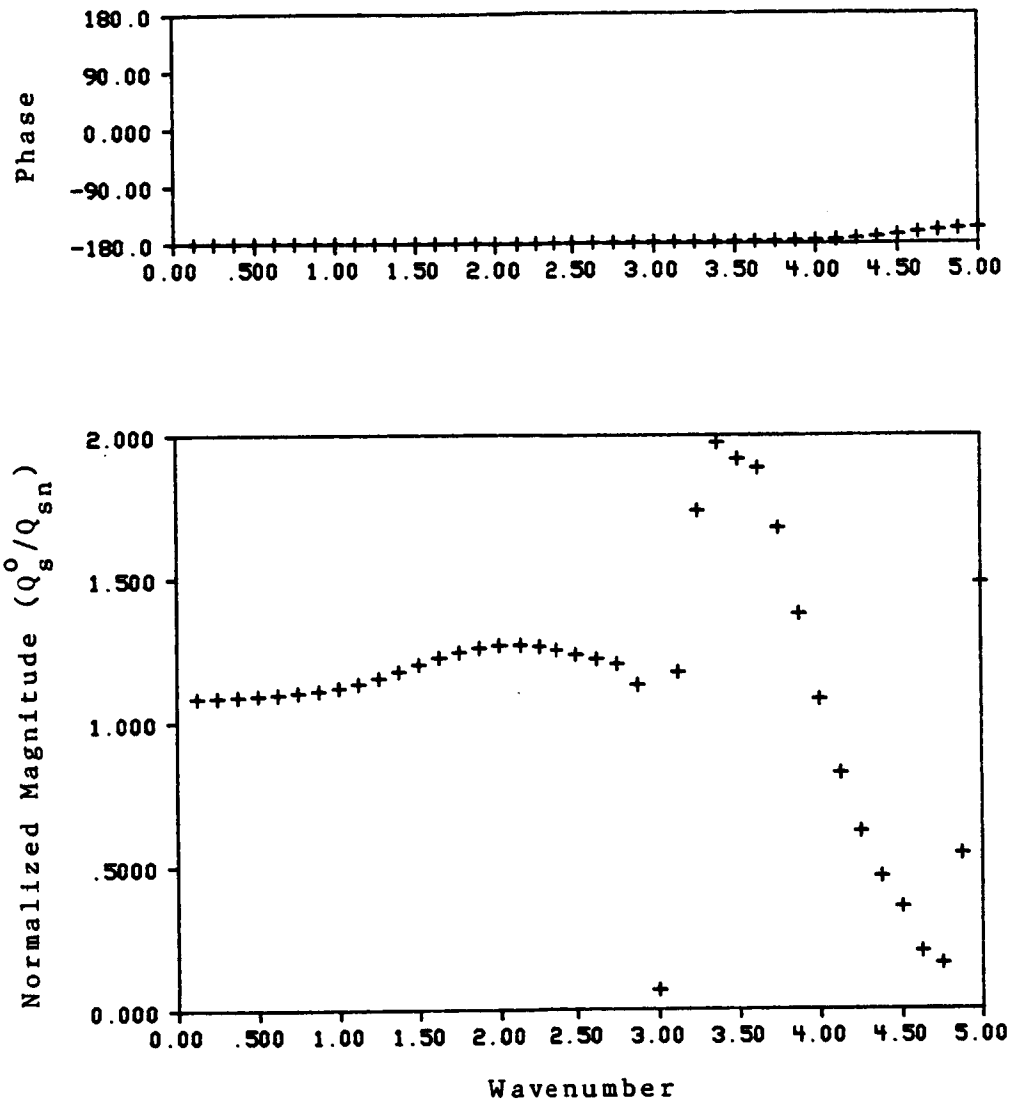


Figure 4.16 - The Normalized Optimal Secondary Source Strengths For A Secondary Source At (0.5m,0.5m,1.5288m) In A Driven-Rigid Cavity, Global Control (Case 11)



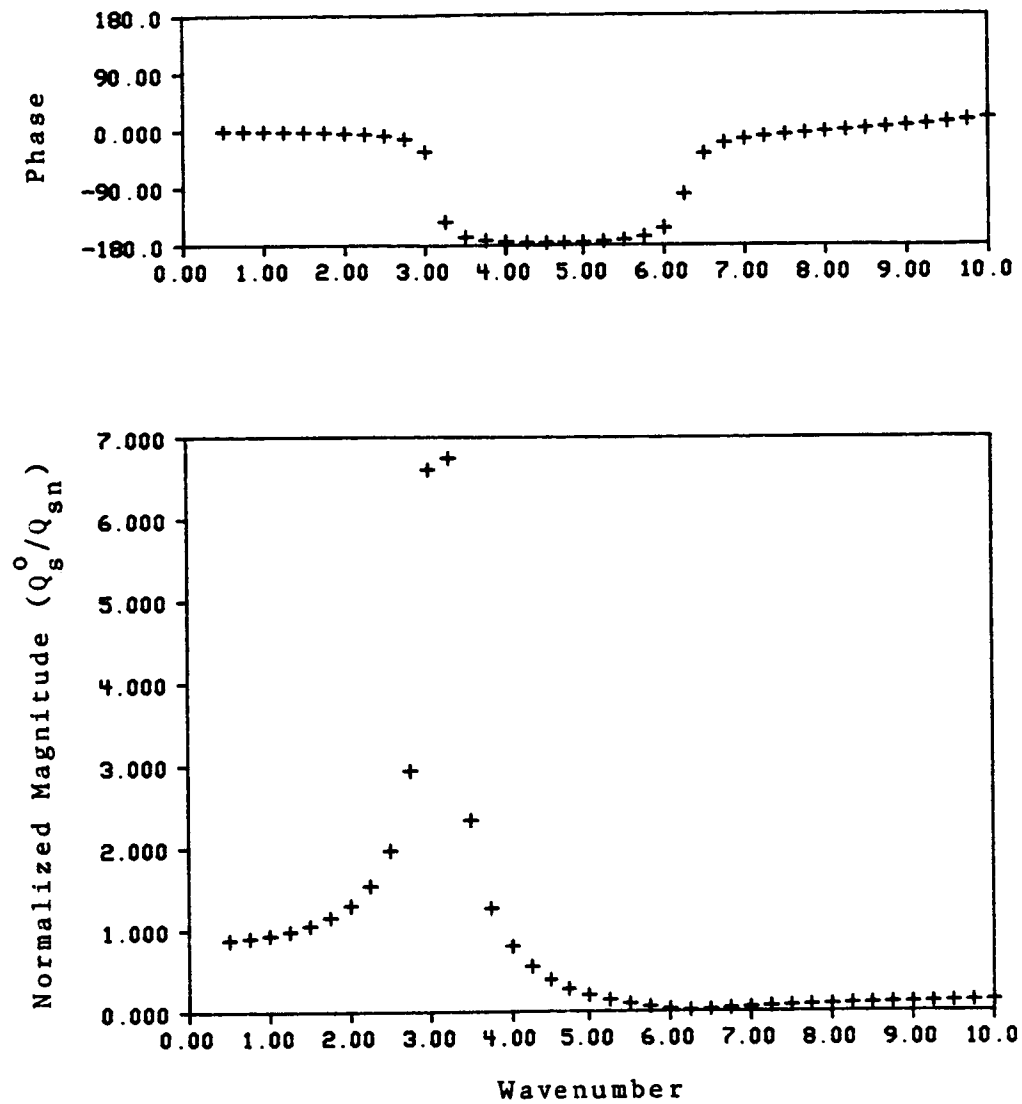


Figure 4.17 - The Normalized Optimal Secondary Source Strengths For One-Point Local Control Using One Secondary Source At Center Of Pulsating Polyhedron (Case 12)

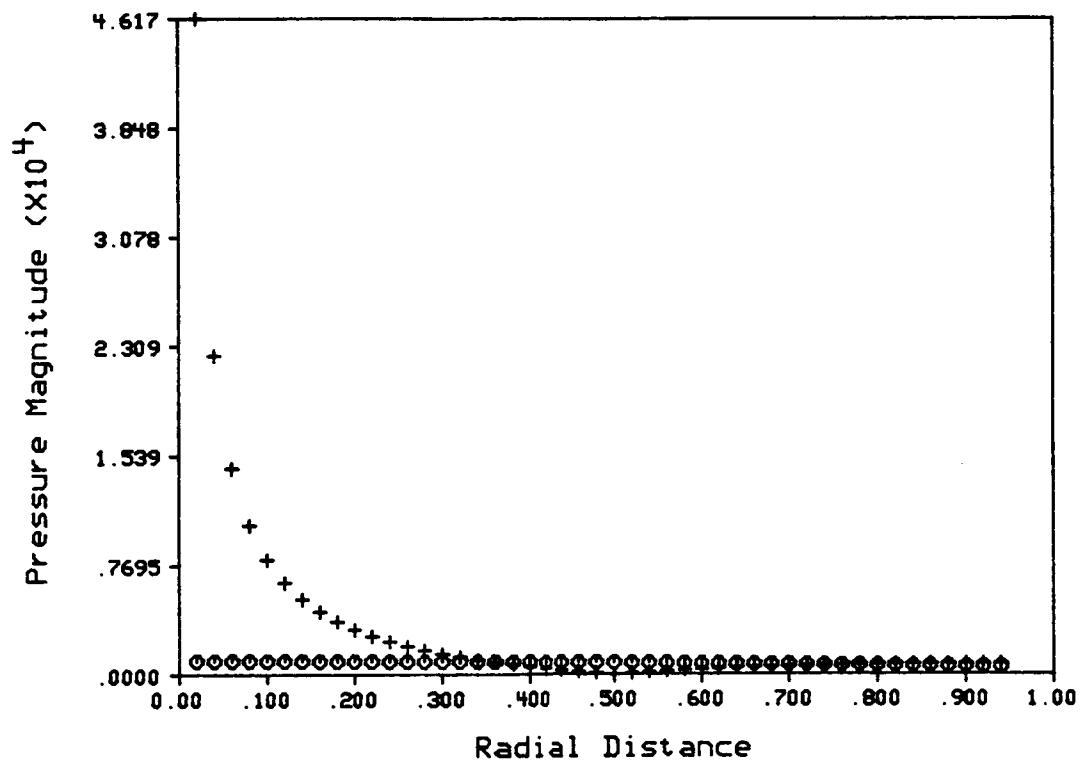


Figure 4.18 - The Uncontrolled And Controlled Pressure Distributions For Case 12 At  $k=2.0$ .  
 o - Uncontrolled Pressure Distribution  
 + - Controlled Pressure Distribution

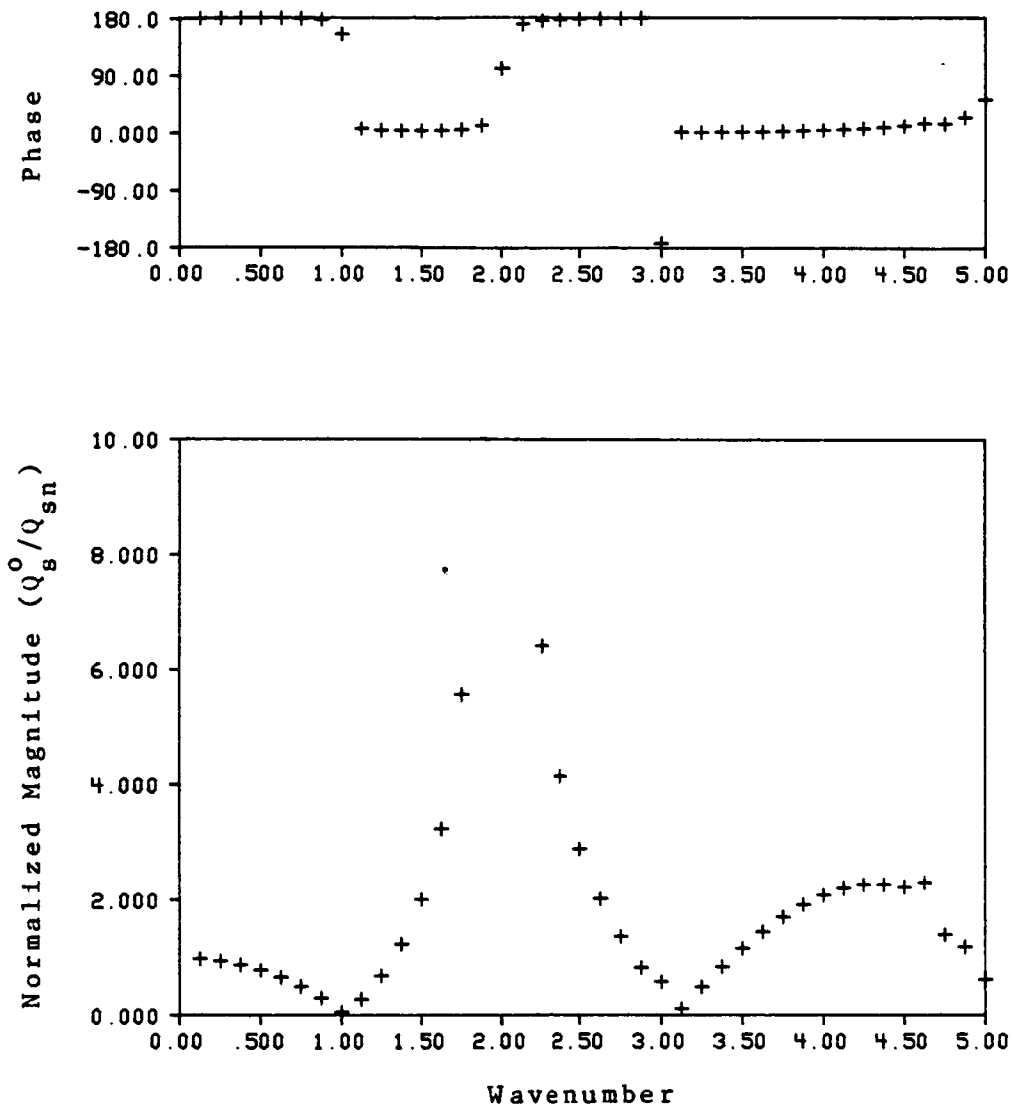


Figure 4.19 - The Normalized Optimal Secondary Source Strengths For One-Point Local Control Using One Secondary Source In A Driven-Rigid Cavity (Case 13)

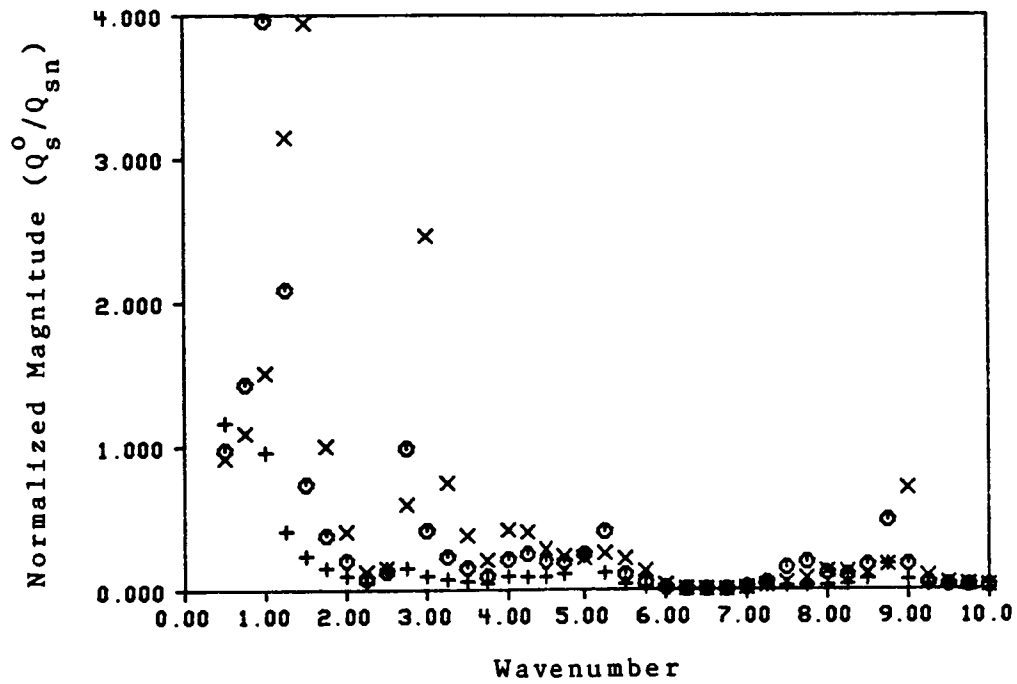


Figure 4.20 - The Normalized Optimal Secondary Source Strengths For A Secondary Source Located A Distance  $d$  From An Observation Point In A Pulsating Polyhedron.

- + -  $d=0.1m$  (Case 14)
- o -  $d=0.2m$  (Case 15)
- x -  $d=0.3m$  (Case 16)

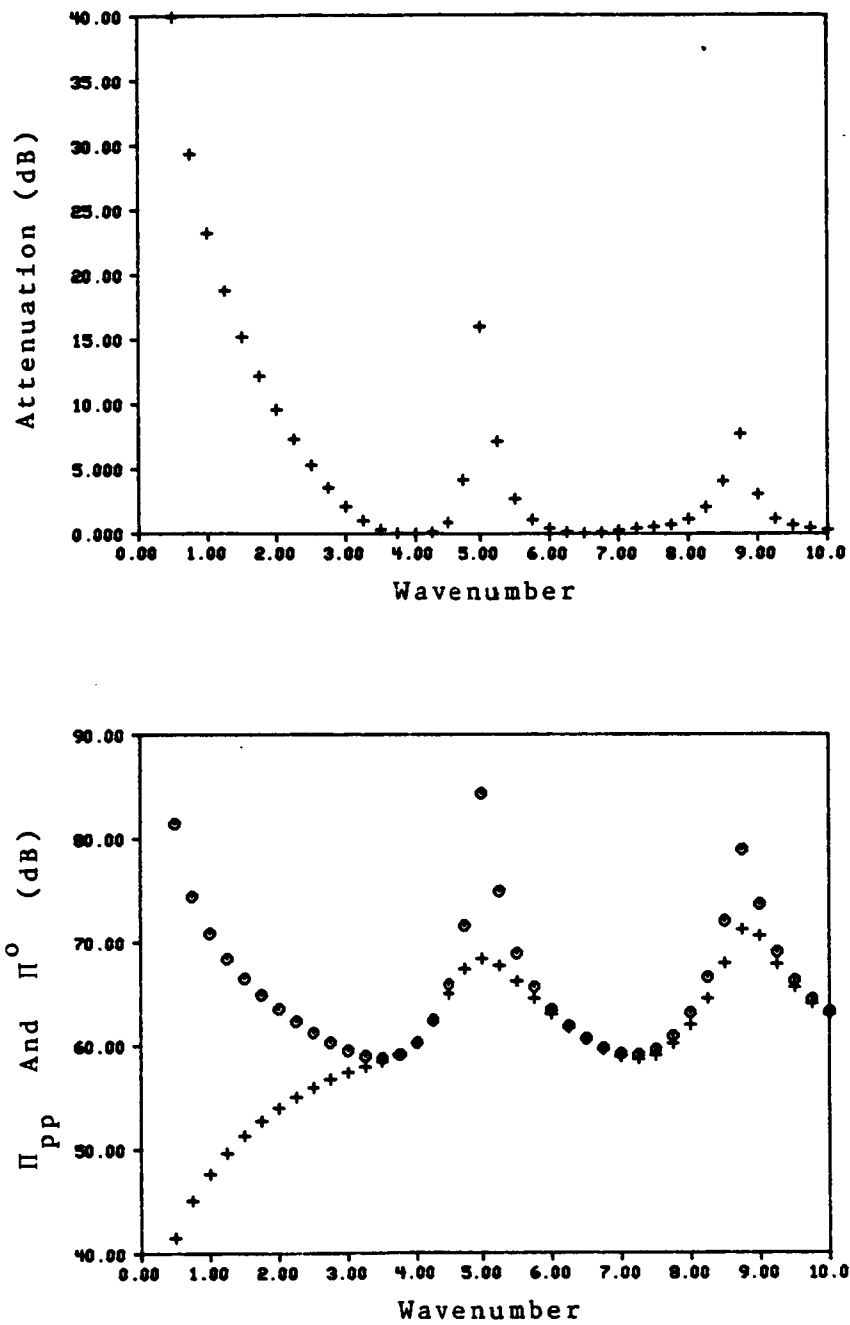


Figure 4.21 - Optimal Active Noise Controller Performance For Two Secondary Sources In A Pulsating Polyhedron, Global Control (Case 17).

+ -  $\Pi_o$   
o -  $\Pi_{pp}$

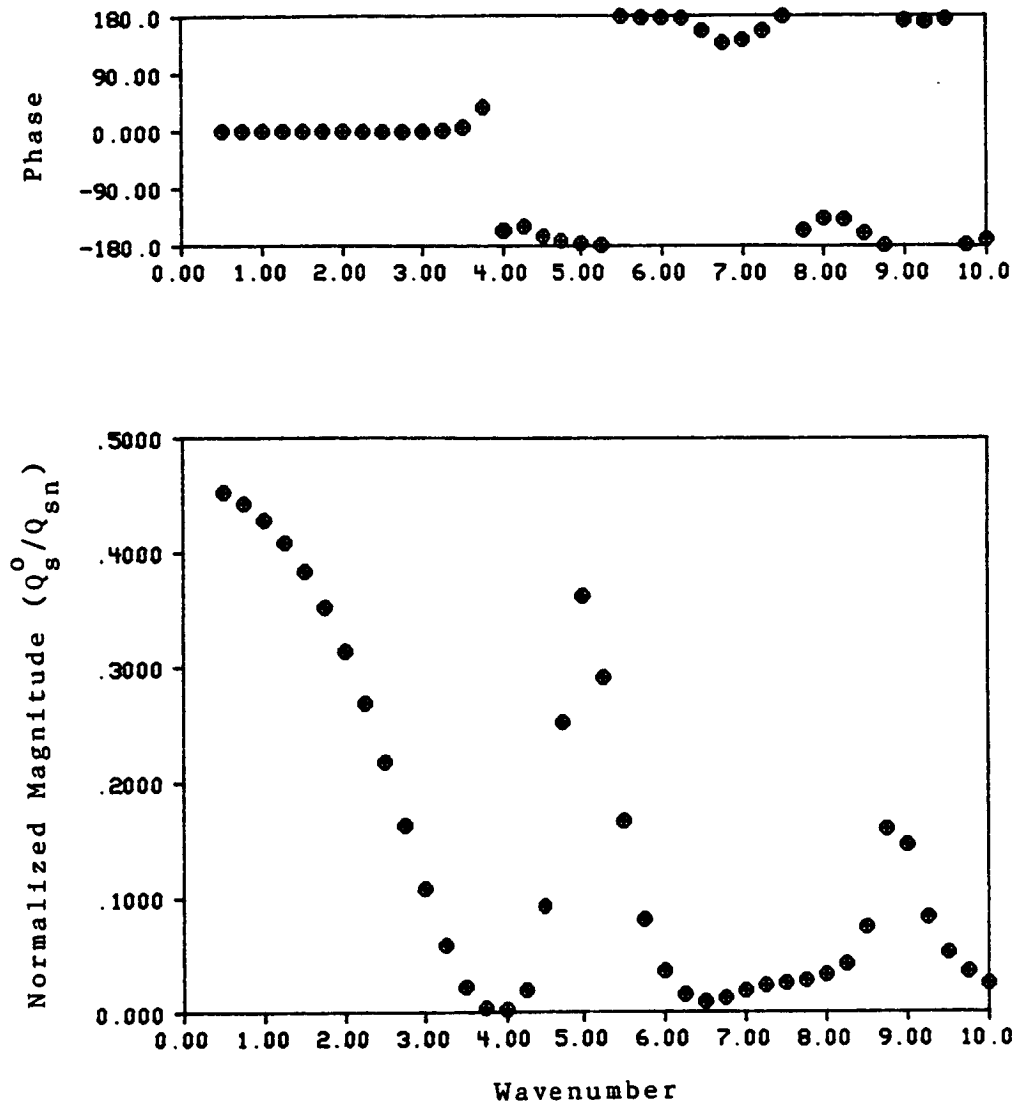


Figure 4.22 - The Normalized Optimal Secondary Source Strengths For Two Secondary Sources In A Pulsating Polyhedron, Global Control (Case 17).

- o - Secondary Source No. 1
- + - Secondary Source No. 2

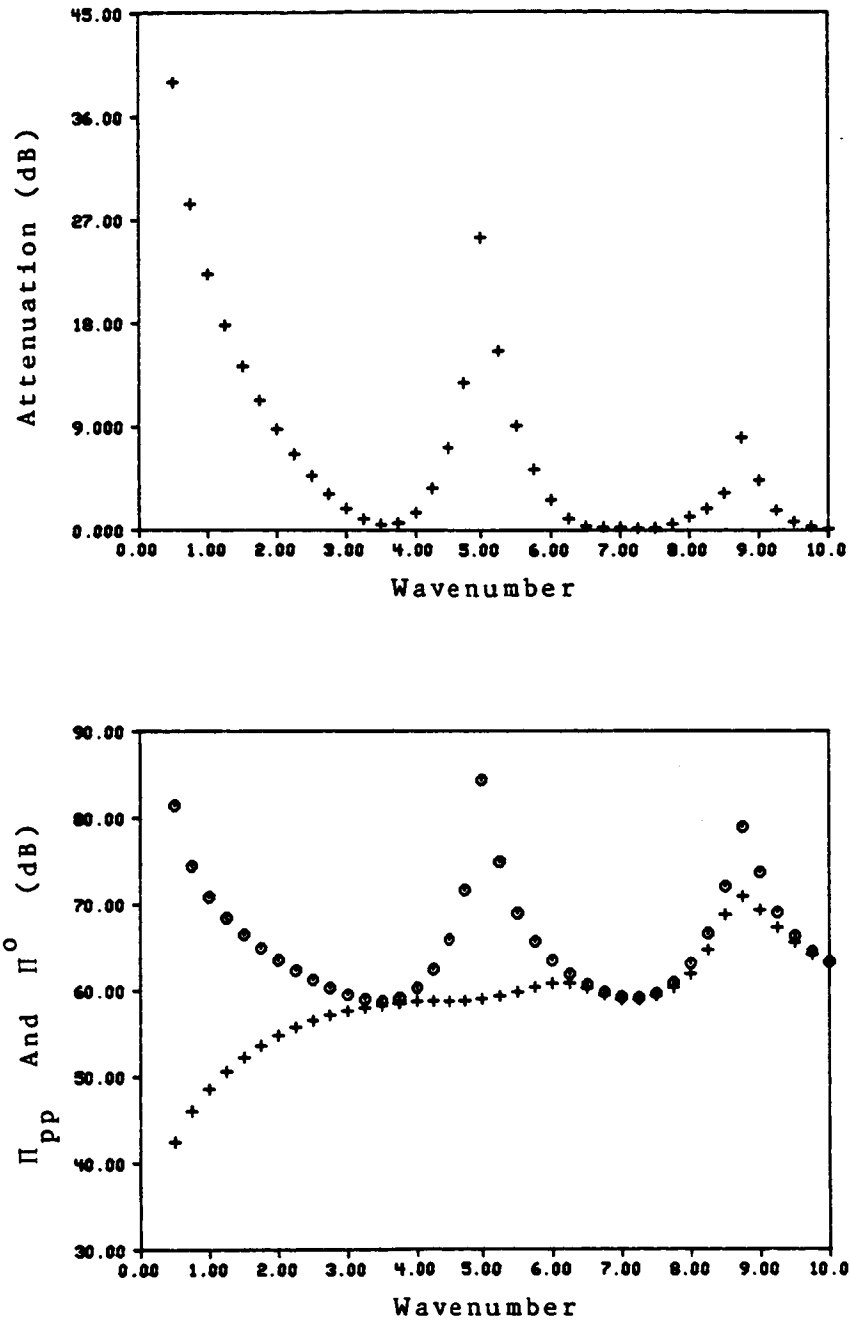


Figure 4.23 - Optimal Active Noise Controller Performance For Four Secondary Sources In A Pulsating Polyhedron, Global Control (Case 18).

+ -  $\Pi_o$   
o -  $\Pi_{pp}$

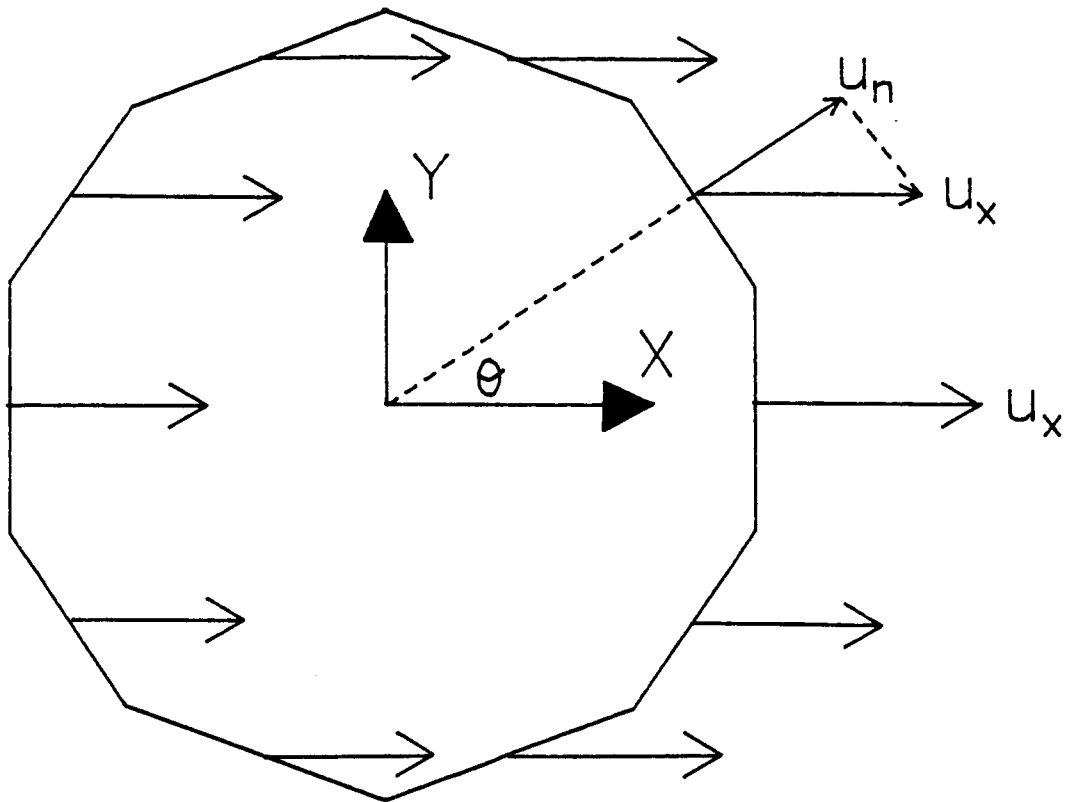


Figure 4.24 - Profile Schematic Of An Oscillating Polyhedron



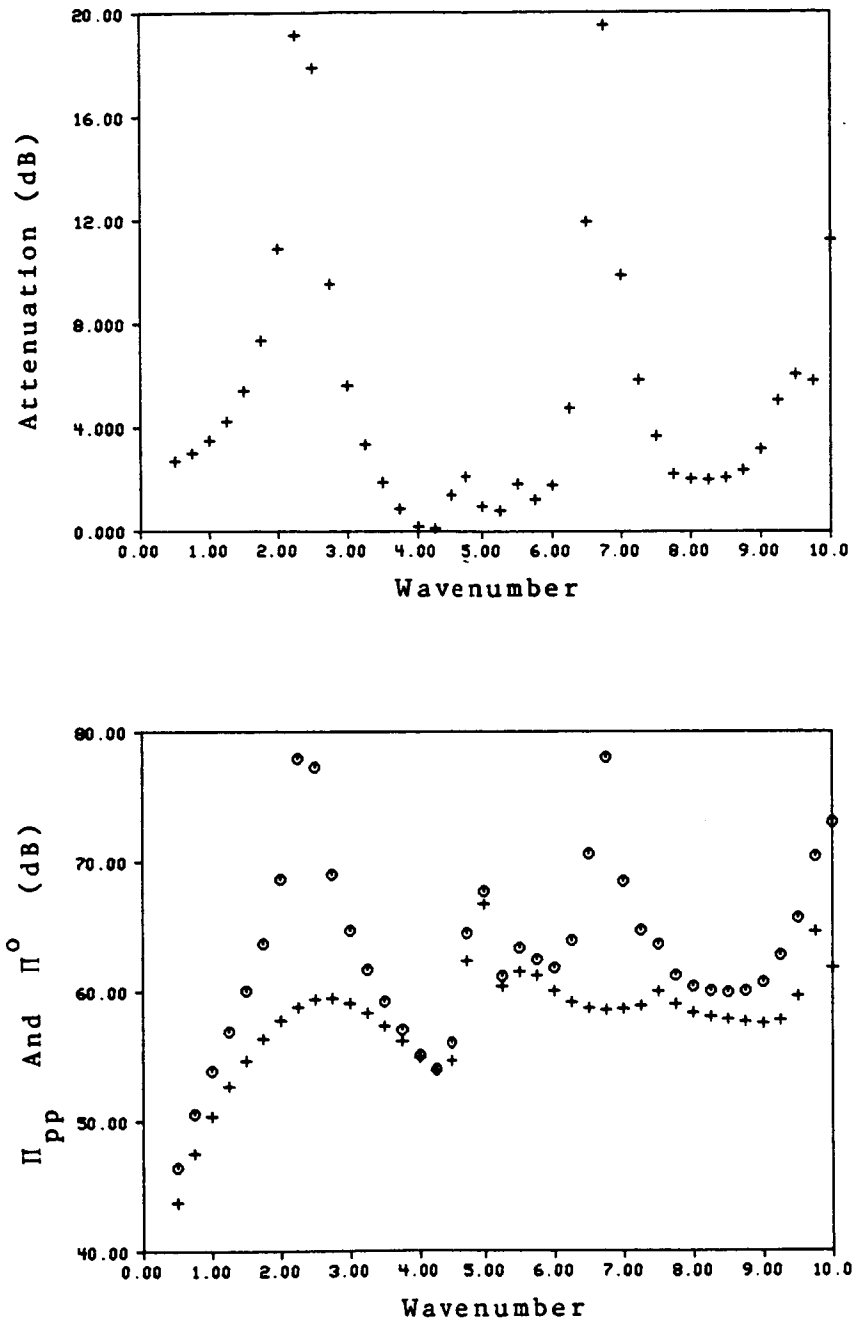


Figure 4.25 - Optimal Active Noise Controller Performance For Two Closely Coupled Secondary Sources At Center Of Oscillating Polyhedron, Global Control (Case 19).

+ -  $\Pi^o$   
o -  $\Pi_{pp}$

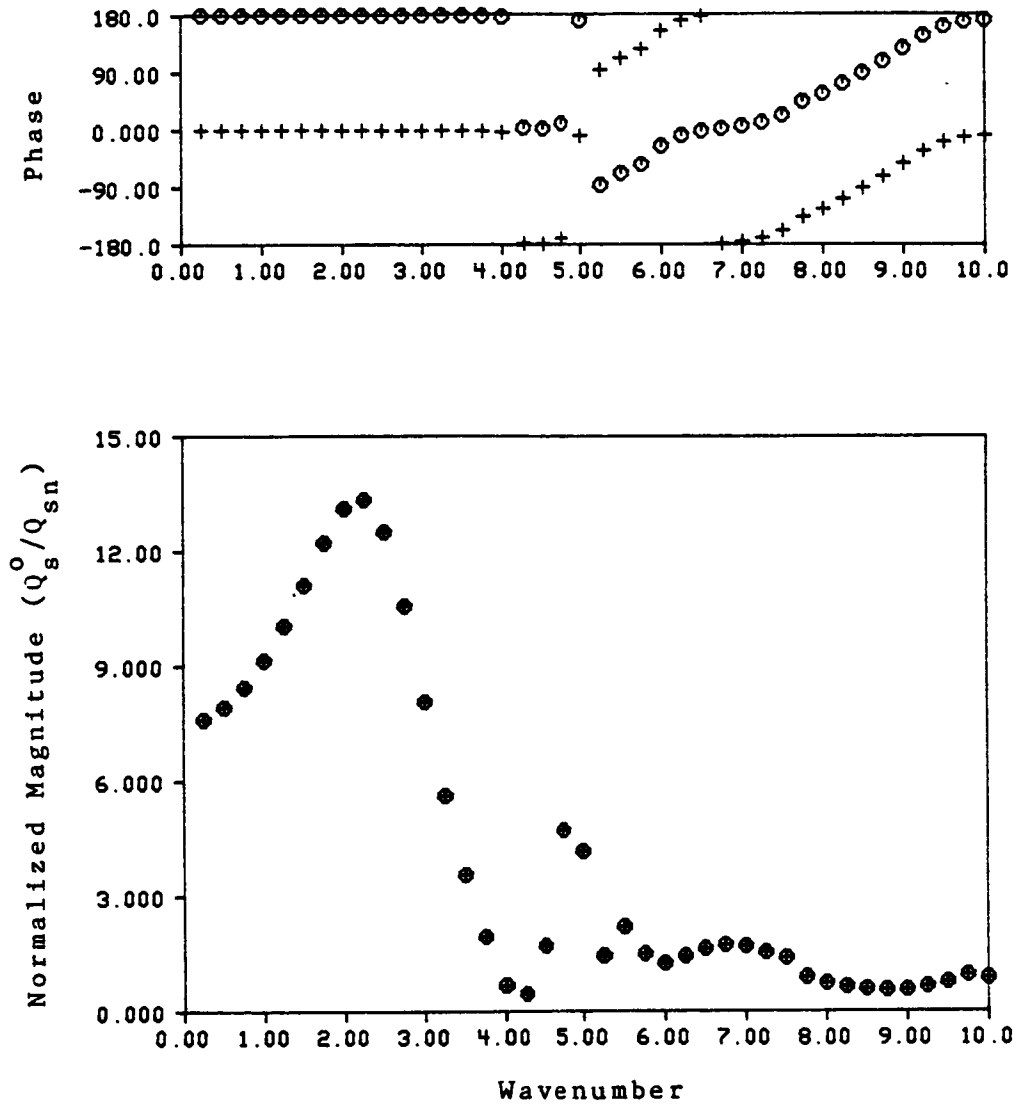


Figure 4.26 - The Normalized Optimal Secondary Source Strengths For Two Closely Coupled Secondary Sources At Center Of Oscillating Polyhedron, Global Control (Case 19).

+ - Secondary Source At (+0.01m,0,0)

o - Secondary Source At (-0.01m,0,0)

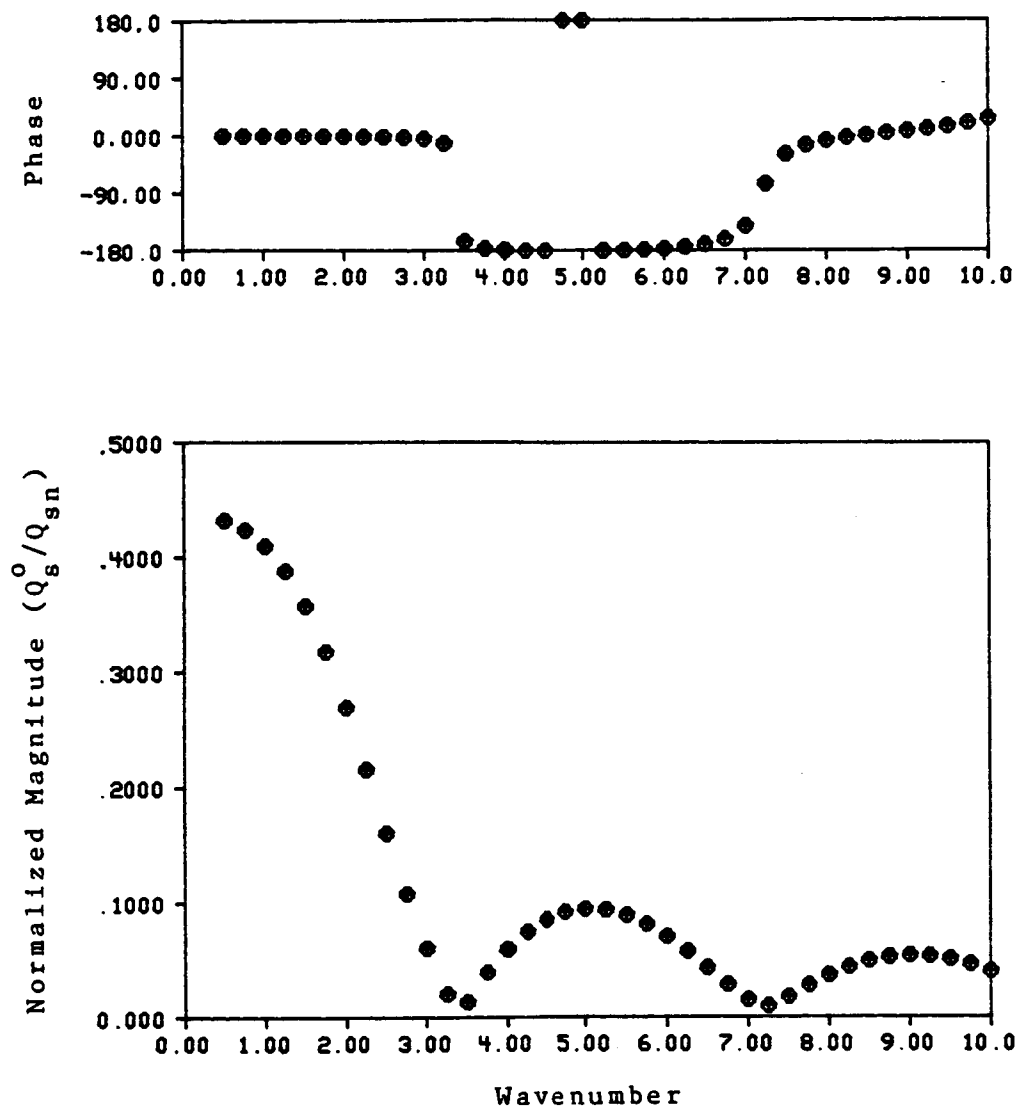


Figure 4.27 - The Normalized Optimal Secondary Source Strengths For Two Tightly-Coupled Secondary Sources At The Center Of A Pulsating 48 Sided Polyhedron.

+ - Secondary Source At (+0.01m,0,0)  
 o - Secondary Source At (-0.01m,0,0)

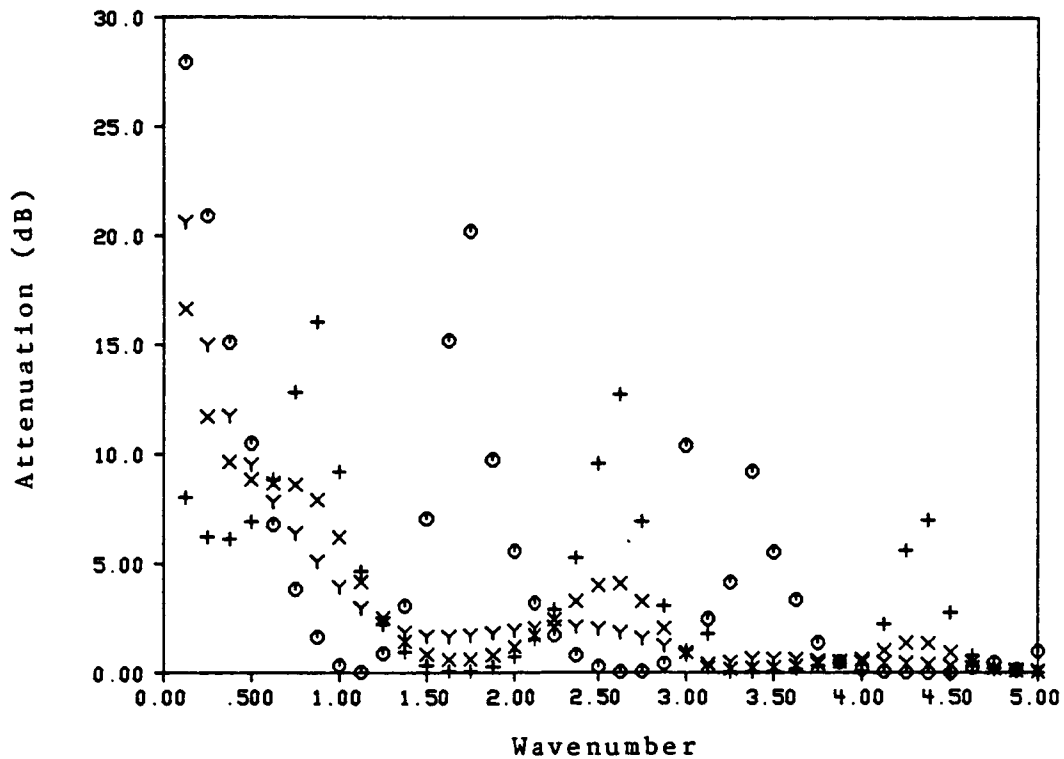


Figure 4.28 - Optimal Active Noise Controller Performance For Different Values Of Resistive Passive Noise Treatment Component, Global Control.

- o - Rigid Walls (Case 20)
- + -  $z=50+j0$  Pa's/m (Case 21)
- x -  $z=200+j0$  Pa's/m (Case 22)
- Y -  $z=350+j0$  Pa's/m (Case 23)

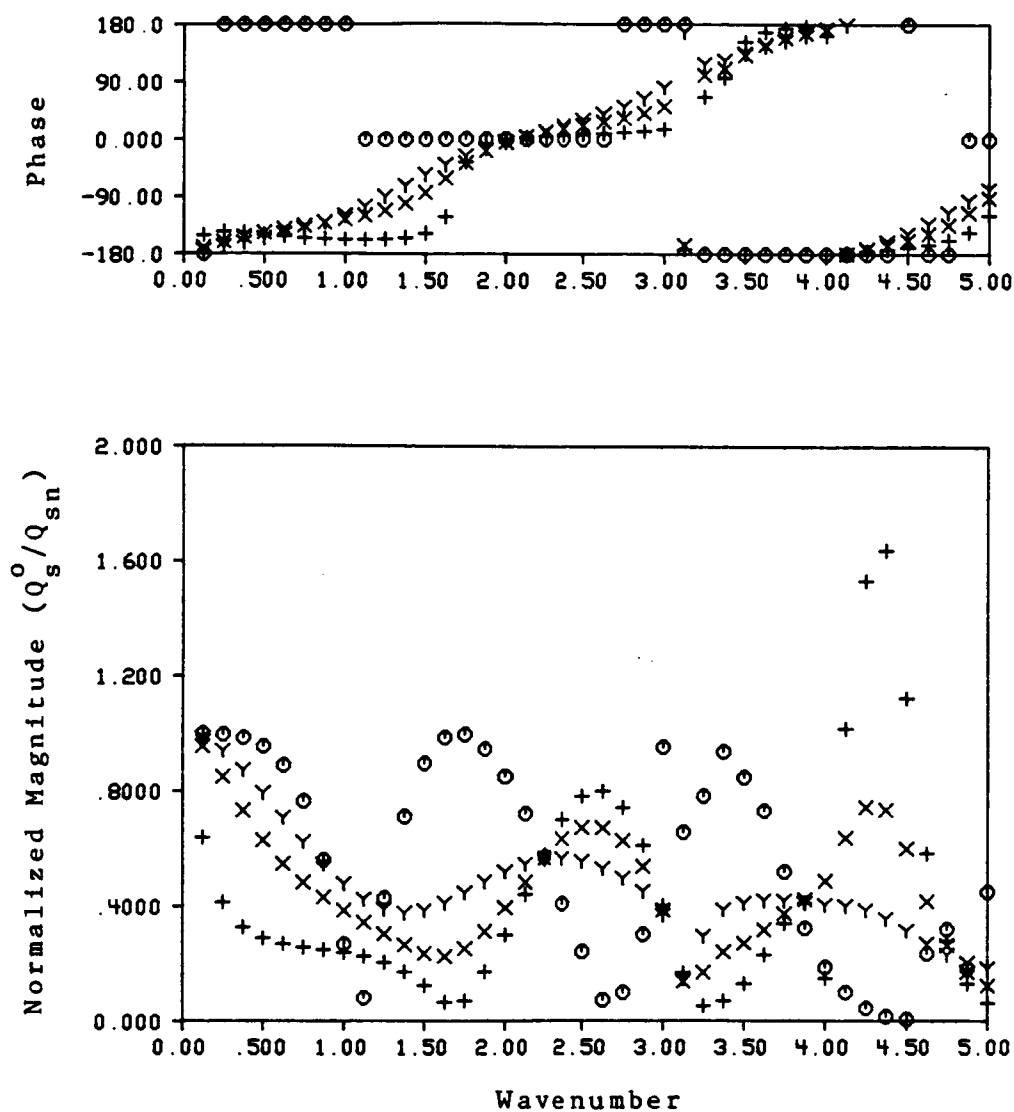


Figure 4.29 - The Normalized Optimal Secondary Source Strengths For Different Values Of Resistive Passive Noise Treatment Component, Global Control.

- $\circ$  - Rigid Walls (Case 20)
- $+$  -  $z=50+j0$  Pa·s/m (Case 21)
- $x$  -  $z=200+j0$  Pa·s/m (Case 22)
- $Y$  -  $z=350+j0$  Pa·s/m (Case 23)

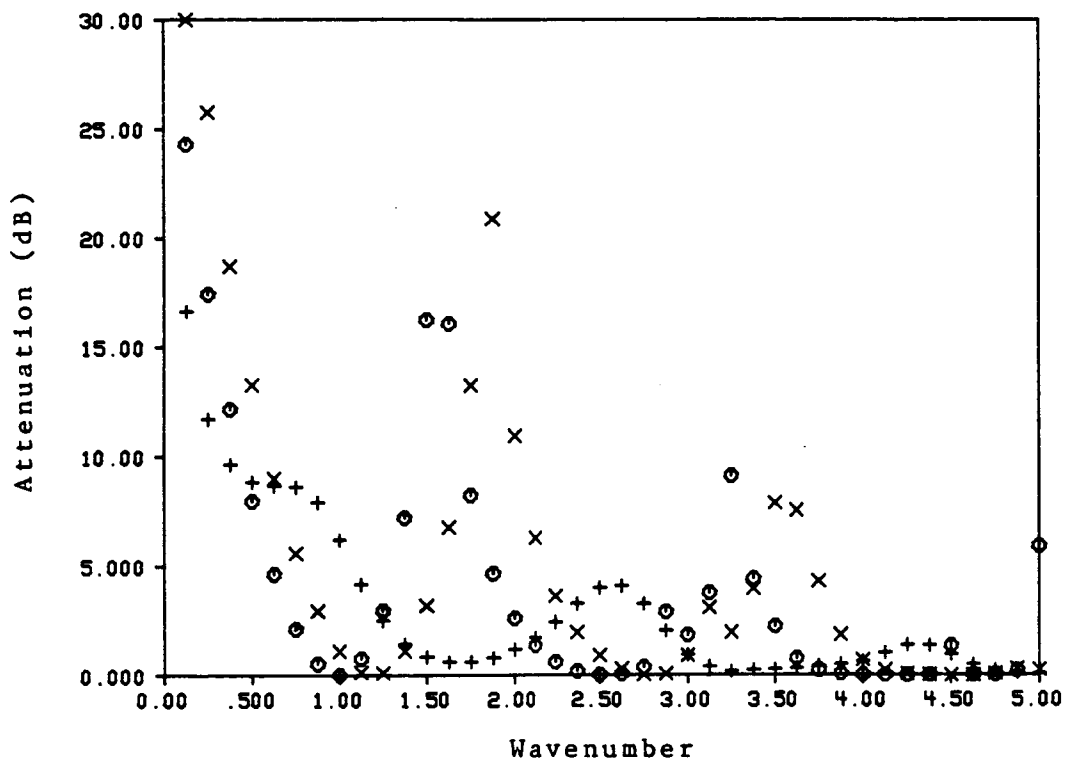


Figure 4.30 - Optimal Active Noise Controller Performance For Different Values Of Reactive Passive Noise Treatment Component, Global Control.

+ -  $z=200+j0$  Pa's/m (Case 22)

x -  $z=200-j1500$  Pa's/m (Case 24)

o -  $z=200+j1500$  Pa's/m (Case 25)

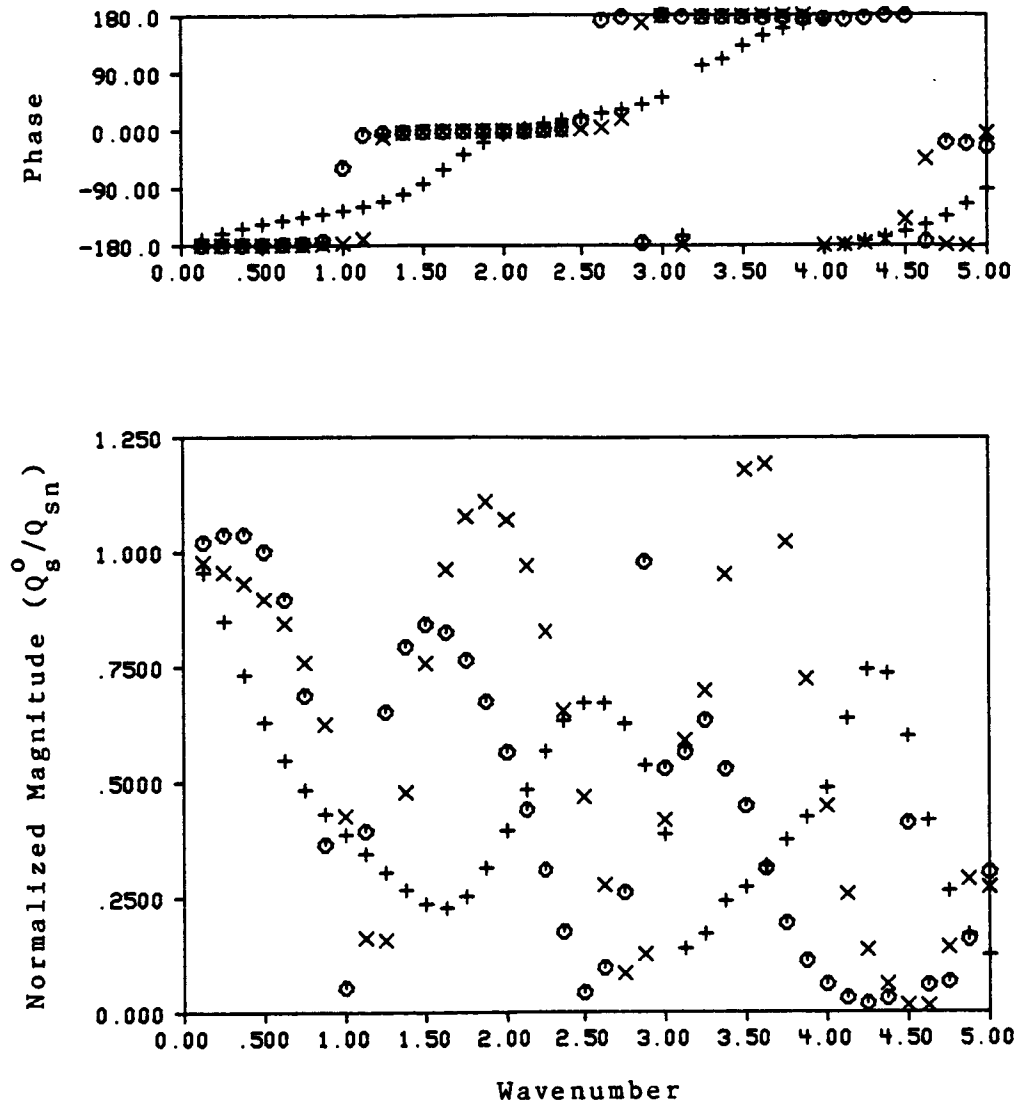


Figure 4.31 - The Normalized Optimal Secondary Source Strengths For Different Values Of Reactive Passive Noise Treatment Component, Global Control.

+ -  $z=200+j0$  Pa $\cdot$ s/m (Case 22)

x -  $z=200-j1500$  Pa $\cdot$ s/m (Case 24)

o -  $z=200+j1500$  Pa $\cdot$ s/m (Case 25)

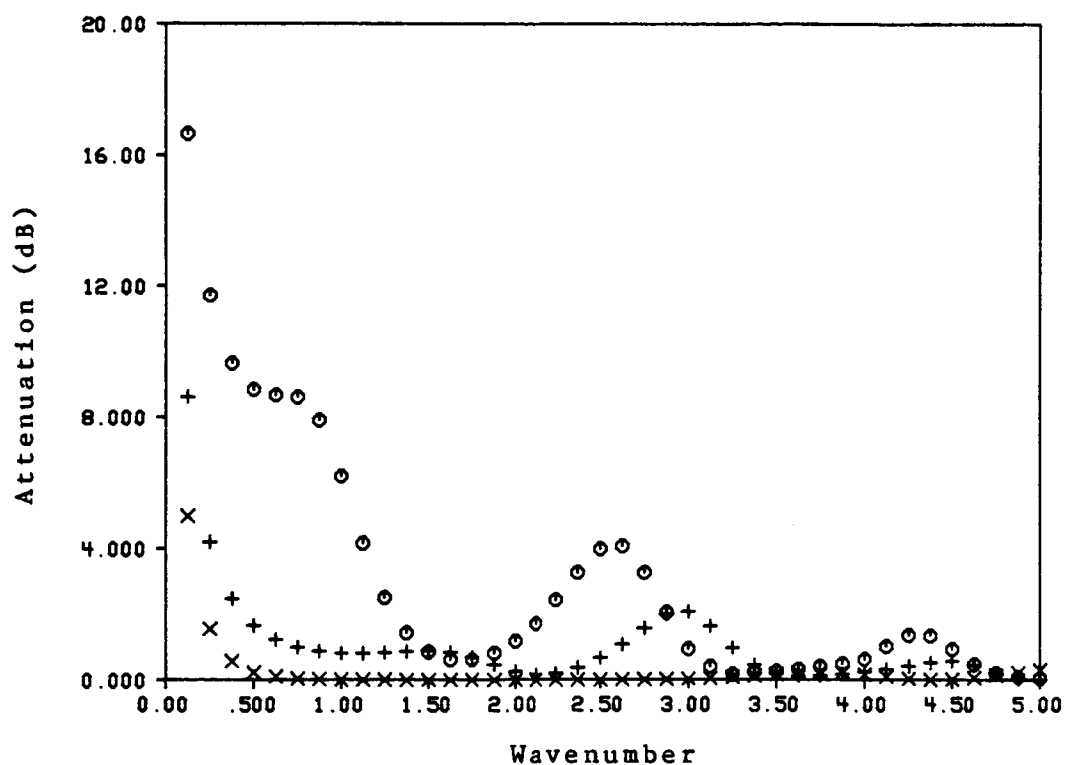


Figure 4.32 - Optimal Active Noise Controller Performance For Different Values Of Passive Noise Treatment Surface Area.

- o - 1 Wall (Case 22)
- + - 2 Walls (Case 26)
- x - 3 Walls (Case 27)



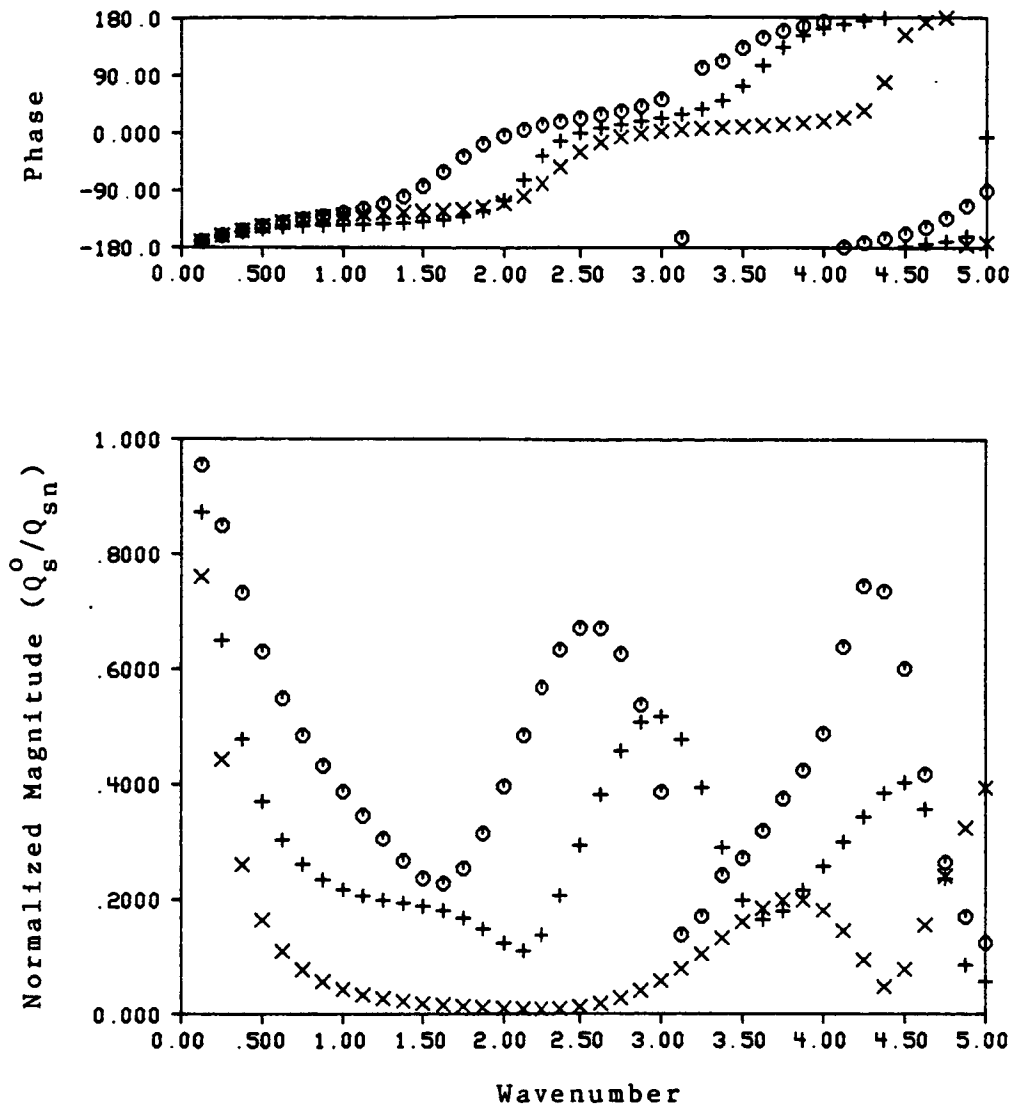


Figure 4.33 - The Normalized Optimal Secondary Source Strengths For Different Values Of Passive Noise Treatment Surface Area.

- o - 1 Wall (Case 22)
- + - 2 Walls (Case 26)
- x - 3 Walls (Case 27)

## CHAPTER 5

## AN OPTIMAL ACTIVE NOISE CONTROLLER FOR FREE

## FIELD RADIATION

Most of the literature on active noise control for free field radiation consists either of experimental procedures [42,43], studies of compact noise sources [30,40], or studies where the noise field is deduced by field point measurements and thus no information about the noise source is required [37]. Very little attention has been given to the general problem of analyzing and minimizing the total sound power of a noise field produced by a generalized distributed source.

The system investigated in this chapter is comprised of two components: a distributed noise source with a known time harmonic surface velocity distribution and an array of canceling (secondary) sources positioned about the noise source. The geometrical shape of the noise source must be known, but the shape is not restricted to any particular form. The relative positions of the noise source and the

secondary sources are also assumed known.

## 5.1 Problem Formulation

In the following sections, the definition and formulation of an optimal active noise controller are presented. The formulation for an optimal active noise controller is derived using the IBEM formulation. In the subsequent formulation, capital letters will denote matrix quantities.

### 5.1.1 The Control Objective Function

The control objective chosen for the research presented here is to minimize the total sound power in the free field. A near-field technique for calculating the sound power output of a source was developed by Levine [38]. Levine's technique is based on an acoustic energy balance at the source, and thus, the need to integrate the far-field intensity in order to calculate the power output of a source is avoided. The technique developed by Levine was applied by Nelson et al. to time harmonic monopole sources [37]. The resulting expression for the source power output,  $w$ , of a monopole with a time harmonic volume velocity source strength  $q$  is

$$w = \frac{1}{2} \operatorname{Re}\{p_{\text{tot}}^* q\} \quad (5.1)$$

where  $p_{\text{tot}}$  is the total sound pressure at the source due to

the source and any incident sound field, and the \* superscript denotes the complex conjugate. The expression  $\text{Re}\{\}$  is an operator signifying "the real part of {}."

In order to use equation 5.1 to calculate the sound power output of a distributed noise source, the noise source is modeled by discretizing the noise source surface (consistent with the IBEM) into elements with constant surface velocity. The discretized elements of the distributed noise source may be assumed to be individual monopole sources characterized by a volume velocity source strength. The volume velocity source strength of an element is given by

$$q_b = us \quad (5.2)$$

where  $u$  is the magnitude of the normal surface velocity of the element, and  $s$  is the surface area of the element.

Applying equation 5.1, the control objective function was formulated as

$$\Pi = \frac{1}{2} \text{Re}\{p_n^H S u_n\} + \frac{1}{2} \text{Re}\{p_s^H q_s\} \quad (5.3)$$

where  $p_s$  is a column vector of the complex pressures at the secondary sources,  $q_s$  is a column vector of the complex volume velocity secondary source strengths,  $p_n$  is a column vector of the complex pressures at the discretized elements of the noise source boundary,  $[S]$  is a diagonal matrix

containing the areas of the noise source surface elements, and  $\underline{u}_n$  is the column vector containing the known velocities of the surface elements. The H superscript denotes the hermitian transpose.

Alternatively, the power radiated from a distributed source could be found by integrating the intensity over the surface as

$$w = \int_s \frac{1}{2} \operatorname{Re}\{p^* u\} dS = \frac{1}{2} \operatorname{Re}\{\underline{p}^H \underline{S} \underline{u}\} \quad (5.4)$$

The integral in equation 5.4 was evaluated by using the fact that the velocity and pressure are constant over each surface element.

#### 5.1.2 IBEM Formulation Of The Control Objective Function

The pressures at the secondary sources are given by equation 3.38:

$$\underline{p}_s = D\underline{\sigma} + E\underline{\phi}_s \quad (5.5)$$

Because there are no primary sources formulated in the problem, the column vector  $\underline{\phi}$  in equation 3.38 contains only secondary source strengths, and thus,  $\underline{\phi}$  will be denoted by  $\underline{\phi}_s$ . The (i,i) element of [E] represents the pressure at the  $i^{\text{th}}$  secondary source due to the  $i^{\text{th}}$  secondary source. Thus, the diagonal of [E] is comprised of singular

functions (refer to equation 3.39b).

The diagonal elements of  $[E]$  are evaluated by taking the limit of the fundamental pressure solution as  $r \rightarrow 0$ :

$$E_{ii} = \lim_{r \rightarrow 0} \frac{e^{-jkr}}{r} = \lim_{r \rightarrow 0} \left[ \frac{\cos kr}{r} - j \frac{\sin kr}{r} \right] \quad (5.6)$$

Applying L'Hospital's rule to equation 5.6 gives  $E_{ii} = \infty - jk$ . Note that the imaginary component of  $E_{ii}$  is finite.

The pressures at the discretized elements of the noise source boundary are also derived from equation 3.38:

$$p_n = D' \underline{\sigma} + E' \underline{\phi}_s \quad (5.7)$$

The fictitious source strength distribution,  $\underline{\sigma}$ , is determined from the known boundary conditions, namely, the surface normal velocities by equation 3.25

$$\underline{u}_n = F \underline{\sigma} + G \underline{\phi}_s \quad (5.8)$$

Thus, solving for the fictitious source strengths gives

$$\underline{\sigma} = F^{-1} (\underline{u}_n - G \underline{\phi}_s) \quad (5.9)$$

Substituting the fictitious source strengths from equation 5.9 into the pressure equations, 5.5 and 5.7, gives the pressures in terms of surface velocities and secondary source strengths:

$$\underline{p}_s = D F^{-1} \underline{u}_n + (E - D F^{-1} G) \underline{\psi}_s \quad (5.10)$$

and

$$\underline{p}_n = D' F^{-1} \underline{u}_n + (E' - D' F^{-1} G) \underline{\psi}_s \quad (5.11)$$

The secondary source strengths are related to the volume velocity secondary source strengths by

$$\underline{\psi}_s = \frac{j k \rho_o c}{4\pi} \underline{q}_s = c_s \underline{q}_s \quad (5.12)$$

By substituting the pressure and source strength relationships from equations 5.10, 5.11, and 5.12 into equation 5.3 and using the identity  $\text{Re}\{\zeta\} = \frac{1}{2}(\zeta + \zeta^*)$  where  $\zeta$  is any complex scalar, the control objective function can be written as

$$\Pi = \frac{1}{4} (\underline{q}_s^H A \underline{q}_s + \underline{q}_s^H B \underline{u}_n + \underline{u}_n^H B^H \underline{q}_s + \underline{u}_n^H C \underline{u}_n) \quad (5.13)$$

where

$$A = c_s (E - D F^{-1} G) + [c_s (E - D F^{-1} G)]^H \quad (5.14a)$$

$$B = D F^{-1} + [c_s (E' - D' F^{-1} G)]^H S \quad (5.14b)$$

$$C = S D' F^{-1} + (D' F^{-1})^H S \quad (5.14c)$$

Note that the uncontrolled free field power is  $\frac{1}{4} \underline{u}_n^H C \underline{u}_n$ .

In equation 5.14a, note that  $[E]$  is multiplied by the purely imaginary constant  $c_s$ . Thus, after  $[E]$  is multiplied by  $c_s$ , the infinite, real components of the diagonal terms of  $[E]$  become the imaginary components of

the diagonal terms. When  $[A]$  is computed, the hermitian transpose of the matrix  $c_s(E - DF^{-1}G)$  is added to itself. Consequently, the (infinite) imaginary components along the diagonal cancel, and thus, the diagonal of  $[A]$  is real and finite.

### 5.1.3 An Optimal Controller

The control objective function in equation 5.13 is a real, positive definite, quadratic function of the volume velocity secondary source strengths. As stated in chapter 4, such a function has a single unique global minimum. Thus, there is a unique combination of secondary source strengths which minimize the total sound power radiated into the free field by the noise source and secondary sources. Utilizing equation 4.12, the minimum value of the control objective function occurs when

$$A\underline{q}_s + B\underline{u}_n = 0 \quad (5.15)$$

Thus, the optimal secondary source strengths are given by

$$\underline{q}_s^o = -A^{-1}B\underline{u}_n \quad (5.16)$$

The corresponding minimum value of the control objective function is

$$\Pi^o = \Pi(\underline{q}_s = \underline{q}_s^o) = \underline{u}_n^H C \underline{u}_n + \underline{u}_n^H B^H \underline{q}_s^o \quad (5.17)$$

The attenuation due to the optimal active noise controller



is computed from

$$ATN = 10 \log \frac{\Pi_{pp}}{\Pi_o} \quad (5.18)$$

where ATN denotes attenuation and  $\Pi_{pp} = \Pi(q_s = 0)$ .

## 5.2 Case Study Results

In this section, the results from a number of active noise control system configurations are presented. For all case studies, the value of  $\rho_o c$  was 415.0 Pa's/m. The optimal controller was analyzed for two differently shaped noise producing mechanisms. The first noise producing mechanism is a pulsating sphere, 1.0m in radius, with a time harmonic surface velocity of 1.0m/s. The pulsating sphere is centered about the origin. The characteristic dimension,  $a$ , of the sphere is 1.0m. The sphere was modeled using 48 triangular superparametric elements.

The second noise producing mechanism is a cylindrical shell which is shown in Figure 5.1. The characteristic dimension,  $a$ , of the shell is 0.1m. One face of the shell was assigned a velocity distribution given by the zero order Bessel function of the first kind,  $J_0(r)$ , such that  $J_0(0)=1.0\text{m/s}$ , and  $J_0(a)$  corresponded to the first zero of the Bessel function [57]. The other sides of the shell were rigid. Such a model and velocity distribution were chosen to approximate the first mode of vibration of the

top of a refrigerant compressor shell. The shell was modeled using 96 triangular superparametric boundary elements.

In some instances, due to numerical integration error, analysis of the optimal controller could not be performed for the very low frequency regime [47]. The numerical integration error increased with decreasing wavenumber, increasing proximity of the secondary source(s) to the noise source, or increasing number of secondary sources. Consequently, the lowest value of frequency for which results are reported is not the same for all case studies.

Cases I, II, and III examined changes in controller performance as a function of the relative placement of a single secondary source. Using the cylindrical shell model, the single secondary source was positioned at (0,0,0.15m), (0,0,0.35m), and (0,0,1.05m) for cases I, II, and III respectively. Hence, the distance between the noise source and the secondary source,  $l$ , is 0.1m, 0.3m, and 1.0m for cases I, II, and III respectively. The active noise controller performance is shown in Figure 5.2 while the normalized optimal secondary source strengths are shown in Figure 5.3 for cases I, II, and III. The advantage of closely coupling the secondary source with the noise source is apparent in Figure 5.2. Note that for  $l > \frac{\lambda}{2}$  ( $ka > 0.1\frac{\pi}{1}$ ), no significant attenuation is possible [30]. In Figure 5.3,

it can be seen that in the low frequency limit, the optimal secondary source forms a dipole with the noise source. Also note that the relative phase of the secondary source is either  $0^{\circ}$  (in-phase) or  $180^{\circ}$  (out-of-phase).

Cases IV, V, and VI also investigated the placement of a single secondary source using the shell model. For cases IV, V, and VI, the secondary source was located to the side of the shell at  $(0.15m, 0, 0)$ ,  $(0.35m, 0, 0)$ , and  $(1.05m, 0, 0)$  respectively. Thus, the values for  $l$  are  $0.05m$ ,  $0.25m$ , and  $0.95m$  for cases IV, V, and VI respectively. The results of cases IV, V, and VI are shown in Figures 5.4 and 5.5. By comparing Figures 5.2 and 5.4, it can be seen that for a remotely located secondary source (cases III and VI), the directional location of the secondary source did not affect the performance. The performance is relatively poor in both cases except at very low frequencies. However, for a closely coupled secondary source (cases I and IV), the directional location affected the performance. The performance improved, particularly at the higher frequencies when the secondary source was located in front of the noise producing face.

Cases VII, VIII, IX, and X investigated changes in active noise controller performance for an increasing number of actuators. The pulsating sphere, which produces a spherically symmetric noise field, was employed for cases

VII through X. The locations and utilization of the secondary sources for cases VII through X are given in Table 5.1.

Table 5.1 - Secondary Source Data For Cases VII-X

Source No.	Location (m)	Cases Used
1	(+2,0,0)	VII VIII IX X
2	(-2,0,0)	VIII IX X
3	(0,+2,0)	IX X
4	(0,-2,0)	IX X
5	(0,0,+2)	X
6	(0,0,-2)	X

The results of cases VII through X are given in Figure 5.6. The advantage of multiple secondary sources in the low frequency regime is apparent in Figure 5.6. For  $l > \frac{\lambda}{2}$  ( $ka > \frac{\pi}{l}$ ), where  $l$  is the distance from the center of the sphere to the secondary source(s), no significant attenuation is possible even with multiple secondary sources. For cases VII through X,  $l=2.0m$ .

The maximum, combined, normalized, optimal secondary source strengths for cases VII, VIII, IX, and X were 1.0, 1.1, 1.25 and 2.2 respectively. Hence, the improvement in attenuation is accompanied by an increase in required secondary source strength. Due to the symmetrical arrangement of the secondary sources, sources 1 and 2 in case VIII were equal in magnitude and phase for all

frequencies considered. Likewise, for cases IX and X, at every frequency all secondary sources were equal in magnitude and phase.

Cases XI, XII, XIII, and XIV examined a symmetric distribution of multiple secondary sources about the cylindrical shell. The placement and utilization of the secondary sources for cases XI through XIV are given in Table 5.2.

Table 5.2 - Secondary Source Data For Cases XI-XIV

Source No.	Location (m)	Cases Used
1	(0,0,+0.4)	XI XII XIII XIV
2	(0,0,-0.4)	XII XIII XIV
3	(0,+0.4,0)	XIII XIV
4	(0,-0.4,0)	XIII XIV
5	(+0.4,0,0)	XIV
6	(-0.4,0,0)	XIV

The results of cases XI through XIV are shown in Figure 5.7. As was shown by cases VII through X, additional secondary sources improve the performance only in the low frequency regime. The maximum, combined, normalized, optimal secondary source strengths for cases XI, XII, XIII, and XIV were 1.0, 1.21, 1.68, and 4.08 respectively. Thus, larger secondary source strengths are required to attain the increase in performance. For cases XII through XIV, sources 1 and 2 were not equal in

magnitude or phase. For case XIII, due to symmetry, sources 3 and 4 were equal in modulus and phase. Likewise, in case XIV, the sources around the perimeter of the shell (3, 4, 5, and 6) were all equal in magnitude and phase.

Cases XV, XVI, XVII, and XVIII investigated an asymmetric distribution of multiple secondary sources about the cylindrical shell. The secondary sources were positioned adjacent to the noise producing face of the shell. All secondary sources were located such that they were 0.4m away from the origin. The cases for which each source was employed and the source locations are given in Table 5.3.

Table 5.3 - Secondary Source Data For Cases XV-XVIII

Source No.	Location (m)	Cases Used
1	(0,-0.28284,0.28284)	XV XVI XVII XVIII
2	(0,+0.28284,0.28284)	XVI XVII XVIII
3	(-0.2,+0.28284,0.2)	XVII XVIII
4	(+0.2,-0.28284,0.2)	XVII XVIII
5	(+0.2,+0.28284,0.2)	XVIII
6	(-0.2,-0.28284,0.2)	XVIII

The results of case XV through XVIII are presented in Figure 5.8.

Several conclusions can be drawn by comparing Figures 5.7 and 5.8. First, note that the symmetrically distributed secondary sources provided better performance

in the low frequency regime. The larger attenuation produced by the symmetric distribution of secondary sources is not surprising because at the lower frequencies, the noise source is small relative to a wavelength. Hence, the noise source is nondirectional and will produce a spherically symmetric pressure distribution. However, at the higher frequencies (around  $ka=1.4$  for example) where the noise source has some directivity, the asymmetric distribution of secondary sources provided slightly better performance than the symmetric distribution. Also note that the additional symmetrically placed secondary sources did not improve the performance at the local maximum at  $ka=1.4$ . However, a slight improvement in the performance around  $ka=1.4$  was attained with additional asymmetrically located secondary sources.

### 5.3 Conclusions

In summary, for increased reduction of the total radiated sound power, all secondary sources employed should be located within  $\frac{\lambda}{2}$  of the noise producing mechanism. Additional secondary sources greatly improve attenuation provided that they are located within the  $\frac{\lambda}{2}$  criterion. If the noise source is directional, an improvement in active noise controller performance is attained when the secondary

sources are located about the pressure lobes of the noise source.

The formulation using the IBEM is relatively straightforward. Such a formulation which minimizes sound power could be used in cavities except that reducing power does not necessarily mean that the potential energy in the cavity is reduced. For example, sound power is zero in an enclosure with no absorption, but the potential energy may be high or low. When using the IBEM formulation, care must be taken to avoid the uniqueness problem discussed in section 3.3.1.



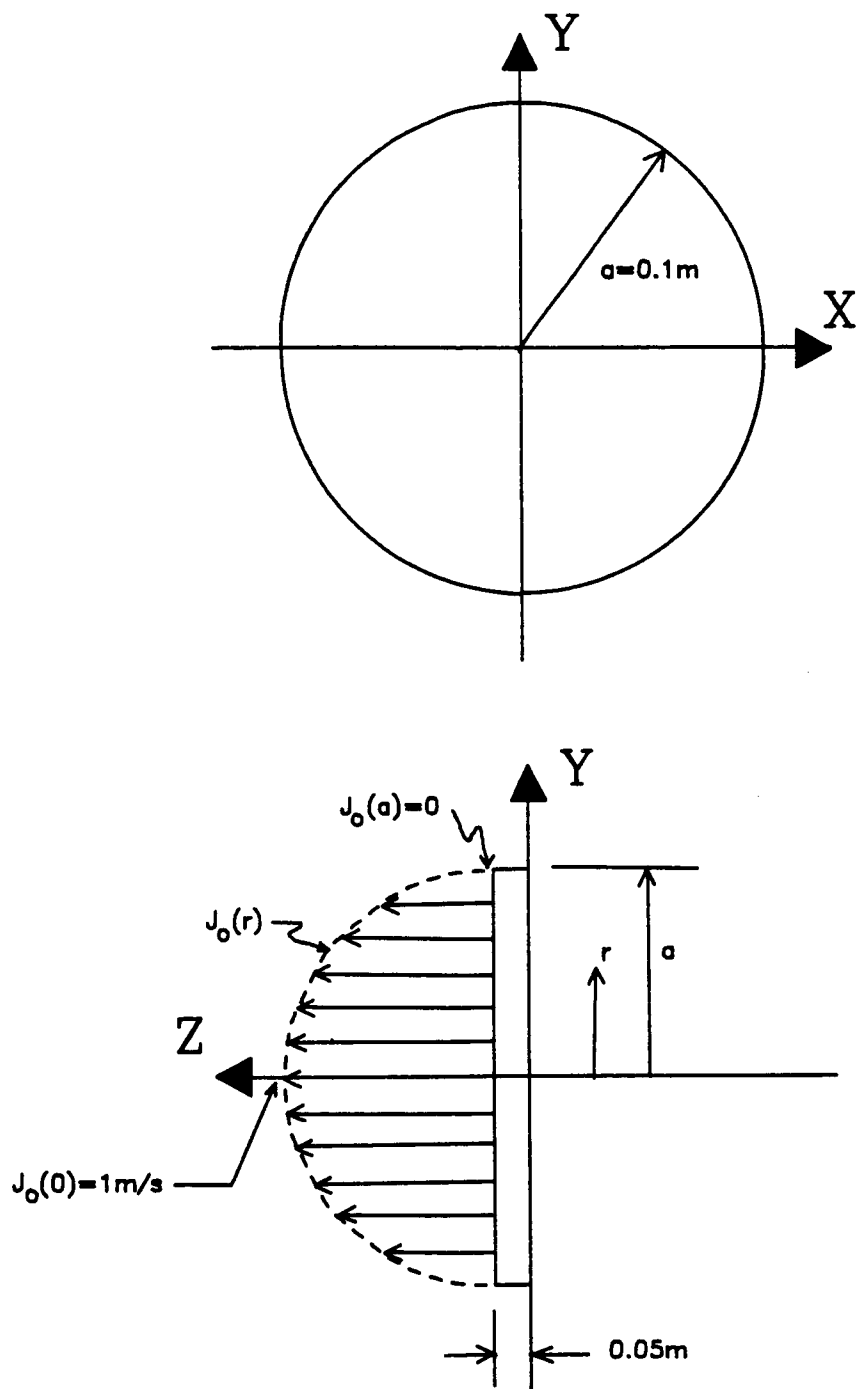


Figure 5.1 - Geometrical Description Of Cylindrical Shell Model

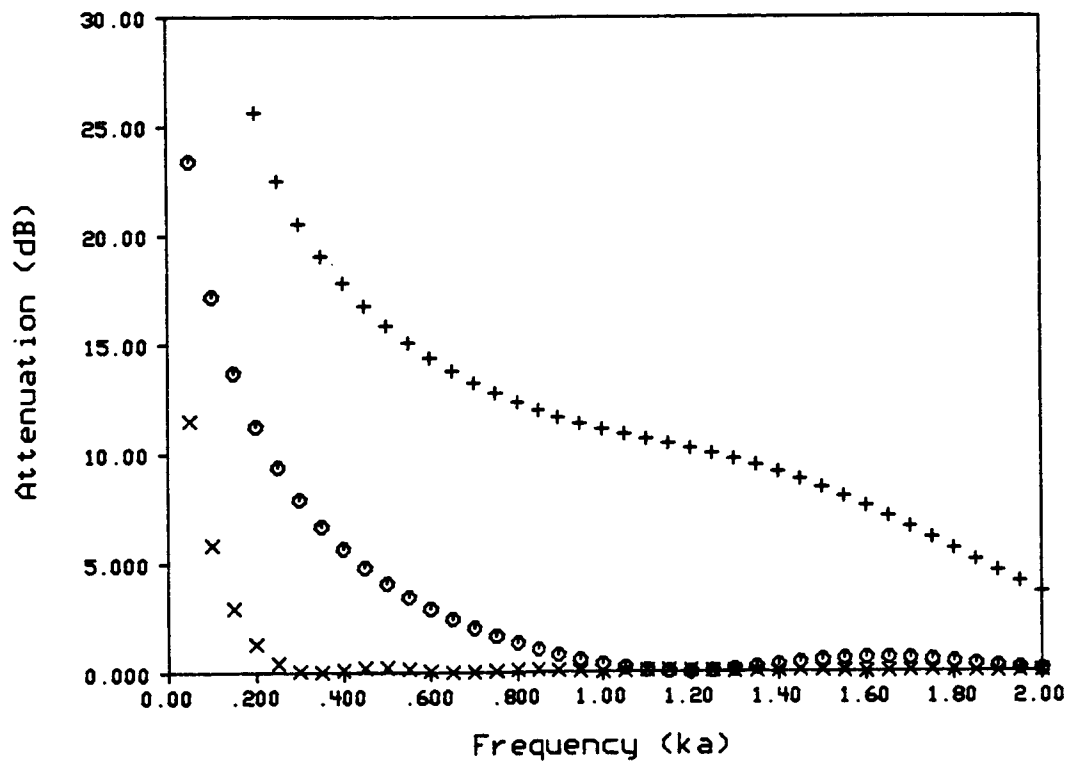


Figure 5.2 - Comparison Of Optimal Controller Performance For Changes In Secondary Source Location (Along Z-axis) About Shell Model ( $a=0.1\text{m}$ ).

- + - Case I ( $l=0.1\text{m}$ )
- o - Case II ( $l=0.3\text{m}$ )
- x - Case III ( $l=1.0\text{m}$ )

C-3

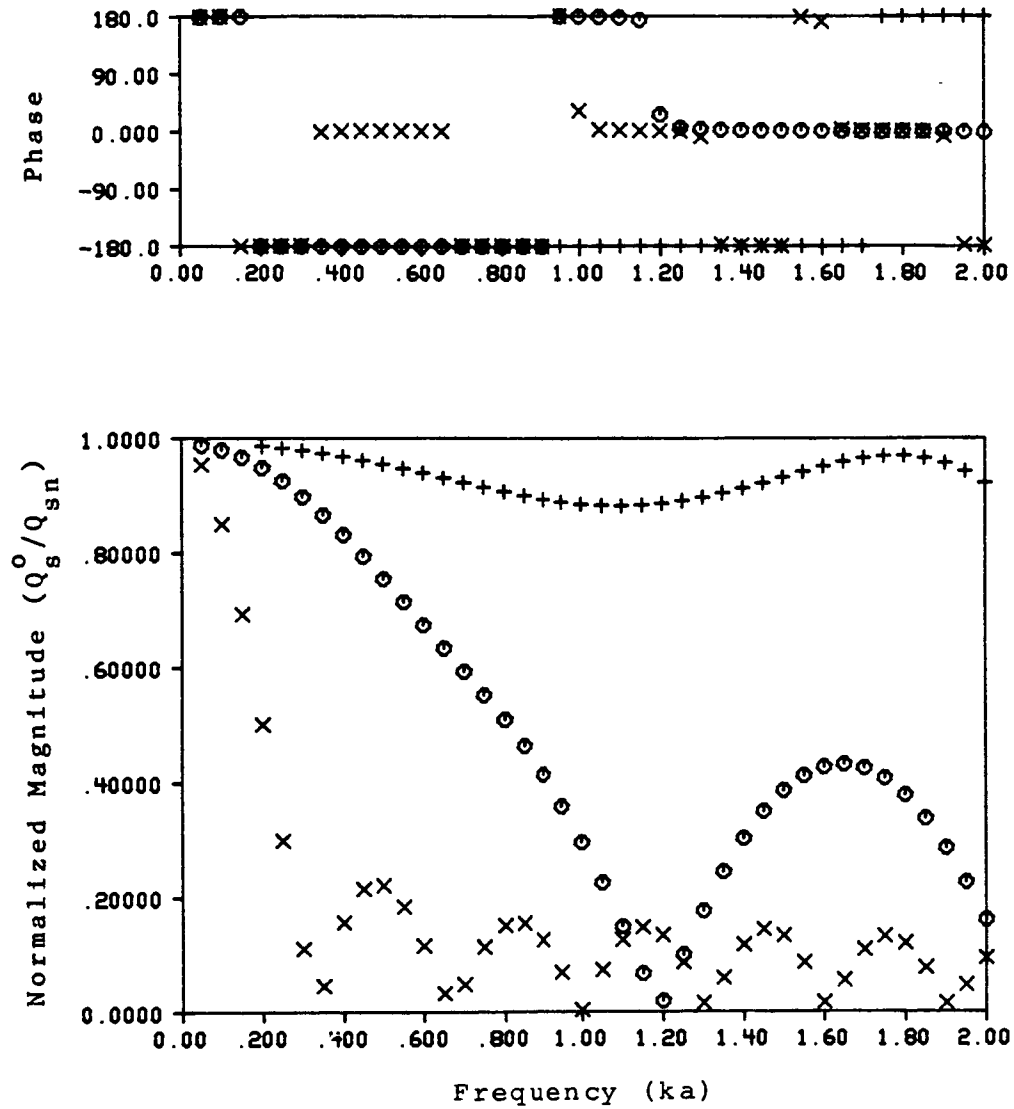


Figure 5.3 - Comparison Of Optimal Controller For Changes In Secondary Source Location (Along Z-axis) About Shell Model ( $a=0.1m$ ).

- + - Case I ( $l=0.1m$ )
- o - Case II ( $l=0.3m$ )
- x - Case III ( $l=1.0m$ )

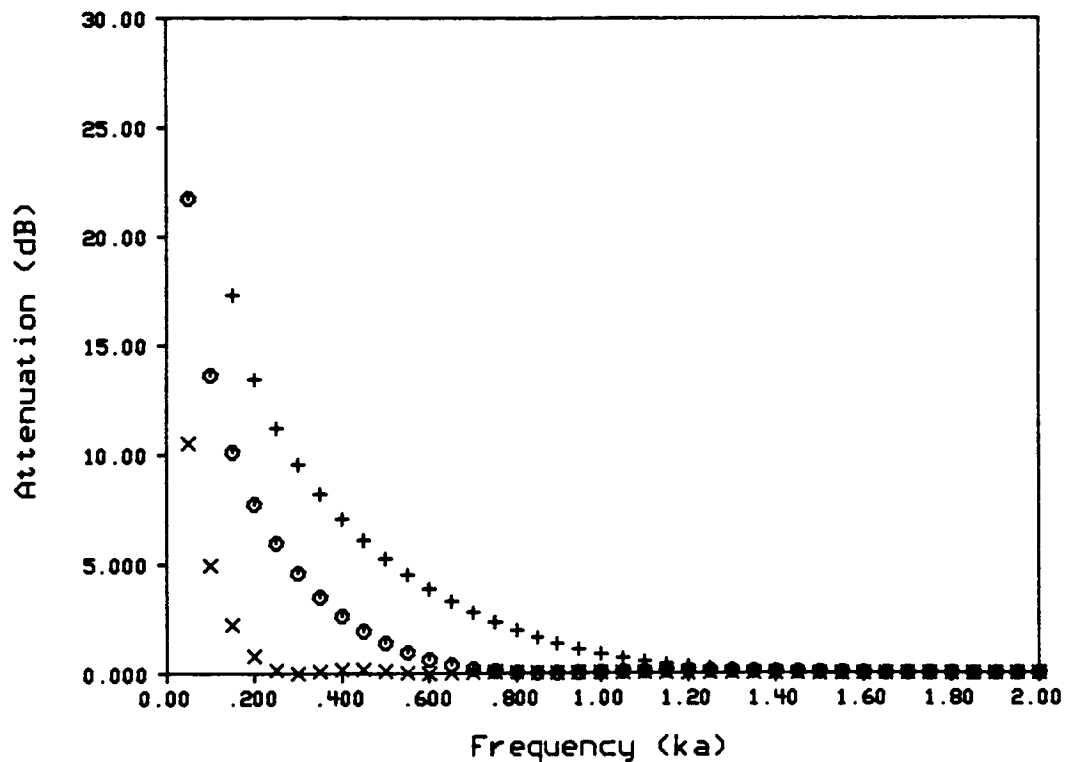


Figure 5.4 - Comparison Of Optimal Controller Performance For Changes In Secondary Source Location (Along X-axis) About Shell Model ( $a=0.1\text{m}$ ).

- + - Case IV ( $l=0.05\text{m}$ )
- o - Case V ( $l=0.25\text{m}$ )
- x - Case VI ( $l=0.95\text{m}$ )

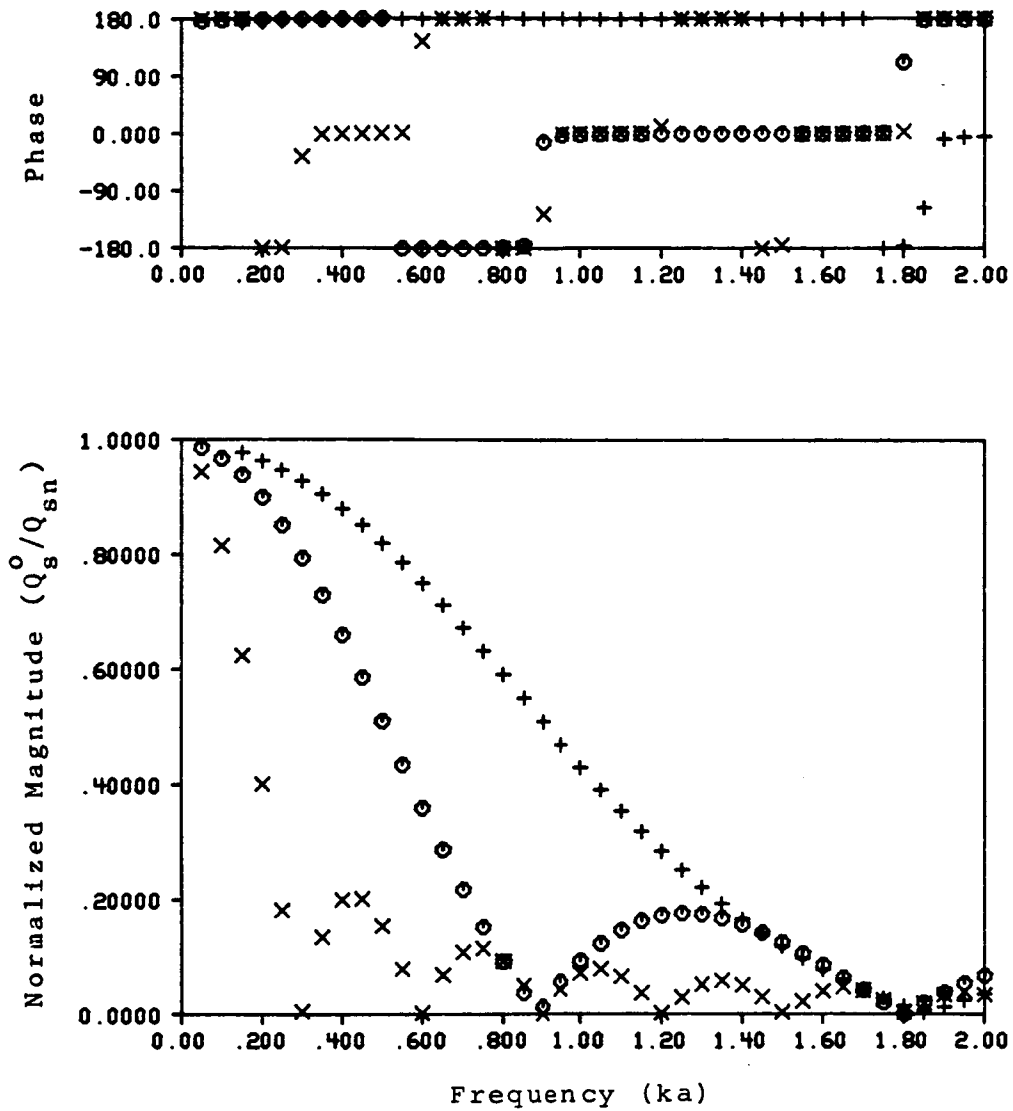


Figure 5.5 - Comparison Of Optimal Controller For Changes In Secondary Source Location (Along X-axis) About Shell Model ( $a=0.1m$ ).

+ - Case IV ( $l=0.05m$ )

o - Case V ( $l=0.25m$ )

x - Case VI ( $l=0.95m$ )

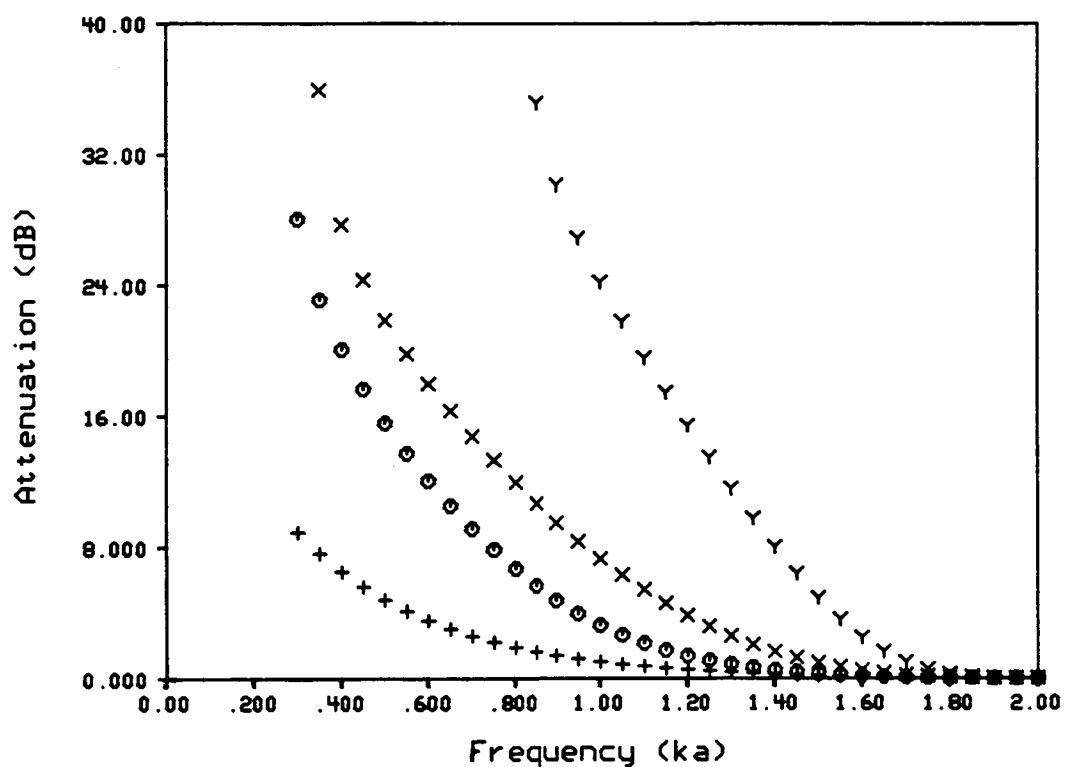


Figure 5.6 - Comparison Of Optimal Controller Performance For Multiple Secondary Sources Symmetrically Located About Pulsating Sphere ( $a=1.0\text{m}$ ).

- + - Case VII (1 Secondary Source)
- o - Case VIII (2 Secondary Sources)
- x - Case IX (4 Secondary Sources)
- Y - Case X (6 Secondary Sources)

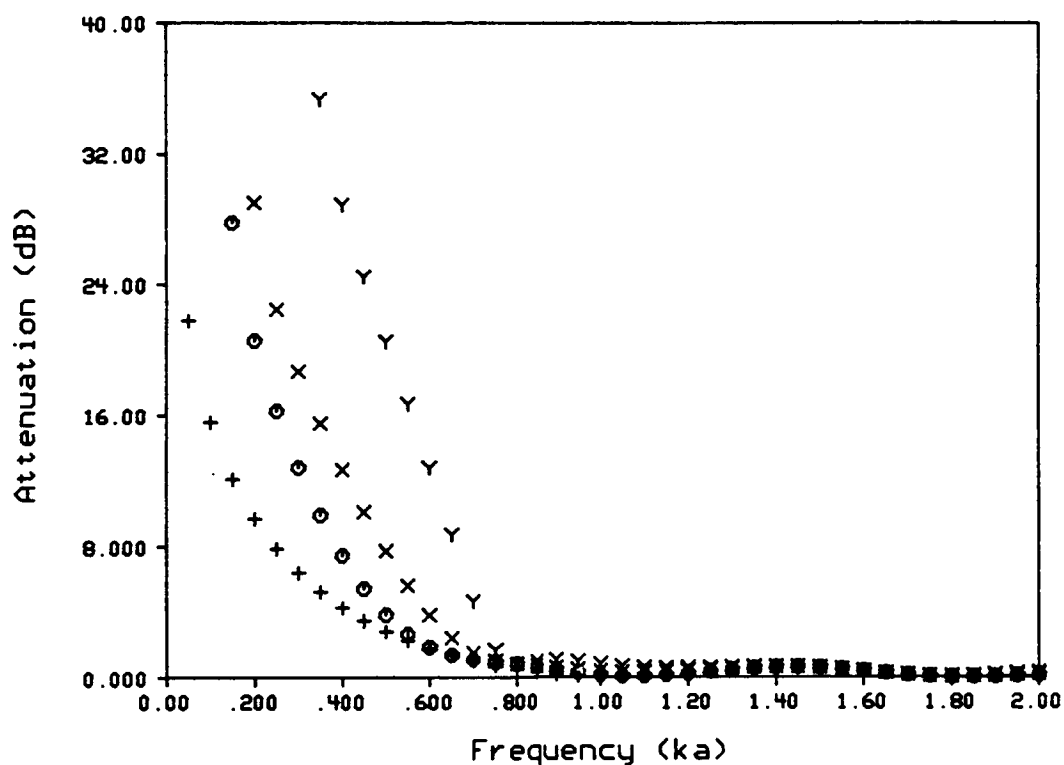


Figure 5.7 - Comparison Of Optimal Controller Performance For Multiple Secondary Sources Symmetrically Located About Shell Model ( $a=0.1m$ ).

- + - Case XI (1 Secondary Source)
- o - Case XII (2 Secondary Sources)
- x - Case XIII (4 Secondary Sources)
- Y - Case XIV (6 Secondary Sources)

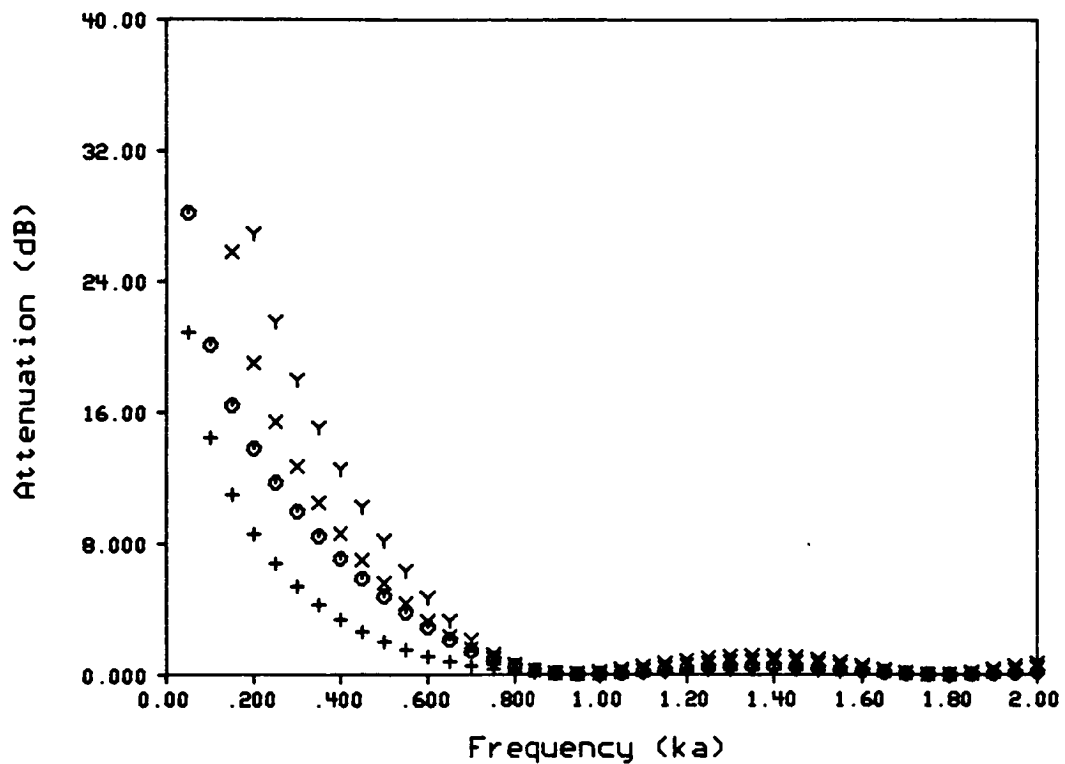


Figure 5.8 - Comparison Of Optimal Controller Performance For Multiple Secondary Sources Asymmetrically Located About Shell Model ( $a=0.1m$ ).

- + - Case XV (1 Secondary Source)
- o - Case XVI (2 Secondary Sources)
- x - Case XVII (4 Secondary Sources)
- Y - Case XVIII (6 Secondary Sources)



## CHAPTER 6

AN OPTIMAL ACTIVE NOISE CONTROLLER FOR ENCLOSED  
SOUND FIELDS WITH INCOMPLETE SYSTEM DESCRIPTION

The active noise controller formulated in chapter 4 assumed that a complete boundary description of the enclosure was known. The formulation provided an optimal transfer function between the noise source strengths and the secondary source strengths. However, in some circumstances, a complete description of the noise sources may not be known. If exact knowledge about the strengths of the noise sources is unobtainable, an array of detector microphones is usually employed to sense the noise field and provide input to the active noise controller. In application, it may not be possible to measure (for input to the controller) all the boundary conditions. In acoustics, it is easier to measure pressure in the field than many boundary conditions. The formulation of chapter 4 is extended in this chapter to include active noise control systems with detector inputs. As was the case for chapter 4, the enclosed sound field is assumed to be time

harmonic, and the boundary geometry is known.

### 6.1 Problem Formulation

A schematic of the overall system formulated in this section is shown in Figure 6.1. The overall system is comprised of five components: the enclosure boundary, point noise (primary) source(s), controllable point (secondary) source(s), observation point(s), and detector location(s). With a couple of exceptions, the first four components listed are as described in section 4.1.1. The first exception is that the strengths of the primary sources are assumed here to be unknown. The second exception is that the enclosure boundary is divided into "active" sections and "passive" sections. Active sections are noise producing whereas passive sections do not contribute to the enclosed sound field. The boundary condition values of the active boundary elements are considered to be unknown.

Detector locations are sites within the enclosure where the sound field is to be measured. For the current formulation, the detectors are assumed to be microphones, and hence, the detected parameter is acoustic pressure. The locations of the detectors must be known.

Given the specifications of the problem, the objective is to determine an optimal transfer function matrix,  $[H^0]$ , such that the acoustic response is minimized at the

observation points. The optimal transfer function matrix is defined as that which produces optimal secondary source strengths given the detector inputs. The optimal secondary source strengths are defined as those which minimize a weighted sum of the magnitudes of the pressures squared at the observation points. Consequently, the control objective function is identical to the one given in equation 4.1:

$$\Pi = \sum_{i=1}^{n_{cp}} |p_i|^2 w_i \quad (6.1)$$

The optimal transfer function is determined by minimizing  $\Pi$  with respect to the secondary source strengths. In the subsequent formulation, capital letters denote matrix quantities.

#### 6.1.1 IBEM Formulation Of The Control Objective Function

If the acoustic pressure at the observation points is written in complex form, the control objective function can be rewritten as

$$\Pi = \mathbf{p}^H \mathbf{W} \mathbf{p} \quad (6.2)$$

where  $[\mathbf{W}]$  is a  $n_{cp} \times n_{cp}$  diagonal matrix with the values of the weighting function on the diagonal, and  $\mathbf{p}$  is a column vector of the pressures at the observation points. The  $\mathbf{H}$

superscript denotes the hermitian transpose.

The pressures at the observation points are given by equation 4.4:

$$\underline{p} = D\underline{\sigma} + E_{p-p}\underline{\phi}_p + E_{s-s}\underline{\phi}_s \quad (6.3)$$

Likewise, the pressures at the detector locations are given by equation 4.4:

$$\underline{p}_d = D'\underline{\sigma} + E'_{p-p}\underline{\phi}_p + E'_{s-s}\underline{\phi}_s \quad (6.4)$$

From equation 4.7,  $\underline{\sigma}$  is found as

$$\underline{\sigma} = A^{-1}(\underline{\alpha} - C_{p-p}\underline{\phi}_p - C_{s-s}\underline{\phi}_s) \quad (6.5)$$

Because the enclosure boundary is composed of an active portion and a passive portion,  $\underline{\alpha}$  and  $[A]^{-1}$  are partitioned as

$$\underline{\sigma} = [A_a^{-1} \mid A_p^{-1}] \begin{bmatrix} \underline{\alpha}_a \\ - \\ \underline{\alpha}_p \end{bmatrix} - A^{-1}C_{p-p}\underline{\phi}_p - A^{-1}C_{s-s}\underline{\phi}_s \quad (6.6)$$

A passive boundary condition is defined as that for which  $\alpha_i = 0$ . The three boundary conditions for which  $\alpha_i = 0$  are rigid wall ( $u=0$ ), pressure release ( $p=0$ ), and specific acoustic impedance. All other boundary conditions are classified as active. Employing the fact that  $\underline{\alpha}_p = \underline{0}$ , equation 6.6 can be rewritten as

$$\underline{\sigma} = A_a^{-1} \underline{\alpha}_a - A^{-1} C_p \underline{\phi}_p - A^{-1} C_s \underline{\phi}_s \quad (6.7)$$

Combining the unknown primary source strengths with the unknown active boundary condition values gives

$$\underline{\sigma} = [A_a^{-1} \mid -A^{-1} C_p] \begin{bmatrix} \underline{\alpha}_a \\ \underline{\phi}_p \end{bmatrix} - A^{-1} C_s \underline{\phi}_s \quad (6.8)$$

For notational simplicity, equation 6.8 is rewritten as

$$\underline{\sigma} = F \underline{\eta} - A^{-1} C_s \underline{\phi}_s \quad (6.9)$$

where

$$F = [A_a^{-1} \mid -A^{-1} C_p] \quad (6.10a)$$

and

$$\underline{\eta} = \begin{bmatrix} \underline{\alpha}_a \\ \underline{\phi}_p \end{bmatrix} \quad (6.10b)$$

Through a similar analysis, equations 6.3 and 6.4 can be rewritten as

$$\underline{p} = (DF + F') \underline{\eta} + (E_s - DA^{-1} C_s) \underline{\phi}_s \quad (6.11)$$

and

$$\underline{p}_d = (D'F + F'') \underline{\eta} + (E'_s - D'A^{-1} C_s) \underline{\phi}_s \quad (6.12)$$

where

$$F' = [0 \mid E_p] \quad (6.13a)$$

$$F'' = [0 \mid E_p] \quad (6.13b)$$

Using equation 6.12, the unknown noise source values are determined from the pressures at the detector locations as

$$\underline{n} = (D'F + F'')^{-1} [p_d + (D'A^{-1}C_s - E_s')\underline{\psi}_s] \quad (6.14)$$

Implicit in equation 6.14 is the stipulation that the number of measurement locations must equal the sum total number of active elements and primary sources. This stipulation is necessary so that the matrix inverted in equation 6.14 is square. However, the problem can be overdetermined by employing more measurement points than unknown noise sources. Then to solve equation 6.12 for the unknown noise source values, a least squares technique could be used. Using a least squares method, the unknown noise sources are found as

$$\underline{n} = (T_{nd}^H T_{nd})^{-1} T_{nd} [p_d + (D'A^{-1}C_s - E_s')\underline{\psi}_s] \quad (6.15)$$

where  $T_{nd} = D'F + F''$ . For the subsequent development, equation 6.14 will be used although equation 6.15 could have been used instead.

The unknown noise source values are eliminated from equation 6.11 by substituting equation 6.14 into equation 6.11. The resulting expression is

$$\underline{p} = R\underline{p}_d + T\underline{\phi}_s \quad (6.16)$$

where

$$R = (DF + F')(D'F + F')^{-1} \quad (6.17)$$

$$T = R(D'A^{-1}C_s - E_s) + E_s - DA^{-1}C_s \quad (6.18)$$

By substituting equation 6.16 into equation 6.2, the control objective function is obtained:

$$\Pi = \underline{\phi}_s^H T^H W T \underline{\phi}_s + \underline{p}_d^H R^H W T \underline{\phi}_s + \underline{\phi}_s^H T^H W R \underline{p}_d + \underline{p}_d^H R^H W R \underline{p}_d \quad (6.19)$$

The uncontrolled, summed acoustic response at the observation points is given by  $\underline{p}_d^H R^H W R \underline{p}_d$ .

#### 6.1.2 An Optimal Controller

As was the case for the control objective function of chapter 4, the control objective function given in equation 6.19 is a real, positive definite, quadratic function of the secondary source strengths. Therefore, there is a unique combination of secondary source strengths which minimize the control objective function. Consequently, there is a unique transfer function matrix between the pressures at the detectors and the secondary source strengths such that the control objective function is minimized. Utilizing equation 4.12, the minimum value of the control objective function is found to occur when

$$T^H WT \underline{\phi}_s + T^H WR \underline{p}_d = 0 \quad (6.20)$$

Solving for the unknown secondary source strengths which minimize  $\Pi$  gives

$$\underline{\phi}_s^o = -[T^H WT]^{-1} T^H WR \underline{p}_d \quad (6.21)$$

Converting  $\underline{\phi}_s^o$  to volume velocity units using

$$\underline{q}_s^o = \frac{4\pi}{jk\rho_o c} \underline{\phi}_s^o \quad (6.22)$$

gives

$$\underline{q}_s^o = j \frac{4\pi}{k\rho_o c} [T^H WT]^{-1} T^H WR \underline{p}_d \quad (6.23)$$

Therefore, the optimal transfer function matrix between the pressures at the detectors and the volume velocity secondary source strengths is

$$H^o = j \frac{4\pi}{k\rho_o c} [T^H WT]^{-1} T^H WR \quad (6.24)$$

### 6.1.3 Stability

A generally recognized problem of active noise controllers is the instability caused by the positive acoustical feedback between the canceling sources and the detector microphones. Insight into the stability of the active noise control system formulated in this chapter is obtained by rewriting equations 6.11 and 6.12 as



$$p = T_{no}\eta + T_{so}q_s \quad (6.25)$$

and

$$p_d = T_{nd}\eta + T_{sd}q_s \quad (6.26)$$

where

$$T_{no} = DF + F' \quad (6.27a)$$

$$T_{so} = j\frac{k\rho_o c}{4\pi} (E_s - DA^{-1}C_s) \quad (6.27b)$$

$$T_{nd} = D'F + F'' \quad (6.27c)$$

$$T_{sd} = j\frac{k\rho_o c}{4\pi} (E_s' - D'A^{-1}C_s) \quad (6.27d)$$

Equations 6.23, 6.25, and 6.26 are represented in block diagram form in Figure 6.2. Note the presence of the positive acoustic feedback loop between the secondary sources and the detectors.

The characteristic equation, which is analyzed to determine stability, of the system in Figure 6.2 is given by

$$I - T_{sd}H^o = [0] \quad (6.28)$$

where  $[I]$  is the identity matrix, and  $[0]$  is the null matrix. A stability matrix,  $[G]$ , is defined as

$$G = -T_{sd}H^0 \quad (6.29)$$

The stability of the active noise control system can be determined by analyzing the characteristic equation

$$I + G = [0] \quad (6.30)$$

using a frequency domain technique such as a Bode diagram or the Nyquist criterion. For the case studies to be presented, Bode diagrams were used to determine stability. Assuming  $G$  is a scalar transfer function (for simplicity), stability is determined by examining the 0 dB and  $-180^\circ$  crossings. If the gain of  $G$  (in dB) is greater than zero when the phase crosses the  $-180^\circ$  axis, the system is unstable.

#### 6.1.4 Observability And Controllability

Observability is defined for the purposes of this research as the ability of the detectors to deduce the noise field. The influence of the noise sources on the pressure at the detector locations is given by  $[T]_{nd}$ . From equation 6.14, it can be seen that it is necessary for  $[T]_{nd}$  to be invertible. If  $[T]_{nd}$  is square (as required in equation 6.14), then the rank of  $[T]_{nd}$  must equal the number of unknown noise sources (or detectors) for the inverse of  $[T]_{nd}$  to exist. If the problem is overdetermined, then the rank of  $T_{nd}^H T_{nd}$  in equation 6.15

must be equal to the number of unknown noise sources for  $[T_{nd}^H T_{nd}]^{-1}$  to exist. Thus, the system is completely observable if the rank of  $[T]_{nd}$  (or  $T_{nd}^H T_{nd}$ ) equals the number of unknown noise sources.

Controllability is defined for the purposes of this research as the ability of the secondary sources to influence the acoustic response at the observation points. Controllability at the  $i^{th}$  observation point is determined by examining the inner product of the  $i^{th}$  row of  $[T]_{so}$  with  $q_s^0$ . If the inner product is zero, the pressure at the  $i^{th}$  observation point is uncontrollable with the current arrangement of secondary sources. Thus, to determine controllability,  $q_s^0$  must first be computed from equation 6.23.

## 6.2 Case Study Results

Although the formulation of the previous section was generalized for a multi-parameter system, all case studies presented in this section consider a scalar system: one unknown noise source, one detector location, one observation point, and one secondary source. Therefore,  $H^0$  and  $G$  are scalar transfer functions. All the case studies presented in this section were observable and controllable. The value of  $\rho_{oc}$  for all cases presented is 415.0 Pa's/m.

To obtain the impulse response of the system, the optimal frequency domain solution is transformed to the time domain using an inverse Fourier transform. In the frequency domain, the optimal secondary source strength is given by

$$Q_s^0(\omega) = H^0(\omega)P_d(\omega) \quad (6.31)$$

To obtain the time domain solution of  $q_s^0(t)$ , a convolution is used [58]:

$$q_s^0(t) = \int_0^t h^0(t-\tau)p_d(\tau) d\tau \quad (6.32)$$

where  $h^0(t)$  is given by the inverse Fourier transform of the controller transfer function [59]:

$$h^0(t) = \frac{1}{2\pi} \int_{-\infty}^{\infty} H^0(\omega)e^{j\omega t} d\omega \quad (6.33)$$

If  $p_d(\tau)$  is an impulse function of unit amplitude, then the time domain solution of the optimal secondary source strength is given by

$$q_s^0(t) = h^0(t) \quad (6.34)$$

Therefore, the impulse response of the system is given by the inverse Fourier transform of  $H^0(\omega)$ . The inverse Fourier transform of  $H^0(\omega)$  was calculated using an inverse fast Fourier transform (IFFT) procedure given by Ramirez [60]

$$h^0(n) = \frac{1}{N} \sum_{k=0}^{N-1} H^0(k) e^{j2\pi kn/N} \quad (6.35)$$

where  $N$  is the total number of data samples.

The system analyzed in case 1 is depicted in Figure 6.3. All of the enclosure walls are rigid. The enclosed sound field is excited by the primary source of unknown strength. The conjugate symmetric expansion of the frequency domain solution of  $H^0(\omega)$  and the impulse response function of the system for case 1 are shown in Figure 6.4. Note that the impulse response function of the system is non-convergent, and the system appears to be unstable. A Bode diagram representation of  $G$  is presented in Figure 6.5. Careful examination of the Bode diagram reveals that the system has a negative gain margin, and hence, the system is unstable.

Because the enclosure was discretized using 80 elements, the accuracy of the results for  $H^0(\omega)$  degrade for  $k$  greater than approximately 6.0. Therefore, the frequency domain spectrum of  $H^0(\omega)$  was smoothly diminished to zero after  $k=5.0$ . To obtain higher resolution in the time domain, the zero-valued frequency data for  $H^0(\omega)$  was not removed from the frequency spectrum. The function used to diminish the frequency domain solution of  $H^0(\omega)$  is given by

$$f_z(\omega) = \frac{1}{2} [1 + \cos(\frac{\omega-1715}{171.5}\pi)] \quad (6.36)$$

for  $1715.0 \leq \omega \leq 1886.5$ . In addition,  $f_z(\omega)=0$  for  $\omega > 1886.5$  rad/sec, and  $f_z(\omega)=1$  for  $\omega < 1715.0$  rad/sec.

Because there were no energy absorbing mechanisms in the system of case i, it is not surprising that the system was unstable. The stability of the system should improve with the addition of an energy absorbing mechanism. Case ii is identical to case i except that the wall at  $Z=0$  was given an infinite termination impedance boundary condition ( $z=\rho_0 c$ ). The results of case ii are shown in Figures 6.6 and 6.7. Note that the impulse response function converged, and the Bode diagram for case ii correspondingly predicts a stable system. However, there appears to be a low frequency noncausal component.

The low frequency noncausal component of the impulse response function for case ii results from the large peak in the imaginary part of  $H^0(\omega)$  at 34.3 rad/sec. Because the accuracy of the IBEM is poor for very low frequency analysis of cavity problems and such very low frequencies are below the audible range, the frequency domain spectrum of  $H^0(\omega)$  was multiplied by a "window" such that the low frequency results for  $H^0(\omega)$  were diminished in value. Furthermore, such a windowing of  $H^0(\omega)$  is reasonable because active noise controllers are unable to operate at very low frequencies due to hardware limitations.

The window which was chosen was obtained from the definition of a Hanning window [61]. The window as a function of frequency is given by

$$W(n) = \frac{1}{2} [1 - \cos(\frac{2\pi n}{N-1})] \quad ; \quad 0 \leq n \leq \frac{N-1}{2} \quad (6.37)$$

where

$$n = \frac{\omega}{\Delta\omega} \quad (6.38a)$$

$$N = 2 \frac{\omega_h}{\Delta\omega} + 1 \quad (6.38b)$$

The quantity  $\Delta\omega$  is the discrete frequency step size, and  $\omega_h$  is the frequency at which  $W(n)=1$ . For frequencies greater than  $\omega_h$  ( $n > \frac{N-1}{2}$ ),  $W(n)=0$ . The frequency domain spectrum of  $H^0(\omega)$  was windowed before it was conjugate symmetrically expanded.

The conjugate symmetric expansion of  $H^0(\omega)W(\omega)$  and the corresponding IFFT for case ii are shown in Figure 6.8. For the results shown in Figure 6.8, the value of  $\omega_h$  was 171.5 rad/sec (27 Hz). There is still a small low frequency component apparent in Figure 6.8. By increasing the window length, the low frequency component is diminished further as shown in Figure 6.9. For the results shown in Figure 6.9,  $\omega_h=514.5$  rad/sec (82 Hz).

Case iii provided insight into a free field analysis of an active noise control system. Case iii is identical

to case i except that the enclosure boundary was completely removed from the problem. The results of case iii are displayed in Figures 6.10 and 6.11. The Bode diagram in Figure 6.11 predicts an extremely stable system. The spike in the system impulse response function occurs at  $t=3.55\text{msec}$ . The discrete time step of the data in Figure 6.10b is  $0.71\text{msec}$ . If an impulse is detected at  $t=0$ , it will arrive at the observation point at

$$t = \frac{1.3\text{m}}{343.0\text{m/sec}} = 3.79 \text{ msec}$$

Because the secondary source is  $0.1\text{m}$  away from the observation point, it has to emit an anti-phase pulse at

$$t = \frac{0.1\text{m}}{343.0\text{m/sec}} = 0.29 \text{ msec}$$

before the detected pulse arrives at the observation point. Therefore, the secondary source should emit the canceling pulse at  $t=3.79\text{msec} - 0.29\text{msec} = 3.50\text{msec}$ . Thus, there is good agreement between the expected solution ( $t=3.50\text{msec}$ ) and the numerically generated solution ( $t=3.55\text{msec}$ ).

As was the situation for case ii, the impulse response function contains a very low frequency noncausal component. However, the system analyzed in case iii should be causal. The low frequency noncausal component is caused by the fact that in the low frequency limit, the imaginary part of  $H^0(\omega)$  approaches infinity. The imaginary part of  $H^0(\omega)$



approaches infinity because the pressure at the detector is approaching zero in the low frequency limit while  $Q_s^0(\omega)$  remains finite and nonzero. As was done for case ii, the low frequency noncausal component can be diminished by using the "Hanning" window. The result of  $H^0(\omega)W(\omega)$  for  $\omega_h = 171.5$  rad/sec and the corresponding IFFT are shown in Figure 6.12. As the window length is increased, the impulse response function approaches the expected solution of a single impulse at  $t = 3.50$  msec.

### 6.3 Conclusions

The formulation presented in this chapter demonstrates that the IBEM is capable of providing insight into such critical issues as stability, observability, and controllability. Although the implications of observability and controllability were not investigated in the case studies presented, the possibility of doing so is provided with the formulation and is relatively straightforward. The case studies presented demonstrated the importance of damping in the system to help ensure stability. It was also found that low frequency noncausal components of the impulse response function can be diminished by windowing the corresponding frequency domain spectrum.

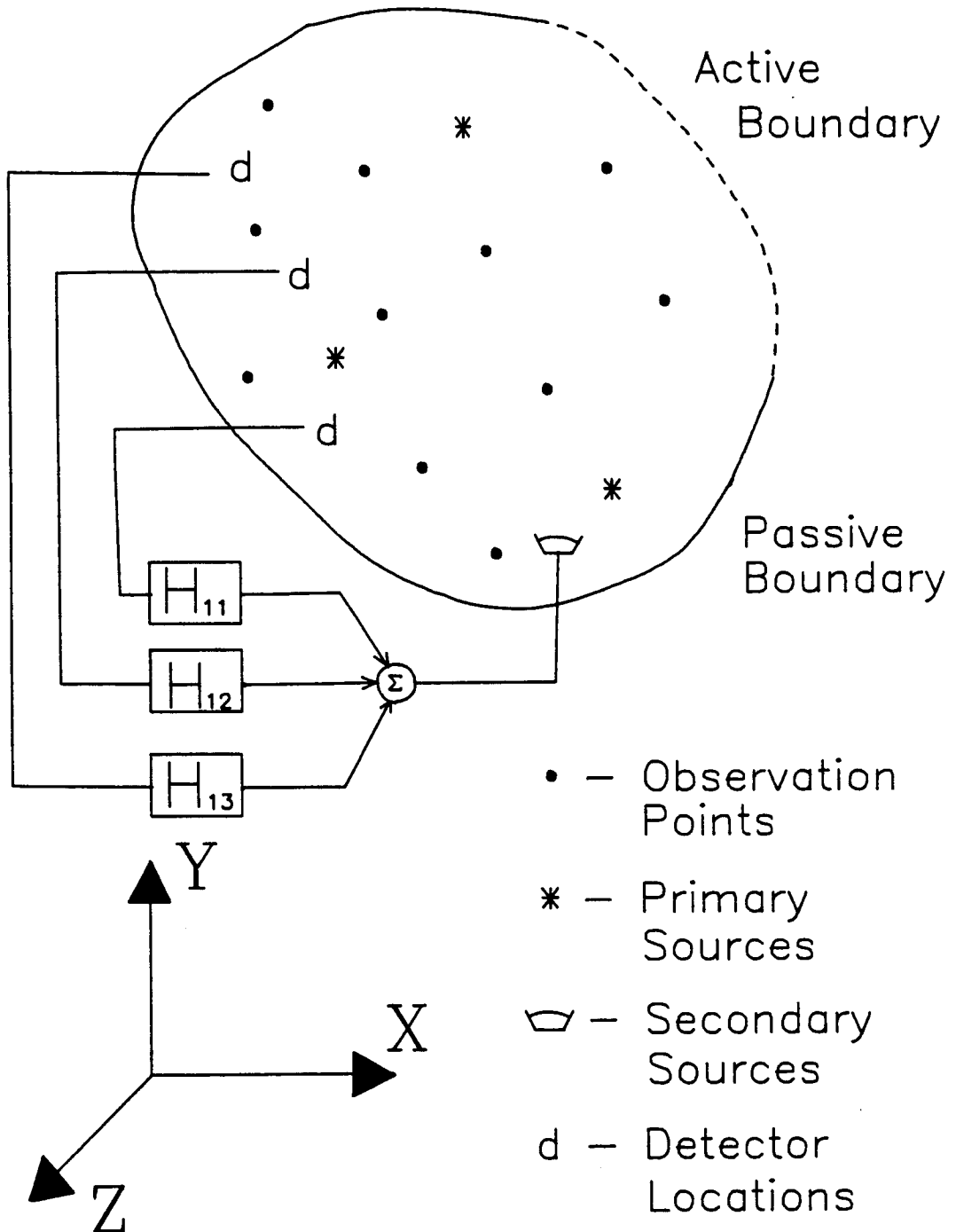


Figure 6.1 - System Schematic For The Active Control Of Sound Fields With An Incomplete System Description

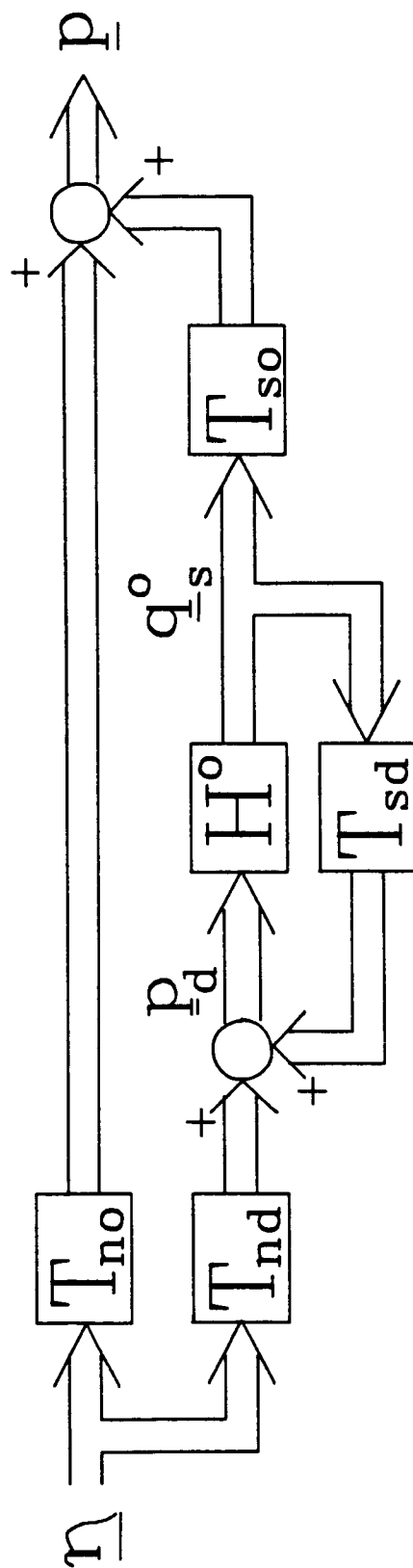
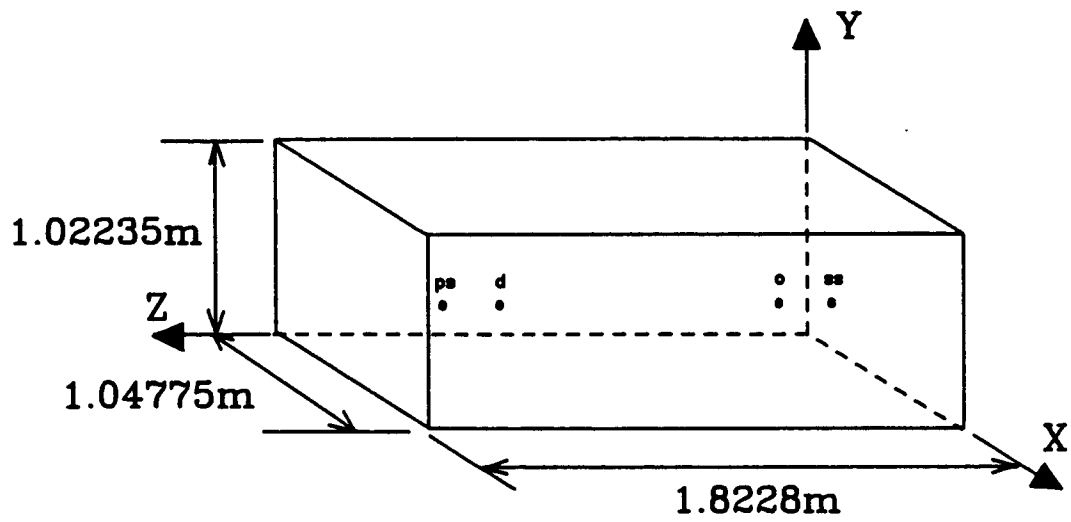


Figure 6.2 - Block Diagram Representation Of The Active Noise Control System



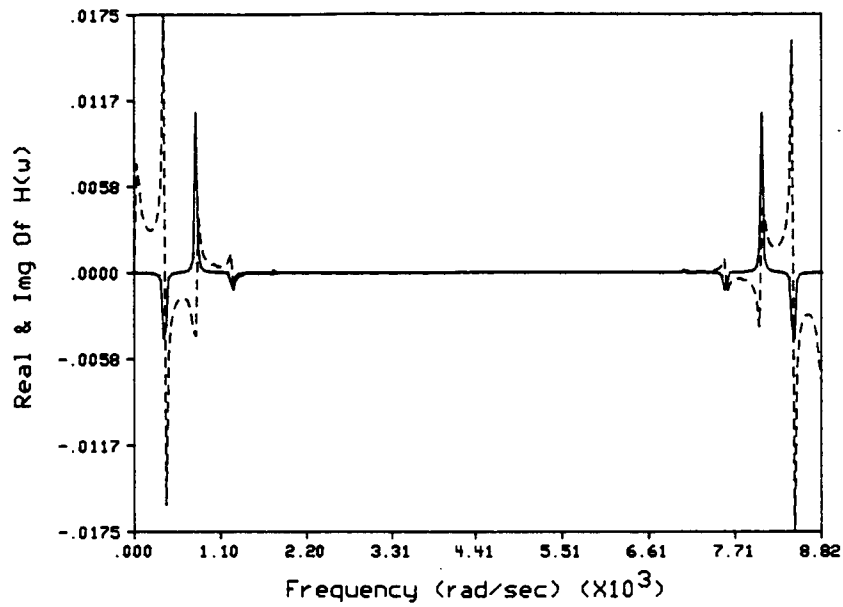
ps – Primary Source: (.5m,.5m,1.7m)

d – Detector: (.5m,.5m,1.6m)

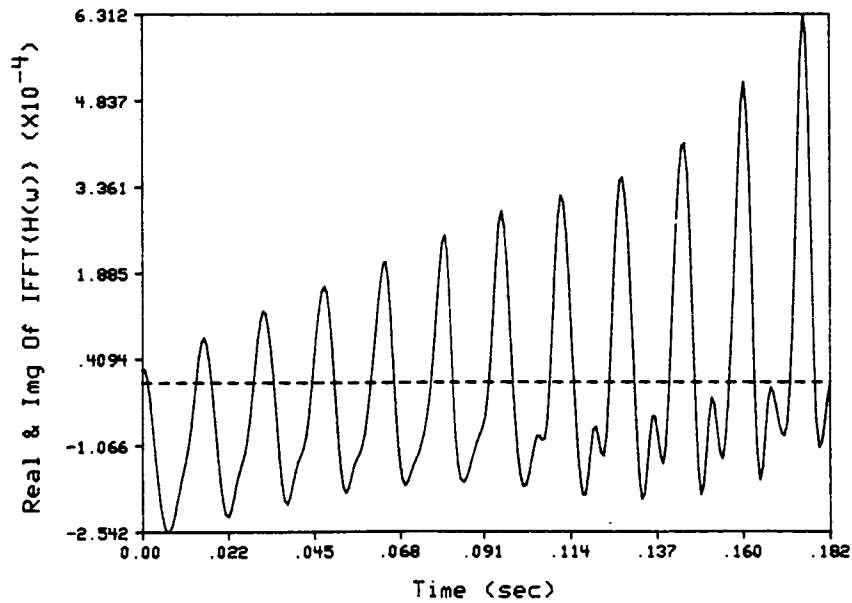
o – Observation: (.5m,.5m,.3m)

ss – Secondary Source: (.5m,.5m,.2m)

Figure 6.3 – Schematic Of The System For Case 1



(a)



(b)

Figure 6.4 - Real And Imaginary Components Of (a)  $H^0(\omega)$  And  
(b) The Impulse Response Function For Case i.

— Real Component  
- - - Imaginary Component

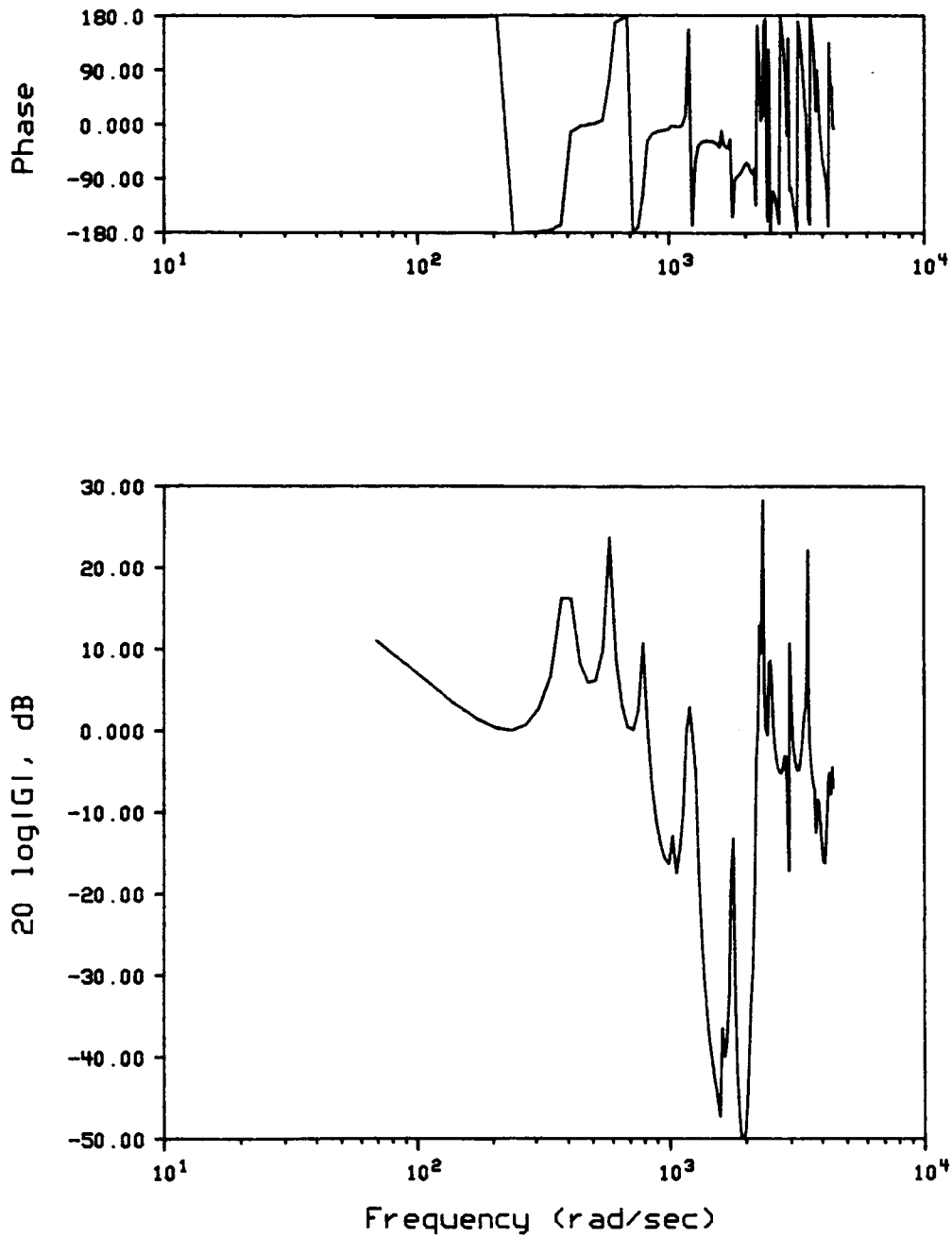
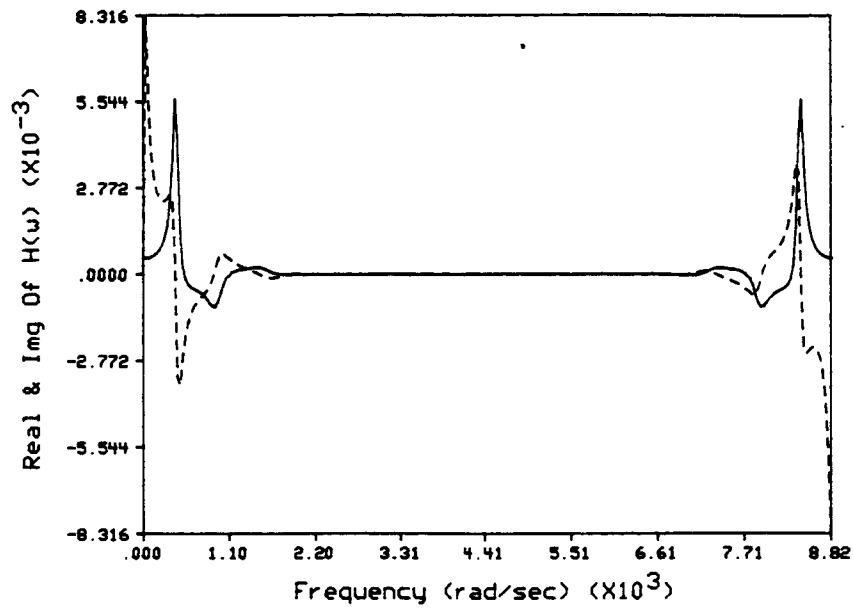
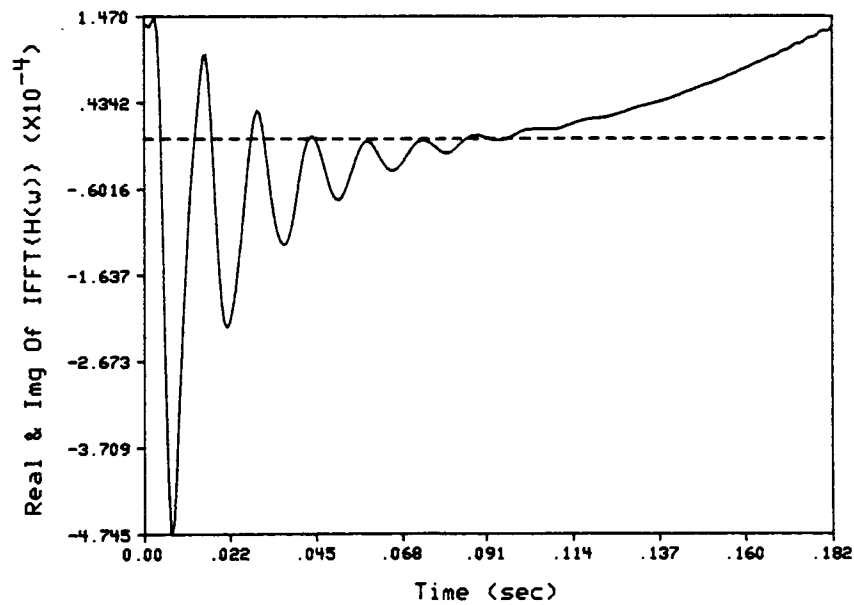


Figure 6.5 - Bode Diagram For Case 1



(a)



(b)

Figure 6.6 - Real And Imaginary Components Of (a)  $H^0(\omega)$  And  
 (b) The Impulse Response Function For Case ii.  
 ——— Real Component  
 - - - Imaginary Component

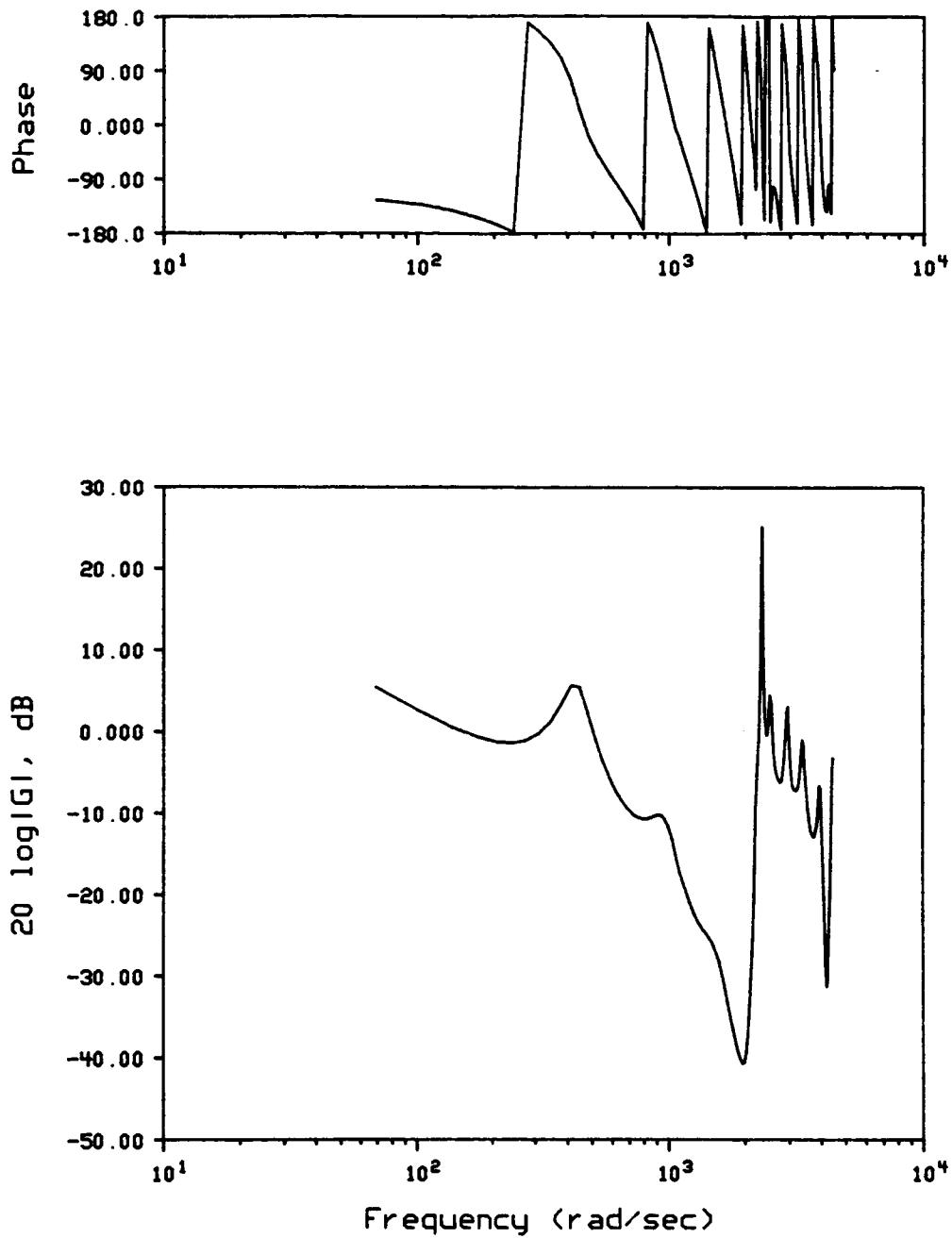
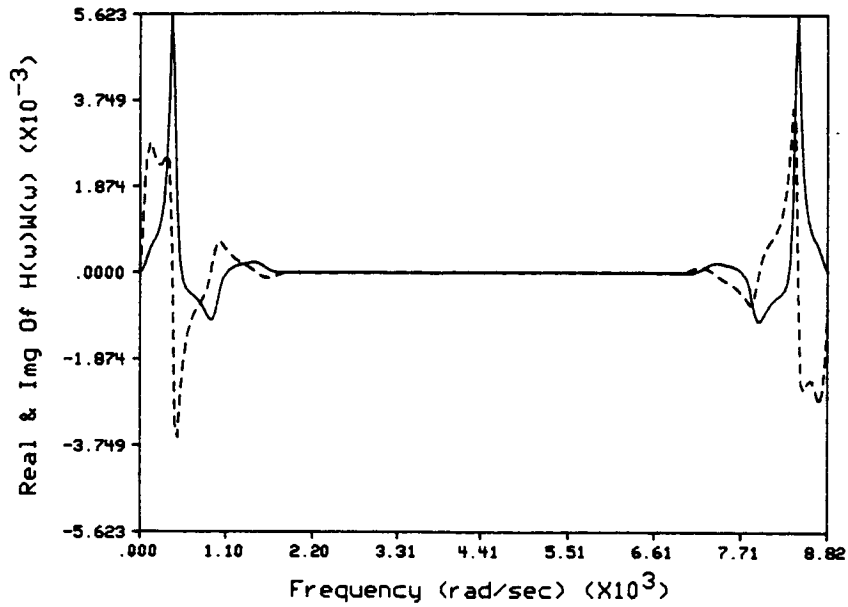
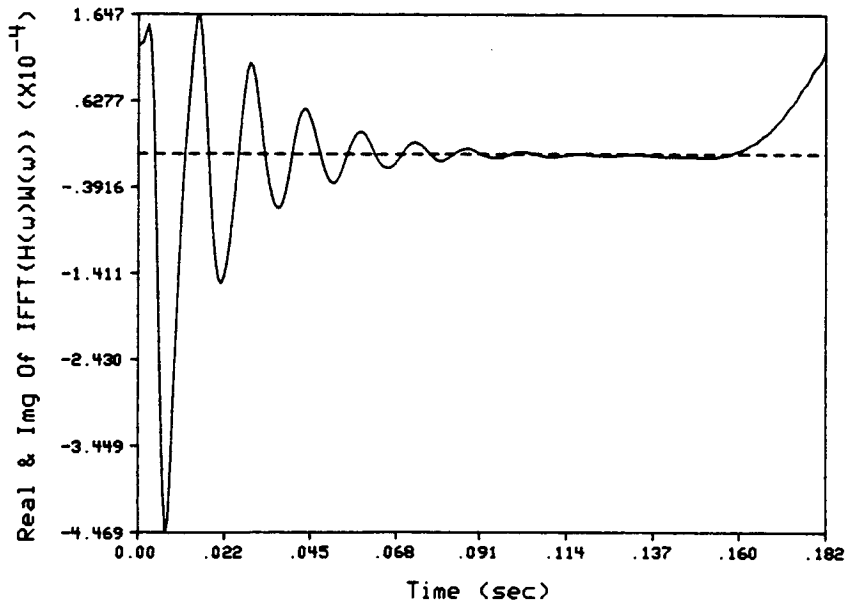


Figure 6.7 - Bode Diagram For Case 11





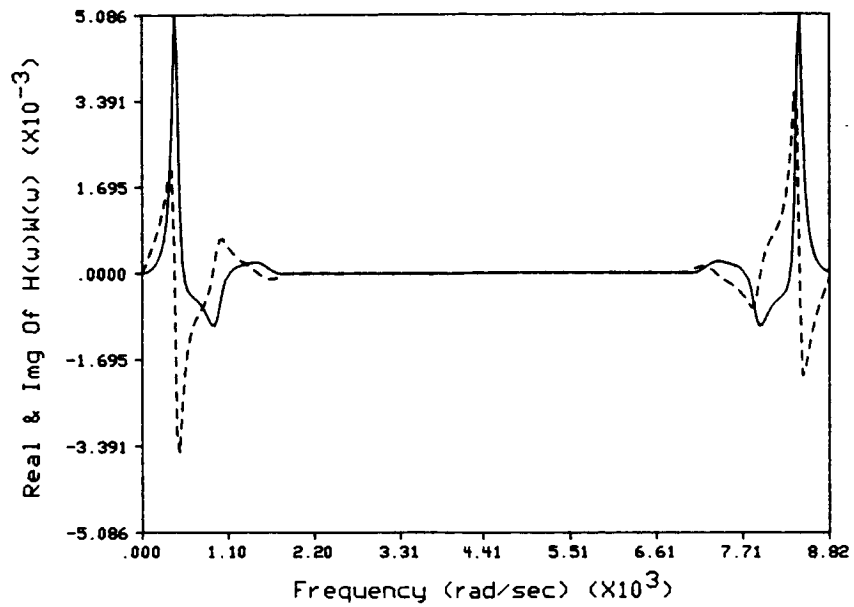
(a)



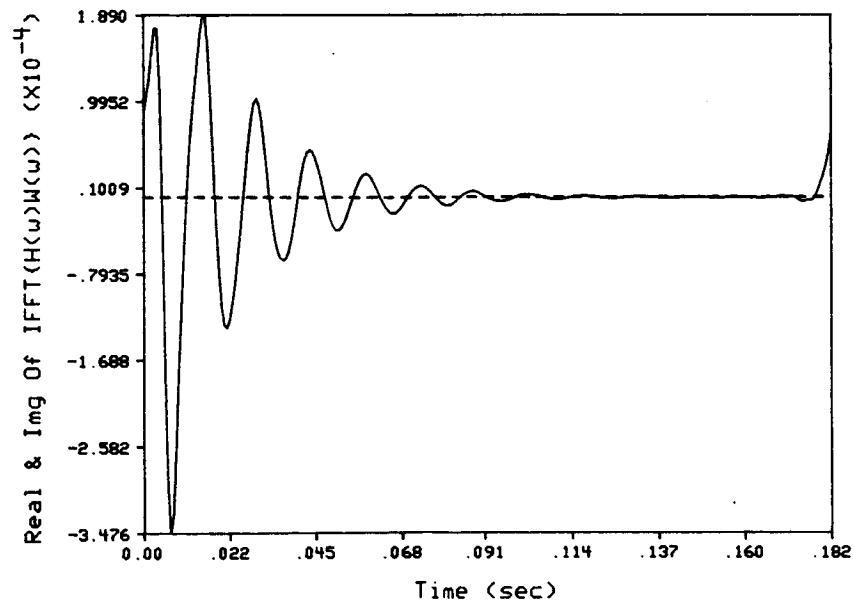
(b)

Figure 6.8 - Real And Imaginary Components Of (a)  $H^0(\omega)W(\omega)$  For  $\omega = 171.5$  rad/sec And (b) The Corresponding IFFT For Case ii.

— Real Component  
 - - - Imaginary Component



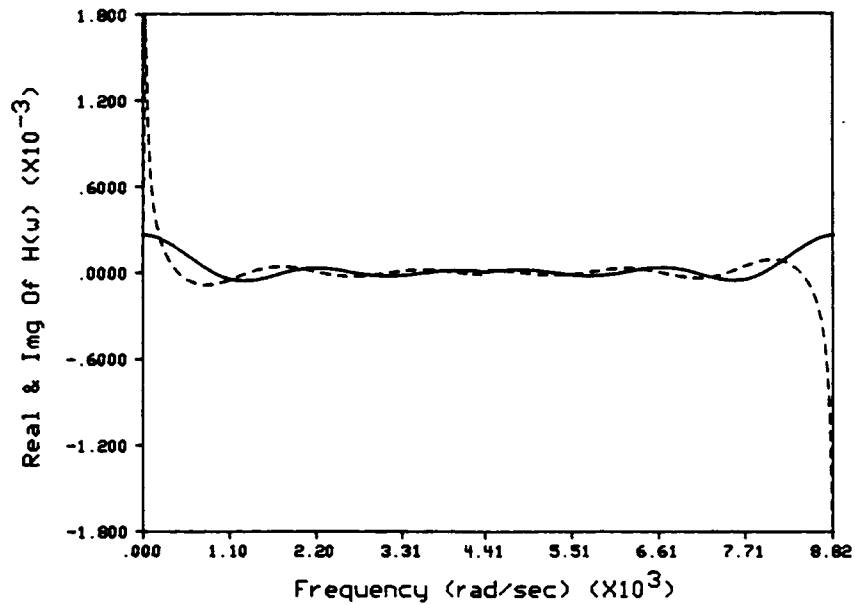
(a)



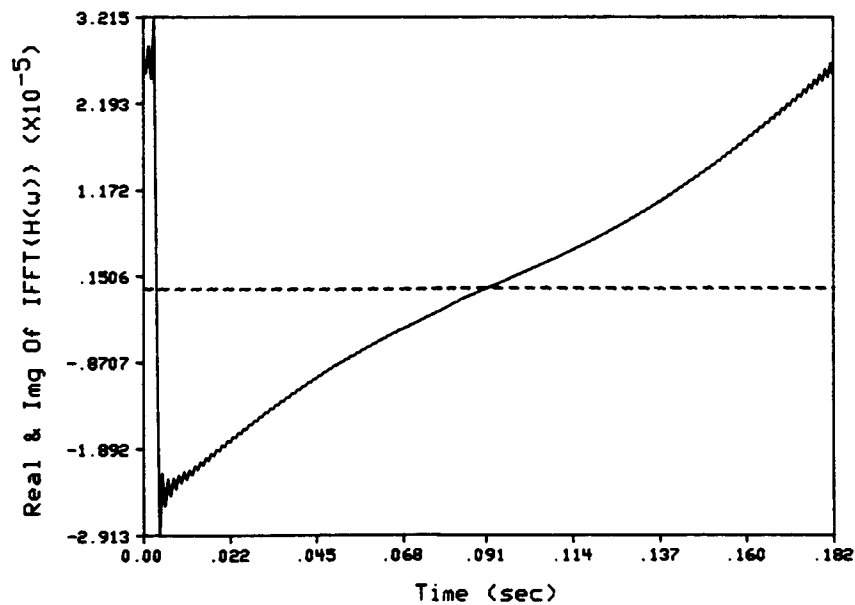
(b)

Figure 6.9 - Real And Imaginary Components Of (a)  $H^0(\omega)W(\omega)$  For  $\omega_n = 514.5$  rad/sec And (b) The Corresponding IFFT For Case ii.

— Real Component  
 - - - Imaginary Component



(a)



(b)

Figure 6.10 - Real And Imaginary Components Of (a)  $H^0(\omega)$  And (b) The Impulse Response Function For Case iii.

— Real Component  
 - - - Imaginary Component

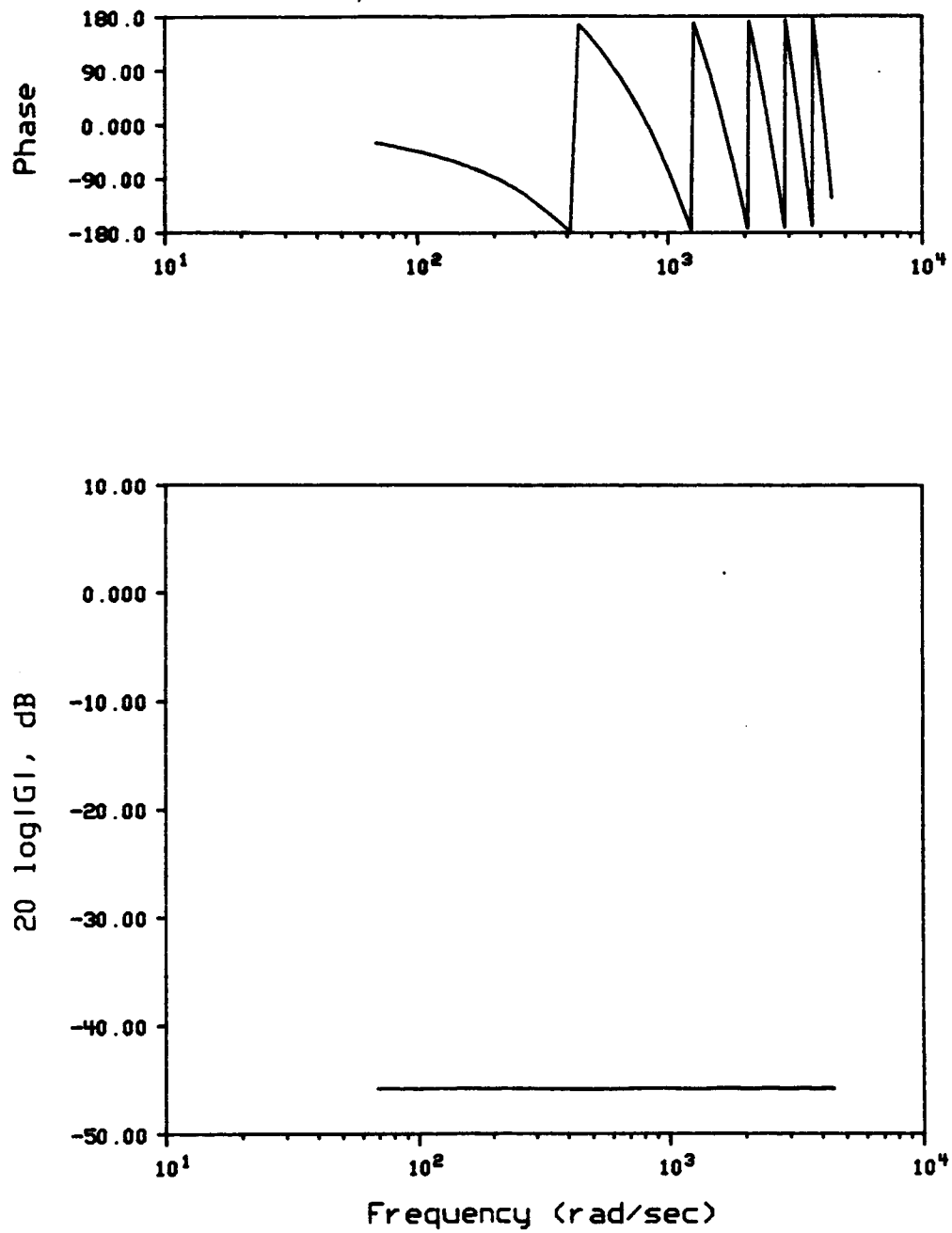
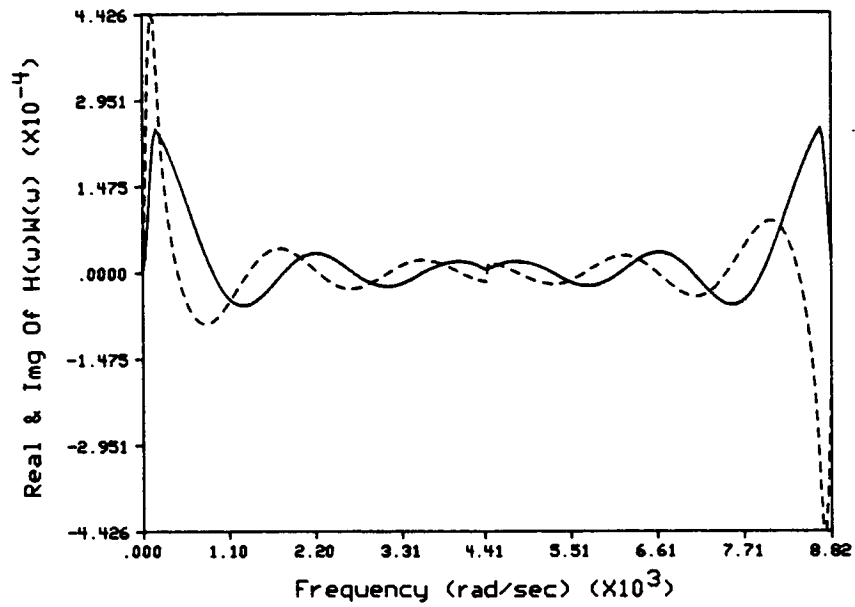
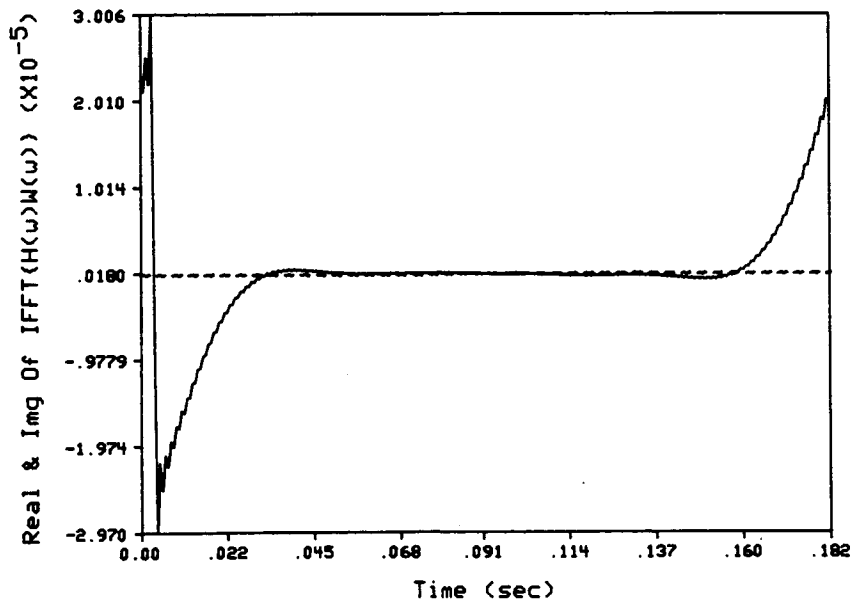


Figure 6.11 - Bode Diagram For Case iii



(a)



(b)

Figure 6.12 - Real And Imaginary Components Of (a)  $H^0(\omega)W(\omega)$  For  $\omega_b = 171.5$  rad/sec And (b) The Corresponding IFFT For Case iii.

— Real Component  
 - - - Imaginary Component

## CHAPTER 7

## CONCLUSIONS AND RECOMMENDATIONS

7.1 Conclusions

The objective of the research presented in this thesis was to develop a numerical analysis method for the evaluation of an optimal active noise controller for the generalized acoustic system. Such a generalized numerical technique is necessary for analysis of acoustic systems with irregularly shaped boundaries, irregular distributed sources, absorption, and consequently complex sound fields. The numerical technique chosen was an indirect boundary element method. The indirect boundary element method proved to be reasonably accurate, computationally efficient, and versatile.

Using the indirect boundary element method, three formulations of an optimal active noise controller were derived. The first formulation provided an optimal transfer function matrix between a known noise source strength and the secondary source strength(s) for the

interior problem. The optimal transfer function was obtained by minimizing the acoustic pressure at a number of discrete interior locations. The first formulation provided insight into the controllability and performance of the system. The second formulation provided an optimal transfer function between a known noise source strength and the secondary source strength(s) for the exterior problem. The optimal solution was determined by minimizing the total sound power radiated into the free field. The third formulation provided an optimal transfer function between the pressures at detector locations and the secondary source strength(s) for the interior problem. The optimal transfer function was obtained by minimizing the acoustic pressure at a number of discrete interior locations. The third formulation provided information on the controllability, stability, and observability of the system.

For all three formulations, the resulting control objective function was a real, positive definite, quadratic function of the secondary source strength(s). Thus, it is possible to attain a unique global minimum of the control objective function. For interior problems, it was found that an actuator is not necessarily needed for every mode of the enclosure to achieve a reduction. However, the global minimum attained with only a few actuators usually

does not have a zero value. Theoretically, complete, global attenuation of an enclosed noise field is possible if one properly employs an actuator for every enclosure mode. However, due to modal spill-over and the fact that there are an infinite number of enclosure modes, complete, global attenuation would require an infinite number of actuators in theory. In practice, a very large number of actuators would be needed for such a modal control strategy because most realistic cavities have high modal density beyond the frequency region of the first ten modes or so.

From the case studies presented, a number of general conclusions can be drawn.

- For enclosed sound fields, active noise control is effective at very low frequencies and at the enclosure resonances.
- The strategies for optimal active noise control in cavities are different for global and local control. For global control it is important to locate the secondary source(s) at the antinodal locations of the uncontrolled enclosure response. For local control it is important to locate the secondary source(s) such that the response at the observation point(s) due to the secondary source(s) is high.



- For local or global control in lightly damped enclosures, the active noise control system is likely to be unstable.
- For free field power radiation, effective active noise control is only attained when the secondary sources are located within a half wavelength of the noise producing mechanism. Additional secondary sources greatly improve the performance provided they are located within a half wavelength of the noise source.
- It is difficult to develop general guidelines for active noise controllers. Each application is unique. Thus, a versatile design analysis tool, such as the one presented here, is attractive.
- Analysis of optimal active noise controllers using a numerical procedure proved to be straightforward and versatile. Changes in boundary geometry, boundary conditions, source quantity and locations were easily implemented by changing input data.

## 7.2 Recommendations

Although the linear superparametric elements used for the current research proved to be reasonably accurate for most circumstances, a more sophisticated higher order element might be useful when accurate modeling of curved

boundary geometries is needed. Because a more sophisticated element would increase computational requirements, it should only be used when accurate results are desired for a specific application.

The control objective functions formulated in this thesis are not necessarily the only choices for all situations. For example, the control objective function formulated in chapters 4 and 6 did not consider the magnitudes of the secondary source strengths. Thus, in some circumstances the optimal solution gave secondary source strength magnitudes approaching infinity. A control objective function of the form

$$\Pi = \underline{p}^H \underline{W}_p \underline{p} + \underline{q}_s^H \underline{W}_s \underline{q}_s \quad (7.1)$$

may be more practical. Due to the flexibility of the indirect boundary element method, changing the control objective function only requires minor restructuring of the optimal active noise controller computer code.

An approach to active noise control which was not formulated in this thesis is that of controlling a portion of the enclosure boundary to achieve cancellation. The actuator in this approach would most likely be a shaker or an array of shakers attached to the boundary. To formulate this approach the boundary condition vector ( $\underline{\alpha}$ ) would be partitioned into a controllable part,  $\underline{\alpha}_c$ , and an

uncontrollable (noise) part,  $\underline{a}_{uc}$ . The resulting control objective function would then be minimized with respect to  $\underline{q}_s$  and  $\underline{a}_c$ .

## LIST OF REFERENCES

## LIST OF REFERENCES

- [1] G.E. Warnaka, "Active Attenuation Of Noise--The State Of The Art," Noise Control Eng. J., Vol. 18(3), (1982), pp. 100-110.
- [2] P. Lueg, 1936 U.S. Patent No. 2043416, "Process Of Silencing Sound Oscillations."
- [3] H.F. Olson and E.G. May, "Electronic Sound Absorber," J. Acoust. Soc. Am., Vol. 25(6), (1953), pp. 1130-1136.
- [4] H.F. Olson, "Electronic Control Of Noise, Vibration, and Reverberation," J. Acoust. Soc. Am., Vol. 28(5), (1956), pp. 966-972.
- [5] W.B. Conover and R.J. Ringlee, "Recent Contributions To Transformer Audible Noise Control," AIEE Transactions, Applications and Industry, 74, Part D, April 1955, pp. 77-86.
- [6] W.B. Conover, "Fighting Noise With Noise," Noise Control, Vol. 92(2), (1956), pp. 78-82.
- [7] W.B. Conover, 1957 U.S. Patent No. 2776020, "Noise Reducing System For Transformers."
- [8] H.G. Leventhall, "Active Attenuators: Historical Review And Some Recent Developments," Proc. of Internoise 80, (1980), pp. 679-682.
- [9] A.R.D. Curtis, P.A. Nelson, S.J. Elliott, and A.J. Bullmore, "Active Suppression Of Acoustic Resonances," J. Acoust. Soc. Am., Vol. 18(3), (1987), pp. 624-631.
- [10] A.R.D. Curtis, P.A. Nelson, and S.J. Elliot, "Active Control Of One-Dimensional Enclosed Sound Fields," Proc. of Internoise 85, (1985), pp. 579-582.

- [11] S.J. Elliott and P.A. Nelson, "The Implications Of Causality In Active Control," Proc. of Internoise 86, (1986), pp. 583-588.
- [12] M.C.J. Trinder and P.A. Nelson, "Active Noise Control In Finite Length Ducts," J. Sound & Vib., Vol. 89(1), (1983), pp. 95-103.
- [13] C.F. Ross, "An Algorithm For Designing A Broadband Active Sound Control System," J. Sound & Vib., Vol. 80(3), (1982), pp. 373-380.
- [14] M.A. Swinbanks, "The Active Control Of Sound Propagation In Long Ducts," J. Sound & Vib., Vol. 27(3), (1973), pp. 411-436.
- [15] M.A. Swinbanks, "Active Noise And Vibration Control," DAGA 85 (Stuttgart), (1985), pp. 87-101.
- [16] R.L. Wanke, 1972 U.S. Patent No. 3936606, "Acoustic Abatement Methods."
- [17] T. Enokida, H. Hamada, T. Miura, M. Takahashi, T. Kuribayashi and K. Asami, "Design Of Electronic Sound Cancellation System For Air Conditioning Ducts," Proc. of Internoise 86, (1986), pp. 589-594.
- [18] M. Takahashi, T. Kuribayashi, K. Asami, H. Hamada, T. Enokida, and T. Miura, "Electric Sound Cancellation In Air Conditioning Duct System," Proc. of Internoise 86, (1986), pp. 607-610.
- [19] Kh. Eghtesadi and H.G. Leventhall, "Active Attenuation Of Noise: The Chelsea Dipole," J. Sound & Vib., Vol. 75(1), (1981), pp. 127-134.
- [20] H.G. Leventhall and Kh. Eghtesadi, "Active Attenuation Of Noise: Dipole And Monopole Systems," Proc. of Internoise 79, (1979), pp. 175-180.
- [21] W.K.W. Hong, Kh. Eghtesadi, and H.G. Leventhall, "The Tight-Coupled Monopole (TCM) And Tight-Coupled Tandem (TCT) Attenuators: Theoretical Aspects And Experimental Attenuation In An Air Duct," J. Acoust. Soc. Am., Vol. 81(2), (1987), pp. 376-388.
- [22] Kh. Eghtesadi, W.K.W. Hong, and H.G. Leventhall, "The Tight-Coupled Monopole Active Attenuator In A Duct," Noise Control Eng. J., Vol. 20(1), (1983), pp. 16-20.

- [23] Kh. Eghtesadi and H.G. Leventhall, "Active Attenuation Of Noise--The Monopole System," J. Acoust. Soc. Am., Vol. 71(3), (1982), pp. 608-611.
- [24] J.E. Ffwocs Williams, I. Roebuck, and C.F. Ross, "Anti-Phase Noise Reduction," Phys. Technol. J., Vol. 16(1), (1985), pp. 19-24.
- [25] R.J. Silcox and S.J. Elliot, "Applicability Of Superposition And Source Impedance Models Of Active Noise Control Systems," Proc. of Internoise 85, (1985), pp. 587-590.
- [26] R.D. Ford, "Power Requirements For Active Noise Control In Ducts," J. Sound & Vib., Vol. 92(3), (1984), pp. 411-417.
- [27] R.D. Ford, "Where Does The Power Go?," Proc. ICA 11th Congress, Vol. 8, (1983), pp. 277-280.
- [28] A.J. Bullmore, P.A. Nelson, and S.J. Elliott, "Active Control Of Harmonic Enclosed Sound Fields Of Low Modal Density; A Computer Simulation," Proc. Institute of Acoust. (IOA) 7, (1985), pp. 55-64.
- [29] A.J. Bullmore, S.J. Elliott, and P.A. Nelson, "The Active Minimisation Of Periodic Sound In Enclosures; An Experimental Investigation," Proc. of Internoise 85, (1985), pp. 575-578.
- [30] P.A. Nelson, A.R.D. Curtis, S.J. Elliott, "Quadratic Optimisation Problems In The Active Control Of Free and Enclosed Sound Fields," Proc. Institute of Acoust. (IOA) 7, (1985), pp. 45-53.
- [31] A.J. Bullmore, P.A. Nelson, and S.J. Elliott, "Active Minimisation Of Acoustic Potential Energy In Harmonically Excited Cylindrical Enclosed Sound Fields," AIAA Paper No. 86-1958 (1986).
- [32] H.C. Lester and C.R. Fuller, "Active Control Of Propeller Induced Noise Fields Inside A Flexible Cylinder," AIAA Paper No. 86-1957 (1986).
- [33] G.E. Warnaka, J. Tichy, J.M. Zalas, and L.A. Poole, "Active Control Of Noise In Interior Spaces," Proc. of Internoise 83, (1983), pp. 415-418.

- [34] L.J. Oswald, "Reduction Of Diesel Engine Noise Inside Passenger Compartments Using Active, Adaptive Noise Control," Proc. of Internoise 84, (1984), pp. 483-488.
- [35] T.S. Berge, "Active Noise Cancellation Of Low Frequency Sound Inside Vehicle Cabs," Proc. of Internoise 83, (1983), pp. 457-460.
- [36] M. Nadim and R.A. Smith, "Synchronous Adaptive Cancellation In Vehicle Cabs," Proc. of Internoise 83, (1983), pp. 461-464.
- [37] P.A. Nelson, A.R.D. Curtis, and S.J. Elliott, "On The Active Absorption Of Sound," Proc. of Internoise 86, (1986), pp. 601-606.
- [38] H. Levine, "On Source Radiation," J. Acoust. Soc. Am., Vol. 68(4), (1980), pp. 1199-1205.
- [39] G.A. Mangiante, "Active Sound Absorption," J. Acoust. Soc. Am., Vol. 61(6), (1977), pp. 1516-1523.
- [40] M.J.M. Jessel and O.L. Angevine, "Active Acoustic Attenuation Of A Complex Noise Source," Proc. of Internoise 80, (1980), pp. 689-694.
- [41] M.J.M. Jessel and G.A. Mangiante, "Active Sound Absorbers In An Air Duct," J. Sound & Vib., Vol. 23(3), (1972), pp. 383-390.
- [42] O.L. Angevine, "Active Acoustic Attenuation Of Electric Transformer Noise," Proc. of Internoise 81, (1981), pp. 303-306.
- [43] M.C.J. Trinder, G.B.B. Chaplin, and P.M. Nelson, "Active Control Of Commercial Vehicle Exhaust Noise," Proc. of Internoise 86, (1986), pp. 611-616.
- [44] P.K. Banerjee and R. Butterfield, Boundary Element Methods In Engineering Science, McGraw-Hill, London, 1981.
- [45] C.A. Brebbia and S. Walker, Boundary Element Techniques In Engineering, Newnes-Butterworths, London, 1980.



- [46] C.R. Kipp, "Prediction Of Sound Fields In Acoustical Cavities Using The Boundary Element Method," M.S. Thesis, Purdue University, 1985.
- [47] B.K. Gardner, "Noise Source Identification Using A Numerical/Experimental Helmholtz Integral Equation Method," M.S. Thesis, Purdue University, 1987.
- [48] Op. Cit., Ref. 44, pp. 122.
- [49] Op. Cit., Ref. 46, pp. 38.
- [50] R.J. Bernhard, B.K. Gardner, C.G. Mollo, and C.R. Kipp, "Prediction Of Sound Fields In Cavities Using Boundary Element Methods," AIAA Paper No. 86-1864 (1986).
- [51] D.J. Zimmerle and R.J. Bernhard, "Integration Of Certain Singular Boundary Integrals For Applications In Linear Acoustics," Herrick Laboratory Report No. HL 85-12, Purdue University, 1985.
- [52] J.N. Reddy, An Introduction To The Finite Element Method, McGraw-Hill, New York, 1984, pp. 159.
- [53] Op. Cit., Ref. 46, pp. 80.
- [54] L.E. Kinsler, A.R. Frey, A.B. Coppens, and J.V. Sanders, Fundamentals Of Acoustics, Third Edition, John Wiley & Sons, New York, 1982, pp. 163.
- [55] Op. Cit., Ref. 54, pp. 168.
- [56] S. Temkin, Elements Of Acoustics, John Wiley & Sons, New York, 1981, pp. 132.
- [57] Op. Cit., Ref. 54, pp. 451.
- [58] R.C. Dorf, Modern Control Systems, Third Edition, Addison-Wesley, London, 1980, pp. 111.
- [59] R.W. Ramirez, The FFT, Fundamentals And Concepts, Prentice Hall, London, 1985, pp. 29.
- [60] Op. Cit., Ref. 59, pp. 68.
- [61] A.V. Oppenheim and R.W. Schaffer, Digital Signal Processing, Prentice Hall, London, 1975, pp. 242.